

Detection of exozodiacal dust: a step toward Earth-like planet characterization with infrared interferometry

THÈSE

présentée pour l'obtention du diplôme de

Docteur en sciences

par

Denis Defrère

Soutenue publiquement le 7 décembre 2009 devant le Jury composé de:

Président : Pr. Serge HABRAKEN

Superviseur : Pr. Jean SURDEJ

Examinateurs : Dr. Olivier ABSIL

Dr. Vincent COUDÉ DU FORESTO

Dr. Malcolm FRIDLUND

Pr. Claude JAMAR

Pr. Jean-Pierre SWINGS

Acknowledgments

The work presented in this thesis has greatly benefited from interactions with many people. First of all, I want to express my deepest gratitude to my academic supervisor, Professor Jean Surdej. Thank you Jean for giving me the opportunity to work in your team, and all your wise advice all along this thesis. I have really appreciated your unconditional enthusiasm and continuous encouragement. Thank you also for having always provided me the financial support that I need to attend my favourite conferences and meetings.

My utmost gratitude goes also to Dr. Olivier Absil for his expert advice and constant guidance all along my PhD thesis. Olivier largely contributed to this thesis, and has been an invaluable source of inspiration since my first steps as PhD student. The present work greatly benefits from his work and insights into stellar/nulling interferometry. I am also very grateful to him for having fostered so many fruitful international collaborations and for his diligence with the corrections of my manuscripts.

I am also grateful to Pr. Serge Habraken, Dr. Vincent Coudé du Foresto, Dr. Malcolm Fridlund, Pr. Claude Jamar, and Pr. Jean-Pierre Swings, for accepting to read and evaluate this dissertation. I also want to express a particular thank to Pr. Jean-Pierre Swings who has given me the opportunity to achieve important experiences in my starting scientific career.

My warmest thank goes also to the former DARWIN Team at ESA/ESTEC. Special thanks go to Malcolm Fridlund and Anders Karlsson, for inviting me at the TE-SAT meetings, and Roland den Hartog for his expert advice about the simulation of nulling interferometers. I take also the opportunity to thank DARWIN/PEGASE collaborators: Marc Barillot, Jean-Michel Le Duigou, Alain Léger, Marc Ollivier, and Yvan Stockman. I wish also to thank American colleagues for important collaborations on TPF/FKSI: Richard Barry, William Danchi, Lisa Kaltenegger, Peter Lawson, Oliver Lay and Chris Stark.

I am also very grateful to my CHARA/FLUOR colleagues for all the good work in obtaining nice fringes at the CHARA array on the Mount Wilson and memorable moments spent in Los Angeles. Thanks a lot to Jean-Charles Augereau, Vincent Coudé du Foresto, Emmanuel Di Folco, Pierre Kervella, Antoine Mérand, and Theo ten Brummelaar. Thanks also to Jean-Philippe Berger, Jean-Baptiste Le Bouquin and Hughes Sana, VLTI collaborators for the good work done in Paranal and the nice moments spent in Santiago.

I would like also to acknowledge the support of all my colleagues and friends at the “Institut d’Astrophysique et de Géophysique de Liège”. First, I would like to thank my officemate, Arnaud Magette (aka Mister ILMT), for the countless discussions about nothing and everything, the famous “tite heure” in which we rebuilt the world, as well as his unconditional availability and kindness all along this thesis. Special thanks go also to Charles Hanot, Emilie Herwats, Dimitri Mawet, and Pierre Riaud (aka Poulpe), who have nicely carried this work forward. Thanks also to Méla, Gi, Lau, Nat, and Antho with whom I spent many good moments at the institute. I would like also to express a particular thought in the memory of Olivier Garbet. Finally, I want also to thank Denise Caro for taking care of my travels and refunds with so much availability and patience.

Last but not least, I take a particular pleasure in thanking my parents and family for their incommeasurable support back from the beginning of my studies. Thanks also a lot to all my friends, particularly Add, Chris, Fred, Greg, Minh, Pierre, Raph and Ren for their support and help during this thesis and a long time before.

This research was supported by a fellowship from the Belgian National Science Foundation (“Boursier FRIA”), the Communauté française de Belgique - Actions de recherche concertées - Académie universitaire Wallonie-Europe, and the International Space Science Institute (ISSI) in Bern, Switzerland (“Exozodiacal Dust discs and Darwin” working group, <http://www.issibern.ch/teams/exodust/>).

Contents

Preface	1
I Introduction	3
1 Extrasolar planetary science	5
1.1 Extrasolar planets	5
1.1.1 Planet population in our galaxy	6
1.1.2 Principles of planet formation	8
1.1.3 Characterization by transit and direct imaging	11
1.1.4 Searching for life	15
1.2 Circumstellar discs	18
1.2.1 Protoplanetary discs	19
1.2.2 Debris discs	21
1.3 Detection and characterization techniques	24
1.3.1 Overview	24
1.3.2 Indirect detection methods	25
1.3.3 Direct detection methods	28
1.4 Prospects for future observations	29
1.4.1 Extrasolar planets	29
1.4.2 Circumstellar discs	31
II Study of debris discs with infrared stellar interferometry	33
2 Overview of stellar interferometry	35
2.1 The need for interferometry	35
2.2 Basics of stellar interferometry	36
2.2.1 Interferometric observables	38
2.2.2 Fringe signal coding	39
2.2.3 Van Cittert-Zernike theorem	40
2.3 Applications of stellar interferometry	42

2.3.1	First and second generation	42
2.3.2	A new generation	43
2.3.3	Upcoming facilities	44
2.3.4	Major scientific results	45
3	Debris disc detection with IOTA/IONIC	47
3.1	Scientific context and goals of the study	47
3.2	The IOTA/IONIC instrument	48
3.3	Principle of interferometric observations	49
3.3.1	Extracting visibility measurements	49
3.3.2	Strategy for near-infrared debris disc detection	51
3.4	Observations of two A-type stars with IOTA/IONIC	53
3.4.1	The targets: Vega and β Leo	53
3.4.2	The observations	55
3.4.3	Data analysis	56
3.4.4	Data reduction	66
3.4.5	Interpretation of the data	69
3.5	Ongoing work and prospects	69
3.5.1	Debris disc programme at the CHARA array	69
3.5.2	Prospects with the Keck nuller	70
3.5.3	Further perspectives: Antarctica and space	71
III	Debris discs: prospects with infrared nulling interferometry	73
4	Overview of nulling interferometry	75
4.1	Principle of nulling interferometry	75
4.1.1	Instrument response	76
4.1.2	Main noise sources	79
4.1.3	Sensitivity to perturbations	81
4.2	The need for chopping	82
4.3	Instability noise	84
4.4	First ground-based nulling instruments	85
4.4.1	BLINC at the MMT	85
4.4.2	Keck Interferometer Nuller (KIN)	86
4.4.3	Large Binocular Telescope Interferometer (LBTI)	86
4.5	The European projects	87
4.5.1	GENIE	87
4.5.2	ALADDIN	88

5 Pegase and FKSI: toward the detection of zodiacal cloud analogs	91
5.1 Introduction	91
5.2 Instrumental concepts	92
5.2.1 PEGASE	93
5.2.2 The Fourier-Kelvin Stellar Interferometer (FKSI)	94
5.3 Main scientific objectives	95
5.3.1 Circumstellar disc science	95
5.3.2 Sub-stellar objects	97
5.3.3 Additional programmes	98
5.4 Performance for exozodiacal disc detection	98
5.4.1 The GENIEsim software	98
5.4.2 Vibrations in the ambient space environment	100
5.4.3 Real-time correction of spacecraft vibrations	102
5.4.4 Paper: <i>Nulling interferometry: performance comparison between space and ground-based sites for exozodiacal disc detection</i>	102
5.5 Summary	114
IV Unveiling hidden worlds with space-based nulling interferometry	115
6 Prospects for single infrared Bracewell interferometers	117
6.1 Science case	118
6.1.1 Hot extrasolar giant planets	118
6.1.2 Super-Earth extrasolar planets	118
6.2 PEGASUS: an enhanced version of PEGASE	120
6.2.1 Concept overview	120
6.2.2 The split-pupil technique	121
6.2.3 The OPD modulation technique	122
6.3 Performance predictions for PEGASE and PEGASUS	123
6.3.1 The simulation software	124
6.3.2 Paper: <i>Potential of space-based infrared Bracewell interferometers for planet detection</i>	127
6.3.3 Complementary results	141
6.4 Performance predictions for FKSI	143
6.4.1 Detection of known super-Earths	143
6.4.2 General sensitivity	145
6.4.3 An enhanced version of FKSI	146
6.5 Summary	147

7 The exo-Earth characterization missions	149
7.1 The DARWIN/TPF mission	149
7.1.1 Instrumental concept	149
7.1.2 Scientific objectives	151
7.2 Instability noise	152
7.3 Science performance predictions	155
7.3.1 DARWINsim, the DARWIN science simulator	155
7.3.2 Paper: <i>Nulling interferometry: Impact of exozodiacal clouds on the performance of future life-finding space missions</i>	157
7.4 Summary	176
Conclusion	177
Notations and acronyms	179
Bibliography	183

Preface

The existence of other habitable worlds and the possible development of life elsewhere in the Universe have been among fundamental questions of mankind for thousands of years. Already in antiquity, the presence of planets like Earth, orbiting other stars and hosting a biological activity, was speculated (Epicurus, 300 B.C.). These interrogations, which remained philosophical for at least 2300 years, are today at the dawn to be answered in scientific terms. One key year was 1995 with the discovery of the first extrasolar planet orbiting around a solar-type star (namely *51 Peg b*, Mayor and Queloz 1995). About 400 extrasolar planets are known today and the recent detection of Earth-mass planets suggests that low mass extrasolar planets exist in abundance. The possibility to identify habitable worlds and even life among them currently contributes to the growing interest about their nature and properties. In particular, another milestone in the quest for extrasolar life has been reached in 2007 with the conclusive detection of water vapor (presumably necessary for the emergence of life) in the atmosphere of hot giant extrasolar planets (Tinetti et al. 2007; Grillmair et al. 2008). While it is unlikely that life exists on such planets, this result supports the idea that significant quantities of water could exist in extrasolar planetary systems.

Most known extrasolar planets have been detected indirectly by measuring the effects they induce on their parent star. Except for bright transiting systems, indirect detections generally do not enable the characterization of planetary atmospheres, mandatory to search for traces of biological activity. Indeed, directly detecting planets around distant stars is a very challenging task due to both the high contrast and the small angular separation between a star and its environment. To tackle this fantastic observational challenge, infrared interferometric techniques have emerged during the past decades. The principle of interferometry is to synthesise the resolving power of a large monolithic telescope by combining the light collected by several smaller telescopes, separated by a distance equivalent to the required diameter of the large telescope. In addition to providing the required spatial resolution, this technique can also allow to strongly reduce the stellar emission by combining the light from two telescopes in phase opposition (so that a dark fringe appears on the line of sight). This technique first proposed by Bracewell (1978), is referred to as *nulling interferometry*. Whereas it is already used in several ground-based instruments, ambitious projects of space-based nulling interferometers promise outstanding science within the next decades. In particular, discovering other worlds similar to the Earth and probing their atmosphere for evidence of life seem within reach with future exo-Earth characterization nulling interferometry missions. By observing in the mid-infrared (6-20 μm), these space-based nulling interferometers would enable the spectroscopic characterization of the atmosphere of habitable extrasolar planets orbiting nearby main sequence stars. The ability to study distant planets will however strongly depend on exozodiacal dust clouds around the stars, which can hamper the planet detection. In that respect, several proposals have been made, using the simplest nulling scheme composed of two collectors (i.e., the original Bracewell interferometer), in order to characterize the circumstellar dust clouds around nearby main sequence stars. Two of these projects are named PEGASE and FKSI. They are conceived as scientific precursors and technological demonstrators for future exo-Earth characterization missions. Their main scientific goals would be to enable the high-angular resolution study of extrasolar planets and exozodiacal dust clouds at infrared wavelengths.

The present dissertation is devoted to the characterization of extrasolar planetary systems using the high angular resolution and dynamic range capabilities of infrared interferometric techniques. After reviewing the current status of extrasolar planetary science in Chapter 1, the second part of this work focuses on the detection of warm dust within the first few astronomical units of massive debris discs around nearby stars with current interferometric facilities (Chapters 2 and 3). In Chapter 4, the principles of nulling interferometry are presented, together with a review of existing facilities. The prospects for the detection and characterization of circumstellar dust around nearby main sequence stars are then presented in Chapter 5, as well as a performance comparison between major ground- and space-based projects.

The last two chapters are dedicated to the search for extrasolar planets from space. In Chapter 6, we investigate the performance for planet detection with PEGASE and FKSI, focusing on hot giant and super-Earth extrasolar planets. Two ambitious Bracewell interferometers, which have been tuned to probe the habitable zone of nearby main sequence stars, are also discussed and investigated: an enhanced version of PEGASE (namely PEGASUS) and an upgraded version of FKSI. Finally, we investigate in Chapter 7 the performance of future exo-Earth characterization missions, and address particularly two major noise sources: exozodiacal dust and instability noise. Considering a space-based infrared nulling interferometer in the Emma X-array configuration, we derive an upper limit on the tolerable exozodiacal dust density, and review the constraints on the instrument stability. We conclude the study by reporting the science performance predictions for future life-finding space mission, the ultimate goal being to characterize the atmosphere of Earth-like extrasolar planets.

Part I

Introduction

1

Extrasolar planetary science

Contents

1.1	Extrasolar planets	5
1.1.1	Planet population in our galaxy	6
1.1.2	Principles of planet formation	8
1.1.3	Characterization by transit and direct imaging	11
1.1.4	Searching for life	15
1.2	Circumstellar discs	18
1.2.1	Protoplanetary discs	19
1.2.2	Debris discs	21
1.3	Detection and characterization techniques	24
1.3.1	Overview	24
1.3.2	Indirect detection methods	25
1.3.3	Direct detection methods	28
1.4	Prospects for future observations	29
1.4.1	Extrasolar planets	29
1.4.2	Circumstellar discs	31

The study of extrasolar planets and the search for other habitable worlds are just beginning. About 400 extrasolar planets are known today and the recent detection of planets with masses approximately 2 times that of Earth confirms that low mass extrasolar planets exist. The possibility to identify habitable worlds and even life among them currently contributes to the growing interest about their nature and properties. Daunting questions about their formation, their evolution, and their ability of sustaining life, are asked more than ever before. These interrogations have triggered the emergence of new technological concepts and a strong will for pushing existing technologies to their limit, with the purpose of tackling the fantastic observational challenges. In the coming decades, next generation space instruments will directly detect photons from planets in the habitable zone of nearby stars, opening the era of comparative planetology. After a brief overview of the current observational results for extrasolar planets and circumstellar discs, this chapter presents the main instruments which promise exceptional breakthroughs in the field of exoplanetary science.

1.1 Extrasolar planets

Extrasolar planets became reality in the 1990s with the first discoveries by Wolszczan and Frail (1992) and by Mayor and Queloz (1995). Since then, the observational field of extrasolar planet search has

seen a rapid evolution leading to numerous additional discoveries of planets orbiting other stars. Several instruments are now operational or foreseen for the near future and first dedicated space-based telescopes are currently finding planets. So far, about 400 extrasolar planets have been reported¹, suggesting that planetary systems are very common in our galaxy. Some of these discovered planets were totally unexpected. After the surprise that planets exist around pulsars (Wolszczan and Frail 1992), the first extrasolar planet detected around another solar-type star (namely *51 Peg*) unveiled a new type of planets: hot Extrasolar Giant Planets (EGPs). Unlike any planet in our Solar system, “*51 Peg b*” is a Jupiter-mass planet (minimum mass of $0.468 M_J$) with a very short orbital period (4.23 days). This corresponds to a semi-major axis of 0.052 astronomical unit (AU) which is much closer than Mercury from the Sun (0.39 AU). Due to this proximity to its parent star, “*51 Peg b*” is heated up to more than 1000 K and is often referred to as a “hot Jupiter”. The existence of such a massive planet that close of its parent star was not predicted by theoretical models of planetary system formation. Another interesting discovery was the extrasolar planetary system with three Neptune-mass planets around HD 69830 (Lovis et al. 2006; Alibert et al. 2006). These discoveries have triggered numerous theoretical studies about the formation and evolution of these planets. Key physical processes in planet formation and evolution could be identified whose importance was not fully realized in previous works based on the Solar system alone.

1.1.1 Planet population in our galaxy

Most of the planets discovered so far, i.e. 377 out of 404 planets, were indirectly detected by the so-called radial velocity (RV) technique in which the wobble of the star moving around the center of mass of the star-planet system is measured with spectral Doppler information. This provides a measurement of $M \sin i$, where M is the planetary mass and i the planetary system inclination with respect to the plane of the sky. The latter being generally unknown, only a lower limit can be inferred for the planetary mass. To date, the lowest mass planet detected by RV is the newly discovered *Gliese 581e* (Mayor et al. 2009b), which has a minimum mass of $1.9 M_\oplus$. This planet orbits at 0.03 AU around a star 3 times less massive than the Sun and causes a radial velocity deflection of about 1.2 meters per second (m/s). Note that to detect Earth-mass planets in the middle of the habitable zone (see the definition in Section 1.1.4), the accuracy on velocity measurements has to be at least a factor 10 better, since Earth causes a reflex motion of order 0.1 m/s in the solar spectrum. Another successful technique for extrasolar planet detection relies on the dimming of the apparent stellar flux as the planet transits in front of the stellar photosphere. Even though the probability to detect such a transit is rather low, 62 hot planets have either been found or confirmed using this technique. From space, transit measurements have recently unveiled *CoRoT-7b*, a $1.68-R_\oplus$ planet orbiting at 0.017 AU around a G9V star located at 140 pc (Leger et al. 2009) while from the ground, transit measurements have enabled the detection of a Neptune-mass planet (*GJ 436b*, Butler et al. 2004; Gillon et al. 2007; Figueira et al. 2009). The transit method has the advantage to provide the radius of the extrasolar planet, which allows to constrain the planet bulk composition if the planet mass is known by radial velocity measurements.

The success of these two techniques is however biased toward the detection of high mass/short orbital period planets. For RV detection, high mass and short orbital period planets are likely to produce a large Doppler shift of the stellar light (depending on the orbital inclination). For the transit technique, massive planets occult a large fraction of the stellar light with a probability inversely proportional to the orbital period. This observational bias explains why among the 404 planets detected so far, about 100 have been found with semi-major axes smaller than 0.1 AU (see Figure 1.1, left), i.e. with orbital periods shorter than about 10 days. The mass distribution of the detected planets is shown in Figure 1.1 (right), with masses ranging from the deuterium-burning limit of $13 M_J$ (Chabrier et al. 2000) down to 2 Earth masses (1 Earth mass $\simeq 0.0031 M_J$). These planets are found in orbits ranging from less than 0.05 AU

¹see Schneider (2009) for an up-to-date list.

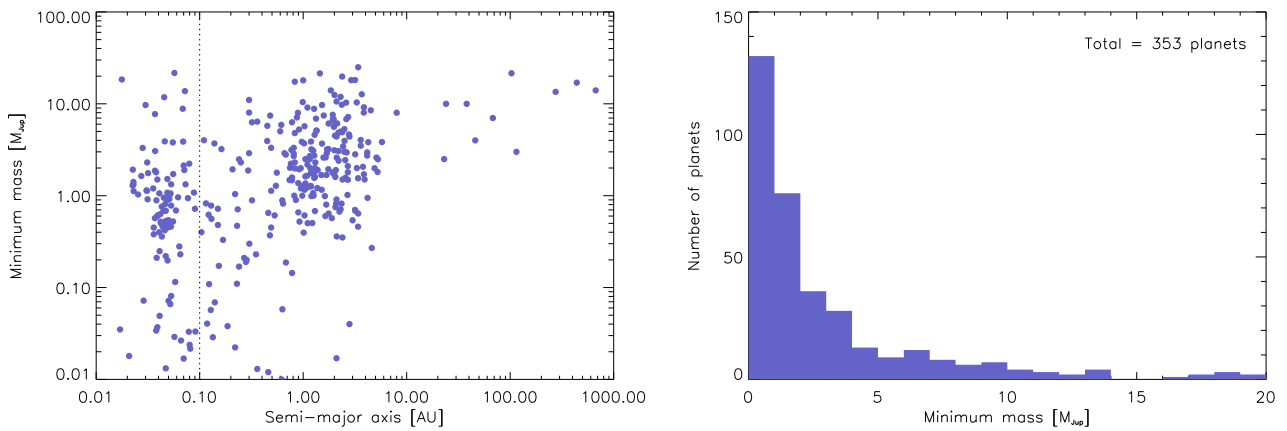


Figure 1.1: *Left:* Extrasolar planet population synthesis (August 2009), distributed as minimum mass versus semi-major axis. Hot regime planets are concentrated at the left of the dotted line. *Right:* number of detected extrasolar planets versus minimum mass. The lack of companions with $M \sin i$ larger than $13 M_J$ confirms the presence of a “brown-dwarf desert” (data taken from Schneider 2009).

out to 670 AU with a wide range of orbital eccentricities. The dearth of companions with $M \sin i$ larger than $13 M_J$, suggests the presence of a “brown dwarf desert”, at least for companions with orbital periods up to about 10 days.

There are several reasons to expect that many more small planets exist, and will be detected with more sensitive instruments (see Section 1.1.2). Despite this inevitable observational bias, remarkable statistical properties have emerged from the 404 known planets:

- The incidence of planets around solar-type stars has been estimated by Lineweaver and Grether (2003). At least $\sim 9\%$ of Sun-like stars have planets in the mass and orbital period ranges $M \sin i > 0.3 M_J$ and $P < 13$ years, and at least $\sim 22\%$ have planets in the larger range $M \sin i > 0.1 M_J$ and $P < 60$ years. This large area of the log(mass)-log(period) plane covers less than 20% of the area occupied by our planetary system, suggesting that this estimate still constitutes a lower limit of the true fraction for Sun-like stars with planets.
- About 40 multiple systems have also been detected so far presenting a tendency for the inner planets to be less massive, which can be interpreted either as suppressed accretion from the outer disc or as a mere selection effect (Marcy et al. 2005).
- The median semi-major axis is about 0.8 AU, partly reflecting an instrumental bias toward smaller values, but also showing that a large number of giant planets exist much closer to their parent star than would be expected from our Solar system case. The inference is that they have migrated from larger distances, which in turn raises many questions about what started and stopped the migration, what happened to planets that were in the migration path, and whether the stars without such migrated planets have terrestrial planets instead (see Section 1.1.2 for further details).

Further statistical investigations have also revealed correlations between stellar metallicity and planet occurrence rate, suggesting that planets form more easily in a metal-rich environment (e.g., Marcy et al. 2005; Santos et al. 2005). Other unexpected behaviors are the prevalence of high eccentric orbits. This is in sharp contrast with the planets of our Solar system. These observational results provide strong reasons to believe that extrasolar planets are formed by a different mechanism than low-mass companion stars and are thereby putting strong constraints on the planetary formation theories.

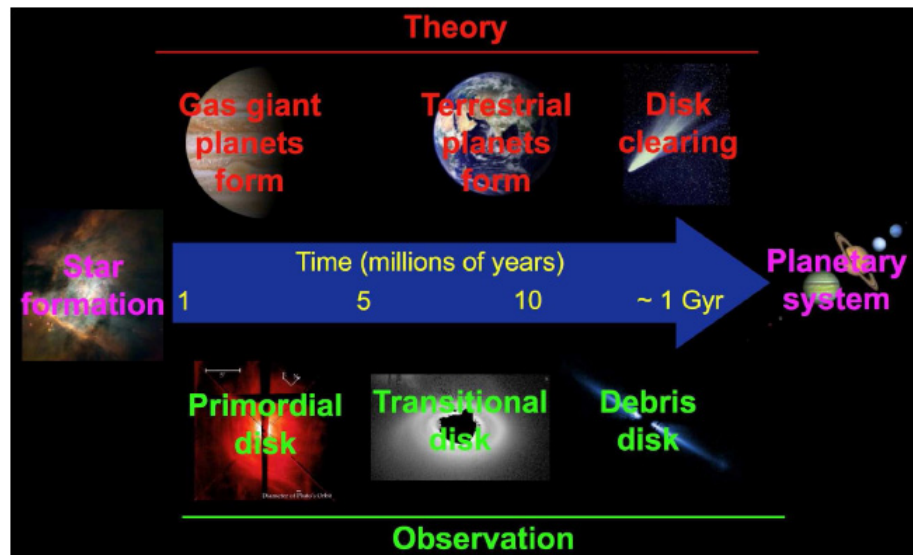


Figure 1.2: Timeline for planet formation and evolution of circumstellar discs (Figure from Roberge et al. 2009). Above the arrow, the main theoretical phases in planetary formation are shown. Below, three classes of circumstellar discs are identified. A coronagraphic image of a disc from each class is shown; AB Aurigae at left (Grady et al. 1999), HD 141569A in the center (Clampin et al. 2003), and AU Microscopii at right (Krist et al. 2005).

1.1.2 Principles of planet formation

Understanding the formation and evolution of planetary systems has become one of the biggest challenges in astronomy, since the imaging of a debris disc around β Pictoris in the eighties (Smith and Terrile 1984) and the discovery of the first extrasolar planet around the Sun-like star 51 Peg during the nineties (Mayor and Queloz 1995). The current paradigm for formation of a mature planetary system has three main phases: formation of gas giant planets, formation of terrestrial planets, and removal of most leftover planetesimals (i.e., asteroids and comets). This timeline is represented in Figure 1.2. Observations have revealed three classes of circumstellar discs that appear to roughly correspond to each phase: primordial discs which are massive and gas-rich, transitional discs which appear to be clearing material from their inner discs and debris discs which are made of material produced by the destruction of planetesimals (see Section 1.2 for further details). The discovery of such discs around nearby stars has provided the opportunity to study planet formation in real time, rather than extrapolating backward from completed or mature systems like the Solar system. These different phases are described hereafter.

Giant planet formation

The presence of planets orbiting other stars is a natural consequence of the process of stellar formation (see e.g., Bodenheimer 1997; Mannings et al. 2000; Boss 2003). Stars are formed out of interstellar clouds of gas and dust where turbulent processes lead sufficiently dense regions to collapse, leading to an embedded pre-stellar core and a circumstellar disc, which retains most of the angular momentum of the cloud. The planets are believed to form from the material in the circumstellar disc, which is in this stage referred to as the “protoplanetary” disc. This material consists in micron-size particles of rocky or icy dust, which makes up about 1% of the mass of a typical protoplanetary disc.

At this stage, two representative models have been proposed to explain the planetary formation process; the core-accretion scenario (Pollack 1984) and the disc instability scenario (Cameron 1978). According to the core-accretion scenario, a heavy element core is first assembled by the accretion of

planetesimals in the outer part of protoplanetary discs, beyond the snow line² (Sasselov and Lecar 2000). As these cores grow, they eventually become sufficiently massive to gravitationally bind the nebular gas. While this gas accretion proceeds slowly in the early phases, it eventually runs away when a critical mass is reached (the so-called cross-over mass, typically at around 10 Earth masses), allowing the formation of a gas giant within 10 Myr (Pollack et al. 1996). Because this timescale is uncomfortably close to the typical lifetime of protoplanetary discs, believed to be of the order of 1-10 Myr (Haisch et al. 2001), a long-discarded mechanism, based on local gravitational collapse of the protoplanetary disc, has been reevaluated by Boss (1998) to allow for a more rapid formation of giant planets. In this disc instability scenario, the discs fragment into a dense core if it is sufficiently massive. Such clumps can contract to form giant gaseous planets in several hundred years. Gas giants are quickly formed before the gas in the disc depletes. Unfortunately, this model is unable to account for the period-eccentricity relations of the observed systems.

In any case, formation scenarios require giant planets to be formed in the outer part of protoplanetary discs. These theories are obviously incompatible with the observation of giant planets orbiting close to their parent star, where a sufficient amount of gas is not available to form such large bodies and the temperature far too high to allow the condensation of solid particles. This apparent contradiction is now understood in the framework of migrating planets, a process already suggested in the eighties in which planetary orbits evolve subsequent to planet formation (Goldreich and Weber 1980). Migration involves the tidal interaction between the protoplanet and the gas in the surrounding protoplanetary disc by means of angular momentum exchange and density waves that propagate on both sides of the planet orbit (Goldreich and Tremaine 1979; Lin et al. 1996). Three types of migration mechanisms can be distinguished:

- *type I migration*, for which planetary embryos embedded in a protoplanetary disc suffer a decay in semi-major axis due to the asymmetric torques produced by the interior and exterior wakes raised by the body (Ward 1997). The increased amount of mass outside the planetary orbit causes the planet to lose angular momentum as the material outside its orbit is moving more slowly. The planet then migrates inwards on timescales short relative to the million-year lifetime of the disc;
- *type II migration*, for which the planet is sufficiently massive (more than about 10 Earth masses) to open a gap in the protoplanetary disc (Goldreich and Weber 1980; Lin and Papaloizou 1986). As material enters the gap over the timescale of the larger accretion disc, the planet and the gap move inward over the accretion timescale of the disc. This is presumably how hot EGPs form;
- *type III migration*, which is a new form of potentially fast migration applicable to massive discs that could be driven by orbital torques (Ward 2004).

Comparison with observations shows that 90% of the detected planets are consistent with the core-accretion model regardless of the spectral type (Matsuo et al. 2007). The remaining 10% are not in the region explained by the core-accretion model, but are instead explained by the disc instability model. Extended core-accretion models, including in particular migration, disc evolution and gap formation, lead to a much more rapid formation of giant planets, making it compatible with the typical disc lifetimes inferred from observations of young circumstellar discs (Alibert et al. 2005). This speed up is due to the fact that migration prevents the severe depletion of the feeding zone as observed in classical core accretion simulations. Hence, the growing planet is never isolated and it can reach the cross-over mass over a much shorter timescale. Based on this extended model, synthetic planet populations can be computed, allowing a statistical comparison with observations (see Figure 1.3). Several studies have shown that the distribution of observed planets in orbital radius and planetary mass is broadly consistent with theoretical expectations based on disc migration within an evolving protoplanetary disc (Armitage

²The snow line refers to the distance from the star at which the mid-plane temperature of the protoplanetary disc drops below the sublimation temperature of ice.

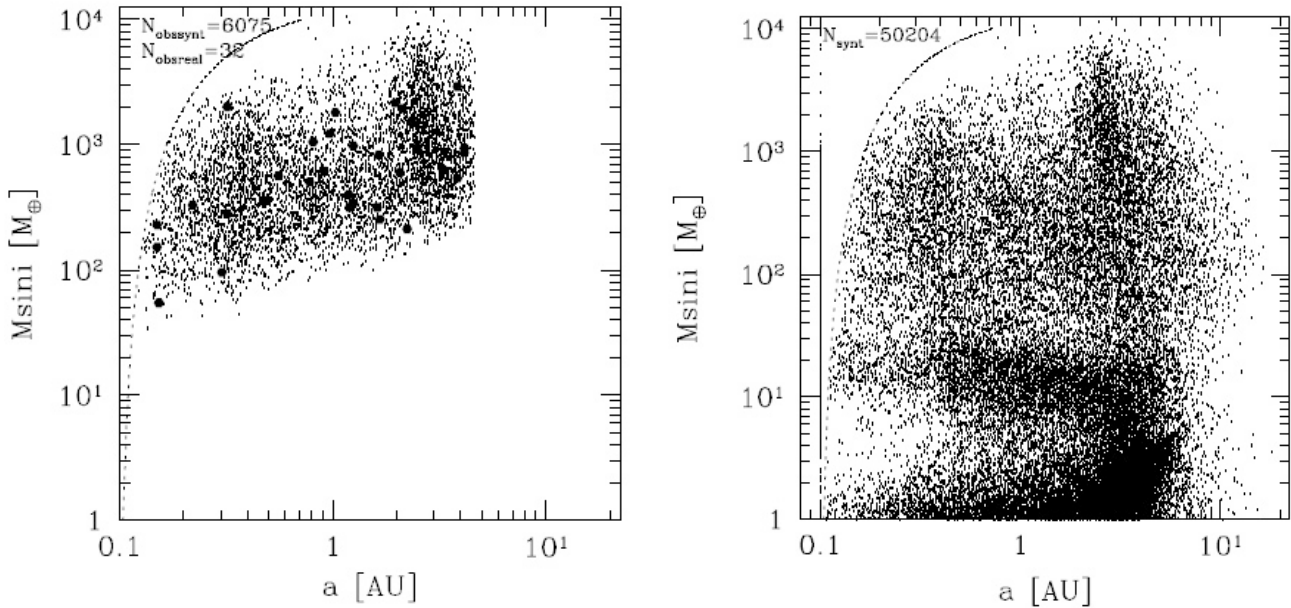


Figure 1.3: *Left:* extrasolar planet population predicted by the extended core accretion scenario and that are potentially detectable by radial velocity technique (with a 10 m/s accuracy). The big dots represent planets actually detected orbiting solar type stars. *Right:* Underlying population of planets. Most embryos do not grow to become gas giants, leaving many potentially detectable lower-mass planets (Figures from Mordasini et al. 2009).

et al. 2002; Trilling et al. 2002; Ida and Lin 2004; Mordasini et al. 2009). While these models are not specific to terrestrial planets (they are initialized with a mass of $0.6 M_{\oplus}$), they demonstrate that if planetary embryos can form, only a small fraction of them will grow sufficiently fast and large to eventually become giant planets. Given that EGPs orbit around about 7% of the stars surveyed, there must be plenty of terrestrial planets out there. According to Mordasini et al. (2009), the planets detected so far might represent only 9% of all the existing planets.

Terrestrial planet formation

Earth-like planets form in the wake of giants. Kenyon and Bromley (2006) have developed models of planetesimal disc evolution that indicate that terrestrial planet formation begins near the star, where the disc surface density is the highest, and propagates outward with time. Terrestrial embryos, being closer to the star, have less material available and hence they empty their feeding zone before growing massive. They must then rely on distant gravitational perturbations to induce further collisions. As a result, the growth of terrestrial planets occurs over longer timescales than for the giants. Simulations have revealed that Earth-like planets can be formed even in the presence of a wandering giant. In particular, a study has shown that planet formation can occur after a giant planet has migrated through the “habitable zone” (Raymond et al. 2006), suggesting that migration does not suppress the formation of Earth-like planets by either capturing protoplanetary material or causing the material to be ejected from the habitable zone. Migration could even support the creation of Earth-like planets by concentrating water and heavier materials into the habitable zone. Since about 40% of known planetary systems may have undergone a migration, more than one third of all known planetary systems would include Earth-like planets.

Terrestrial planets have not yet been detected but low-mass companions are discovered at an accelerating pace, with the detection of so-called “hot Neptunes” or “super-Earths”. These planets have masses

2-10 times larger than Earth and are mainly found on close-in orbits with periods of 2-15 days. These detected intermediate-mass planets raise the question of their possible internal composition. In this respect, the diversity of the discovered systems so far was fully unexpected and new kinds of planets have been imagined such as “ocean planets” (Léger et al. 2004) and “carbon planets” (Kuchner and Seager 2005). It is interesting to note that ocean planets would rather be easily detectable by transit space missions (CoRoT, Kepler, Selsis et al. 2007).

1.1.3 Characterization by transit and direct imaging

Theoretical planet emission

From a theoretical point of view, the total emergent flux from a planet can be decomposed as the sum of three contributions (Chabrier et al. 2004):

- the emission due to the reflection of starlight by the atmosphere and the surface of the planet, which strongly depends on the star-planet distance and the spectral type of the host star. The reflected-light luminosity ($L_{\text{pl}}^{\text{refl}}$) is given by

$$L_{\text{pl}}^{\text{refl}}(t) = A_{\text{pl}} \times L_{\star} \times \frac{\pi R_{\text{pl}}^2}{4\pi a^2} \quad (1.1)$$

with A_{pl} the planet Bond albedo³, L_{\star} the luminosity of the star, R_{pl} the planet radius and a the distance from the planet to the star. Depending on the proximity of the planet to its parent star, the Bond albedo can take various values ranging from 0.02 to 0.8 for giant planets (Sudarsky et al. 2000). Physical processes taking place in the atmosphere of irradiated giant planets have been investigated by several authors (e.g., Barman et al. 2001; Sudarsky et al. 2000, 2003; Burrows et al. 2004, see Fig. 1.4).

- the thermal emission of the planet ($L_{\text{pl}}^{\text{eq}}$), which strongly depends on the spectral type of the star and is characterized by spectral features, mostly due to CH₄ and H₂O absorption bands (Fig. 1.4), commonly found in spectra of Saturn mass objects up to brown dwarfs (0.3 - 30 M_{J}). The corresponding luminosity is given by

$$L_{\text{pl}}^{\text{eq}} = 4\pi R_{\text{pl}}^2 \times \sigma T_{\text{eq}}^4, \quad (1.2)$$

where T_{eq} is the equilibrium temperature of the planet given by

$$T_{\text{eq}} = T_{\star} \times (1 - A_{\text{pl}})^{1/4} \times \sqrt{\frac{R_{\star}}{2a}}, \quad (1.3)$$

where T_{\star} and R_{\star} are respectively the temperature and the radius of the star. Approximating the thermal emissions from the star and the planet by the equivalent blackbody emissions at effective temperatures T_{\star} and T_{eq} respectively, this equilibrium temperature results from the balance between the received and the emitted fluxes (Paczynski 1980).

- the intrinsic emission of the planet, due to residual cooling after their formation

$$L_{\text{pl}}^{\text{eff}} = 4\pi R_{\text{pl}}^2 \times \sigma T_{\text{eff}}^4, \quad (1.4)$$

where T_{eff} is the intrinsic effective temperature of the planet. In the absence of external irradiation, the photosphere of a gaseous planet would cool down to an intrinsic temperature of about 100 K in a few Gyr (Baraffe et al. 2003). The equilibrium temperature of hot EGPs is therefore much higher than their intrinsic temperature (Chabrier et al. 2004). Under such conditions, the surface temperature is simply equal to the equilibrium temperature.

³The Bond albedo is defined as the ratio between the total reflected and total incident powers.

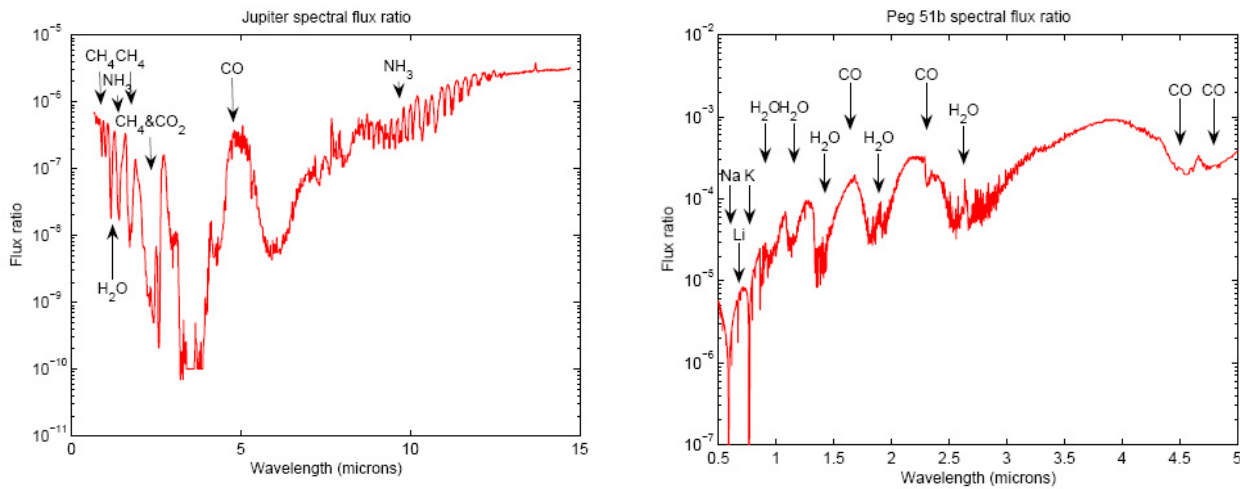


Figure 1.4: Left: Jupiter spectral contrast, dominated by methane features notably at $1.65\ \mu\text{m}$ (Mawet 2006). Right: Peg 51b (EGP) expected spectral contrast, very different from that of Jupiter (Sudarsky et al. 2003).

The left part of Figure 1.5 shows the relative fluxes of Earth and Jupiter with respect to the Sun from the visible to the thermal infrared wavelengths. The reflected flux is dominant at short wavelengths (in the visible) where the star is brighter while the thermal emission is dominant in the thermal infrared. The right part of Figure 1.5 shows the corresponding flux ratio with respect to the Sun, showing the difficulty of high contrast imaging of extrasolar planets. Indeed, the flux reflected by Earth-like planets is not expected to represent more than a few 10^{-10} of the stellar flux in the visible range, while its thermal emission should amount to a few 10^{-7} of the stellar flux around $10\ \mu\text{m}$, where it peaks.

Based on the above expressions, the wavelength-dependent infrared flux emitted by the planet and actually detected by an Earth-based observer reads:

$$F_p(\lambda) = A_\lambda \frac{\pi R_\star^2}{d^2} B_\lambda(T_\star) \Phi(\Theta) \frac{\pi R_p^2}{4a^2} + \frac{\pi R_p^2}{d^2} B_\lambda(T_p), \quad (1.5)$$

where $B_\lambda(T)$ represents the surface brightness per wavelength unit for a blackbody at temperature T , d the distance to the target star, A_λ the albedo and $\Phi(\Theta)$ a phase function affecting the reflected emission only. Such phase variations have been observed by the Spitzer space telescope (Werner et al. 2004) at $24\ \mu\text{m}$, revealing a temperature difference between day and night faces of several EGPs (e.g., Barman et al. 2005; Harrington et al. 2006; Knutson et al. 2009, see Figure 1.6). Such observations help in constraining the temperature, radius, and albedo of the planets and enable the study of the weather on distant planets. Two techniques have chiefly allowed the characterization of extrasolar planets: direct imaging and transit. The main results obtained so far with these techniques are described in the following sections.

Characterization by transit

Characterizing the composition of extrasolar planets is a huge observational challenge because it requires to distinguish the planet spectrum from the stellar light. Whereas the radial velocity technique is not appropriate for such a task, physical and atmospheric characteristics of transiting extrasolar planets can be inferred when the contrast is not too large. The first method consists in measuring the absorption of starlight passing through the planet atmosphere during transit. This tells us the composition and scale height of the extrasolar planet atmosphere (e.g., Charbonneau et al. 2002; Swain et al. 2008b; Pont et al. 2009). Another successful technique relies on the fact that almost all planets that transit their stars will

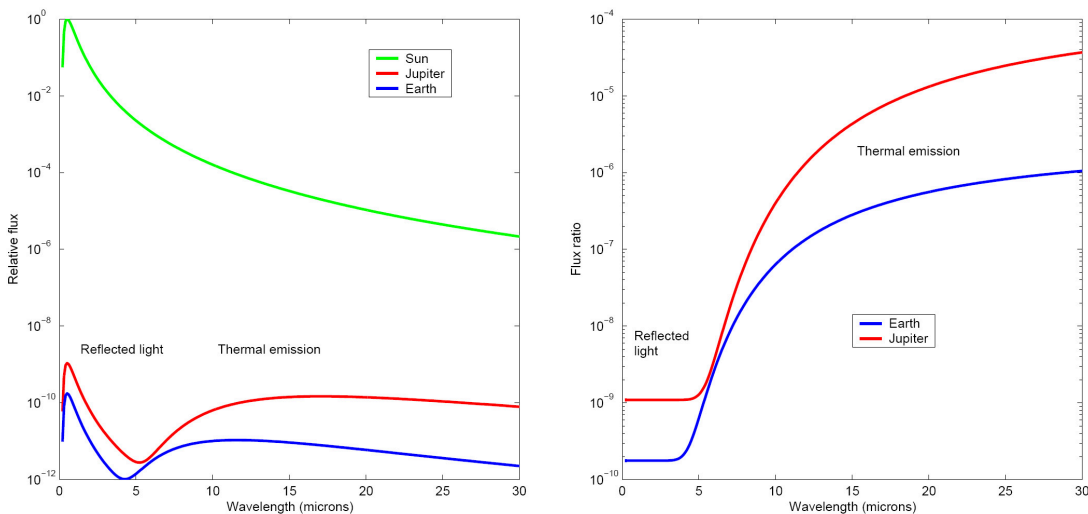


Figure 1.5: *Left:* Comparison between Sun, Jupiter and Earth spectral fluxes from the visible to thermal infrared wavelengths. *Right:* Flux ratio for Jupiter and Earth with respect to the Sun (Figures from Mawet 2006).

also pass behind the star at a given time. Measuring the system before or after this secondary eclipse⁴ gives the light of the star plus its planet, but a measurement of the system when the planet is behind the star gives the stellar light in isolation. Subtracting one measurement from the other reveals the contribution of the planet. This technique has allowed the physical characterization of several transiting planets with the detection at infrared wavelengths⁵ by the Spitzer Space Telescope (e.g., Charbonneau et al. 2005; Deming et al. 2005; Burrows et al. 2006; Grillmair et al. 2007; Richardson et al. 2007; Swain et al. 2008a). Using the secondary eclipse technique with Spitzer, Grillmair et al. (2008) have reported the unequivocal signature of water vapour in the atmosphere of HD 189733b, the brightest transiting exoplanet yet detected. Previous results from primary transit observations of HD 189733b using Spitzer had already been published but led to two different conclusions: Tinetti et al. (2007) concluded that water vapor was detected in the atmosphere of the planet, whereas Ehrenreich et al. (2007) claim that uncertainties on the measurements are too large to draw any firm conclusion. Independently, a detection of water, carbon monoxide and carbon dioxide has also been obtained using observations from the Hubble Space Telescope (Swain et al. 2009). While it is unlikely that life exists on HD 189733b, these results support the idea that significant quantities of water could exist in extrasolar systems.

The different geometries of transit and secondary eclipses provide distinct clues on the atmospheric composition: transit spectroscopy probes the atmospheric interface between the day and night hemispheres of a tidally-locked planet (Swain et al. 2008b), whereas secondary eclipse measurements probe the emergent spectrum of the dayside. Moreover, measurements of transiting systems can be extended well beyond the times of transit and eclipse, to include observations in the combined light of the star and the planet at a large range of orbital phases (see Figure 1.6). For instance, such measurements can be inverted if the planet is tidally locked to its orbit to yield the distribution of emergent intensity versus longitude on the planet (Knutson et al. 2007). The observational techniques used for transiting systems can also be extended to non-transiting systems, so it is valuable to consider a generalization of the transit technique, namely exoplanet characterization in combined light. Without a transit, the planet radius cannot be measured directly, but much can be learned, from observing fluctuations in IR intensity that are phased to the planet known radial velocity orbit (e.g., Harrington et al. 2006).

⁴The secondary eclipse is the phase during which the planet is occulted by its host star.

⁵Since the planet emergent radiation peaks in the infrared spectral range, secondary eclipse measurements rely primarily on observations in the infrared.

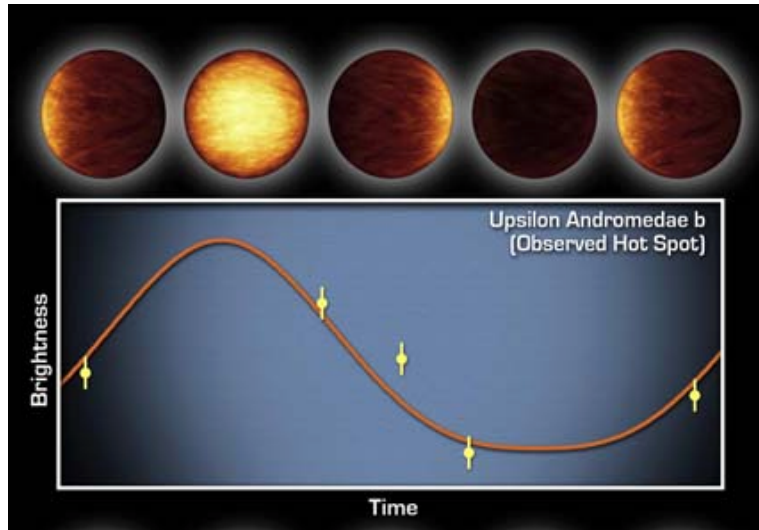


Figure 1.6: The Spitzer telescope has detected the thermal emission of the EGP companion of Upsilon Andromedae, throughout the entire 4-day period. The solid curve shows a model of a tidally locked planet with a sub-stellar point that is considerably hotter than the backside due to the relatively poor global circulation of winds (Harrington et al. 2006).

Characterization by direct imaging

Whereas the ability to find planets using radial velocity and transit techniques rapidly decreases for semi-major axes beyond about 5 AU, direct imaging of extrasolar planets is a powerful technique that can reveal giant planets in wider orbits and enable the detailed characterization of their atmospheres. Imaging detections are challenging because of the combined effect of small angular separation and large luminosity contrast between a planet and its host star. The first image of a planetary mass companion in a different system than our own has been reported 10 years after the detection of Peg 51b by Chauvin et al. (2005a) who presented deep VLT⁶/NACO⁷ infrared imaging observations of the young, nearby brown dwarf 2MASSWJ1207334-393254. Around this $25-M_J$ brown dwarf located 70 pc from Earth, Chauvin et al. (2005a) identified a very faint companion at an angular separation of 778 mas (55 AU). The characteristics of the planet according to evolutionary models are a mass of about $5 M_J$ and effective temperature of about 1250 K.

Since the discovery of Chauvin et al. (2005a), several other companions have been imaged around low-mass stars (e.g., Neuhäuser et al. 2005; Chauvin et al. 2005b; Biller et al. 2006). Most of these imaged companions are only a few Myr old so that they are generally much brighter than older sub-stellar objects because of on-going contraction and possibly accretion. In addition, they orbit a low luminosity star so that the contrast is favorable and the imaging of these objects much easier. The planetary status of these companions is not yet clearly established since the derived mass of these objects is very close to $13.6 M_J$ (the mass threshold dividing planets from brown dwarfs).

More recently, several authors have reported the imaging of low-mass companions around A stars (e.g., Kalas et al. 2008; Marois et al. 2008; Lagrange et al. 2009). So far, A stars have been mostly neglected due to their higher stellar luminosity (and thus less favorable contrast). However, main sequence A-type stars have some other advantages. The higher-mass A stars can retain heavier and more extended discs and thus might form massive planets at wide separations, making their planets easier to detect. The most famous detection was made by Kalas et al. (2008) around Fomalhaut, a bright A star

⁶VLT stands for “Very Large Telescope”. This observatory of the European Southern Observatory (ESO) is installed in Cerro Paranal (Chile).

⁷NACO stands for NAOS-CONICA, i.e., Nasmyth Adaptive Optics System Coronagraphic Near-Infrared Camera. This adaptive optics system is installed on the VLT’s fourth Unit Telescope (UT4, Yepun).

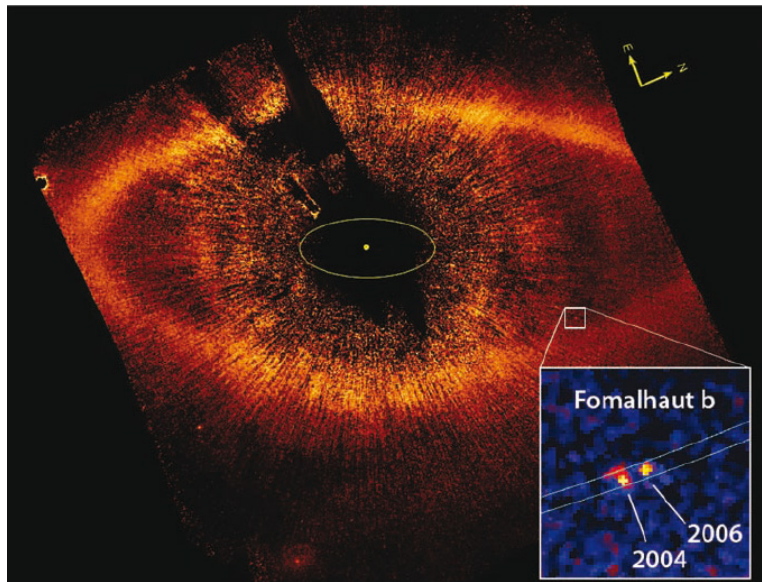


Figure 1.7: HST coronagraphic image of Fomalhaut at $0.6 \mu\text{m}$, showing the location of *Fomalhaut b* (white square) 12.7 arcsec radius from the star and just within the inner boundary of the dust belt. The yellow circle marks the location of the star behind the occulting spot. The yellow ellipse has a semi-major axis of 30 AU at Fomalhaut (3.9 arcsec) that corresponds to the orbit of Neptune in our Solar system. The inset is a composite image showing the location of *Fomalhaut b* in 2004 and 2006 relative to Fomalhaut (Kalas et al. 2008).

located at about 8 pc from Earth, and harboring a belt of cold dust with a structure consistent with gravitational sculpting by an orbiting planet (see Figure 1.7). Using HST, Kalas et al. (2008) imaged *Fomalhaut b* lying about 119 AU from the star and 18 AU from the dust belt, matching predictions of its location (Kalas et al. 2005). Dynamical models of the interaction between the planet and the belt indicate that the mass of the planet is at most three times that of Jupiter; a higher mass would lead to gravitational disruption of the belt.

1.1.4 Searching for life

The habitable zone (HZ) is defined as the region around a star within which a planet can sustain liquid water on its surface, a condition necessary for photosynthesis. Within the HZ, starlight is sufficiently intense for a greenhouse atmosphere to maintain a surface temperature above 273 K, and low enough not to initiate runaway greenhouse conditions that can vaporize the whole water reservoir, allowing photo-dissociation of water vapor and the loss of hydrogen to space (Kasting et al. 1993). If the region remains habitable for a duration longer than 1 Gyr, the HZ is then referred to as “continuous”. For the Sun, the continuous habitable zone extends roughly from 0.76 to 1.6 AU. The limits of the continuous HZ as a function of the stellar mass is represented in Figure 1.8.

Planets located inside the HZ are not necessarily habitable. For instance, planets which are too small, like Mars, cannot maintain active geology since most of their atmosphere escapes in space. They can not either be too massive, like *HD 69830d*, that accreted a thick H₂-He envelope below which water cannot be liquid (Lovis et al. 2006). Anyhow, planet formation models predict abundant Earth-like planets with the right range of masses ($0.5\text{--}8 M_{\oplus}$) and water abundances (0.01-10% by mass, Raymond et al. 2006).

In order to determine if a planet in the HZ is actually “inhabited”, its atmosphere has to be probed to search for the spectral features that are specific to biological activity, the biosignatures. According to Lovelock (1975), the simultaneous presence of large amounts of reducing and oxidizing gases in an atmosphere out of thermodynamic equilibrium can be a criterion for the presence of biological activity.

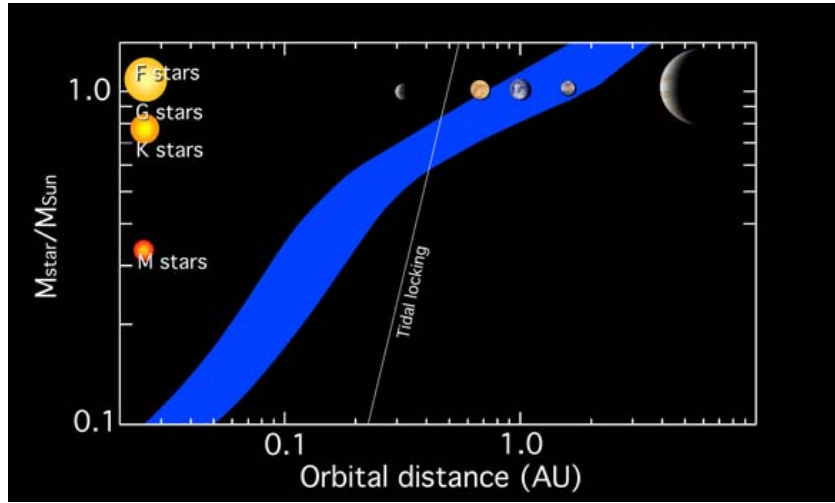


Figure 1.8: Continuous Habitable Zone (blue region) around M, K, G, and F stars. The region around the Sun that remains habitable during at least 5 Gyr extends from approximately 0.76 to 1.63 AU (adapted from Kasting 1998)).

All planetary atmospheres are out of thermodynamic equilibrium because their photochemistry is driven by UV photons from their parent star. For instance, Owen (1980) argued that a large-scale biological activity on a telluric planet necessarily produces a large quantity of oxygen (O_2). By analogy with Earth, the following elements are considered as potential biosignatures:

- **Water vapor (H_2O)**. A baseline sign, indicating the presence of liquid water, a requirement of known life;
- **Carbon dioxide (CO_2)**. Although it can be created by biological and non-biological processes, it is necessary for photosynthesis and it may indicate the possible presence of green plants;
- **Methane (CH_4)**. It is considered as suggestive of life, it can also be made both by biological and non-biological processes;
- **Oxygen (O_2) and its tracer, Ozone (O_3)**. The best indicator of biological modification of a planetary atmosphere.

Unless molecular oxygen in the Earth atmosphere is constantly replenished by photosynthesis, it is quickly consumed in chemical reactions, in the atmosphere, on land and in seawater. So the presence of a large amount of oxygen in an extrasolar planet's atmosphere would be a sign that it might host an ecosystem like that of present-day Earth. Concerning methane, detecting it on a distant world would not automatically indicate the presence of life, although it is often biogenic. For instance, Jupiter and Saturn have traces of it. However, a sufficiently high methane level (around 1000 ppm) may have been produced as a waste byproduct by primitive microorganisms. Even if methane is largely considered as a suggestive but not convincing biosignature, finding oxygen along with methane might constitute the most convincing biosignature.

In addition, the reliability of O_2 and O_3 as signatures of biological activity has been thoroughly addressed by Léger et al. (1999) and Selsis et al. (2002). Considering various abiotic production processes, such as photo-dissociation of CO_2 and H_2O , and the possible escape of hydrogen from the atmosphere, they conclude that a simultaneous detection of a significant amount of H_2O and O_3 in the atmosphere of a planet in the habitable zone presently stands as a criterion for large-scale photosynthetic activity on the planet. Such an activity on a planet illuminated by a Sun-like star is likely to be a significant

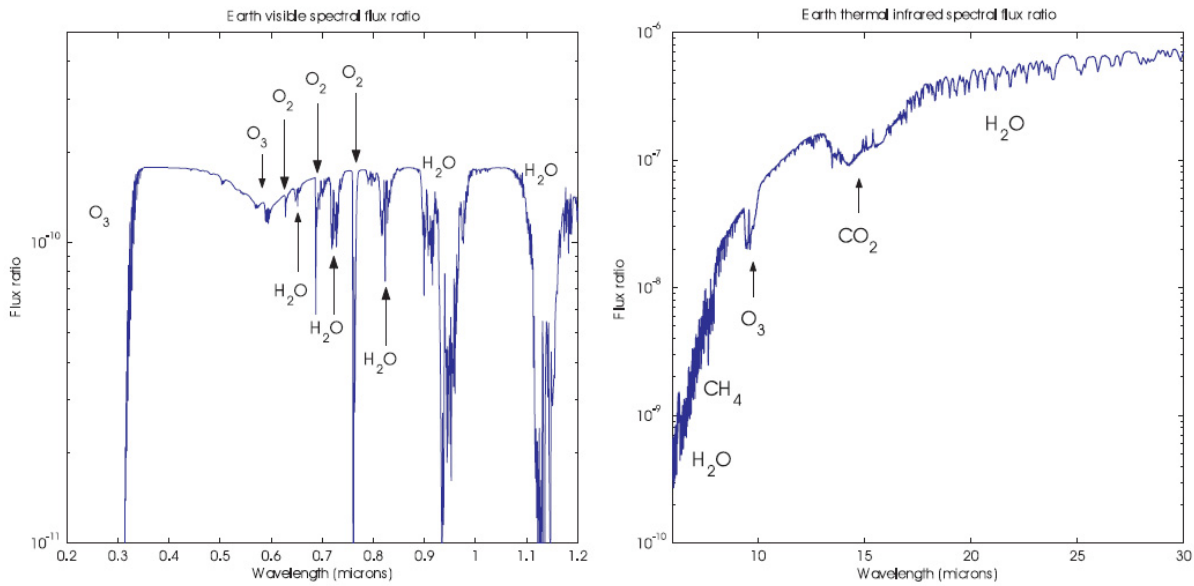


Figure 1.9: *Left:* Earth spectral contrast in the visible. Spectral features of biosignatures like O₂, O₃ and H₂O clearly appear. Note that the CO₂ feature is absent in the visible. *Right:* Earth spectral contrast in the thermal infrared where the CO₂ feature is present (Figure from Mawet 2006).

indication that there is local biological activity. Detecting O₃ in addition to H₂O seems to be a robust biosignature because no counter example has been identified. This is not true for O₂ for which false positive could be detected (Selsis et al. 2002).

To reveal the effects of these biosignatures, low-resolution mid-IR (6-20 μ m) observations are particularly suited. As shown in Figure 1.9, the wavelength range displays the 9.6 μ m O₃ band, the 15 μ m CO₂ band, the 6.3 μ m H₂O band and the H₂O rotational band that extends longward of 12 μ m. The visible wavelength range presents also the main biosignature features but the planet-star contrast is much less favorable than in the mid-IR (see Figure 1.9, left). Note also that a low-resolution spectrum spanning the 6-20 μ m region has the advantage to allow the measurement of the effective temperature of the planet, and thus its radius and albedo. For all these reasons, the mid-IR range is currently considered as an optimal observation window for the future life-finding missions.

The atmosphere spectrum also depends on the distance between the planet and its host star. Within the HZ, the partial pressure of CO₂ and H₂O at the surface of an Earth-like planet is a function of the distance from the star. Water vapour is a major constituent of the atmosphere for planets between 0.84 AU (inner edge of the HZ) and 0.95 AU. Figure 1.10 shows the estimated evolution of the H₂O, O₃ and CO₂ features in the spectra of an Earth-like planet as a function of its location in the HZ. Carbon dioxide is a tracer for the inner region of the HZ and becomes an abundant gas further out.

Considering the solar system, the right part of Figure 1.10 shows the spectra of Venus, Earth and Mars. For instance, Venus, closer to the Sun than the HZ, has lost its water reservoir and accumulated a thick CO₂ atmosphere. Planets like Venus can be identified as uninhabitable by the absence of water and by the high-pressure CO₂ absorption bands between 9 and 11 μ m. The Earth's spectrum is also clearly distinct from that of Mars which does not present any H₂O and O₃ feature. According to Segura et al. (2003), the ozone absorption band is observable for O₂ concentrations higher than 0.1% of the present terrestrial atmospheric level. Concerning the Earth spectrum, it has displayed this feature for the past 2.5 Gyr (Kaltenegger et al. 2007b). Other spectral features of potential biological interest include methane (CH₄ at 7.4 μ m), and species released as a consequence of biological fixation of nitrogen, such as ammonia (NH₃ at 6 and 9-11 μ m), nitrous oxide (N₂O at 7.8, 8.5 and 17 μ m) and nitrogen dioxide (NO₂ at 6.2 μ m). The presence of these compounds would be difficult to explain in the absence of

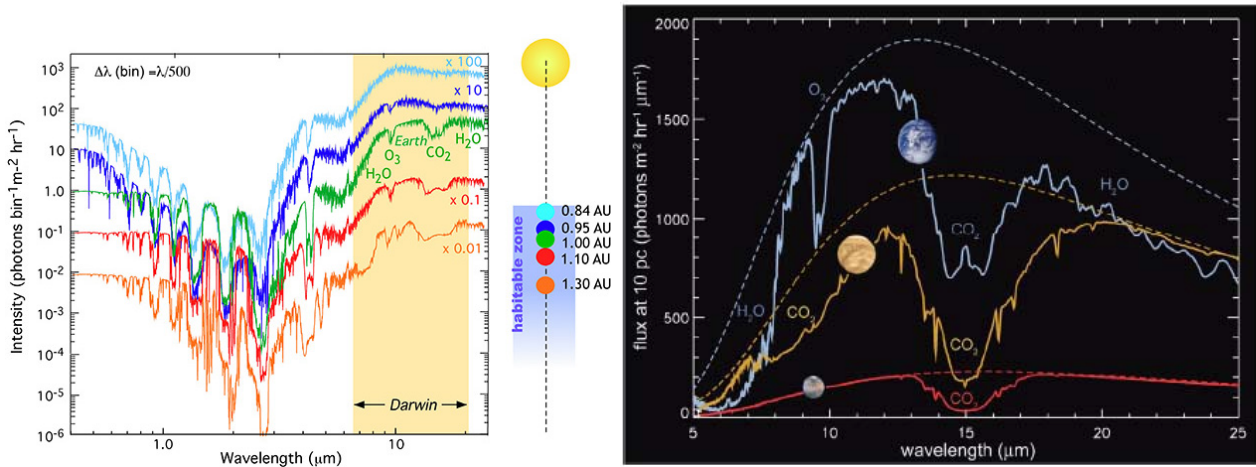


Figure 1.10: *Left:* Synthetic spectra of an Earth-like planet computed at different orbital distances across the solar habitable zone (courtesy J. Paillet). *Right:* Mid-IR spectra of Venus, Earth and Mars as seen from a distance of 10 pc (Léger and Herbst 2007).

biological processes.

1.2 Circumstellar discs

The presence of dust around a mature main sequence star is a reminder that the star was born by accretion in a dense protostellar disc of gas and dust and that any planet orbiting the host star was born out of that same material (see Section 1.1.2 for further information on planet formation). In the process of star and planet formation, circumstellar discs represent different evolution stages between spherical collapsing clouds and fully assembled main sequence stars surrounded by planets. Disc evolution is typically divided into four observationally-determined evolutionary classes (0, I, II, and III)⁸:

- **Class 0** objects are thought to be protostars surrounded by roughly spherical collapsing envelopes from which forming young stars are still accreting substantial fractions of their final mass. Because of the very high columns of cold dust in these envelopes, these objects emit most of their radiation at sub-millimeter wavelengths.
- **Class I** objects are still deeply embedded and have high mass accretion rates. At this time, bipolar outflows appear and start to clear away material from the polar regions. These sources are still not directly visible, and emit most of their radiation at far-IR wavelengths due to reprocessing of the stellar radiation by warm dust.
- **Class II** sources or Young stellar objects (YSO), including Herbig Ae/Be⁹ and T Tauri¹⁰ stars respectively with masses above and below $2 M_{\oplus}$, are optically-visible young stars, which have probably already assembled almost all of their final mass. They show excess emission at infrared and millimeter wavelengths indicative of optically-thick circumstellar discs.
- **Class III** sources appear to be pre-main sequence stars that have already depleted most of the gas reservoir in their circumstellar discs so that the accretion has stopped, leaving planetesimals

⁸This classification scheme was originally defined based on infrared spectral index and the ratio of sub-millimeter to bolometric luminosity (Lada et al. 1984; Wilking et al. 1984; Lada 1987).

⁹Herbig Ae/Be stars are pre-main sequence stars (younger than 10 Myr) of spectral types A and B, still embedded in gas-dust envelopes and surrounded by a circumstellar disc.

¹⁰T Tauri stars are a class of variable stars named after their prototype, T Tauri. They are found near molecular clouds and identified by their optical variability and strong chromospheric lines.

and forming planets in a more tenuous disc. This marks the end of the protoplanetary disc phase and the start of the debris disc phase, which is likely replenished by collisions of planetesimals.

While the first image of a circumstellar disc was obtained from scattered light by a dust disc around the nearby main sequence star β Pic (Smith and Terrile 1984), images of protoplanetary discs around young pre-main sequence stars have now been obtained as well (e.g., Koerner and Sargent 1995; Dutrey et al. 1996; Malbet et al. 1998; Millan-Gabet et al. 1998). The current observational results are summarised below for the protoplanetary and debris disc phases separately. Photometric and interferometric results are also presented separately for each case, the latter allowing to investigate the inner disc properties which is of utmost importance for understanding the initial conditions and steps of planet formation.

1.2.1 Protoplanetary discs

Studying gas-rich protoplanetary discs is very important since relatively modest amounts of gas could strongly affect the dynamics of small dust grains, leading to the formation of azimuthally symmetric structures such as cleared zones or dust rings (Takeuchi and Artymowicz 2001). This conclusion is supported by other modelling effects (Klahr and Bodenheimer 2006), which also showed that such gas-formed structures can persist after the gas is completely gone. Gas-rich circumstellar discs around YSOs have now been detected convincingly in several cases. Infrared excess emission from Herbig Ae/Be and T Tauri stars was initially detected by photometric surveys (e.g., Mendoza V. 1966; Rydgren et al. 1976). It was originally explained by the presence of geometrically thin, optically thick discs (Lada and Adams 1992; Hillenbrand et al. 1992), a model that has been modified to include central-star irradiation (Calvet et al. 1991), disk flaring (Chiang and Goldreich 1997; Kenyon and Hartmann 1987), and other structures to explain features in the spectral energy distributions, such as an inner hole, innerwall heating, and self-shadowing (Dullemond et al. 2001, 2002). Alternative explanations for circumstellar emission take the form of dusty envelope models (Hartmann et al. 1993; Miroshnichenko et al. 1999), as well as optically thin “halos” in combination with discs (Vinković et al. 2003, 2006). The Orion nebula (M42, NGC1976) has been the most observed and studied area, harboring one of the richest and youngest clusters in the solar neighborhood, spanning the full spectrum of masses (from stellar to a few M_J , Lucas and Roche 2000). Since the early 1990s, HST observations of the Orion nebula have been fundamental for clarifying the main characteristics of YSOs and their protoplanetary discs. Disc-like brightness distributions have been imaged directly at optical wavelengths, showing flattened distributions of dust and gas in the Orion nebula (e.g., McCaughrean and O’dell 1996; O’dell and Wong 1996). Following these discoveries, other HST programs have increased the number of known objects (e.g., Bally et al. 1998, 2000; O’Dell et al. 2001; Smith et al. 2005), and a total of about 200 discs in the Orion nebula are known so far (Ricci et al. 2008). In the meantime, a wealth of information has been obtained on YSOs by stellar interferometry. The main results are presented hereafter.

Interferometric view

During the last decade, the study of circumstellar discs by stellar interferometry has been mostly limited to YSO surrounded by significant amounts of dust and gas arranged in optically thick accretion discs. In particular, infrared interferometers directly probe the temperature and density structure of gas and dust within the first few AU of YSO discs, which are relevant parameters driving the planet formation process. The discoveries brought by interferometry have been strongly supported by major advances in theoretical models of YSO in the past ten years, which have seen simple accretion scenarios of passively-heated discs be complemented by a richer set of phenomena (Hartmann et al. 1993; Chiang and Goldreich 1997).

The first YSO observed by stellar interferometry was achieved with the Palomar Testbed Interferometer (PTI, see Section 2.3 for further details) on FU Ori, a rare type of T Tauri star whose emission

is dominated by accretion luminosity (Malbet et al. 1998). The disc size was then found to be roughly consistent with expectations from a simple flat disc model. Four T Tauri stars were then resolved at PTI, revealing a larger near-infrared emitting region than predicted by simple accretion models (Akeson et al. 2000). This result was confirmed two years later (Akeson et al. 2002) by additional observations of T Tau and SU Aur, and by the first scientific observations of the Keck-I on DG Tau (Colavita et al. 2003). In the meantime, the first Herbig Ae/Be star was resolved by interferometry using the IOTA interferometer (see Section 3.2, Millan-Gabet et al. 1998). The near-infrared emission of AB Aur was found to be much larger than expected from theoretical models. This discovery was then confirmed by a survey of 15 similar stars at IOTA (Millan-Gabet et al. 2001). In addition, no variation of the visibilities was observed while the baseline orientation was changed, favouring a spherical envelope for the dust emission. The same survey, complemented by observations of T Tauri stars, was used by Monnier and Millan-Gabet (2002) to produce a diagram showing a significant correlation between the size of the near-infrared excess emission and the luminosity of the star, as one would expect for an inner dust disc (or envelope) truncated by dust evaporation close to the star. An optically thin cavity was thus suggested around YSOs, while the classical model assumed the presence of optically thick gas. This result was later confirmed by additional observations at the Keck-I (Monnier et al. 2005).

Based on these observations, new models have been built, including disc flaring and puffed-up inner rims as proposed by Dullemond et al. (2001) except for the most massive Herbig Be stars. Further observations at PTI (Eisner et al. 2004; Akeson et al. 2005a) and Keck-I (Eisner et al. 2005) are generally in agreement with these revised models, and show that the presence of gas within the sublimation radius of dust, probably extending down to the magnetospheric truncation radius, can also be a significant component to the inner disc flux. Unlike the previous one, the survey of Eisner et al. (2004) allowed for a determination of the disc inclination for most targets, which reconciles the interferometric view with a disc-like geometry. A range of inner dust disc properties have been recently suggested by Akeson et al. (2005b) with the Keck-I, possibly related to the various evolutionary statuses of the target sources. These observations also have important implications for planet formation scenarios, as the measured inner dust radii (typically ranging from 0.04 to 0.3 AU) prove the presence of dust in the habitable zone (near 1 AU) at early stages of planet formation. This suggests that giant planets can penetrate the sublimation zone by migration mechanisms triggered by the large quantity of gas. Finally, observations of FU Ori (Malbet et al. 2005) have confirmed that, unlike most T Tauri stars, this source is compatible with a standard disc model, i.e., geometrically flat and optically thick. This may be due to the enhanced accretion rate, as suggested by Eisner et al. (2005) on another accretion-dominated source. Such a behaviour has also been observed on massive Herbig Be stars (Eisner et al. 2004). However, observations of three FU Orionis objects by Millan-Gabet et al. (2006) contradict these conclusions, as a simple accretion disc does not reproduce the low visibilities measured with the Keck Interferometer. A significant contribution to the near-infrared flux might come from scattering in the upper atmosphere of the disc (the presence of an optically thin inner disc is very implausible in the case of FU Orionis objects). This scenario is supported by recent models where circumstellar haloes account for both infrared spectroscopic and imaging data (Vinković et al. 2006).

The VLTI has also recently obtained important results on Herbig Ae/Be stars. In particular, the MIDI instrument has provided the first spatially and spectrally resolved mid-infrared view of these objects, with characteristic sizes of 1 to 10 AU for the mid-infrared emitting regions (Leinert et al. 2004). Although in qualitative agreement with the predictions from passively heated models, the data show quantitative discrepancies with these models and therefore ask for a next step in the modelling of circumstellar discs. This study supports the phenomenological classification of Herbig Ae/Be stars into categories by their mid-infrared colour and the distinction of these categories by flaring-dominated versus non flaring-dominated circumstellar dust distributions. The spectroscopic capabilities have also contributed to the study of these stars, showing the dust in the innermost regions of the disc to be highly crystallised and to be dominated by olivine, while outer regions have a lower degree of crystallinity (van Boekel et al. 2005). These observations imply that silicates crystallise before any terrestrial planets are

formed. Other results obtained from VLTI are observations with the AMBER instrument of MWC 297, an embedded Be star, which have shown the star to be surrounded by a possibly still accreting flat equatorial disc and an outflowing wind presenting a much higher velocity in the polar region than at the equator (Malbet et al. 2005). More recently, the radial structure of the circumstellar inner disc around AB Aur has been directly determined by MIDI, revealing a flared inner disc (Di Folco et al. 2009)

Finally, nulling interferometry has also been used to observe YSOs, reporting conclusive resolved warm dust surrounding three objects: HD 100546, AB Aur, and HD 179218 (Hinz et al. 2001; Liu et al. 2003, 2005, 2007). Assuming a Gaussian disc or a ring, the spatial extent of the emitting region in the resolved systems ranges from 15 to 30 AU in diameter. Both HD 100546 and AB Aur show a significant variation of the null versus the position angle of the emitting region semi-major axis, evidencing an elongated structure such as an inclined disc. For HD 179218, little variation of null was detected, consistent with an axisymmetric distribution (such as a face-on disc) for the dust, although a significant inclination cannot be ruled out given the lack of accuracy in the measurements (Liu et al. 2007).

1.2.2 Debris discs

First discovered by the InfraRed Astronomical Satellite (IRAS), the “Vega phenomenon” characterizes main sequence stars presenting a significant deviation from their expected Rayleigh-Jeans emission (Aumann et al. 1984). These photometric excesses are now commonly understood as the signature of dust surrounding the stars, analogous to the zodiacal cloud and/or the Kuiper belt in our own solar system (Backman and Paresce 1993). This dust originates mainly from collisions between small bodies or from outgassing comets (Beust et al. 1996), and has a limited lifetime due to physical effects such as radiation pressure, collisions and drag. Extrasolar systems with infrared excess presumably have their own supply of large, solid planetesimals and, perhaps, large planets like those in our system. In fact, the few resolved images of debris discs obtained so far in the visible (e.g., Heap et al. 2000; Kalas et al. 2004, 2006) and sub-millimetric (e.g., Holland et al. 1998, 2003; Greaves et al. 2004) regimes have revealed the presence of extended structures associated with a void of matter in the central region (< 50 AU). Warps, gaps and clumpy structures have been repeatedly detected and attributed to the gravitational influence of planets, which may also be the cause for the apparent void of matter in the inner region (e.g., Wyatt and Dent 2002).

All these elements raise the question of how planets, planetesimals and dust grains interact and evolve in extrasolar systems. One of the main questions is whether inner dust reservoirs can survive the suspected planetary migration, and continue to replenish the inner disc at advanced ages. It is in fact expected that planetesimals trapped in mean motion resonances with the migrating planet could be pushed toward the innermost regions as the planet migrates inwards during the early system evolution, and thereby constitute a significant reservoir of solid bodies.

So far, debris discs have mostly been observed on relatively large spatial scales, probing material located tens to hundreds of AU from their host star, by photometry missions like IRAS, ISO and more recently the Spitzer Space Telescope. These circumstellar regions are more analogous to our solar system’s dusty “Kuiper belt”, located beyond our planetary belt, than to the AU-scale zodiacal disc inside our solar system’s asteroid belt. Characterization of warm circumstellar dust (≥ 300 K) in the inner part of debris discs is particularly important to understand the physical and dynamical properties of the discs, including planetary formation and evolution mechanisms in the regions where terrestrial planets are supposed to be located. Several studies have already searched for warm dust in these cavities using mid-infrared photometry, but with poor results. For instance, Fajardo-Acosta et al. (1998) have only found 5 systems with weak $10\mu\text{m}$ excess, suggesting the presence of dust between 1 and 10 AU with median grain temperatures ranging between 200 and 350 K. More recent mid-infrared photometric surveys revealed a few hot inner debris discs (e.g., Stapelfeldt et al. 2004; Beichman et al. 2005b), but they do not have the required accuracy to detect the signature of these discs in the near-infrared,

even around stars known to be surrounded by large amounts of cold dust in Kuiper Belt-like structures. During the last few years however, infrared interferometry has enabled the detection of hot (1000-1500 K) dust populations around several main sequence stars known to harbor cold (≤ 200 K) debris discs (e.g., Absil et al. 2006b; Di Folco et al. 2007; Absil et al. 2008b; Akeson et al. 2009; Absil et al. 2009). In the following, we briefly review the main results of photometric and interferometric surveys separately.

Photometric view

The surveys performed by IRAS, ISO and the Spitzer Space Telescope have greatly improved our understanding on the incidence of debris discs as a function of age, spectral type and metallicity. About 15% of mature solar-type stars (F0 - K0) have been shown to harbour cold debris discs (Beichman et al. 2006b). This proportion does not seem to vary significantly for planet-bearing stars (Bryden et al. 2009), nor with respect to the stellar metallicity (Greaves et al. 2006), but rather with the age of the star (older stars usually present less infrared excess than younger ones, Beichman et al. 2005b).

At $70 \mu\text{m}$, Spitzer is sensitive to levels of exozodiacal emission in the range of 35 - 75 K dust with $L_{\text{disc}}/L_{\star} \sim 10^{-6}$ to 10^{-5} , or roughly 10 - 100 times the expected level of emission of our own Kuiper Belt. A wide variety of Spitzer programmes have found the following characteristics of debris disc emission:

- Approximately $14 \pm 3\%$ of mature, solar type stars (spectral type in the F5-G5 range) have detectable $70 \mu\text{m}$ debris disc emission at a level of $L_{\text{disc}}/L_{\star} = 10^{-5}$ to 10^{-6} (Bryden et al. 2006). This rate is somewhat higher among A and early F stars ($\pm 25\%$) and smaller for stars later than K ($< 4\%$) (Beichman et al. 2006a). A more recent study including 350 main sequence AFGKM stars has shown that the incidence of debris discs is about 4.2% at $24 \mu\text{m}$ for a sample of 213 Sun-like (FG) stars and about 16.4% at $70 \mu\text{m}$ for 225 Sun-like (FG) stars. The excess rates for A, F, G, and K stars are statistically indistinguishable, but with a suggestion of decreasing excess rate toward the later spectral types, suggesting an age effect (Trilling et al. 2008).
- Emission at $10 \mu\text{m}$, corresponding to dust in the HZ and thus most relevant to DARWIN/TPF, is very rare at the Spitzer sensitivity level for mature stars. However, the unfavorable contrast ratio at this wavelength means that Spitzer can detect emission only at a level ~ 1000 times brighter than our own zodiacal cloud. Initial estimates based on Infrared Astronomical Satellite (IRAS, Mannings and Barlow 1998; Fajardo-Acosta et al. 2000) and Infrared Space Observatory (ISO, Laureijs et al. 2002) observations were that $\leq 2\%$ of systems have detectable discs at $10 \mu\text{m}$, while the largest Spitzer sample studied to date of 150 stars suggests a rate less than 1% (Beichman et al. 2006a). While a few individual objects, including A stars like β Pic and β Leo and the 2-4 Gyr old K0 star HD 69830 (Beichman et al. 2005a), show bright emission from small grains in the HZ, such stars are very rare.
- Debris disc emission is both more intense and more frequent (up to 30% at $24 \mu\text{m}$) at ages less than ~ 150 Myr (Rieke et al. 2005; Siegler et al. 2007; Hillenbrand et al. 2008), but at stellar ages longer than about 1 Gyr, the incidence of debris disc emission shows little dependence with age.

These observational results can begin to guide the expectations for the amount of zodiacal emission around the majority of mature main sequence stars. Models based on collisions between planetesimals can be developed to reconstruct the evolution of debris discs and confronted with the properties of the emerging population of Sun-like stars that have hot dust. Considering a solar type star, the curves in Figure 1.11 show the evolution of $f = L_{\text{disc}}/L_{\star}$ as a function of time depending on the mass and location of the parent disc (Wyatt et al. 2007).

The predicted level of debris disc emission drops well below 10 times that of our system by the time the star reaches a few Gyr. The right-hand curves show the variation of the expected emission

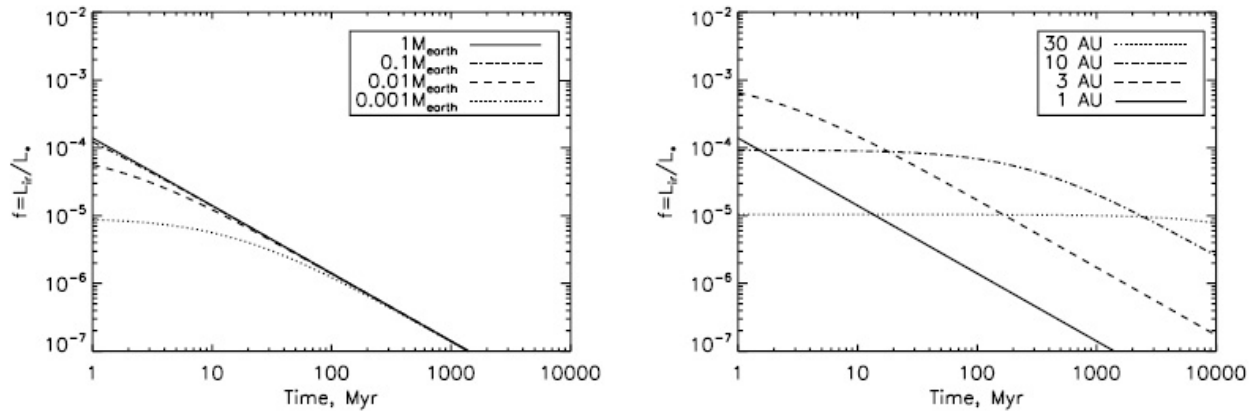


Figure 1.11: Models of the evolution of the total exozodiacial emission as a function of time for different total disc masses (left) and disc locations (right). After a few Gyr, solar-type stars with discs interior to 10 AU reach zodiacal levels comparable to our own, $f = L_{\text{disc}}/L_{\star} = 10^{-7}$ (Figure from Wyatt et al. 2007).

for different disc sizes (1, 3, 10, 30 AU). The 3-AU case corresponds to the location of our asteroid belt and reproduces almost exactly the level of emission in our own solar System, $L_{\text{disc}}/L_{\star}$, a few 10^{-7} . The 10-AU and 30-AU cases predict a higher level of debris disc emission than is presently seen in the solar system. Nevertheless, this model ignores the clearing action of the Jupiter and Saturn which would either have incorporated much of the planetesimal material into a solid core, or ejected the material. While the theoretical understanding is far from complete, these results, once validated by present and future observations of discs, should give confidence that the expected level of emission required for the detection of terrestrial planets around many nearby stars (see Chapter 7).

Interferometric view

Due to the limited spatial resolution of photometry missions, the localization of the grains cannot be accurately inferred in the region where physical and dynamical processes need to be studied. Resolving the star-disc system is therefore the most reliable way to assess the presence of small quantities of warm dust around solar-type stars and only infrared interferometry can investigate the inner disc in a thorough manner.

The first attempt to detect a debris disc was performed at the Palomar Testbed Interferometer (PTI) by Ciardi et al. (2001) on the prototypical debris disc star Vega. A simple debris disc model, accounting for 3 to 6% of Vega's near-infrared flux and emanating from a region within 4 AU, was proposed. However, the determination of the circumstellar disc emission was rather imprecise due to the limited and inappropriate spatial frequency range. A second, more thorough study, was then performed by Di Folco et al. (2004) with the VINCI instrument at the Very Large Telescope Interferometer (VLTI) on five Vega-like stars. Due to the limited precision of the VLTI observations at that time, and to the unavailability of short baselines, this study did not allow an unambiguous detection of warm dust around these stars. Finally, a study on debris discs has been performed by nulling interferometry using the Bracewell Infrared Nulling Cryostat (BLINC) instrument at the Multi-Mirror Telescope (MMT, see the description in Section 4.4.1, Liu et al. 2004). The nulling ratio measured on Vega in the N band was found to be consistent with the point-source calibrators within an uncertainty of 0.7%. This allowed for an upper limit of 2.1% to be placed on the circumstellar emission of Vega relative to its photosphere at $10.6 \mu\text{m}$, valid for separations larger than 0.8 AU (equivalent to the resolution of BLINC at MMT).

Interferometric observations of Vega with the FLUOR (Fiber Linked Unit for Recombination) instrument at the CHARA array (ten Brummelaar et al. 2008) have revealed the expected near-IR signature

of a faint debris disc, accounting for 1.3% of the stellar flux in the K band (Absil et al. 2006b). The resolved excess seems to emanate mostly from hot sub-micron carbonaceous grains located within 1 AU from the photosphere, close to their sublimation limit. Because such grains have a very short lifetime (a few tens of years at most), this result can be interpreted as a possible evidence for massive evaporation of cometary bodies. A dozen of comets similar to Hale-Bopp should be currently orbiting in the star's vicinity in order to permanently replenish the disc. Migration of giant planets in the young (350 Myr) Vega system could trigger such a cometary shower, in a mechanism similar to the Late Heavy Bombardment in the solar system (Gomes et al. 2005). Further observations with the CHARA/FLUOR interferometer have brought new detections of circumstellar emission excess. First, Di Folco et al. (2007) reported the detection of warm dust around the 10-Gyr old sun-like star τ Cet (G8V) with an emission excess as high as 1-2% of the stellar flux at $2\mu\text{m}$. At the same time, no excess was detected for the sun-like star ϵ Eri (K2V), with a similar precision of about 0.25 %.

A somewhat larger survey was then reported by Absil et al. (2008b), focusing on a sample of six bright A- and early F-type stars with CHARA/FLUOR. These observations brought to light the presence of resolved circumstellar emission around one of the six target stars (ζ Aql, A0V) at the 5σ level. However, the morphology of the emission source cannot be directly constrained because of the sparse spatial frequency sampling of the interferometric data. The latter are in agreement either with the presence of hot dust within 10 AU from ζ Aql, producing a total thermal emission equal to $1.69 \pm 0.31\%$ of the photospheric flux in the K band, or with the presence of a low-mass companion characterized by a K-band contrast of four magnitudes, a most probable mass of about $0.6 M_{\oplus}$ and an orbit between about 5.5 AU and 8 AU from its host star. Recent observations with CHARA/FLUOR of two A-type stars, β Leo and ζ Lep, have shown visibility deficits of a few percent likely due to the presence of dust grains located within several AU of the central star (Akeson et al. 2009). For β Leo, the NIR excess-producing grains are spatially distinct from the dust which produces the previously known mid-infrared excess while for ζ Lep, the NIR excess may be spatially associated with the MIR excess-producing material. Finally, thermal emission from hot dusty grains located within 6 AU from Fomalhaut (A4V) and producing a relative flux of $0.88\% \pm 0.12\%$ with respect to the stellar photosphere has been detected using VINCI/VLTI (Absil et al. 2009).

Recently, nulling interferometry has also been used at the MMT to observe debris disc stars. Liu et al. (2009) reported $10\mu\text{m}$ observations of six nearby main sequence stars (α CrB, α Lyr, β Leo, γ Ser, ϵ Eri, and ζ Lep) for which no evidence for a positive detection of warm debris in the habitable zone was detected. These results place a 3σ upper limits on dust density of these systems ranging from 220 to 10^4 zodi.

1.3 Detection and characterization techniques

1.3.1 Overview

To detect and characterize extrasolar planets, several techniques exist and the most successful have already been partly described in Section 1.1.1. Some techniques achieve the detection indirectly by measuring the effects induced by the planet on its host star (such as radial velocity) and others directly by detecting the photons from the planet (such as coronagraphy and interferometry). They can be classified into four main families, represented by the diagram in Figure 1.12, according to the way they can lead to the detection of a planet by: (1) monitoring the photometric signals, (2) observing dynamical effects on the host star, (3) microlensing effects (astrometric or photometric), (4) miscellaneous effects (such as magnetic super-flares or radio emission). Each method has its own advantages and drawbacks. Figure 1.12 summarizes the results of each method in terms of planets detected. Dashed lines indicate techniques which are not yet available to detect extrasolar planets. They should provide complementary discoveries in the next years. In the coming section, some ongoing and foreseen observational instruments

are presented.

1.3.2 Indirect detection methods

As indicated in the previous paragraph, almost all planets discovered so far have been detected by indirect methods, which rely on effects induced by the planet on its parent star. The most successful technique relies on precise measurements of the host star's radial velocity through spectroscopic observations, showing small shifts in the stellar spectral lines (typically one tens of meters per second) as the star moves back and forth due to the gravitational pull of its planet. Another successful technique relies on the dimming of the apparent stellar flux as the planet transits in front of the stellar disc. Astrometric data are also used to detect planets. These techniques are briefly described hereafter.

- **Astrometry** consists in measuring the periodic displacement of the apparent position on the sky of a star, due to the planetary gravitational influence. It is the oldest search method for extrasolar planets and originally popular because of its success in characterizing astrometric binary star systems. The first extrasolar planet discovered by astrometry has been reported very recently. Using the 5-m Hale telescope at the Palomar Observatory, Pravdo and Shaklan (2009) detected a $6.5-M_J$ planet orbiting one of the smallest known star (VB 10, a very small M-type red dwarf star located about 6 pc away from Earth).
- **Radial velocity** or “Doppler shift” method has been the most successful extrasolar planet detection method to date, detecting the vast majority of planets. Radial velocity variations cause a wobble in the parent star so that very high precision spectral line measurements (one part in a hundred

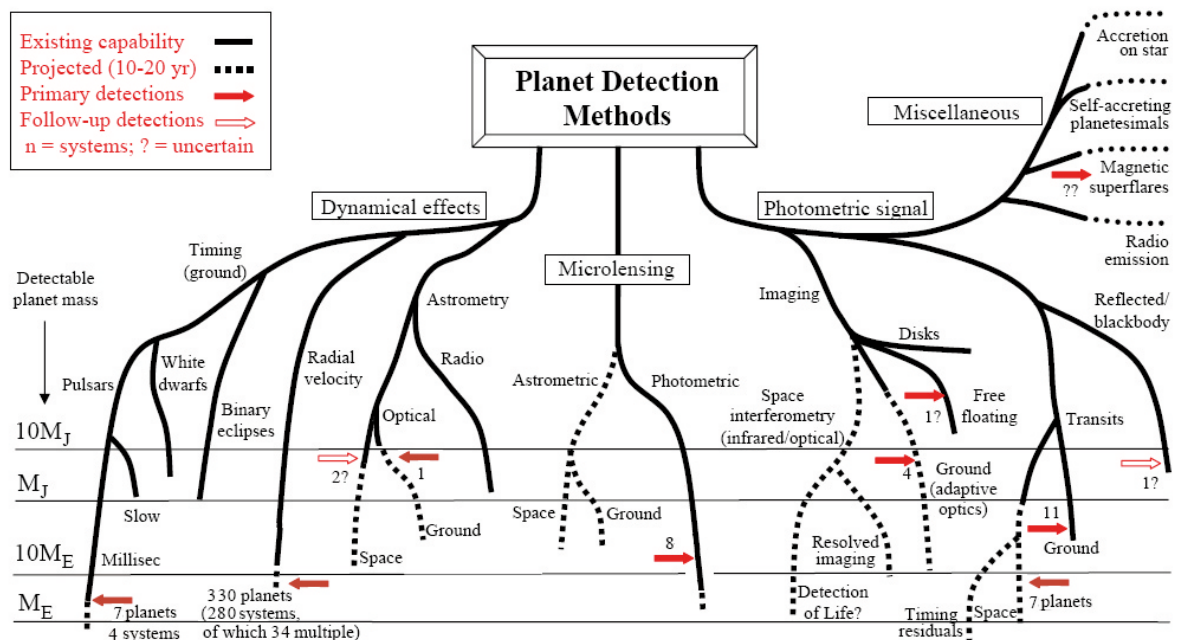


Figure 1.12: Diagram of detection and characterization methods for extrasolar planets (updated in August 2009 from Perryman 2000). The lower extent of the solid lines indicates, roughly, the detectable masses that are in principle within reach with the available instruments. The expected level of detection of future instruments is shown by the dashed lines (see the mass scale on the left). The miscellaneous signatures to the upper right are less well quantified in mass terms. Solid arrows indicate (original) detections according to approximate mass, while open arrows indicate further measurements of previously detected systems. A question mark indicates uncertain or unconfirmed detections.

million of a spectral line width) can be performed by superimposing a comparison spectrum with many lines on to the stellar spectrum for a precise measurement of a periodic displacement in the star spectral lines. The spectral line variations only measure the component of the motion directed toward or away from the observer, and hence it is only possible to measure the minimum mass of the planet ($M_p \times \sin i$).

- **Pulsar timing** revealed the first planetary-mass objects around another star. Unexpectedly, the detected objects were closer to terrestrial-mass than to jovian-mass planets, a $2.8\text{-}M_\oplus$ planet with a period of 98.22 days and a $3.4\text{-}M_\oplus$ body with a period of 66.54 days (Wolszczan and Frail 1992). The parent star was the pulsar PSR B1257+12, located 500 pc from Earth. The detection method consists in precisely measuring the radio pulse rates of pulsars (seconds to milliseconds) and their stability (variations in pulse timing on the order of only about a trillionth of a second per year). If a planet is present, the pulsar moves around the planet-pulsar barycentre so that a delay of the periodic variations in the timing of the pulsar pulses can be precisely measured.
- **Transit** method relies on the dimming of the apparent stellar flux as the planet transits in front of the stellar photosphere. The main advantage of the transit method is that the size of the planet can be determined from the lightcurve. When combined with the radial velocity method (which determines the planet mass), the density of the planet can be inferred, and hence we can investigate the planet's physical structure. Even though the probability to detect such a transit is rather low (about 10% for a hot Jupiter), 60 planets have been either found or confirmed using this technique.

From the ground, radial velocity measurements are currently limited to the detection of planets about 2 times as massive as Earth in short-period orbits around Sun-like and low-mass stars (Mayor et al. 2009a) while the transit method is limited to Neptune-size planets (Gillon et al. 2007). Thanks to the very high precision photometry enabled by the stable space environment, ongoing space missions promise to push the detection level down to Earth-size planets for semi-major axes as large as a few AU. Future space-based astrometry missions will complete the survey of low-mass extrasolar planets by unambiguously providing their mass. The main missions are briefly described hereafter:

- **CoRoT** (Convection Rotation and planetary Transits) is a space mission led by the French Space Agency (CNES) in conjunction with the European Space Agency (ESA) and other international partners (Baglin et al. 2007). Launched in 2006, the mission has two objectives: searching for extrasolar planets and performing asteroseismology by measuring solar-like oscillations in stars. CoRoT consists in a 27-cm aperture telescope with a 3.5 deg^2 field of view (cf. Figure 1.13, left). For the planetary programme, five fields containing approximately 12000 stars will be continuously monitored during at least 150 days. CoRoT is expected to detect over 10000 planets in the 1 to $5\text{ }R_\oplus$ range within 0.3 AU, assuming all stars have at least one such a planet (Bordé et al. 2003). More realistic simulations show that CoRoT will detect about 100 transiting planets down to a size of $2\text{ }R_\oplus$ around G0V stars and $1.1\text{ }R_\oplus$ around M0V stars.

Since its first detection in 2007 (*CoRoT-1b*, a $1.8\text{-}R_J$ hot EGP orbiting at 0.03 AU around a sun-like star located at about 450 pc), CoRoT has detected several other planets. Because the transit signal is proportional to the planet projected surface, the first published CoRoT results (e.g., Barge et al. 2008; Alonso et al. 2008; Moutou et al. 2008) were focused on the population of rather massive planets, one of which has even been quoted as “the first inhabitant of the brown-dwarf desert”, with a well-defined mass ($20 \pm 1\text{ }M_J$) and a well-defined radius ($1.0 \pm 0.1\text{ }R_J$, Deleuil et al. 2008). However, and fortunately, CoRoT has the capability of detecting significantly smaller planets, as proven by the recent detection of the first transiting Super-Earth with a measured radius (*CoRoT-7b*, Leger et al. 2009). *Corot-7b* is a $1.7\text{-}R_\oplus/\leq 11\text{-}M_\oplus$ planet orbiting at 0.017 AU around a K0V star located at 140 pc.

- **Kepler** is a discovery mission of NASA (National Aeronautic and Space Administration) designed to determine the frequency of Earth-size and smaller planets in and near the HZ of about 100000 main sequence stars (Borucki et al. 2007). The instrument consists of a 0.95-m aperture telescope (cf. Figure 1.13, right) able to perform high precision photometry in order to reveal the sign of a transiting planet. After 4 years, this mission (launched in March 2009) should have discovered several hundred terrestrial planets (i.e. planets up to twice the diameter of Earth) with periods between one day and 400 days if such planets are common. In particular, about 100 Earth-size planets in the HZ could be discovered. This number increases to 650 planets if most terrestrial planets have a size of $2 R_{\oplus}$. A null result would imply that terrestrial planets are rare.

Aside from detecting Earth-size planets in the HZ, Kepler will advance the hot Neptune and hot Earth studies started by CoRoT, detecting up to hundreds of them down to a size as small as that of Mercury. Both Kepler and CoRoT will reveal exciting extrasolar giant planet science with tens of transiting giant planets with semi-major axes in the 0.02-1 AU range and even giant planets in orbits beyond 1 AU can be detected. Very recently, a phase variation of the dayside thermal emission (plus reflected light) from the previously known giant transiting extrasolar planet HAT-P-7b has been detected during the commissioning phase (Borucki et al. 2009).

- **GAIA** is an ESA mission which intends to measure stellar positions with a $\sim \mu\text{as}$ precision in order to make the largest and most precise three-dimensional map of the Milky Way (Crifo and The French Gaia Team 2006). For stars within a distance of approximately 50 pc from the Sun, GAIA is expected to find every Jupiter-size planet with an orbital period of 1.5 - 9 years. Estimates suggest that GAIA will detect between 10000 and 50000 extrasolar planets (Sozzetti et al. 2003).

GAIA is the acronym of Global Astrometric Interferometer for Astrophysics, a name that reflected the optical technique of interferometry, originally planned for use on this telescope. Even if the working method has now changed, the name of GAIA has remained.

- **SIM** (Space Interferometry Mission) is an astrometric mission that will be able to search for terrestrial planets in the HZ of nearby stars with $1\text{-}\mu\text{as}$ relative astrometric accuracy (Shao 2006). The instrument combines the light from two 30-cm aperture telescopes structurally-connected and separated by 9 m. It will use precise measurements of fringe positions to determine orbits of planets with masses 0.5-5.0 times that of Earth around 220 of the closest stars. It will also perform a broader survey of over 2000 stars to look for planets the size of Neptune and larger. Note that a somewhat reduced version of SIM (namely SIM-lite) has been recently proposed. This down-scoped version presents a 6-m carbon boom (instead of 9-m) that allow the search for $1\text{-}M_{\oplus}$ extrasolar planets in mid-habitable zone locations around about 60 nearby stars ($\text{S/N}=5.5$, using roughly 50% of the mission time).

In addition, note that the PRIMA (Phase-Referenced Imaging and Micro-arcsecond Astrometry) instrument will use astrometry to detect extrasolar planets (Reffert et al. 2006). PRIMA will be an ESO facility at the VLT Interferometer (Cerro Paranal, Chile), currently under commissioning. With PRIMA/VLTI, it will then be possible to perform relative astrometry with an accuracy of the order of $10 \mu\text{as}$ over angles of about $10''$. The main science driver for this astrometric capability is the detection and characterization of extrasolar planets, including the observation of known radial velocity planets and planetary systems to fully constrain their orbital geometry and accurately determine the mass of the planet, a search for extrasolar planets around stars which are less suitable for the radial velocity method (for example young and active stars as well as early type stars), and a systematic search around the most nearby stars to detect low mass planets (Uranus or Neptune masses).

Figure 1.14 summarizes the sensitivity of the different ongoing or planned observational instruments, described in the previous paragraphs. In particular, it shows the improved sensitivity of Kepler with respect to CoRoT and the complementarity between radial velocity surveys and astrometric measurements. The planets of the solar system are indicated by the first letter of their name written on a blue



Figure 1.13: *Left:* CoRot, a 27-cm aperture telescope aimed at detecting short orbital period transiting planets down to the size of Earth. *Right:* Kepler, a 0.95-m aperture telescope aimed at detecting Earth-size planets in the habitable zone (see text for details).

filled circle. Extrasolar planets already detected are also represented. Space-based instruments become critical to search for terrestrial planets in the habitable zone. Although these instruments for transit searches (CoRoT, Kepler) or astronomic surveys (GAIA, SIM) are expected to push the detection limit down to a few Earth masses (see Figure 1.14), they will still be mostly restricted to the measurements of orbital parameters and will therefore provide limited information on the physics of these supposedly rocky bodies. Indirect techniques still have many bright years ahead, but will gradually be complemented and replaced by direct techniques, which aim at extrasolar planet imaging and could eventually lead to the detection of biosignatures.

1.3.3 Direct detection methods

Direct imaging in the visible or infrared consists in collecting the photons of the planet rather than measuring indirect effects induced by the planet on its host star. Although it is obviously the most promising way to characterize extrasolar planets, direct imaging is very challenging due to the huge contrast (see Figure 1.5) and the small angular separation between the planet and its host star. To date, direct imaging of extrasolar planets has been reported in only 11 (favorable) cases where the star-planet contrast was not too high (a few hundredths) and the angular separation not too small. These discoveries have first been made possible by the advent of adaptive optics (AO) systems on large ground-based telescopes and then completed by space-based observations with HST and Spitzer (see Section 1.1.3). However, only massive giant planets in wide orbits have been directly imaged so far. To go beyond and directly image lower mass planets, the next major step will be taken by ground-based high-contrast adaptive optics systems such as the Gemini Planet Imager (GPI, Macintosh et al. 2008) and Spectro-Polarimetric High-contrast Exoplanet Research at VLT (SPHERE Beuzit et al. 2008). GPI and SPHERE will detect giant extrasolar planets in the outer regions (beyond 5 AU from the star) of the planetary systems of nearby main sequence stars. By probing large semi-major axis separations that are currently inaccessible to indirect methods, GPI and SPHERE will reveal the zone where the majority of gas giant planets are expected to reside. In particular, this will show whether or not the architecture of our own planetary system with gas giants located between 5-10 AU is unique.

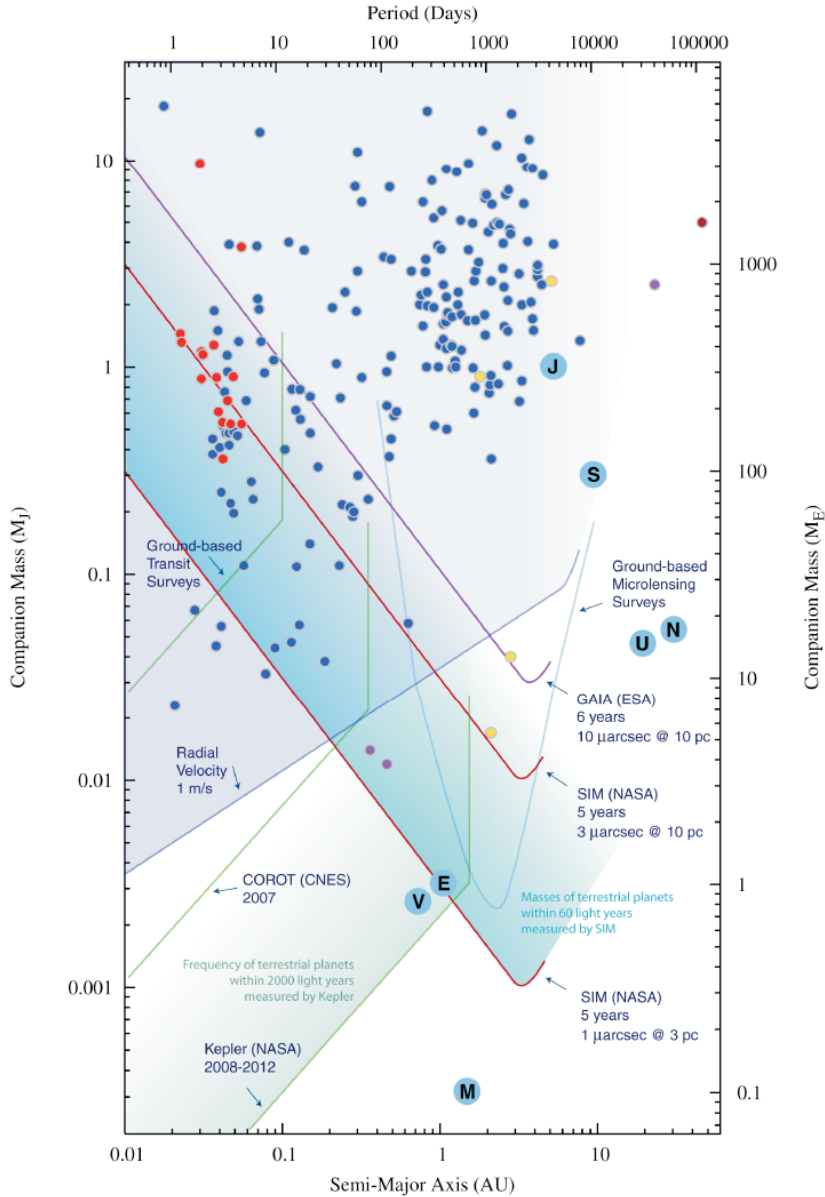


Figure 1.14: Global view of the limiting sensitivity of a wide variety of space and ground-based instruments as a function of planet sizes and orbital locations. The filled circles indicate the planets found at the date of October 2006 by radial velocity surveys (blue), transit surveys (red) and microlensing surveys (yellow). Also indicated by the filled circles are pulsar planets (violet) and the companion to a young brown dwarf (dark red). Planets in our solar system are also indicated. Space-based techniques become critical to search for terrestrial planets in the habitable zone (Figure from Lawson and Traub 2006).

1.4 Prospects for future observations

1.4.1 Extrasolar planets

The focus of exoplanet research is now shifting towards finding planets that are the most promising candidates for supporting life, and searching for indicators of biological processes (biosignatures, see Section 1.1.4) in their visible and infrared spectra. Coronagraphy and interferometry are generally the two techniques considered to achieve this huge observational challenge. A coronagraph is an instrument designed specifically to block the starlight, either by an occulting disc or by an appropriate phase mask,

so that nearby objects can be resolved. Phase mask coronagraphs are transparent but induce spatially-distributed phase shifts with the goal of destructively rejecting the starlight (see Mawet 2006 for a detailed description of phase-mask coronagraphs). Nulling interferometry is a technique in which the beams coming from two telescopes are combined in phase opposition so that a dark fringe appears on the line of sight, which strongly reduces the starlight emission. This technique is thoroughly addressed in Chapter 4. The prospects for detecting extrasolar planets with space-based nulling interferometry is one of the main purpose of this thesis (see Chapters 6 and 7). In the following paragraphs, some of the main space-based mission projects using one of these techniques are presented.

- **EPIC/PECO/SEE-COAST** are similar projects for a visible coronagraph. EPIC (Extrasolar Planetary Imaging Coronagraph), PECO (Pupil-mapping Exoplanet Coronagraphic Observer), and SEE-COAST (Super-Earth Explorer - Coronagraphic Off-Axis Space Telescope) consist of ~ 1.5 -m class coronagraphic telescope aimed at delivering high-contrast images of extrasolar systems, and low resolution spectra of the gas giant planets. In particular, these missions should be able to image dozens of Jupiter-like planets in the 1-5 AU range around nearby stars (within 15 pc). Low-resolution spectroscopic capabilities will permit a first characterization of their atmosphere in the visible, searching for H_2O , CH_4 and NH_3 .
- **FKSI** (Fourier-Kelvin Stellar Interferometer, NASA) is a project consisting of a structurally connected infrared space interferometer with 0.5-m diameter telescopes on a 12.5-m baseline, and passively cooled down to 60 K (Danchi et al. 2006). The FKSI operates in the thermal infrared from 3-8 μm in a nulling mode for the detection and characterization of extrasolar planets, debris discs, exozodiacal dust, and for high angular resolution astrophysics. FKSI will have the highest angular resolution of any space instrument operating in the thermal infrared ever made with a nominal resolution of 40 mas at a 5 μm center wavelength. This resolution exceeds that of Spitzer by a factor of 38 and JWST by a factor of 5. The FKSI mission is conceived as a “probe class” or “mid-size” strategic mission that utilizes technology advances from flagship projects like JWST, SIM, Spitzer, and the technology programs of DARWIN/TPF. FKSI will be able to detect and characterize a large variety of extrasolar planets, including super-Earths in the habitable zone of nearby M stars (see Chapter 6 for further details).
- **JWST** (James Webb Space Telescope, NASA and ESA) will by 2015 be the largest telescope operating in space, providing a wide and continuous spectral coverage from the visible (0.6 μm) to the mid-IR (28 μm , Clampin 2007). With a diameter of 6.57 m, the main objectives of JWST are to improve our understanding of the evolution of the Universe, the birth and formation of stars and their planetary systems. Using phase-mask coronagraphy, JWST is expected to enable the direct imaging of giant extrasolar planets with a temperature higher than 400 K and orbiting nearby stars at typical distances of 5-10 AU (Baudoz et al. 2006; Hanot et al. 2009).
- **TPF-C** (Terrestrial Planet Finder Coronagraph) is a NASA project of mission presenting a 3.5×8 -m elliptical single-aperture telescope and using a coronagraph to suppress the stellar emission (Traub et al. 2006). TPF-C would observe nearby Sun-like stars in the visible to search for Earth-like planets able to support life. It will be deployed beyond the Moon’s orbit for a mission lifetime of 5 years, possibly extended to 10 years.
- **DARWIN/TPF-I** (Terrestrial Planet Finder Interferometer) is an infrared nulling interferometry project, aimed at the detection and characterization of Earth-like extrasolar planets. During a mission lifetime of 5 years, over 200 Earth-size planets could be detected with a spectroscopic characterization (CO_2 , O_3 and H_2O) for about 20 of them. DARWIN/TPF-I achieves this sensitivity by using four 2-m telescopes operating in the infrared. The DARWIN mission and its expected performance are described in details in Chapter 7.

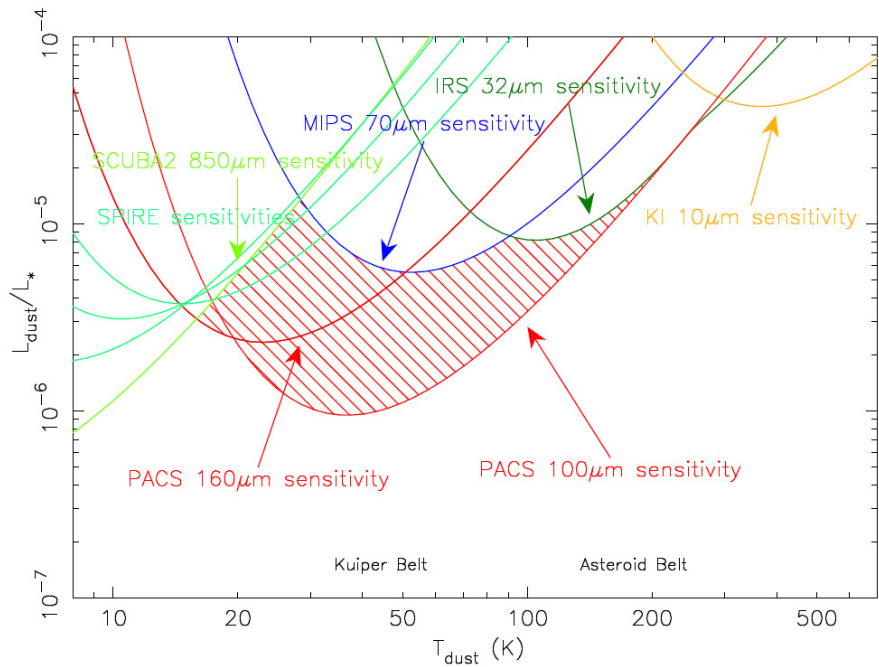


Figure 1.15: Detection limits for a G5V star located at 20 pc, following the Bryden et al. (2006) approach. The assumed 1- σ fractional flux accuracies are 20% for Spitzer/MIPS at 70 μm , 2.5% for Spitzer/IRS at 32 μm , 10% for PACS at 100 μm (i.e., SNR=10), and 100% for PACS at 160 μm (SNR=1).

1.4.2 Circumstellar discs

These prospects for extrasolar planets will be completed by complementary observations of circumstellar discs. Launched in 2009, Herschel (the ESA far-infrared and sub-millimeter space observatory) is of particular interest for the study of the cold circumstellar material around young and main sequence stars. With a 3.5-m effective telescope diameter, Herschel is the largest mirror ever built for a space telescope until the JWST flies. Onboard instruments (namely, PACS and SPIRE) offer imaging photometry at 70, 100, 160, 240, 350, and 500 μm , providing an unprecedented sensitivity for the detection of circumstellar material down to Kuiper belt analogs (see Figure 1.15, right).

JWST will also have a large impact on disc research, by probing the overall evolution of extrasolar planetary systems with a sensitivity about 30-100 times better than Spitzer. Operating in the infrared (0.6 to 5 μm for NIRCam and 5 to 28 μm for MIRI), it will be able to image the faint outer disc structure beyond 100 AU where at least one planet was detected (Fomalhaut b, Kalas et al. 2008) and substantial evidence was gathered for structures such as spiral arms and arcs (e.g., Grady et al. 1999). It will also be able to probe the vertical disc structure and underlying gas-dust physics through combined spectroscopy and imaging, as well as studying debris discs that may be in the terrestrial planet forming phase.

The pictures provided by Herschel and JWST of the outer parts of circumstellar discs will be completed by observations with interferometric facilities. In the submillimeter and millimeter wavelength ranges (from 0.3 to 9.6 mm), the “Atacama Large Millimeter Array” (ALMA) will determine the dynamics of dust-obscured protostellar accretion discs, the rate of accretion and infall from the nascent molecular clouds, the mass distribution over the disc, and the structure of molecular outflows. In the infrared regime, several instrument will directly probe the habitable zone of nearby main sequence stars. On the American side, the Large Binocular Telescope Interferometers (LBTI, see Section 4.4.3), will be able to measure the 10- μm exozodiacal emission that arises in the HZ. European projects such as ALADDIN (see Section 4.5.2) is also very promising to measure the near-infrared emission of the circumstellar disc

inner regions to an unprecedented level. From space, the FKSI project could reach the detection of zodiacal cloud analogs in the near infrared (between 3 and 8 μm , see a performance comparison of these instruments in Chapter 5). With Herschel measuring excesses from 70 to 200 μm down to Kuiper belt analogs, KI, LBTI, ALADDIN and FKSI pushing to Solar system levels in the near-and mid- infrared, we will have a global view to understand the physics of circumstellar discs and confirm that a population of stars with low levels of zodiacal emission does indeed exist.

Part II

Study of debris discs with infrared stellar interferometry

2

Overview of stellar interferometry

Contents

2.1	The need for interferometry	35
2.2	Basics of stellar interferometry	36
2.2.1	Interferometric observables	38
2.2.2	Fringe signal coding	39
2.2.3	Van Cittert-Zernike theorem	40
2.3	Applications of stellar interferometry	42
2.3.1	First and second generation	42
2.3.2	A new generation	43
2.3.3	Upcoming facilities	44
2.3.4	Major scientific results	45

During the last two decades, optical stellar interferometry has become an important tool for astronomical observations, providing a spatial resolution well beyond that of traditional telescopes. After a brief historical review, this chapter introduces the principles of stellar interferometry and the required mathematical background for the next chapter, as well as some technical aspects. Then, a brief description of current interferometric facilities is given together with a selection of important astrophysical discoveries made with them. Finally, we discuss the main features of upcoming facilities.

2.1 The need for interferometry

As adaptive optics (AO) systems are already pushing toward the theoretical diffraction-limit of a single-dish telescope, a conceptual move has to be taken to gain further resolution in optical astronomy. Indeed, the angular resolution of monolithic optical instruments is limited due to the wave nature of light which is embodied in the Rayleigh criterion, stating that the angular resolution of a telescope is ultimately diffraction limited according to $\theta = 1.22\lambda/D$, where λ is the wavelength and D the aperture diameter. For instance, the angular separation between an Earth-like planet orbiting at 1 AU from its host star located at 20 pc is 50 mas which requires at least a 30-m diameter telescope to resolve the system in the N band (8-13 μ m). Similar conclusions can be drawn for the observations of the inner part of circumstellar discs. The need for higher angular resolution has led to the development of instruments with larger and larger mirrors, finally reaching 10 m with the most recent telescopes (see the Keck description in Section 2.3). Adaptive optic systems have been designed to achieve the full potential of these giant telescopes in terms of angular resolution, overcoming the harmful perturbations of atmospheric turbulence. However, in the mid-infrared regime, the desired angular resolution to resolve

extrasolar systems can hardly be accomplished with current monolithic telescopes, where the angular resolution is limited to about 250 mas. Large telescopes, up to 100-m aperture diameter, are currently being studied but, as such large apertures are not expected to be feasible in space, they will still be limited by the presence of the Earth's atmosphere which degrades the images and restricts the observations to the infrared transparency windows (e.g., the N band).

Another way to achieve high angular resolutions without building gigantic telescopes is to combine light beams from several telescopes in order to synthesise a larger aperture. The resolution of the instrument is then equivalent to the resolution of a single-dish telescope with a diameter equivalent to the distance between the individual telescopes. The most basic principles of optical (i.e., visual and infrared) interferometry were already formulated in 1868 by Fizeau, who proposed to place a mask with two holes in front of a telescope aperture Fizeau and Foucault (1868). Fizeau suggested measuring the diameter of stars by finding the hole separation at which the formed interference pattern (the fringe) vanished. This technique was used five years later by Stéphan to obtain an upper limit on the diameter of some stars and was successfully applied by Michelson to measure for the first time the diameter of the Galilean moons (Michelson 1891). In 1919, Michelson enhanced the resolution of the 2.5-m Hooker telescope at the Mount Wilson Observatory by mounting a 20-foot beam on top of it, resulting in the first measurement of a stellar diameter (Michelson and Pease 1921). Another milestone was reached in 1974 when Antoine Labeyrie succeeded in combining in the visible the light of two separate telescopes, located 12 m apart (Labeyrie 1975). At this stage, the radio astronomy community had already developed important concepts for long baseline radio interferometry which could be adopted to optical wavelengths. Some important contributions were the development of Earth rotation aperture synthesis (e.g., Ryle and Hewish 1960) and the concept of the phase closure (Rogers et al. 1974), allowing to obtain accurate phase information even in presence of strong atmospheric perturbations. The first optical aperture synthesis images were presented by Buscher et al. (1990) and Baldwin et al. (1996), who imaged the surface of Betelgeuse and the binary star Capella, respectively. Today, interferometry has become a widespread technique used in several instruments and projects.

2.2 Basics of stellar interferometry

Optical stellar interferometry consists in recombining the light collected by different telescopes in order to produce information with high angular resolution (see Figure 2.1). The expression of the monochromatic light collected by each telescope and emitted by the same object can be written as the product of a stationary planar wave $\Psi_s(\vec{s})$ and a time-dependent propagation term, according to the Maxwell equations:

$$\Psi(\vec{s}, t) = \Psi_s(\vec{s}) \exp^{-i(ckt + \phi)}, \quad (2.1)$$

where $k = 2\pi\nu/c = 2\pi/\lambda$ is the wave number, ϕ the phase of the wave, c the speed of light in vacuum, ν the frequency, and λ the wavelength. For long-baseline interferometry, each telescope collects a sample of the same electromagnetic wave Ψ . While propagating throughout the optical system, the wave experiences optical path differences, which are taken into account by including a delay term τ_i for each spatially filtered wave front. In addition, the phase of the wave is also rapidly changing due to the atmosphere (this effect is taken into account by ζ_i). Therefore, the wave reaching the detector from aperture i , can be written as:

$$\psi_i(\vec{s}, t) = \sqrt{P_i(\vec{s})} \Psi_i(\vec{s}, t) \exp^{-ick(\tau_i + \zeta_i)}, \quad (2.2)$$

where $P_i(\vec{s})$ is the pupil function of aperture i (including transmission). The intensity I_i of the light from this telescope is then given by the absolute square of the complex wave-function ψ_i . Due to the finite sampling time, we compute the time-averaged intensity with

$$I_i(\vec{s}, t) = \left\langle |\psi_i(\vec{s}, t)|^2 \right\rangle = P_i(\vec{s}) \left\langle |\Psi_i(\vec{s}, t)|^2 \right\rangle. \quad (2.3)$$

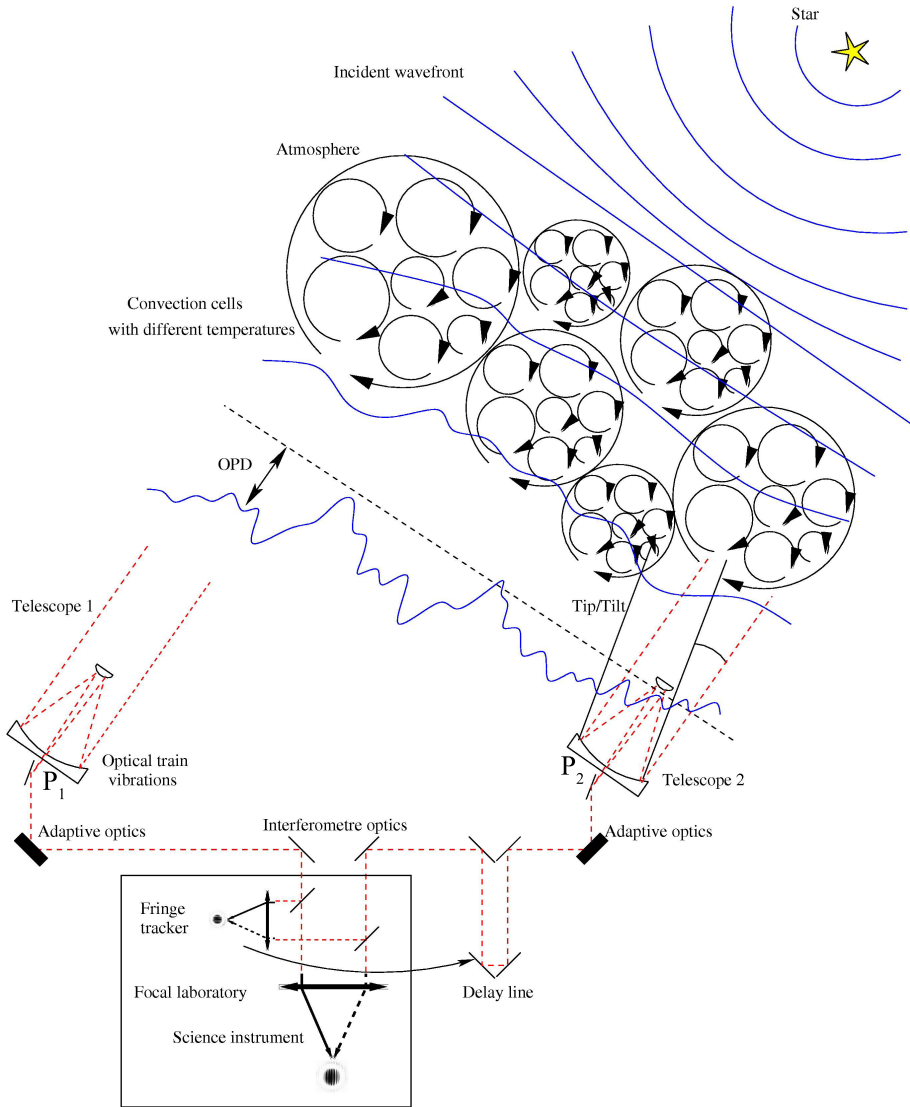


Figure 2.1: Schematic representation of a two-telescope stellar interferometer (Figure from Millour, 2009).

If light from N apertures is superimposed, the measured signal is then given by

$$\begin{aligned}
 I(\vec{s}, t) &= \left\langle \left| \sum_{i=1}^N \psi_i(\vec{s}, t) \right|^2 \right\rangle \\
 &= \sum_{i=1}^N I_i + \sum_{i < j}^N 2\sqrt{I_i I_j} \Re \left[\frac{\langle \Psi_i \Psi_j^* \rangle}{\sqrt{\langle |\Psi_i|^2 \rangle \langle |\Psi_j^*|^2 \rangle}} \exp^{-i[ck(\tau_i + \zeta_i) - ck(\tau_j + \zeta_j)]} \right] \\
 &= \sum_{i=1}^N I_i + \sum_{i < j}^N 2\sqrt{I_i I_j} \Re \left[\mathcal{V}_{ij} \exp^{-ick(\tau_i + \zeta_i - \tau_j - \zeta_j)} \right], \tag{2.4}
 \end{aligned}$$

where the first term corresponds to the constant continuum (which has generally to be removed in the data reduction process) and the second term corresponds to the interference pattern which contains the high angular information. Ψ_i^* is the complex conjugate of Ψ_i and \mathcal{V}_{ij} is defined as the complex visibility

(which is identical to the complex degree of coherence) such that:

$$\mathcal{V}_{ij} = \frac{\langle \Psi_i \Psi_j^* \rangle}{|\Psi_i| |\Psi_j^*|}. \quad (2.5)$$

The fringe pattern γ_{ij} at the detector shows a cosine modulation, with an amplitude given by the visibility ($|\mathcal{V}_{ij}|$):

$$\begin{aligned} I(\vec{s}, t) &= \sum_{i=1}^N I_i + \sum_{i < j}^N 2\sqrt{I_i I_j} |\mathcal{V}_{ij}| \cos [ck(\tau_i + \zeta_i - \tau_j - \zeta_j) + \phi_i - \phi_j] \\ &= \sum_{i=1}^N I_i + \sum_{i < j}^N 2\gamma_{ij} \sqrt{I_i I_j}, \end{aligned} \quad (2.6)$$

where γ_{ij} equals to $|\mathcal{V}_{ij}| \cos [ck(\tau_i + \zeta_i - \tau_j - \zeta_j) + \phi_i - \phi_j]$.

2.2.1 Interferometric observables

Fringe visibility

The fundamental observable in interferometry is the fringe contrast, given by the amplitude of the complex visibility (see definition in 2.5). The fringe contrast is defined as the ratio between the fringe amplitude and the average intensity. For a two-telescope interferometer, the fringe contrast is given by (from Eq. 2.6):

$$\mathcal{V} = \frac{I_{\max} - I_{\min}}{I_{\max} + I_{\min}}, \quad (2.7)$$

where I_{\max} and I_{\min} are respectively the maximum and minimum intensity of the fringes. While the phase of \mathcal{V}_{ij} is strongly affected by atmospheric perturbations, the atmospheric (and instrumental) effects on the fringe amplitude vary rather smoothly and can be corrected using measurements on calibrator stars. Therefore, it is common to use the (phase independent) absolute square of the complex visibility as observable \mathcal{V}_{ij}^2 . This quantity can be extracted from the interferogram power spectrum and \mathcal{V}_{ij}^2 estimators that properly take into account the noise bias can be constructed (Perrin 2003).

Phase closure and phase referencing

Besides the fringe amplitude (i.e., \mathcal{V}^2 , as defined in equation 2.5), the phase of the complex visibility carries additional information about the source brightness distribution. The Fourier phase ϕ of the complex visibility is given by

$$-\phi = \arg(\mathcal{V}) = \tan^{-1} \frac{\Im(\mathcal{I})}{\Re(\mathcal{V})}. \quad (2.8)$$

However, extracting this quantity from ground-based measurements is generally difficult because it is completely corrupted by the piston introduced by the turbulent atmosphere (see equation 2.2). The rms atmospheric phase shift is generally larger than 1 radian and even after averaging over many states of the atmosphere does not provide an estimate of the intrinsic source phase (Monnier 2000). One possibility for overcoming this phase corruption is phase referencing, which consists in using a reference object to determine the atmospheric phase and to correct the phase of the target source accordingly. For this technique to work, the target and reference sources must be affected by the same atmospheric turbulence, i.e., be separated by an angle smaller than the isoplanetic angle (the angle over which image distortions are correlated). Because the isoplanetic angle is only a few arcseconds in the optical regime,

this technique is limited by the presence of a sufficiently bright source angularly close to the target. It has been applied to narrow-angle astrometry where fringe phase information is used to determine precise relative positions of nearby stars (Shao and Colavita 1992) and will be used for the VLTI with the PRIMA fringe tracker (Delplancke 2008). Note that this technique can also be used to increase the effective atmospheric coherence time, allowing longer integrations on the target source.

Another possibility to retrieve (part of) the phase information makes use of the fact that for observations with three or more apertures, the atmospheric disturbance terms ζ cancel out when adding the phase terms in a closed triangle telescope configuration. Considering the case for 3 telescopes and combining them in pairs, we obtain the following interferogram phases:

$$\varphi_{12} = \phi_1 - \phi_2 - ck(\zeta_1 - \zeta_2 + \tau_1 - \tau_2) \quad (2.9)$$

$$\varphi_{23} = \phi_2 - \phi_3 - ck(\zeta_2 - \zeta_3 + \tau_2 - \tau_3) \quad (2.10)$$

$$\varphi_{31} = \phi_3 - \phi_1 - ck(\zeta_3 - \zeta_1 + \tau_3 - \tau_1), \quad (2.11)$$

so that their sum is insensitive to the phase corruption introduced by atmospheric turbulence (ζ). The phase closure (PC) $\varphi_{12} + \varphi_{23} + \varphi_{31}$ therefore only depends on the brightness distribution of the source, so that one third of the phase information can be retrieved from measurements on a single triplet of telescopes. Due to this property, phase closures are also self-calibrating; i.e., no calibrator measurements are needed to monitor changes in the atmospheric conditions (as required for \mathcal{V}^2 measurements). For an array of N telescopes, the number of independent closure phases measured on triplets of telescopes is given by $(N - 1)(N - 2)/2$, equivalent to holding one telescope fixed and forming all possible triangles with that telescope (Monnier 2000). Because there are $N(N - 2)/2$ independent Fourier phases, the information provided by closure phase measurements is incomplete, and given by $(N - 2)/N$. For instance, this corresponds to 60%, 80% and 96% of the phase information for 5, 10 and 50 telescopes respectively (if the baselines are not redundant).

Differential observables

From spectrally dispersed interferograms, differential observables can be extracted in addition to the above-mentioned absolute observables. In analogy to the \mathcal{V}^2 estimator, the differential visibility measures the relative change of the visibility in adjacent spectral channels. The differential phase is also very interesting. One of its remarkable feature is that, for non resolved (i.e., smaller than λ/b) sources, it is proportional to the variation of the photocenter of the source (Petrov 1989). Given a sufficient SNR, the photocenter variation with λ can be measured on very unresolved sources with many very rich astrophysical applications (e.g., circumstellar discs, imaging of unresolved spotted stars). Similar to the CP, differential observables are self-calibrating; i.e., they do not require a calibrator measurement to compensate for atmospheric effects. They can be measured for instance with AMBER (Petrov et al. 2007).

2.2.2 Fringe signal coding

In order to ensure a coherent recombination of the light coming from different telescopes, two distinct strategies can be used: co-axial or multi-axial (Malbet et al. 1999; Schöller et al. 2000). While the co-axial combination scheme superimposes the beams on one pixel of the detector and modulates the delay between them (*temporal coherence*), the multi-axial combination scheme records the interferogram at one time, but spread in space (*spatial coherence*).

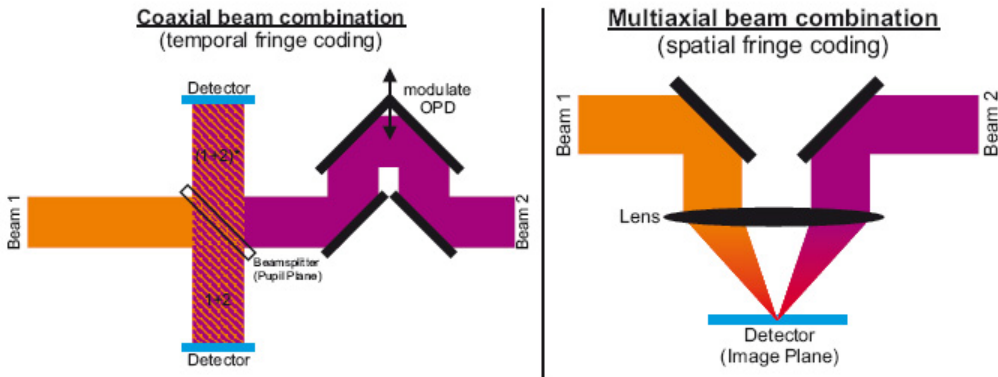


Figure 2.2: Basic principles used in the current generation of optical interferometric beam combiners. *Left:* Coaxial beam combination. *Right:* Multiaxial beam combination (Figure from Kraus 2007).

Co-axial beam combination

The co-axial combination scheme consists in superimposing pair-wise the beams on a 50/50 beam splitter. The principle of this technique is illustrated in the left part of Figure 2.2. The signals from the beam combiners are focused at a detector so that the fringes are encoded temporally on two single-pixel detectors placed at each output of the beam splitter. To temporally modulate the signals, the OPD is systematically modified by introducing an additional delay of known amplitude. Technically, this can be realized, for instance, using piezo-electric scanners, which introduce a delay on $N - 1$ of the N baselines (at one baseline the delay is kept fixed).

Co-axial beam combination is similar to the one applied in the Michelson-Morley interferometer (Michelson and Pease 1921) and is today the most widely used technique (e.g., IOTA, CHARA/FLUOR, VLTI/VINCI, VLTI/MIDI).

Multi-axial beam combination

In multi-axial beam combination, the beams are brought together at a common focus from various directions, producing the equivalent of Young's fringes. The principle of this technique is illustrated in the right part of Figure 2.2. The fringe signal is recorded at one time (in one exposure), but is spread in the image plane over many pixels on the detector plane. The spatial fringe coding is achieved by placing the exit pupils at certain distances to each other and then to superimpose the beams using, for instance, a lens, introducing geometric path differences. For $N > 2$ telescopes, confusion between the fringes can be avoided by placing the corresponding exit pupils at varying distances to each other. This results in different frequencies in the carrying waves, which allows one to separate the interferograms from the different baselines during data reduction. This method has been implemented at GI2T and is nowadays used at VLTI/AMBER (see Section 2.3 for a description of this stellar interferometer).

2.2.3 Van Cittert-Zernike theorem

Under certain assumptions (source incoherence and small-field approximation), the complex visibility (as defined in equation 2.5) can be related to the source brightness distribution $I(x, y)$ through the van-Cittert-Zernike theorem, which provides the basic theory for any modeling of interferometric data. In fact, the visibility is exactly proportional to the amplitude of the image Fourier component corresponding to the spatial frequency ($u = b/\lambda$) related to the baseline b . Also, the phase of the fringe pattern is equal to the Fourier phase of the same spatial frequency component. Then, the van-Cittert-Zernike theorem

relates \mathcal{V} with the Fourier transform of the brightness distribution, i.e.:

$$\mathcal{V} = \int_{-\infty}^{+\infty} \int_{-\infty}^{+\infty} I(x, y) \exp^{-iki(ux+vy)} dx dy, \quad (2.12)$$

where u and v are coordinates measured in the frequency space. For a point source (unresolved) $\mathcal{V}=1$, whereas for uniformly bright background emission filling the whole field-of-view (over-resolved source) $\mathcal{V}=0$. In practice, interferometric fringes never have a perfect contrast ($\mathcal{V} = 1$), even for a point source, because of atmospheric and instrumental effects. One must therefore accompany each measurement of the target by a similar measurement of an unresolved calibration source. The true visibility of the object is then the observed visibility of the object divided by the observed visibility of the calibrator.

Based on the van-Cittert-Zernike theorem, it is straightforward to compute the visibility profile for arbitrary brightness distributions. The visibilities for a uniform disc, a gaussian disc and a binary source are commonly used. The derivation of these analytic descriptions can be found in the literature (Boden et al. 2000; Millan-Gabet et al. 2001).

- **Uniform disc (UD):** The visibility function for a disc with diameter θ_{UD} and of uniform brightness I , depends on the projected baseline as

$$\mathcal{V}(b_{\perp}, \lambda, \theta_{UD}) = \left[\frac{2J_1(\pi\theta_{UD}b_{\perp}/\lambda)}{\pi\theta_{UD}b_{\perp}/\lambda} \right]^2, \quad (2.13)$$

where b_{\perp} is the length of the baseline vector projected onto the sky plane and J_1 denotes the Bessel function of first kind and first order. For an unresolved star ($\theta_{UD} \ll \lambda/b_{\perp}$), the visibility is close to 1. It decreases for increasing baseline lengths and finally reaches zero for $\theta_{UD}=1.22\lambda/b_{\perp}$. The star is then said to be resolved.

- **Gaussian Brightness Distribution:** If we consider a Gaussian brightness distribution of full width half maximum (FWHM) diameter θ_G , the visibility profile is given by

$$\mathcal{V}(b_{\perp}, \lambda, \theta_G) = \exp \left[\frac{-(k\theta_G b_{\perp})^2}{4\ln 2} \right]. \quad (2.14)$$

- **Binary source:** If two binary components have an intensity (I_1 and I_2) and a visibility profile (\mathcal{V}_1 and \mathcal{V}_2), the complex visibility depends on the component separation vector \vec{s} as.

$$\mathcal{V}(\vec{s}) = \frac{I_1 \mathcal{V}_1 + I_2 \mathcal{V}_2 \exp^{-ik\vec{b}\vec{s}}}{I_1 + I_2}, \quad (2.15)$$

where \vec{b} is the baseline vector.

From the measurements of Fourier components (amplitude and phase) in the spatial frequency plane, it is in principle possible to reconstruct the image, provided that the sampling of the (u,v)-plane is sufficiently dense. Reconstruction algorithms such as CLEAN (Hogbom and Brouw 1974) or the maximum entropy method (MEM, Skilling 1984) are routinely used in radio-interferometry. A good sampling of the (u,v)-plane can be achieved either by repeating the interferometric measurements with various telescope pairs or by using the Earth's diurnal rotation. The latter method, called supersynthesis, has been extensively used in the past years as most interferometric facilities are composed of a limited number of fixed telescopes. By observing the same star at different moments in time with the same (fixed) telescopes, one obtains information at different spatial frequencies since the projected baseline length (b_{\perp}) and orientation changes due to the Earth rotation.

Table 2.1: Selected optical/infrared interferometers given with their date of first fringes (see main text for further details, table adapted from Quirrenbach 2009).

Name	Location	Year	Comments
I2T	Obs. Côte d'Azur (France)	1974	Fringes with separate telescopes
Mark I	Mount Wilson (USA)	1979	Fringe tracking
GI2T	Obs. Côte d'Azur (France)	1985	Interferometric spectroscopy
Mark III	Mount Wilson (USA)	1986	Astrometry
ISI	Mount Wilson (USA)	1988	10 μ m heterodyne
SUSI	Narrabi (Aus)	1992	$B_{\max}=640$ m
COAST	Cambridge (UK)	1991	5 \times 40 cm
IOTA	Mount Hopkins (USA)	1993	3 \times 4.45 cm
NPOI	Anderson Mesa (USA)	1995	Imaging and astrometry
PTI	Mount Palomar (USA)	1995	Dual-star astrometry
CHARA	Mount Wilson (USA)	2001	6 \times 1 m
KI	Mauna Kea (USA)	2001	2 \times 10 m, nulling
VLTI	Paranal (Chile)	2001	4 \times 8.2 m + 4 \times 1.8 m
MRO	Magdalena Ridge (USA)	2010	6 \times 1.4 m, $B_{\max}=340$ m
LBT	Mount Graham (USA)	2011	6 \times 1.4 m in single mount

2.3 Applications of stellar interferometry

2.3.1 First and second generation

After the successful application of interferometry to distant telescopes with the “Interféromètre à Deux Télescopes” (I2T, Labeyrie 1975), various interferometric projects have been initiated around the world. The first one was the successor of I2T, namely the “Grand Interféromètre à 2 Télescopes” (GI2T, 1985) at the “Observatoire de la Côte d'Azur”. With its two innovative 1.5-m telescopes, GI2T was used to develop interferometric spectroscopy. It has been successful in studying the circumstellar environment of active hot stars (Be stars, Stee 2003) and the stellar magnetism (Rousselet-Perraut et al. 2004). GI2T has been dismantled in 2006 due to several mechanical problems on the telescopes.

In the meantime, active fringe tracking was first demonstrated by the Mark I interferometer on Mount Wilson (Shao and Staelin 1980), which evolved later into the Mark II and Mark III instruments (Shao et al. 1988). The Mark III was specifically designed to perform wide-angle astrometry, but a variable baseline that could be configured from 3 m to 31.5 m provided the flexibility needed for various astronomical programs. Thanks to the full computer control of the siderostats and delay lines, almost autonomous acquisition of stars and data taking were allowed so that the Mark III could observe up to 200 stars in a single night. This capability was an important factor for the calibration of instrumental effects, and for the scientific productivity of the instrument. The Mark III was scientifically very productive, yielding stellar diameter and limb darkening measurements (e.g., Quirrenbach et al. 1996; Mozurkewich et al. 2003), binary orbits (e.g., Hummel et al. 1994a), the geometry of Be star discs (Quirrenbach et al. 1997), and a demonstration of wide-angle astrometry (Hummel et al. 1994b).

In the mid-infrared, interferometry was pioneered with the Infrared Spatial Interferometer (ISI, Hale et al. 2000). Located on Mount Wilson, ISI uses heterodyne techniques¹¹ similar to those familiar from radio facilities. Using three 1.65-m telescopes, ISI operates at wavelengths from 9 to 12 μ m, using a CO₂ laser as local oscillator. The ISI has mostly been used to study dust shells around evolved late-type stars (e.g., Danchi et al. 1994; Weiner 2004) and accurate angular diameter measurements (e.g., Weiner et al.

¹¹The heterodyne technique consists in detecting a signal by non-linear mixing with radiation of a reference frequency (likely a laser).

2000, 2003). ISI was also used to image the dust discs around young stars (Tuthill et al. 2002).

The first closure-phase images from an optical synthesis array, showing the two components of the binary system Capella, were produced by the Cambridge Optical Aperture Synthesis Telescope (COAST, Baldwin et al. 1996). With five 40-cm siderostats arranged in a Y-shaped configuration, COAST was the first interferometer to produce true synthesis images at optical wavelengths (visible and near-infrared). The power of synthesis imaging in the near-infrared was also demonstrated by Tuthill et al. (1999), who were able to reconstruct the dust distribution in the Wolf-Rayet¹² binary WR 104 from data obtained by masking the entrance aperture of the Keck telescope with a non-redundant arrangement of holes.

In addition to these pioneering instruments, a number of permanent interferometric facilities have been built in the nineties: the Sydney University Stellar Interferometer (SUSI, 1992), the Infrared-Optical Telescope Array (IOTA, 1993), the Navy Prototype Optical Interferometer (NPOI, 1994), the Palomar Testbed Interferometer (PTI, 1995), the Mitaka optical and InfraRed Array (MIRA, 1998). They are generally characterized by small aperture telescopes and operation in the visible or near-infrared domains (see Table 2.1 for the main characteristics). PTI and IOTA have been particularly scientifically productive. Using three 45-cm siderostats arranged on short baselines (≤ 40 m), IOTA has been extensively used to measure the diameters of Mira and supergiant stars (e.g., Perrin et al. 2004). The study of YSOs has also greatly benefited from the IOTA capabilities, with the important result that the characteristic sizes of the near-infrared emitting regions are larger than previously thought (Millan-Gabet et al. 2001). The addition of a third telescope and of a new 3-way integrated optics beam combiner (IONIC) has improved the facility with imaging capabilities. IOTA will be described in more detail in Section 3.2. With similar apertures (40 cm) combined pair-wise in the near-infrared, PTI has obtained important results on high-precision astrometric measurements of multiple stars (Muterspaugh et al. 2005; Lane and Muterspaugh 2004) as well as on the oblateness of rapidly rotating stars (van Belle et al. 2001).

2.3.2 A new generation

Based on the success of the first and second generation facilities, new interferometers with improved performances have been built. The major design driver of new generation arrays has followed two different tracks: larger baselines to get higher angular resolutions and larger telescope diameters to reach fainter magnitudes. The Keck-I and the VLTI, which combine both large baselines and large apertures, are leading the way. Both have obtained their first fringes in 2001 and are equipped with various instruments with a wavelength coverage from the near- to the mid-infrared. Another facility, more modest yet very performing, is the CHARA array which presents long and numerous baselines with 1-m class telescopes. Technical details related to these facilities are given hereafter.

- **Center for High Angular Resolution Astronomy (CHARA, 1998)** is an interferometric array located on Mount Wilson, commissioned in 1999 but extensively used for science only since 2004 (ten Brummelaar et al. 2005). The array consists in six 1-m class telescopes arranged on a non-redundant Y-shaped configuration. The maximum baseline length of the array is 330 m, corresponding to an angular resolution of 0.3 to 1 mas from visible to near-infrared respectively. The first beam combiner available at CHARA was CHARA Classic, a simple bulk-optics, pupil-plane combiner capable of combining two telescopes at a time, operating from 1.5 to 2.5 μ m. Several other beam combiners have followed (namely FLUOR, MIRC, PAVO, and VEGA, see Table 2.2 for more details).

During the past few years, the CHARA array has produced unique science in the two-telescope and four telescope configuration. Notably it has provided the first detection of gravitational darkening

¹²Wolf-Rayet stars are evolved, massive stars (over $20 M_{\odot}$), which are losing mass rapidly by means of a very strong stellar wind, with speeds up to 2000 km/s.

Table 2.2: Performances of beam combiners at CHARA.

Instrument	Faintest magnitude reached	Wavelength [μm]	R $\lambda/\Delta\lambda$	Visibility accuracy	CP accuracy [degree]
CHARA Classic	7.5	1.50-2.50	NA	5-10%	NA
FLUOR	6.0	2.20	NA	1%	NA
MIRC	4.5	1.50-2.20	40,150,400	10%	0.1-0.5
VEGA	7.4	0.45-0.90	30000,5000,1700	3%	TBD
PAVO	8.2	0.66-0.95	40	2%	TBD

in a rapidly rotating star (McAlister et al. 2005; van Belle et al. 2006), the first detection of warm circumstellar dust around a main sequence star (Absil et al. 2006b), measurement of the diameter of an extrasolar planet using transit and interferometric diameter of the host star (Baines et al. 2007), the first image of a main sequence star (Monnier et al. 2007) and the first image of an interacting binary (Zhao et al. 2008).

- **The Keck Interferometer (KI, 2001)** is a NASA-funded ground-based interferometer located at the summit of Mauna Kea, Hawaii (see Figure 4.8, left). KI combines light from the two 10-m aperture telescopes of Keck (the world’s largest optical telescopes). The mirrors are composed of 36 hexagonal segments that work in concert as a single piece of reflective glass. KI presents a 85-m baseline length, corresponding to a spatial resolution of 5 mas at $2.2\ \mu\text{m}$, and 24 mas at $10\ \mu\text{m}$. The sub-systems of the interferometer include adaptive optics, laser metrology to control optical delay lines, and fringe tracking to measure the interference in the combined light from the two telescopes. Since 2004, KI offers H- and K-band fringe visibility measurements, in addition to a $10\ \mu\text{m}$ nulling mode, for which first nulling data were collected in 2005 (further details on the nulling mode are given in Section 4.4.2).
- **The Very Large Telescope Interferometer (VLT-I, 2001)** located at the Cerro Paranal Observatory (Chile) is one of the most advanced optical telescopes worldwide (see Figure 2.3). It currently consists in four 8-m reflecting Unit Telescopes (UTs) and four 1.8-m Auxiliary Telescopes (ATs). The UTs are set on fixed locations while the ATs can be relocated on 30 different stations, providing baselines ranging from 47 m to 130 m with the UTs and 8 m to 202 m with the movable ATs. The telescopes can be combined in groups of two or three. After the light beams have passed through a complex system of mirrors and the delay lines, the combination at near- and mid-infrared is performed by the instruments AMBER and MIDI, and a test instrument called VINCI, which obtained the first VLTI fringes in March 2001. A complex and high performance dual-feed system PRIMA that allows phase-referenced imaging and μm -astrometry is currently under commissioning. The VLTI infrastructure also comprises a number of subsystems improving the global performance of the facility. First, the four UTs are all equipped with an adaptive optics system called MACAO (Arsenault et al. 2004), providing typical Strehl ratios of 50% in the K-band, while tip-tilt correction is performed on the ATs with the STRAP system. FINITO, a three beam fringe tracker operating in the H band, provides beam co-phasing with a residual OPD as small as 150 nm rms (performance routinely achieved on the ATs but not yet on the UTs, Le Bouquin et al. 2008). Finally, an infrared tip-tilt tracker (IRIS) is available in the interferometric laboratory and corrects for tip-tilt perturbations in the delay line tunnel at the 10 mas level and a frequency of 10 Hz.

2.3.3 Upcoming facilities

- **Large Binocular Telescope (LBT)** is a ground-based interferometer currently under development by the University of Arizona and collaborators (Mount Graham, Arizona, Hinz et al. 2008a).



Figure 2.3: Panoramic view of the ESO/VLT on Cerro Paranal in Chile showing the four UTs (Unitary Telescopes) and three of the four ATs (Auxiliary Telescopes).

LBTI combines the infrared light from two 8.4-m telescopes placed side by side (14.4 m apart) on a single rigid alt-azimuth mount (see Figure 4.8, right). The resulting instrument will have a maximum baseline of 22.8 meters. In addition to its Fizeau mode, LBTI will also host a nulling beam combiner with 14.4 m baseline (further details on the nulling mode are given in Section 4.4.3). Both instruments will strongly benefit from the original design of the LBT, where delay lines are not needed and a small number of mirrors are required to propagate the light to the (cryogenic) interferometric beam combiner. The instrument was delivered and installed on the telescope in July 2008 and is presently undergoing initial testing. Plans call for the instrument to be re-installed in 2010 after the first adaptive secondary is commissioned. Scientific operations will likely start sometime in early 2011.

The main goal of LBTI will be the study of extrasolar planetary systems. LBTI will focus on the characterization of exozodiacal dust around nearby stars and the direct detection of thermal emission from giant extrasolar planets.

- **Magdalena Ridge Observatory Interferometer (MROI)** is nominally a 10-element 1.4-m aperture optical and near-infrared interferometer being built on Magdalena Ridge (New Mexico, Creech-Eakman et al. 2008). The interferometer layout is an equilateral Y-shaped configuration with baselines extending from 8 to 400 m. The main science goals are the study of the environments of nearby AGN, stellar formation and the earliest phases of planet formation. The first fringes are expected in late 2010.

In addition, new extensions of current facilities are foreseen within the next few years. For 2012–2015, VLTI will be equipped with second-generation instruments: GRAVITY (Eisenhauer et al. 2008), MATISSE (Lagarde et al. 2008) and VSI (Malbet et al. 2008) which will be capable of exploiting the imaging capability of the array by combining four beams for the first and second and six for the third.

2.3.4 Major scientific results

Optical interferometers have made substantial contributions in several areas, such as astrophysics of stars, circumstellar environments and Active Galactic Nuclei (AGN). This section is divided in two major areas, astrophysics of stars and general astrophysics, for which the major scientific results are presented. The main results for circumstellar environments have been previously discussed (see Section 1.2).

Astrophysics of stars

The most fruitful area of investigation of optical interferometers has been stellar astrophysics, in particular the study of nearby single stars. In the last decades, several parameters of stars have been investigated providing a new way to test the formation and evolutionary models of stars.

One of the earliest identified applications of optical interferometry was to directly measure the effective temperature and diameter of stars. The effective temperature scale for a wide variety of stars is now well-established, and hundreds of the diameter measurements have been obtained by many interferometers (e.g., Mozurkewich et al. 1991; Nordgren et al. 1999; Ségransan et al. 2003; Baines et al. 2008). Optical interferometry has been also widely used to study binary systems, and provided accurate measurements of their physical properties, such as component masses and luminosities or the possible presence of a third companion (e.g., Boden et al. 2000, 2005; Mutterspaugh et al. 2005, 2006; Tango et al. 2009). Oblateness measurements of Be stars have provided new insights on the Be star disc formation due to rapid rotation, opening new perspectives in basic problems in stellar physics such as rotationally enhanced mass loss of early-type stars (e.g., Domiciano de Souza et al. 2003). Coupling diameter measurements with asteroseismic observations has also proven very successful to test the evolutionary status of various stars (Kervella et al. 2003; Creevey et al. 2007). The study of Cepheids has also much benefited from interferometric measurements. Thanks to precise measurements of their angular diameters and pulsations, the distances to several of these “standard candles” have been precisely determined (e.g., Kervella et al. 2004b; Mérand 2008). These observations have enabled for the calibration of the period-radius and period-luminosity relations (Kervella et al. 2004a), which are at the basis of extragalactic distance measurements.

Other important results regarding the astrophysics of stars have been achieved by optical interferometry: direct measurements of stellar winds (van Boekel et al. 2003), the study of evolved stars which has provided more precise models for these stars and their environments (Perrin et al. 2004), first estimations of the gravity darkening coefficient (e.g., Domiciano de Souza et al. 2005; McAlister et al. 2005), the first image of a main sequence star (Monnier et al. 2007), the first image of an interacting binary (Zhao et al. 2008), and the spin-orbit alignment of the Fomalhaut planetary system (Le Bouquin et al. 2009).

General astrophysics

Another major breakthrough is related to the observations of extragalactic objects. In the near-infrared, the KI has revealed an unexpectedly compact source of ≤ 0.1 pc for NGC 4151 (Swain et al. 2003), suggesting that the emission mainly originates in the central accretion disc. Measurements with the VINCI instrument at VLTI resolved the complex structure of NGC 1068 consisting of a hot partially resolved component of approximately 0.7 pc and a warm resolved component of a few pc in size (Wittkowski et al. 2004). Additional observations of NGC 1068 obtained with MIDI at VLTI have revealed warm (320 K) dust in a structure 2.1 pc thick and 3.4 pc in diameter, surrounding a smaller hot structure (about 800K, 1.35 pc long, Jaffe et al. 2004; Raban et al. 2009). Such a configuration requires a continual input of kinetic energy to the cloud system from a source coexistent with the AGN.

3

Debris disc detection with IOTA/IONIC

Contents

3.1	Scientific context and goals of the study	47
3.2	The IOTA/IONIC instrument	48
3.3	Principle of interferometric observations	49
3.3.1	Extracting visibility measurements	49
3.3.2	Strategy for near-infrared debris disc detection	51
3.4	Observations of two A-type stars with IOTA/IONIC	53
3.4.1	The targets: Vega and β Leo	53
3.4.2	The observations	55
3.4.3	Data analysis	56
3.4.4	Data reduction	66
3.4.5	Interpretation of the data	69
3.5	Ongoing work and prospects	69
3.5.1	Debris disc programme at the CHARA array	69
3.5.2	Prospects with the Keck nullder	70
3.5.3	Further perspectives: Antarctica and space	71

*A*s explained in the previous chapter, ground-based infrared stellar interferometry is nowadays the best suited technique to probe the inner parts of extrasolar planetary systems. Investigating this region around nearby stars is not only relevant for our understanding of the planetary formation and evolution but also for preparing future exo-Earth characterization missions. In this chapter, we report observations of two A-type stars (namely Vega and β Leo) obtained with the Infrared-Optical Telescope Array (IOTA). Unlike previous studies of these two stars, the observations discussed here have been carried out in the H band. This will provide additional information to further constrain the models describing the circumstellar dust surrounding these stars and considerably improve our understanding of the nature of the detected resolved emission. This chapter ends by a short overview of the ongoing work and prospects for exozodiacal dust detection.

3.1 Scientific context and goals of the study

Studying the inner parts of debris discs, the extrasolar counterparts of the zodiacal dust cloud, is of prime importance to characterize the global architecture of planetary systems. Furthermore, the presence of large quantities of warm dust around nearby main sequence stars represents a significant challenge for

future space missions dedicated to the direct detection and characterization of Earth-like planets. The occurrence of bright exozodiacal discs around solar-type stars is currently mostly unknown. So far, debris discs have mostly been observed on relatively large spatial scales, probing material located tens to hundreds of AU from their host star. These circumstellar regions are more analogous to our solar system's dusty "Kuiper belt", located beyond our planetary belt, than to the AU-scale zodiacal disc inside our solar system's asteroid belt. The main challenge with the study of inner debris discs comes from the high requested contrast, generally larger than 100 in the near-infrared, in addition to the small angular separation between the star and the disc. Over the last few years however, photometric surveys have revealed a few hot inner debris discs in the mid-infrared (e.g., Stapelfeldt et al. 2004; Beichman et al. 2005b) but they do not have the required accuracy to detect the signature of these discs in the near-infrared, even around stars known to be surrounded by large amounts of cold dust in Kuiper Belt-like structures. Owing to its high dynamic range and high angular resolution, stellar interferometry is currently the best way to peer into these faint circumstellar structures.

During the last few years, infrared interferometry has enabled the detection of hot (1000-1500 K) dust populations (bright exozodiacal discs) around several main sequence stars known to harbor cold (≤ 200 K) debris discs. These dust grains, located within the first AU from their parent stars, are thought to be produced by collisions between larger rocky bodies and/or by the evaporation of comets, as in the solar zodiacal disc. The detected discs are however much hotter and more massive than the zodiacal cloud. Their grain populations would be expected to be expelled from the inner planetary system by radiation pressure within only a few years, which indicates inordinate replenishment rates. In practice, the steady state collisional grinding of a massive asteroid belt cannot be at the origin of these hot populations, which are most likely produced by isolated catastrophic events (e.g., major asteroid collision, break-up of a massive comet), or by major dynamical perturbations such as the "falling evaporating bodies" phenomenon in the β Pictoris inner disc (Beust and Morbidelli 2000) or the Late Heavy Bombardment that happened early in the history of our own planetary system (Gomes et al. 2005).

These discoveries have been recently made possible thanks to high-accuracy K-band interferometric measurements with CHARA/FLUOR and VLTI/VINCI. The detection of hot dust populations, residing in the first AU around nearby main sequence stars, has now been reported for five main sequence stars: the A-type stars Vega (Absil et al. 2006b), ζ Aquilae (Absil et al. 2008b), β Leo (Akeson et al. 2009), Fomalhaut (Absil et al. 2009), and the G-type star τ Ceti (Di Folco et al. 2007). More detections of this kind are currently being investigated by an on-going survey at the CHARA array, with several more candidates identified to date (Absil in prep.).

Even though these observations are only providing an estimation of the integrated flux of the inner disc in the K band, radiative transfer modeling allows first predictions to be made on the grain properties. It suggests in particular that the grains are submicron-sized, and contain significant fractions of carbonaceous species. However, due to the absence of observations of these exozodiacal discs at other wavelengths, the conclusions are still very speculative. In that context, observations of debris disc stars have been performed in June 2006 with the IOTA/IONIC instrument. The main objective of these observations was to confirm the exozodiacal disc around Vega, and provide additional constraints on the dust properties with a multi-color analysis. We report in this chapter the results of these observations, starting with an introduction on IOTA/IONIC and a description of the method used to detect exozodiacal dust discs.

3.2 The IOTA/IONIC instrument

The IOTA interferometer (Infrared-Optical Telescope Array, see Fig. 3.1) is a three telescope interferometer located at the Fred Whipple Observatory atop Mount Hopkins (Arizona, USA). It was jointly constructed by the Smithsonian Astrophysical Observatory, Harvard University, the University of Mas-

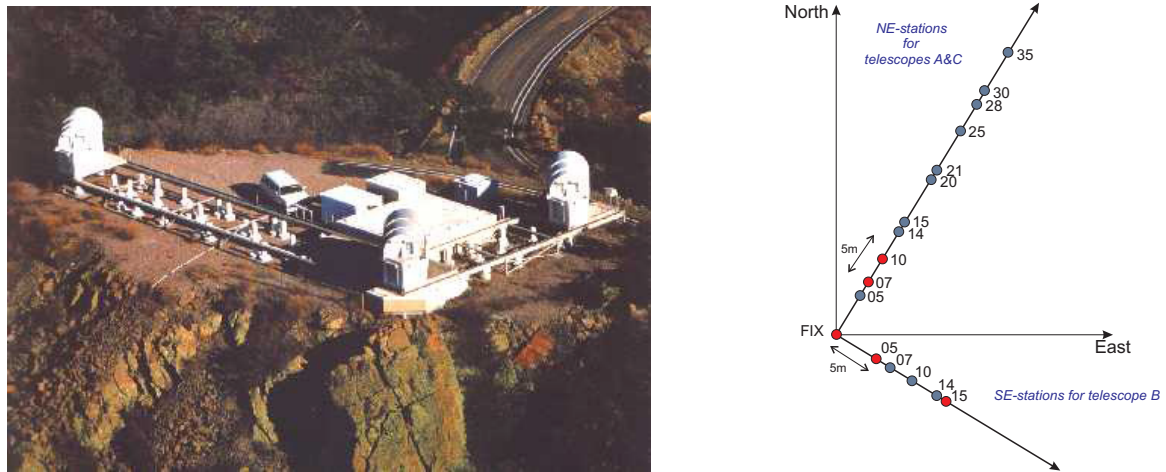


Figure 3.1: *Left:* The 3-telescope IOTA interferometer located atop Mount Hopkins (Arizona, USA). *Right:* Array geometry given with the available stations. Stations used during the observations presented in this chapter are in red. Telescopes A and C can move on stations located along the 35 m north-eastern arm, while telescope B can move along the 15 m south-eastern arm.

sachusetts, the University of Wyoming, and the MIT/Lincoln Laboratory (Traub et al. 2003). The telescopes of IOTA are movable among several stations along an L-shaped track (telescopes A and C can move along the 35 m north-eastern arm, while telescope B moves along the 15 m south-eastern arm, see Fig. 3.1), allowing an aperture of $35\text{ m} \times 15\text{ m}$ to be synthesized (corresponding to an angular resolution of about 5-12 mas at $1.65\text{ }\mu\text{m}$). The collecting optics consist of 0.45 m Cassegrain primary mirrors, which are fed by siderostats. Tip-tilt servo systems mounted behind the telescopes compensate for the atmospherically induced motion of the images while delay lines actively track the fringes by adjusting the optical path delay between the different baselines. All the beams are deflected by a series of mirrors into the laboratory, where they are coupled into single-mode fibers. The fibers then feed the spatially filtered signal into the IONIC3 integrated optics beam combiner (Berger et al. 2003), which combines the beams coaxially and pairwise with a ratio of 50:50. For each baseline, the beam combination produces two complementary outputs, which are shifted in phase by π with respect to each other, and which are recorded on a PICNIC camera (Pedretti et al. 2004). Although the information recorded by these two channels is in principle redundant, it is used to remove residual photometric fluctuations simply by subtracting the signals from the two channels (see section 3.3.1). The PICNIC detector array is a 256×256 pixel array, arranged in four quadrants of 128×128 pixels and sensitive to the $0.8\text{--}2.5\text{ }\mu\text{m}$ wavelength region. The pixel readouts are performed in a non-destructive way, so that the value of the accumulated charge does not change on the pixel.

3.3 Principle of interferometric observations

3.3.1 Extracting visibility measurements

The method to obtain visibility measurements from the raw interferograms in a single-mode interferometer follows the principles described by Coudé du Foresto et al. (1997). The first step consists in correcting the recorded interferograms (see Eq. 2.6) for photometric fluctuations. This requires to record the photometry simultaneously to the interferometric signal. Two-telescope beam combiners (like FLUOR, VINCI, or MIDI) or multiaxial beam combiners (like AMBER) obtain this photometric information by separating a certain fraction of the light before combining the beams and recording the photometry in separate channels. However, if three or more telescopes are combined pairwise, the photometric information can also be extracted from the interferometric signal without additional channels. Indeed, there

is a relation between the signal measured on a pixel (I_k , where k is the pixel number) and the input flux on each telescope (F_i , where i is the telescope number):

$$\begin{aligned} I_k &= \sum_{i=1}^N \kappa_{ki} F_i + \sum_{i < j}^N 2\gamma_{ij} \sqrt{\kappa_{ki} \kappa_{kj}} F_i F_j \\ &= I_k^{\text{incoh}} + I_k^{\text{coh}}, \end{aligned} \quad (3.1)$$

where the κ coefficients define the transfer matrix, which is proportional to the overall gain of the detector and the transmission of the coupler (Coudé du Foresto et al. 1997). For a three-telescope interferometer like IOTA, this corresponds to the following system of 6 equations (one for each output of the coupler):

$$I_1 = \kappa_{1A} F_A + \kappa_{1B} F_B + \kappa_{1C} F_C + 2\gamma_{AB}^+ \sqrt{\kappa_{1A} \kappa_{1B} F_A F_B} \quad (3.2)$$

$$I_2 = \kappa_{2A} F_A + \kappa_{2B} F_B + \kappa_{2C} F_C + 2\gamma_{AB}^- \sqrt{\kappa_{2A} \kappa_{2B} F_A F_B} \quad (3.3)$$

$$I_3 = \kappa_{3A} F_A + \kappa_{3B} F_B + \kappa_{3C} F_C + 2\gamma_{AC}^+ \sqrt{\kappa_{3A} \kappa_{3C} F_A F_C} \quad (3.4)$$

$$I_4 = \kappa_{4A} F_A + \kappa_{4B} F_B + \kappa_{4C} F_C + 2\gamma_{AC}^- \sqrt{\kappa_{4A} \kappa_{4C} F_A F_C} \quad (3.5)$$

$$I_5 = \kappa_{5A} F_A + \kappa_{5B} F_B + \kappa_{5C} F_C + 2\gamma_{BC}^+ \sqrt{\kappa_{5B} \kappa_{5C} F_B F_C} \quad (3.6)$$

$$I_6 = \kappa_{6A} F_A + \kappa_{6B} F_B + \kappa_{6C} F_C + 2\gamma_{BC}^- \sqrt{\kappa_{6B} \kappa_{6C} F_B F_C}, \quad (3.7)$$

where A , B and C denote the three telescopes. The coherence factors corresponding to the same baseline (γ_{ij}^+ and γ_{ij}^-) are complementary outputs of IONIC and are shifted in phase by π with respect to each other, so that $\gamma_{ij}^+ = -\gamma_{ij}^-$. For a perfect detector, the κ coefficient corresponding to the telescope which does not contribute to a certain output (e.g., κ_{1C} for I_1) is equal to zero. However, the PICNIC detector is known to exhibit detector biases due to the fact that some pixels on the detector are not completely independent (Pedretti et al. 2004). When focusing a bright star on a target pixel, the bias corresponds to a small constant signal on the adjacent pixel in the same row of the detector¹³. If we stay in the linear regime (no saturation), the bias on the adjacent pixel is assumed to be proportional to the incoming flux on the telescope which does not contribute to the considered output. This is taken into account by the κ coefficients which have the opposite sign than the κ for the contributing telescopes.

By adding the outputs from each beam-combiner pairwise, the coherence factors disappear and the input fluxes at each telescope can be easily computed by inversion of the following system:

$$\begin{pmatrix} I_1 / \sqrt{\kappa_{1A} \kappa_{1B}} + I_2 / \sqrt{\kappa_{2A} \kappa_{2B}} \\ I_3 / \sqrt{\kappa_{3A} \kappa_{3C}} + I_4 / \sqrt{\kappa_{4A} \kappa_{4C}} \\ I_5 / \sqrt{\kappa_{5B} \kappa_{5C}} + I_6 / \sqrt{\kappa_{6B} \kappa_{6C}} \end{pmatrix} = \mathbf{M} \times \begin{pmatrix} F_A \\ F_B \\ F_C \end{pmatrix}, \quad (3.8)$$

with

$$\mathbf{M} = \begin{pmatrix} \sqrt{\frac{\kappa_{1A}}{\kappa_{1B}}} + \sqrt{\frac{\kappa_{2A}}{\kappa_{2B}}} & \sqrt{\frac{\kappa_{1B}}{\kappa_{1A}}} + \sqrt{\frac{\kappa_{2B}}{\kappa_{2A}}} & \frac{\kappa_{1C}}{\sqrt{\kappa_{1A} \kappa_{1B}}} + \frac{\kappa_{2C}}{\sqrt{\kappa_{2A} \kappa_{2B}}} \\ \sqrt{\frac{\kappa_{3A}}{\kappa_{3C}}} + \sqrt{\frac{\kappa_{4A}}{\kappa_{4C}}} & \sqrt{\frac{\kappa_{3B}}{\kappa_{3C}}} + \sqrt{\frac{\kappa_{4B}}{\kappa_{4C}}} & \sqrt{\frac{\kappa_{3C}}{\kappa_{3A}}} + \sqrt{\frac{\kappa_{4C}}{\kappa_{4A}}} \\ \frac{\kappa_{5A}}{\sqrt{\kappa_{5B} \kappa_{5C}}} + \frac{\kappa_{6A}}{\sqrt{\kappa_{6B} \kappa_{6C}}} & \sqrt{\frac{\kappa_{5B}}{\kappa_{5C}}} + \sqrt{\frac{\kappa_{6B}}{\kappa_{6C}}} & \sqrt{\frac{\kappa_{5C}}{\kappa_{5B}}} + \sqrt{\frac{\kappa_{6C}}{\kappa_{6B}}} \end{pmatrix}, \quad (3.9)$$

in which the diagonal terms (upper right to lower left) correspond to the detector bias terms and are equal to 0 for a perfect detector. The inversion of this matrix gives access to the simultaneous photometry provided that the κ coefficients are known. These are generally obtained by using four calibration files which are acquired after each observation. One of these files measures the camera background signal with the light from all the telescopes blocked out (this is required for subtraction of the thermal background). For the other three files, the beams coming from two telescopes are blocked out alternately. Using the

¹³Note that when the pixel well is depleted, it is known that there is an increased constant signal on the adjacent pixel. The magnitude of the increase is roughly 15% of the target signal. The cause is currently not known.

obtained photometric information, the interferograms can be corrected for photometric fluctuations. For instance, the coherence factors of the two first pixels (γ_{AB}^+ and γ_{AB}^-) can be easily obtained from Eqs. 3.2 and 3.3:

$$\gamma_{AB}^+ = \frac{I_1 - \kappa_{1A}F_A - \kappa_{1B}F_B - \kappa_{1C}F_C}{2\sqrt{\kappa_{1A}\kappa_{1B}F_A F_B}}, \quad (3.10)$$

$$\gamma_{AB}^- = \frac{I_2 - \kappa_{2A}F_A - \kappa_{2B}F_B - \kappa_{2C}F_C}{2\sqrt{\kappa_{2A}\kappa_{2B}F_A F_B}}. \quad (3.11)$$

The remaining photometric fluctuations, due to errors in the estimation of the simultaneous photometry, can be removed by subtracting the two channels, yielding the final interferograms. For the AB baseline, the final interferogram is given by:

$$\gamma_{AB} = \frac{\gamma_{AB}^+ - \gamma_{AB}^-}{2}. \quad (3.12)$$

The coherence factors for the other baselines can be obtained similarly. An important advantage of obtaining the photometry from the interferometric measurements is the reduced complexity of the optical design and the increased flux in the interferometric channels.

After correcting for intensity fluctuations and subtracting out bias terms from read noise, residual intensity fluctuations, and photon noise, the computation of the visibilities from the OPD-modulated interferograms is performed in the frequency domain (i.e., by measuring the fringe power in the power spectrum of the coherence factors). The advantage of this frequency-domain approach is that the power spectra of an arbitrary number of interferograms can be averaged, even if the fringe packet moves due to the influence of atmospheric piston. In the averaged power spectrum, the fringe power can be easily obtained by integrating the power over the fringe peak to estimate the fringe amplitude (squared visibility, \mathcal{V}^2).

Note that other approaches have been proposed and used to extract the visibility from an interferogram. For instance, a technique widely used is the continuous wavelet transform which decomposes the signal into a localized mother wavelet function. This has the advantage that the information about the position of the fringe in the OPD is conserved, and can be used to effectively separate the fringe from underlying non-localized signals (Kervella et al. 2004c; Kraus 2007).

3.3.2 Strategy for near-infrared debris disc detection

The strategy for near-infrared debris disc detection has been extensively described elsewhere (Absil 2006) and we remind here the main principles, which are necessary for the understanding of this chapter. The idea is that an extended structure (a debris disc typically) and a compact source (such as the stellar photosphere) have very different signatures in the Fourier spatial frequency plane: a debris disc is resolved at much shorter baselines than its host star. For instance, the angular diameter of the photosphere of an A-type star located at 20 pc is typically around 1 mas, while the circumstellar disc extends beyond the sublimation radius of dust grains (at around 10 to 20 mas for black body grains sublimating at 1500 K). The debris disc is therefore generally fully resolved at short baselines (10 to 20 m) in the near-infrared, while the photosphere is only resolved at long baselines (a few hundreds meters). Using the visibility of a uniform disc given by Eq. 2.13, the squared visibility of a star-disc system is given by the weighed sum of the two components:

$$\mathcal{V}^2(b_\perp, \lambda) = \left[(1-f) \frac{2J_1(\pi\theta_{\text{UD}} b_\perp / \lambda)}{\pi\theta_{\text{UD}} b_\perp / \lambda} + f\mathcal{V}_{\text{disc}}(b_\perp, \lambda) \right]^2, \quad (3.13)$$

assuming that the disc contributes a fraction f of the total flux of the system and has a visibility $\mathcal{V}_{\text{disc}}(b_\perp, \lambda)$. Because it is resolved at shorter baselines, the disc has a lower visibility than the star, and thus reduces the visibility of the system compared to a single star. For the baselines at which the disc is

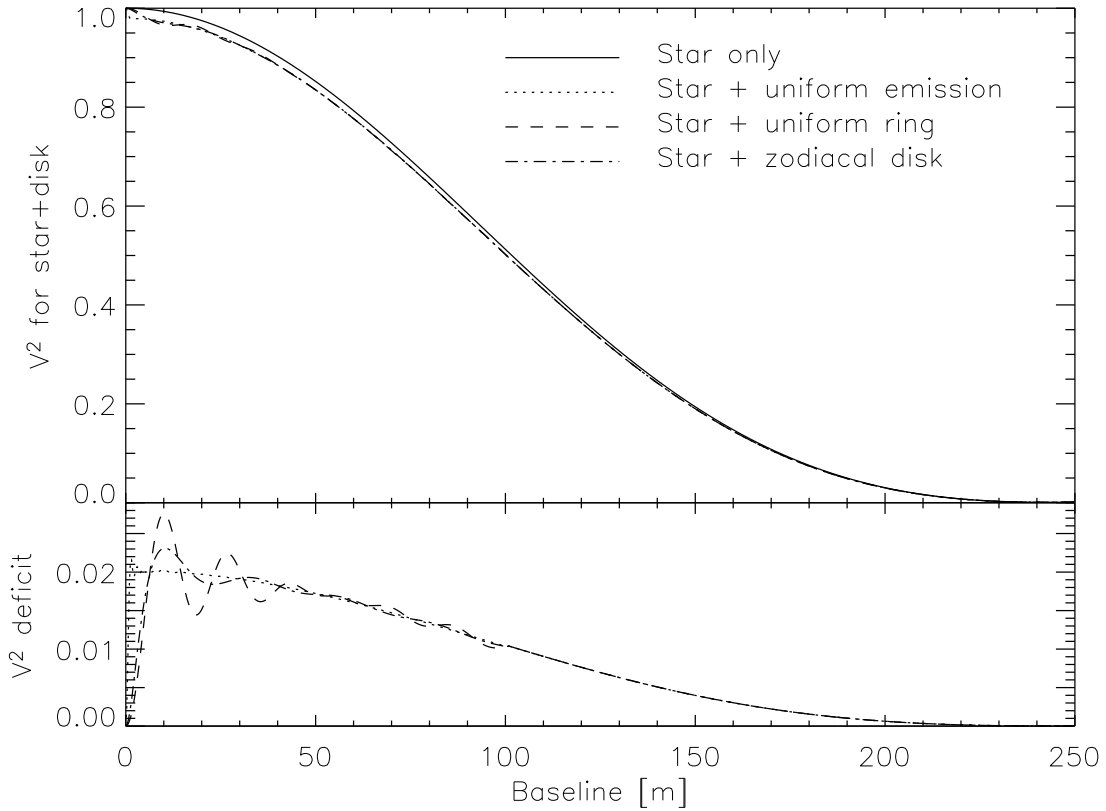


Figure 3.2: Squared visibility of a star surrounded by circumstellar emission compared to the visibility of the star only (an A0V star at 10 pc for this illustration), observed in the K-band. Three different morphologies have been assumed for the circumstellar emission: a uniform emission spread over the whole field-of-view, a ring-like structure located between 0.2 AU (sublimation radius) and 0.3 AU from the star, and a more realistic debris disk model similar to the solar zodiacal disk. All have been scaled so that their integrated brightness represents 1% of the photospheric emission (Figure from Absil 2006).

completely resolved, we have $\mathcal{V}_{\text{disc}} \approx 0$ (equivalent to a purely incoherent emission) and thus, assuming that the star is not resolved ($\theta_{\text{UD}} < \lambda/b_{\perp}$) and a small flux ratio ($f \ll 1$):

$$\mathcal{V}^2(b_{\perp}, \lambda) = (1 - 2f) \left[\frac{2J_1(\pi\theta_{\text{UD}}b_{\perp}/\lambda)}{\pi\theta_{\text{UD}}b_{\perp}/\lambda} \right]^2. \quad (3.14)$$

showing a visibility deficit of twice the flux ratio with respect to a single star. This is illustrated in Figure 3.2 for various morphologies of the debris disc, using a flux ratio $f = 1\%$ between the stellar photosphere and the integrated disc brightness in all cases. For instance, a uniform circumstellar emission, spread over the entire field-of-view, produces a smooth visibility deficit as it acts as a purely incoherent source and therefore produces a relative deficit of 2% at all baselines. On the other hand, a ring-like structure produces sinusoidal fluctuations of the visibility deficit around its mean, because it is more compact.

The strategy to detect the presence of a debris disc is then to compare short-baseline data with a simple stellar model to detect a potential deficit of squared visibility related to the resolved circumstellar disc (the deficit is then equal to twice the flux ratio between the star and the circumstellar disc). A simple uniform disk (UD) stellar model can be derived using visibilities obtained at long baselines (in the lower first lobe and/or second lobe), which provide a precise and almost unbiased estimation of the stellar angular radius. In fact, the contribution of the circumstellar emission at these spatial frequencies is generally negligible as compared to other effects appearing at high frequencies, such as limb-darkening, spots, or even bandwidth smearing. Moreover, it does not affect the position of the first null in the

Table 3.1: Fundamental parameters and estimated angular diameter for Vega and β Leo. These values are mainly taken from Absil et al. (2008b) and Akeson et al. (2009), respectively for Vega and β Leo. The H-band magnitude (m_H) is taken from (Cutri et al. 2003). The $1-\sigma$ errors are given in superscript.

Name	HD	Type	Dist. [pc]	Mass [M_\odot]	Age [Myr]	$v \sin i$ [km.s $^{-1}$]	m_V	m_H	Mean θ_{LD} [mas]
Vega	172167	A0V	7.8	2.30	350	22	0.03	-0.03	$3.312^{0.067}$
β Leo	102647	A3V	11.1	2.0	50-520	110	2.14	1.92	$1.341^{0.013}$

visibility curve.

Even at short baselines, detecting the signature of a debris disc requires a very good precision on the measured visibilities (about 1% in the case illustrated here). Given the fact that IOTA has been dismantled, CHARA/FLUOR is today the only stellar interferometer worldwide able to achieve such a precision (see Table 2.2). With an even better precision (a few 0.1%), observations at various baselines would potentially be sufficient to study the morphology of the circumstellar emission. Even if such a precision is not achieved, one precise measurement of the flux ratio between the star and the disc at a given near-infrared wavelength is already sufficient to estimate some of the major parameters of the inner debris disc, such as its mass and fractional bolometric luminosity. In combination with upper limits on the disc brightness provided at other wavelengths by single-aperture photometry, some physical properties of the dust grains can also be inferred, but with rather large uncertainties due to the poor constraints provided by photometry. Of course, obtaining interferometric measurements at different wavelengths greatly helps to improve the modelling of the discs.

Note also that the possible inclination of the system can potentially be a problem as a debris disc does not have the same signature when it is inclined with respect to the line of sight (it will appear more compact along one direction). Baselines with different orientations will therefore measure different visibility deficits. Such a behaviour can be easily confused with the signature of an oblate stellar photosphere, which has different angular diameters along the equatorial and polar directions. In fact, a large fraction of Vega-type stars are expected to be elongated as they are usually of rather early spectral type (typically A type) and often show a significant rotational velocity.

3.4 Observations of two A-type stars with IOTA/IONIC

3.4.1 The targets: Vega and β Leo

Debris discs are the most visible signposts of extrasolar planetary systems, representing direct evidence for the presence of larger bodies. They are generally detected by their infrared or submillimeter flux, which can be detected photometrically if it represents a large enough fraction (typically at least 5-10%) of the photospheric flux of their host star. In that context, the two A-type target stars considered in this study (namely Vega and β Leo) have been extensively observed during the past decades by a successive generation of instruments (IRAS, ISO, Spitzer and ground-based stellar interferometers), which have detected significant excesses at various wavelengths in the infrared regime. The dust found around these main sequence stars cannot be primordial material left over from the star-forming stage, because the timescale to remove primordial material (about 10 Myr) is too short compared to the age of these stars (Vega and β Leo are estimated as 350 and 50-520 Myr old). Hence, the dust must be resupplied and second generation dust in such systems is thought to arise primarily from collisions between planetesimals and from cometary activity. In order to further constrain the properties of the inner debris disc surrounding these stars, data in the H band have been obtained with IOTA/IONIC. The results are described in section 3.4.4 and a brief overview of the targets is given hereafter.

Table 3.2: Summary of the data obtained with IOTA/IONIC in June 2006. The columns 1 and 2 give the date and UT timespan of the observations of the target star given in column 3. Column 4 gives the stations used in accordance to Fig. 3.1. The calibrators are given in the last column.

Date	UT timespan	Target	Array	PICNIC	
			config. [A,B,C]	mode	Calibrators
2006/06/09	4h-5h	β Leo	NE07-SE05-FIX	1L4R	δ Leo, 27 Com
	5h-12h	Vega	NE07-SE05-FIX	1L1R	κ Lyr, λ Lyr, π Her, θ Her
2006/06/10	3h30-5h	β Leo	NE07-SE05-FIX	1L4R	δ Leo, 24 Com
	5h-12h	Vega	NE07-SE05-FIX	1L1R	κ Lyr, λ Lyr, π Her, θ Her
2006/06/13	8h-12h	Vega	NE10-SE15-FIX	1L1R	κ Lyr, λ Lyr, π Her, θ Her
2006/06/14	7h-12h	Vega	NE10-SE15-FIX	1L1R	κ Lyr, λ Lyr, π Her, θ Her

- **Vega (HD 172167, A0V, 7.76 pc)** is one of the most studied stars in astrophysics, and has been used as a photometric standard for more than a century (Hearnshaw 1996). It was first identified to have an infrared excess (beyond $12\ \mu\text{m}$) with respect to its expected photospheric flux in the eighties (Aumann et al. 1984). This was initially interpreted as the thermal emission from a circumstellar disc of cool dust located at about 85 AU from Vega, and then re-interpreted as a dust envelope with a radius of 140 AU (van der Blieck et al. 1994). The latter analysis concludes that a significant fraction of the dust grains is larger than $0.1\ \mu\text{m}$, but smaller than $10\ \mu\text{m}$. ISO observations show a smooth, resolved, face-on disc with a radius of about 80 AU at $60\ \mu\text{m}$ and about 145 AU at $90\ \mu\text{m}$ (Heinrichsen et al. 1998). Mauron and Dole (1998) attempted to detect Vega’s disc through optical scattered light by using linear photopolarimetry. Their upper limit implies that the debris around Vega contains a very small number of $0.01\text{--}0.3\ \mu\text{m}$ grains. Sub-millimeter observations ($850\ \mu\text{m}$, see Figure 3.3) with the Submillimeter Common-User Bolometer Array (SCUBA) have shown an elongated bright central region oriented north-east south-west with a bright peak offset by about 70 AU at the north-east of Vega’s position (Holland et al. 1998). Observations at 1.3 mm resolved dust emission peaks offset from the star, appearing to be associated with a ring of emission at a radius of 60-95 AU (Koerner et al. 2001; Wilner et al. 2002). Observations with the Spitzer space telescope revealed an angular size much larger than previously found with a radius of the disc of at least of 330 AU, 543 AU, and 815 AU in extent at 24, 70, and $160\ \mu\text{m}$, respectively (Su et al. 2005; Rieke et al. 2005). This study also suggests a circular and smooth disc at all three wavelengths, with an inner boundary at a radius of 86 AU and containing about $3 \times 10^{-3} M_{\oplus}$ of dust grains.

Photometric observations of the outer parts of Vega’s disc have been recently complemented by infrared interferometric observations of the warm inner parts. The first attempt was made by Ciardi et al. (2001), who observed Vega with the PTI interferometer on a 110-m long baseline in dispersed mode. The poor spatial frequency coverage of their observations did not allow clear conclusions, although a simple model of a star and a uniform dust disk with a 3-6% flux ratio was proposed to explain the observations. A more thorough study of Vega with the CHARA array has evidenced a K-band flux ratio between the stellar photosphere and the debris disc of $1.29 \pm 0.19\%$ within the FLUOR field-of-view (about 7.8 AU, Absil et al. 2006b). Using a more realistic model for the stellar photosphere (Aufdenberg et al. 2006), this flux ratio has been revisited and amounts now to $1.26 \pm 0.27 \pm 0.06\%$ (Absil et al. 2008b). In the N band, the best constraint on the thermal emission from warm dust has been obtained by nulling interferometry, with no resolved emission above 2.1% of the level of stellar photospheric emission at separations larger than 0.8 AU (Liu et al. 2009).

- **β Leo (HD 102647, A3V, 11.1 pc)** was identified as having an infrared excess from IRAS observations (Aumann and Probst 1991). Mid-infrared imaging has not resolved the disk (Jayawardhana et al. 2001), although differences between the IRAS and ISO fluxes have suggested that the disc emission may be somewhat extended in the ISO beam (Laureijs et al. 2002). The Spitzer space

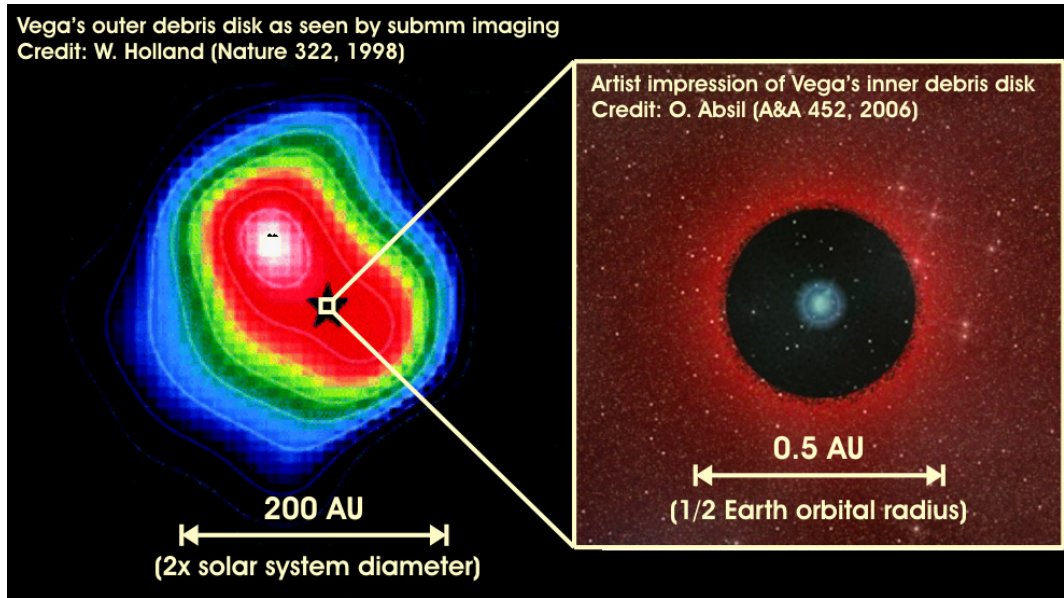


Figure 3.3: The Vega system as viewed in the sub-millimeter (left, Holland et al. 1998) and the near-infrared (right, Absil et al. 2006b).

telescope using the Infrared Spectrograph (IRS) observed β Leo and found a featureless continuum spectrum consistent with dust at about 120 K and located at 19 AU from the central star (Chen et al. 2006). Recently, a near-infrared excess of 1%-2% has been detected by interferometric observations at the CHARA array using the FLUOR beam combiner (Akeson et al. 2009). The data are interpreted as due to the presence of a thin ring of dust grains at (or near) the sublimation radius in addition to the previously known mid-infrared emitting belt. These observations allow some constraints to be put on the dust composition and morphology. Small non-silicate grains are required to be consistent with the near- and mid-infrared excesses. The minimum grain size required (about $0.1 \mu\text{m}$) is an order of magnitude smaller than the nominal radiation pressure blowout radius for spherical grains, and therefore requires a high production rate of small grains. This near-infrared excess cannot arise from dust generated by the planetesimal belt which produces the mid-infrared excess. β Leo has also been observed in the N band but no significant constraint on the thermal emission was derived (Liu et al. 2009).

3.4.2 The observations

Interferometric observations of Vega and β Leo were obtained with IOTA/IONIC in June 2006. The particularity of the IOTA/IONIC data with respect to CHARA/FLUOR is twofold. First, the data have been obtained in the H band whereas the CHARA/FLUOR ones have been obtained in the K band. Secondly, light was split in two orthogonal polarization axes with a Wollaston prism after beam combination and have been recorded simultaneously. This choice was initially made to improve the stability of the data and thus, their quality since the change in visibility is expected to be very small (of the order of 1%). An overview of the observations is shown in Table 3.2. It gives the date of the observations (first column), the target star (second column), the array configuration (third column), the UT timespan (fourth column), the PICNIC detector read-out mode (fifth column) and the calibrators used (last column). The characteristics of the calibrator stars are given in Table 3.3.

Table 3.3: Calibrator stars used for this programme given with their HD number, spectral type, H magnitude, limb-darkened disc (LD) angular diameter (in milliarcsec) and limb-darkening H-band coefficient (Cohen et al. 1999; Bordé et al. 2002; Cutri et al. 2003; Mérand et al. 2005). The $1-\sigma$ errors are given in superscript.

Identifier	HD number	Sp. type	m_H	$\theta_{LD} \pm 1\sigma$	μ_λ	Target
π Her	156283	K3I	-0.112	$5.29^{0.055}$	0.420	Vega
θ Her	163770	K1II	1.056	$3.15^{0.034}$	0.403	Vega
λ Lyr	176670	K2.5III	1.743	$2.41^{0.026}$	0.415	Vega
κ Lyr	168775	K2III	1.989	$2.28^{0.025}$	0.410	Vega
δ Leo	97603	A3V	2.191	$1.165^{0.022}$	0.192	β Leo
27 Com	111067	K3III	2.051	$2.05^{0.022}$	0.420	β Leo
24 Com	109511	K2III	2.538	$1.62^{0.03}$	0.410	β Leo

3.4.3 Data analysis

In this section, we perform several tests on the data described in the previous section in order to check their sanity and select the best sample for the data reduction. These tests include checking the photometry consistency between the interferometric and matrix files, the photometric stability during the scans and the κ matrix. Tests on the impact of saturation on the measured squared visibilities are also reported. Reduction of the data was carried out using established IDL routines described by Monnier et al. (2004, 2006), and following the method outlined in section 3.3.1. The statistical error on the estimation of the final visibility, related to the detection process, is expected to be of the order of 1%. The instrumental transfer function is estimated by observing calibrators before and after each target data point. The calibrator stars used during these observation are given in Table 3.3, and were mainly chosen from two catalogues developed for this specific purpose (Bordé et al. 2002; Mérand et al. 2005).

Photometry consistency

The first test consists in comparing the photometry of the interferometric measurements (all shutters open) with the cumulated photometry of the 3 matrix files (one shutter opened for each). Since the matrix files are saved just after the interferometric files, it is expected that their sum is not significantly different from the flux in the interferometric files. The photometry is averaged over the whole scan and for the 200 scans of the interferometric files (resp. 50 scans for the matrix), so that the fringe pattern is smeared in the case of the interferometric measurements. The total flux is therefore equal to the sum of the three telescopes in both cases, except that the three telescopes are recorded simultaneously for the interferometric files and sequentially for the matrix files. The results are presented in Figure 3.4 for the 2006/06/10 data.

Each of the twelve boxes in Figure 3.4 represents a different pixel on the camera. The first column is associated to the first polarization and the second column to the second polarization. The 6 pixels per column correspond by pairs to the 3 baselines of IOTA: the first two pixels to the A-B baseline, the third and fourth pixels to the A-C baseline and the last two pixels to the B-C baseline (see the baselines of IOTA in Figure 3.1 and the configuration used in Table 3.2). Looking at the Vega data (in green), there is a large difference between the photometry of the interferometric (circles) and the matrix files (stars). This discrepancy might be due to saturation of the illuminated pixels, which then present a nonlinear regime in which the amount of detected photo-electrons is not proportional to the incoming flux. Whereas each individual telescope does not give enough flux to saturate the detector, the sum of the three may produce a significant saturation, and therefore produce a smaller total flux than the sum of the three individual photometries. This phenomenon is particularly pronounced for the first polarization

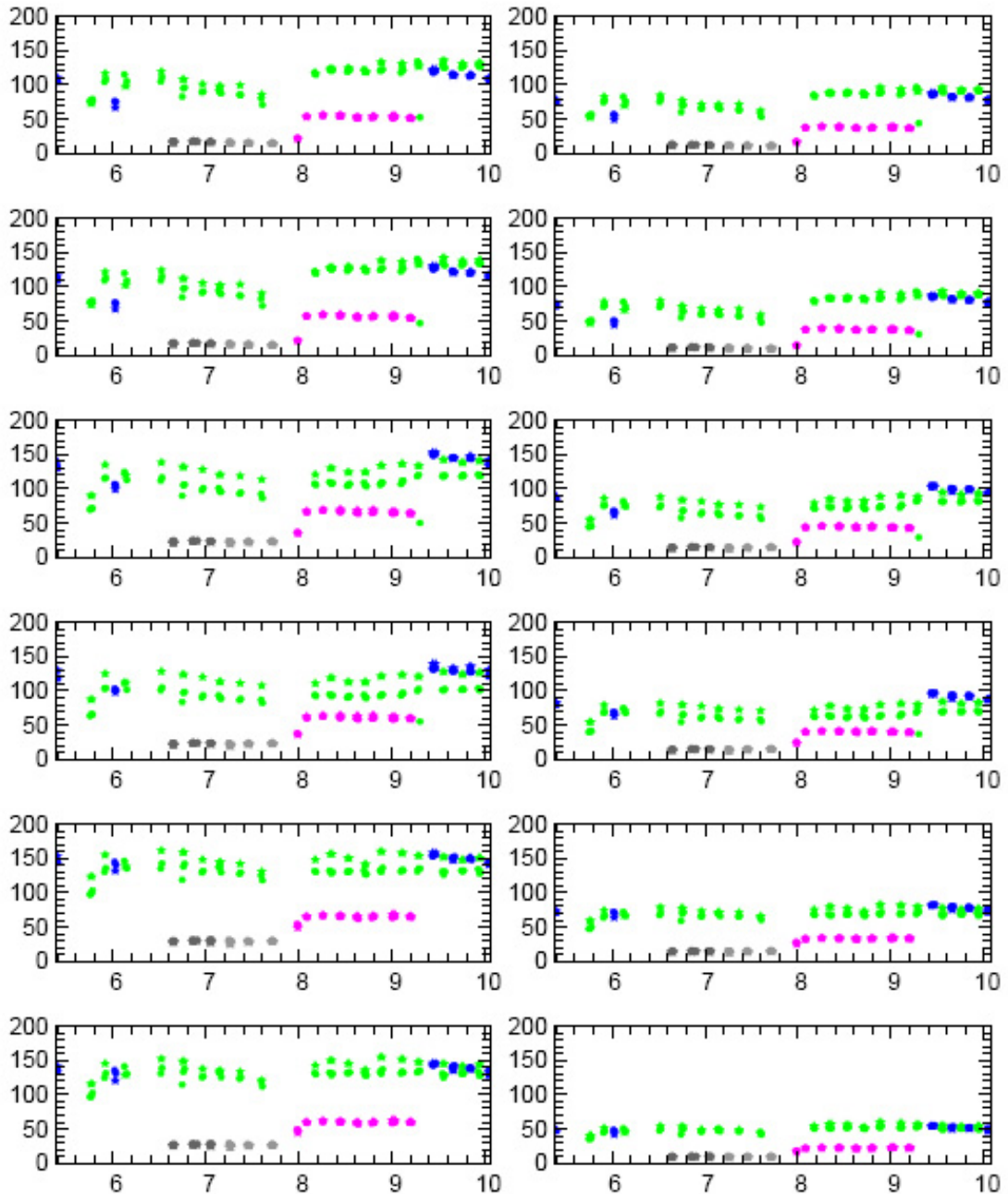


Figure 3.4: Flux in ADU in the twelve illuminated pixels as a function of UT time (2006/06/10 data). The circles and stars represent the photometry of the interferometry and matrix files, respectively. Vega is in green, π Her ($H = 0.1$) in blue, θ Her ($H = 1.2$) in magenta, λ Lyr ($H = 1.8$) in grey and κ Lyr ($H = 1.9$) in black.

in the case of the A-C and B-C baselines. However, the behaviour of Vega and its calibrators is quite different regarding this criterion: the two photometries are generally in agreement for the calibrators. This could be due to the fact that saturation is reached only in the Vega ($H = 0.0$) data. However, the photometric level (roughly 100-150 ADU) and magnitude of π Her ($H = 0.1$, in blue) are similar to those of Vega, while the behaviour of these data points are not pathologic. This strange behaviour of the photometry is therefore not completely accounted for by the possible presence of saturation. The behaviour of the photometry seems to be better explained by a colour-dependent effect, as Vega is an A0V star while the calibrators are all K giants. Further tests are performed in the following to address this issue.

Photometric agreement

The photometric agreement provides another way to check the validity of the photometry. Instead of comparing the photometry in the interferometric files and the matrix files, the photometric agreement consists in comparing the flux in the interferometric files with the simultaneous photometry. For the pixel k , the photometric agreement P_k^{ag} is given by:

$$P_k^{\text{ag}} = \frac{\text{mean}[I_k(x)]}{\text{mean}[I_k^{\text{incoh}}(x)]} - 1, \quad (3.15)$$

where $I_k(x)$ and $I_k^{\text{incoh}}(x)$ are respectively the flux and the incoherent flux measured on the pixel k (given by Eq. 3.1). The incoherent flux is computed using the simultaneous photometry, so that the photometric agreement writes:

$$\begin{aligned} P_k^{\text{ag}} &= \frac{\text{mean}\left[I_k(x) - \sum_{i=1}^N \kappa_{ki} P_i(x)\right]}{\text{mean}\left[\sum_{i=1}^N \kappa_{ki} P_i(x)\right]} \\ &= \frac{\text{mean}\left[\sum_{i < j}^N 2\gamma_{ij} \sqrt{\kappa_{ki} \kappa_{kj} F_i(x) F_j(x)}\right]}{\text{mean}\left[\sum_{i=1}^N \kappa_{ki} P_i(x)\right]}, \end{aligned} \quad (3.16)$$

where κ_{ij} is the transfer coefficient from telescope i to pixel j and $P_i(x)$ the simultaneous photometry from telescope i computed by matrix inversion. As explained in section 3.3.1, the transfer matrix (κ_{ij}) is determined at each change of target by blocking all beams but from one telescope and measuring the intensity on each pixel (using then $\kappa_{ij} = I_j / \sum_j I_j$). We will assume here that the detector stays in the linear regime during the measurements of the κ_{ij} coefficients (each pixel collects twice less photons than in the coherent mode). If all the illuminated pixels stay in the linear regime, the simultaneous photometry (P_i) and the actual photometry (F_i in Eq. 3.1) are equivalent so that the photometric agreement becomes:

$$P_k^{\text{ag}} = \frac{\text{mean}[I_k^{\text{coh}}(x)]}{\text{mean}[I_k^{\text{incoh}}(x)]}, \quad (3.17)$$

so that the photometric agreement is expected to be close to 0 (see Eq. 3.1). However, if some pixels enter in a nonlinear regime, the flux measured on pixel k takes the following form:

$$\begin{aligned} I_k(x) &= \sum_{i=1}^N \kappa_{ki} s_k(x) F_i(x) + \sum_{i < j}^N 2\gamma_{ij} \sqrt{\kappa_{ki} s_k(x) \kappa_{kj} s_k(x) F_i(x) F_j(x)} \\ &= \sum_{i=1}^N \kappa_{ki}^s F_i(x) + \sum_{i < j}^N 2\gamma_{ij} \sqrt{\kappa_{ki}^s(x) \kappa_{kj}^s(x) F_i(x) F_j(x)}, \end{aligned} \quad (3.18)$$

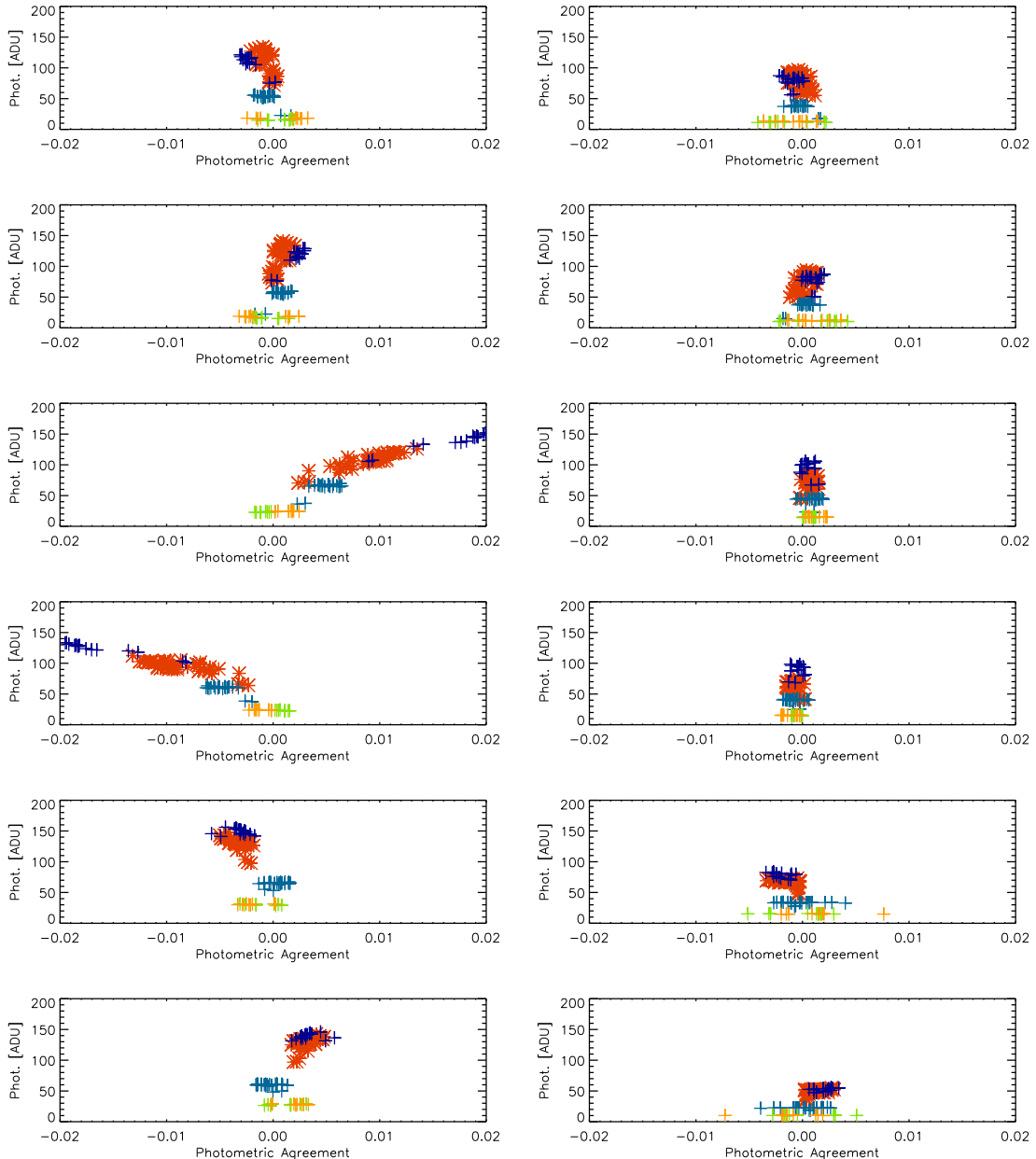


Figure 3.5: Photometric agreement as a function of flux for June 10. Data from June 9 present a similar behaviour. Vega is represented by red asterisks, and the calibrators by cross signs (π Her in blue, θ Her in light blue, λ Lyr in green, and κ Lyr in orange).

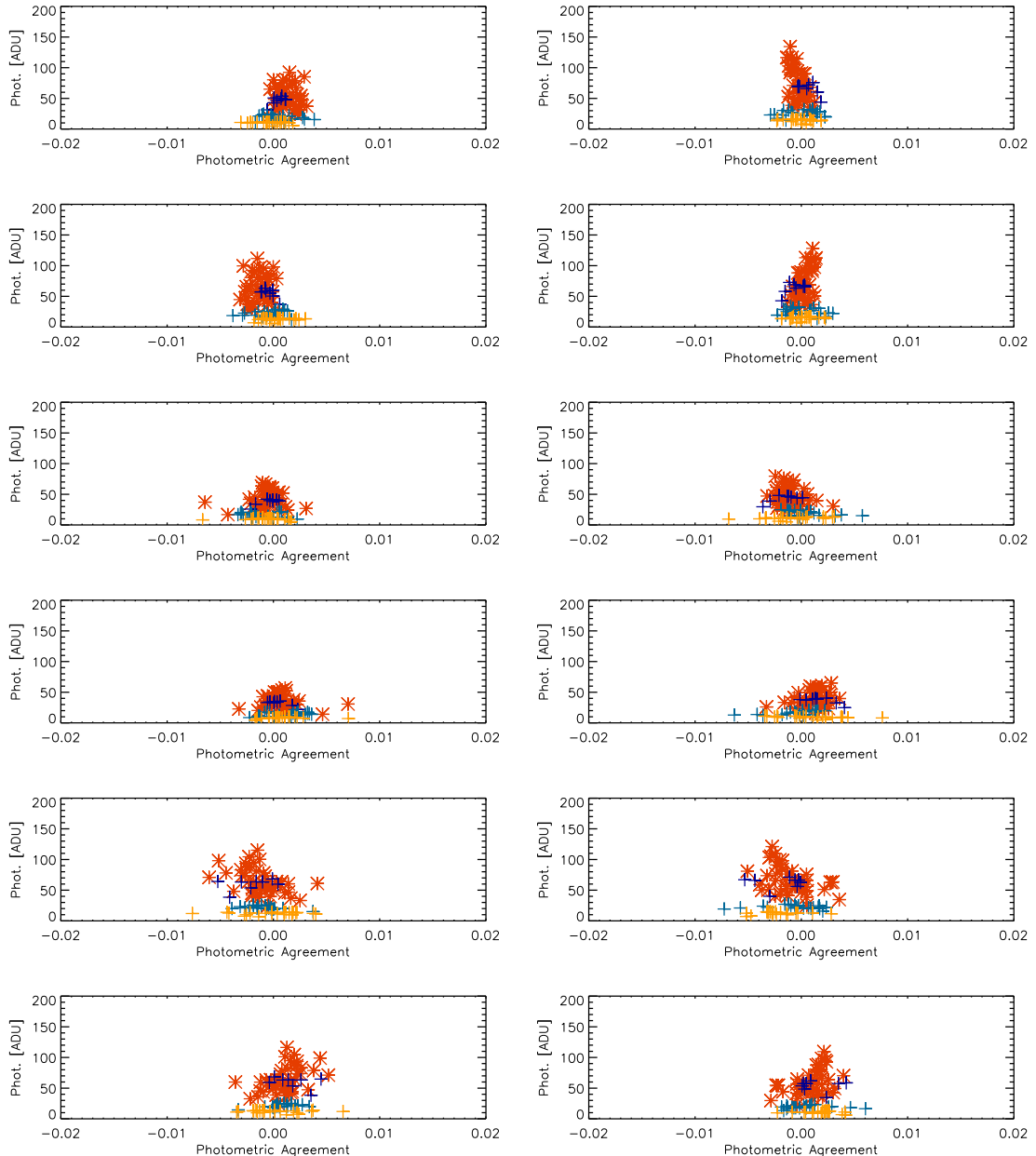


Figure 3.6: Photometric agreement as a function of flux for June 14. Data from June 13 present a similar behaviour. Vega is represented by red asterisks, and the calibrators by cross signs (π Her in blue, θ Her in light blue, λ Lyr in green, and κ Lyr in orange).

where $s_k(x)$ is the saturation law of pixel k and $\kappa_{kj}^s(x) = \kappa_{kj}s_k(x)$. Consequently, the simultaneous photometry computed by inversion of the matrix (using the κ_{ij} and not the κ_{ij}^s) is wrong and affected by the saturation law of each pixel. Using the expressions 3.17 and 3.18, the photometric agreement becomes:

$$P_k^{\text{ag}} = \frac{\text{mean} \left[\sum_{i=1}^N \kappa_{ki} [s_k(x)F_i(x) - P_i(x)] + \sum_{i < j}^N 2\gamma_{ij} \sqrt{\kappa_{ki}^s(x)\kappa_{kj}^s(x)F_i(x)F_j(x)} \right]}{\text{mean} \left[\sum_{i=1}^N \kappa_{ki}s_k P_i(x) \right]}, \quad (3.19)$$

where P_i is now the wrong simultaneous photometry. Because some pixels have entered in a nonlinear regime, the first term in Eq. 3.19 is not null anymore and the photometric agreement is different from 0. By systematically computing the photometric agreement, it is then possible to reveal that some pixels are in a nonlinear regime.

The photometric agreement of our Vega observations is represented in Figure 3.5 (June 10 data) and Figure 3.6 (June 14 data), as a function of the flux, for the two different polarizations. Data from June 9 (resp. June 13) present a similar behaviour as data from June 10 (resp. June 14). On the pixels corresponding to the A-C baseline and the first polarization, there is a high correlation between the photometric agreement and the stellar flux for the data of June 10, confirming that these data are affected by saturation problems. Data from June 14 seem healthy, which is not completely surprising since the instrumental setup has been changed between June 10 and June 13 nights. The data obtained on β Leo, which present significant lower fluxes, seem healthy as well. We will show in the following that saturation can introduce biases in the computed squared visibilities, which is very problematic for our high-accuracy application.

Photometric stability

The presence of saturation revealed in the previous analysis does not explain alone the behaviour in Figure 3.4. The flux difference between the matrix and interferometry files seen in the Vega data and not in the π Her data cannot be correlated (or at least not entirely) to the presence of saturation, because these two stars have the same H-band magnitude. To better isolate this lack of correlation, we have directly looked at the flux measured during the fringe scan. This is illustrated by the solid curves in Figure 3.7 for Vega (left) and π Her (right), showing the evolution of the flux during the scans in the interferometric files (averaged over 200 scans, see the solid curves) compared to the flux in the matrix files (averaged over 50 scans, see the dotted curves). It must be noted that fringes can still be seen despite the average made over the 200 scans. This indicates the exceptional atmospheric stability during this night, as well as the good ability of coherencing of the IOTA fringe tracker. The plots clearly show a drop in the continuum for some of the pixels, particularly for the pixels corresponding to the A-C baseline in the first polarization. This drop comes from the non-destructive readout mode of the camera, for which the rate of accumulated charge decreases as pixels enter in an nonlinear regime (under a constant flux).

Plotting the mean flux with respect to the mean of the difference between two adjacent points (i.e. the slope), Figure 3.9 shows that the higher the flux, the steeper the slope for Vega and their respective calibrators. This is another proof that pixel response becomes more and more nonlinear as the input flux increase (i.e., a behaviour akin to saturation). It must also be noted that the nonlinear regime is also reached in some matrix files, especially for the two outputs of the A-C baseline and the first output of the B-C baseline in the first polarization, which seem to be recorded on pathologic pixels (with a low saturation level compared to the others). However, this loss of flux induced by such slopes during the scan is not significant enough to explain the flux discrepancy between the interferometric and matrix files in the Vega data (see Figure 3.4). Looking again at Figure 3.7, a significant discrepancy between the initial photometric levels in the matrix and interferometry files can be noted in the Vega data. This

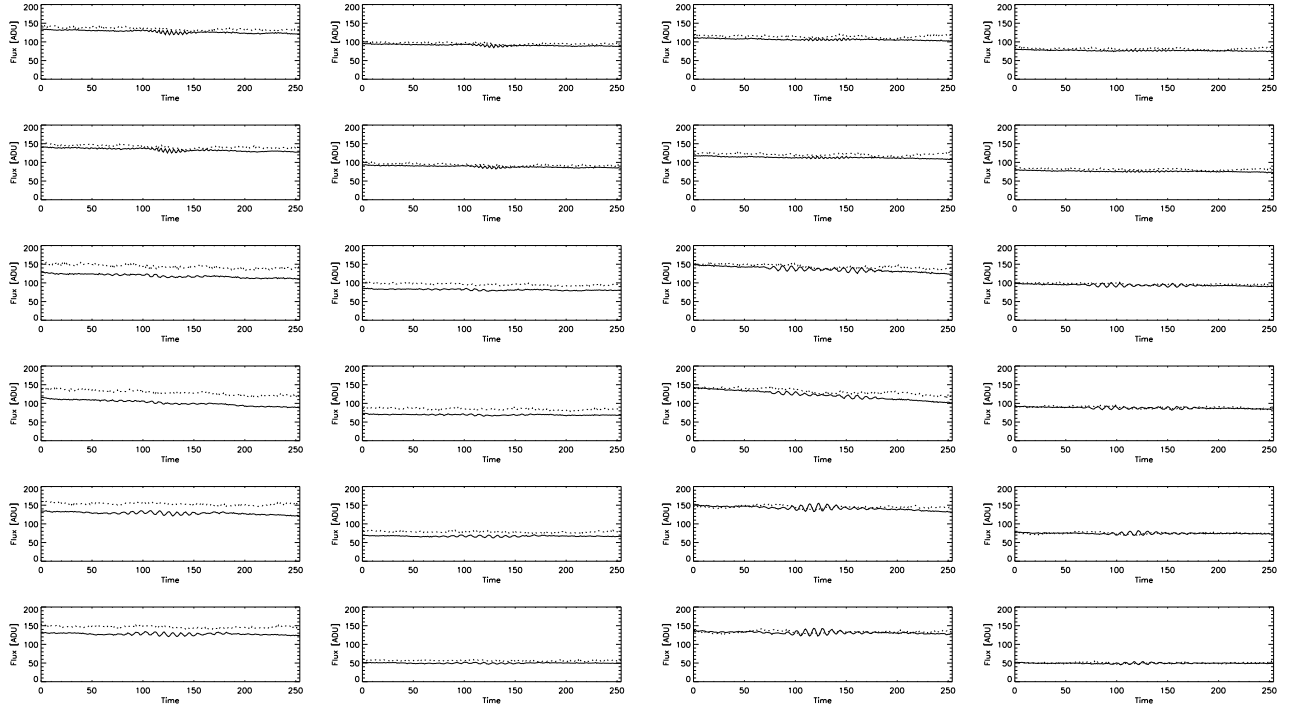


Figure 3.7: Typical flux in ADU in the twelve illuminated pixels as a function of time during the scan for Vega (left) and π Her (right). The solid lines indicate the flux measured in the interferometric files (averaged over the 200 scans) while the dotted lines indicate the sum of the fluxes in the matrix files (averaged over the 50 scans).

behaviour is predominantly affecting the saturated pixels but is not present in the case of π Her data (and the other calibrator stars). This suggests that the discrepancy between the initial photometric levels in the matrix and interferometry files is a color-dependent side-effect of saturation. The origin of this discrepancy is not well known but is clearly related to a colour-depend response of pathologic pixels (those corresponding to the A-C baseline and the first polarization in June 9 and June 10 data) on the PICNIC camera.

Finally, it is interesting to note that the second polarization has significantly lower fluxes compared to the first one, and that the saturation is almost absent according to this test. One can still see a trend in the slope-flux diagram (Figure 3.7), but the data mostly remain within 1σ , except for the A-C baseline which seems a bit more problematic (this is also the baseline with the highest flux, which partly explains the higher slope).

Analysis of the transfer matrix

The discrepancy between the photometry in the interferometry and matrix files could find its origin in the transfer matrix. As described in section 3.3.1, the transfer matrix indicates the part of the incoming flux from one telescope which makes it to a specific pixel. By checking the transfer matrix for the different stars, it is possible to identify a possible flux unbalance as a function of the target color and brightness. The transfer matrix for the night of June 10 is shown in Figure 3.8 (one of the three telescopes), with the same conventions as before. The κ coefficients of Vega and its calibrator are consistent so that the origin of the discrepancy has to be searched elsewhere. The transfer matrix from June 9 shows the same behaviour, whereas the transfer matrices from June 13 and 14 June are perfectly stable.

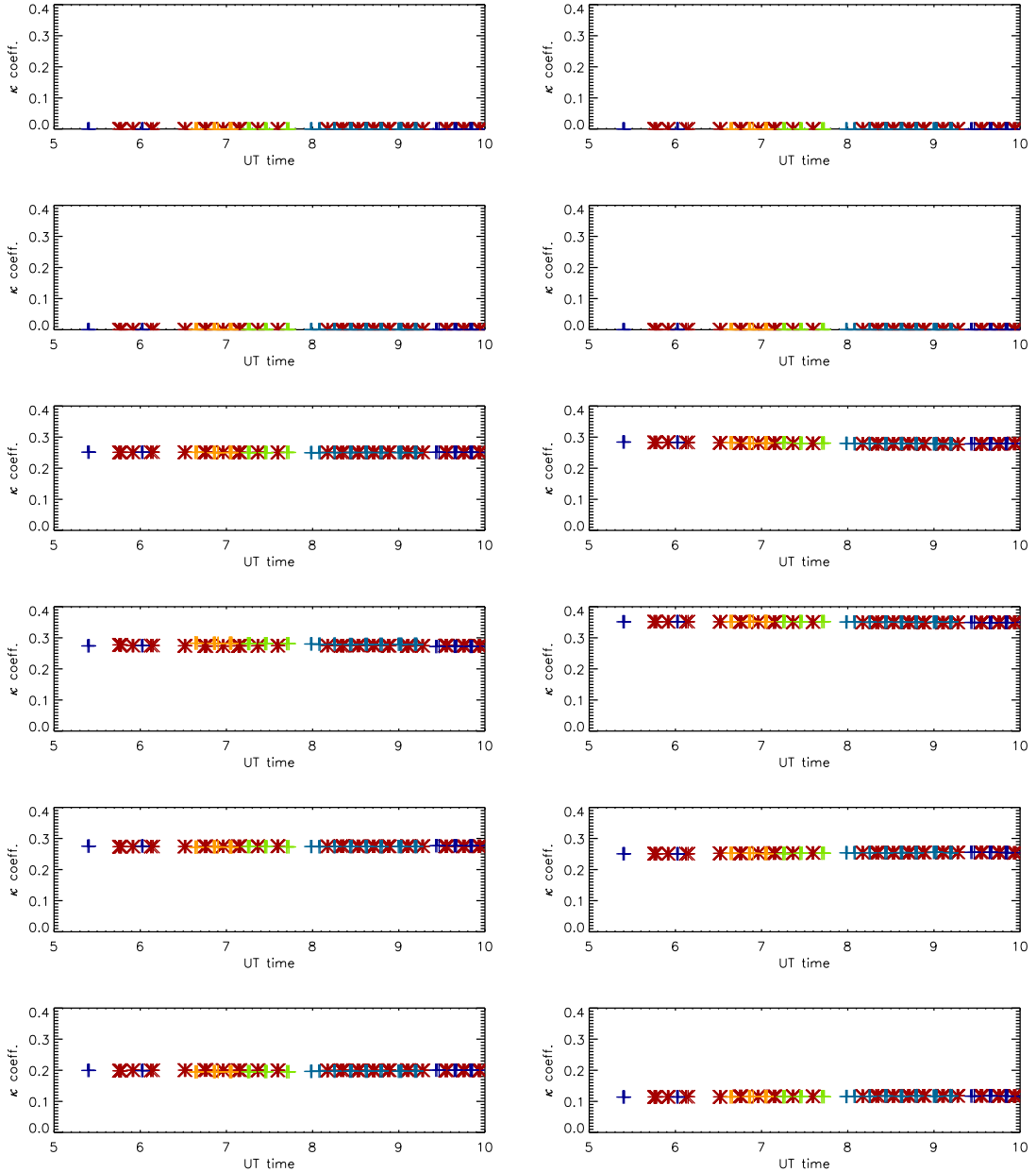


Figure 3.8: κ coefficients for telescope 1 (left) and telescope 2 (right). Vega is in green, π Her ($H=0.1$) in blue, θ Her ($H=1.2$) in magenta, λ Lyr ($H=1.8$) in grey and κ Lyr ($H=1.9$) in black. Vega is represented by red asterisks, and the calibrators by + signs (π Her in blue, θ Her in light blue, λ Lyr in green, and κ Lyr in orange).

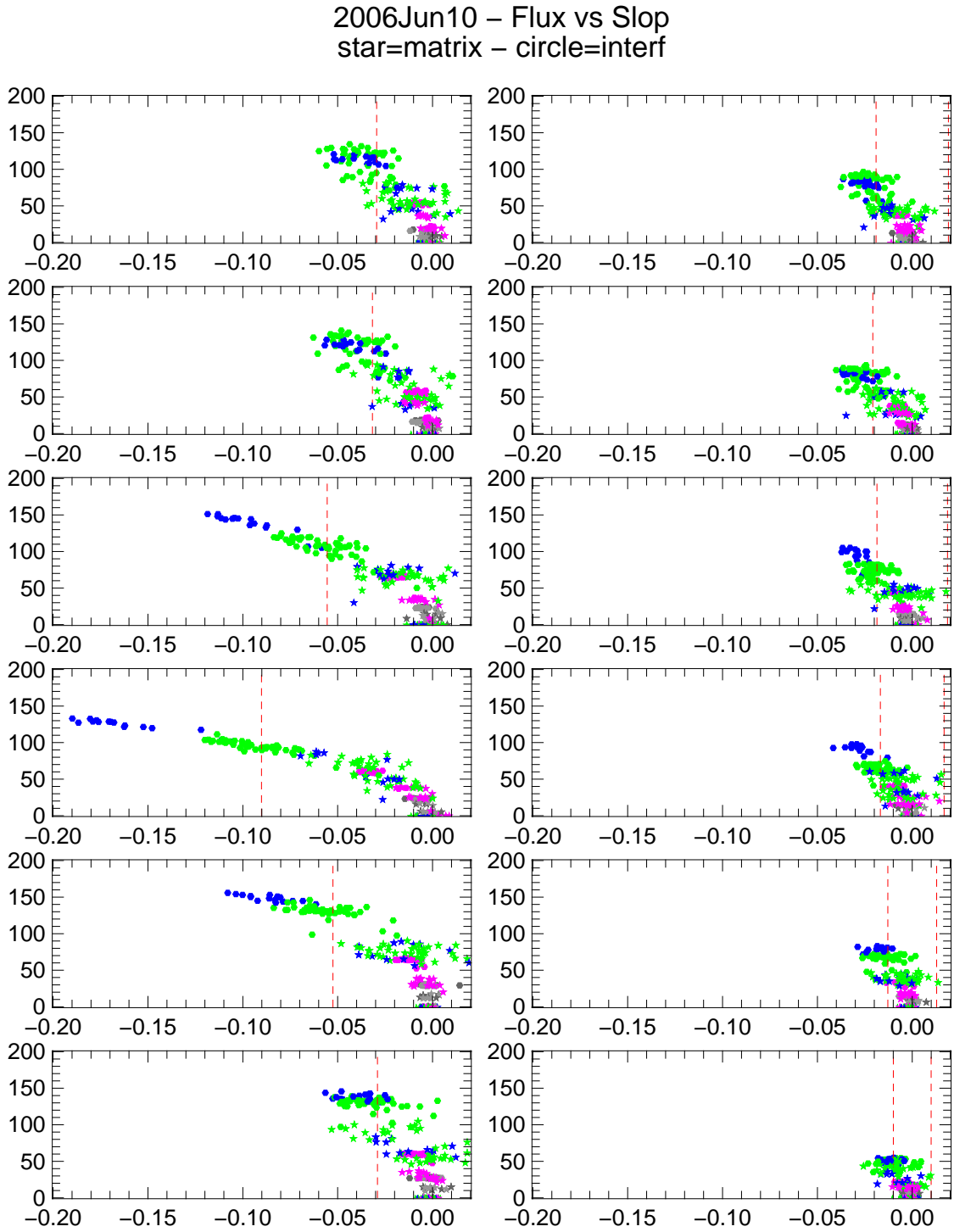


Figure 3.9: Flux as a function of the slope of the photometry during the scans (2006/06/10 data). Vega is in green, π Her ($H = 0.1$) in blue, θ Her ($H = 1.2$) in magenta, λ Lyr ($H = 1.8$) in grey and κ Lyr ($H = 1.9$) in black. The circles and stars represent the photometry of the interferometry and matrix files, respectively.

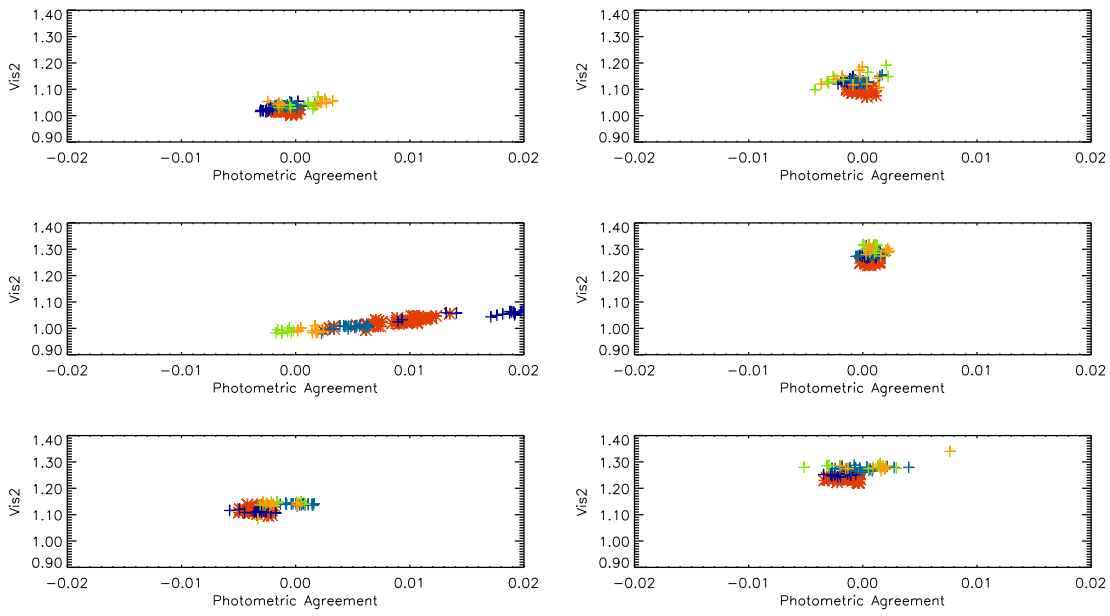


Figure 3.10: Raw squared visibilities with their error bars as a function of the photometric agreement for June 10. Each pixel is related to a specified baseline for a given polarization.

Impact of saturation on the squared visibility

After the various analyses on the photometry healthiness performed in the previous sections, we focus in this section on the main observable, i.e. the squared visibility, and we investigate the impact of saturation. As explained in section 3.3.1, the major step in order to compute the squared visibilities is to measure the fringe power in the power spectrum of the corrected interferogram (see Eq. 3.12). The situation is complicated if some pixels enter in a nonlinear regime, since the photometric variations are not fully corrected and some extra power might contribute to the fringe power.

To investigate this possible behaviour, Figure 3.10 and 3.11 show the raw squared visibilities with their error bars as a function of the photometric agreement for June 10 and June 14 respectively. The notations and layout for this figure are the same as before, except that the two pixels corresponding to the same baseline and the same polarization state have been merged (following Eq. 3.12). This figure shows that there is a correlation between the reduced squared visibilities and the photometric agreement. This indicates that the detector nonlinearities are affecting the squared visibilities, which is very problematic for our scientific programme. This behavior can be partly explained by the expression 3.19, which shows that the photometric agreement is proportional to the coherence factor (γ).

It is in principle possible to retrieve squared visibilities for the saturated data, by determining the saturation law $s_k(x)$ of each pixel, and then computing the simultaneous photometry with the corrected transfer matrix (κ_{ij}^s). The core of the problem is thus to determine these saturation laws, which are different for each pixel. The most straightforward solution would be to fit a polynomial function to the flux measured on each pixel. However, this approach could seriously jeopardize the data quality and we gave up it given the accuracy required for our scientific programme.

Conclusions

From the various tests and investigations presented in this section, several conclusions can be drawn about these data:

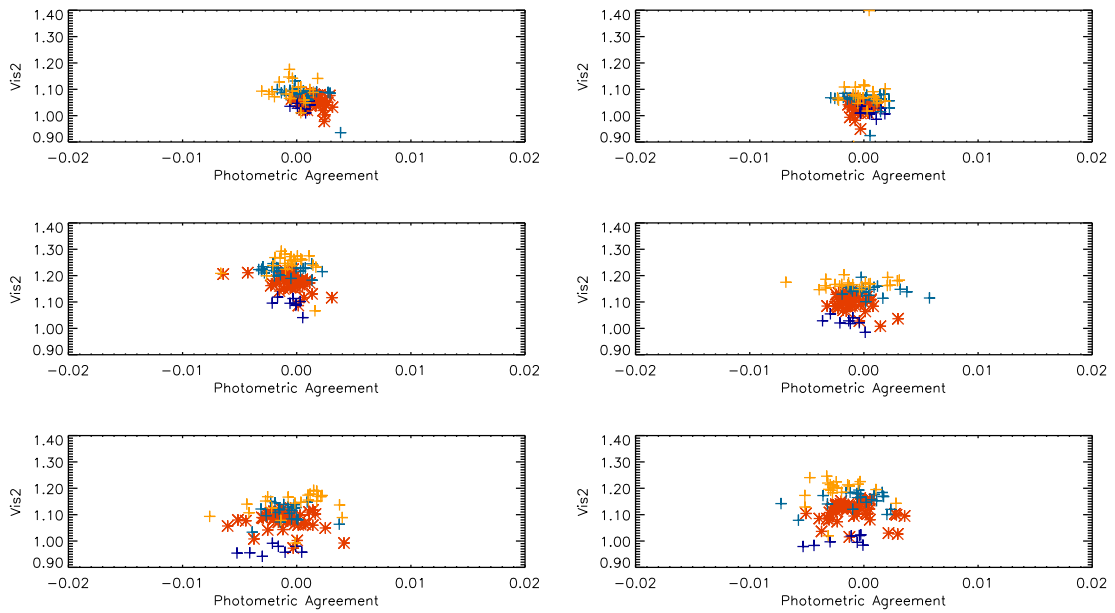


Figure 3.11: Raw squared visibilities with their error bars as a function of the photometric agreement for June 14. Each pixel is related to a specified baseline for a given polarization.

1. A nonlinear regime of the detector, probably related to partial saturation effects, is observed for several pixels in the Vega data from June 9 and June 10. This nonlinearity arises only on the pixels corresponding to the first polarization, which presents significantly higher fluxes than the second one. This behaviour is not observed in the data of June 13 and June 14 in both polarizations.
2. Saturation affects the measured squared visibilities. This bias could possibly be estimated by determining the saturation law of each pixel and then computing the simultaneous photometries with an adapted transfer matrix. However, determining the saturation law of each pixel would not be easy (all the more that IOTA has been dismantled and the PICNIC detector is now used for other applications) and the recovered data would most probably not be sufficiently precise for this scientific programme.
3. There is a color-dependent response in the nonlinear regime of pathologic pixels. This discrepancy does not have an impact on the squared visibilities.
4. This nonlinear behaviour is not present in the β Leo data.

3.4.4 Data reduction

Based on the various tests presented in the previous section, we decided to disregard the first polarization in the Vega data from June 9 and June 10, which has been shown to present serious saturation problems, and only keep the second polarization. For the nights of June 13 and June 14, we keep both polarizations which are healthy and consistent with each other. In order to achieve a sufficiently good precision on the measured squared visibilities, we also decide to only keep the data corresponding to hour angles ranging between -2 and 2 hours. We obtain a lot of data on Vega, covering a wide range of hour angles, and this selection process largely improves the stability of the transfer function which significantly decreases for large hour angles (particularly if Cirri are present as it was the case during the nights of June 13 and June 14). For the β Leo data, we keep both polarizations from each night as explained in the previous section. No selection on the hour angle was applied since the sky was mostly clear during the observations.

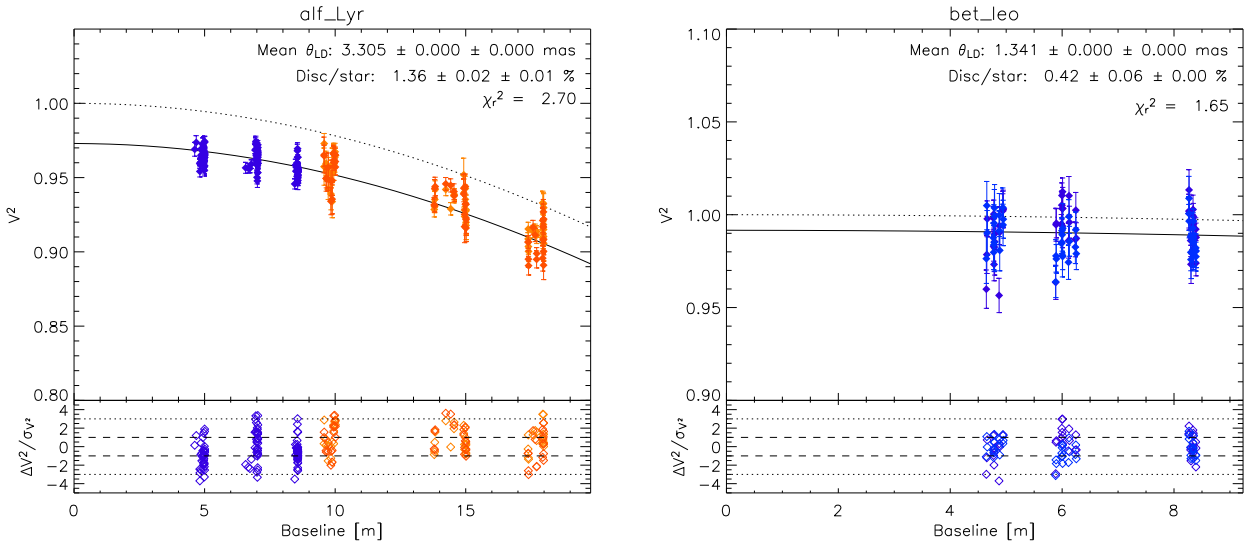


Figure 3.12: Squared visibilities with error bars as a function of the baseline, recorded for Vega (left) and β Leo (right) for the various IOTA baselines. The best-fitted model of a limb darkened photosphere surrounded by a uniform circumstellar emission is represented by the black solid line.

Given our best sample of data, the strategy to detect the presence of circumstellar emission around the target stars follows the method described in section 3.3.2. The interferometric measurements are compared to the expected squared visibility of the stellar photosphere in order to detect a possible deficit of \mathcal{V}^2 . The visibility of the bare stellar photosphere is computed taking into account the limb-darkening profile of the star. Assuming a linear limb darkening law, the monochromatic stellar visibility is given by (Hanbury Brown et al. 1974):

$$\mathcal{V}^2(b_{\perp}, \lambda) = \left(\frac{1 - u_{\lambda}}{2} - \frac{u_{\lambda}}{3} \right)^{-2} \left[(1 - u_{\lambda}) \frac{J_1(x)}{x} + \frac{u_{\lambda} \sqrt{\pi}}{\sqrt{2}} \frac{J_{3/2}(x)}{x^{3/2}} \right], \quad (3.20)$$

where u_{λ} is the linear limb-darkening coefficient and $x = \pi \theta_B b_{\perp} / \lambda$, with θ_B the limb-darkened diameter of the star along the direction of the baseline. If the orientation of the photosphere is unknown, the possible difference between the major and minor angular radii is considered as an additional uncertainty on the stellar diameter along the IOTA baseline. The wide-band visibilities are then computed by integrating the above expression on the IONIC bandpass, using the stellar spectrum as a weighing factor and taking into account the instrumental transmission of IOTA/IONIC (see Di Folco et al. 2007).

Using expression 3.20 and the values for the limb-darkened diameter listed in Table 3.1, it is straightforward to compute the expected squared visibility of the bare photosphere. It is represented as a function of the baseline by the black dotted curve in Figure 3.12 for Vega (left) and β Leo (right). The measured squared visibilities are also shown, with the data from June 9 and June 10 plotted in blue and the data from June 13 and June 14 in red. Each polarization can be distinguished by a different tone of the color. For Vega, these measured squared visibilities are clearly below the expected level of the bare photosphere, whereas they are much closer for β Leo. To better illustrate the deficit of squared visibility in the case of Vega, the data are also represented as a function of the hour angle in Figure 3.13 for each baseline. In order to assess the amount of incoherent emission needed to explain this visibility deficit, a diffuse emission uniformly distributed across the field-of-view has been added to the model to the stellar photospheric model (see Eq. 3.14). The only parameter to be fitted is then the flux ratio between the integrated circumstellar emission and the photosphere. The best-fit model is represented by the solid black curve, together with the statistical error bar and the reduced χ^2 . The second term in the error budget is related to the uncertainty on the photospheric models, both for the

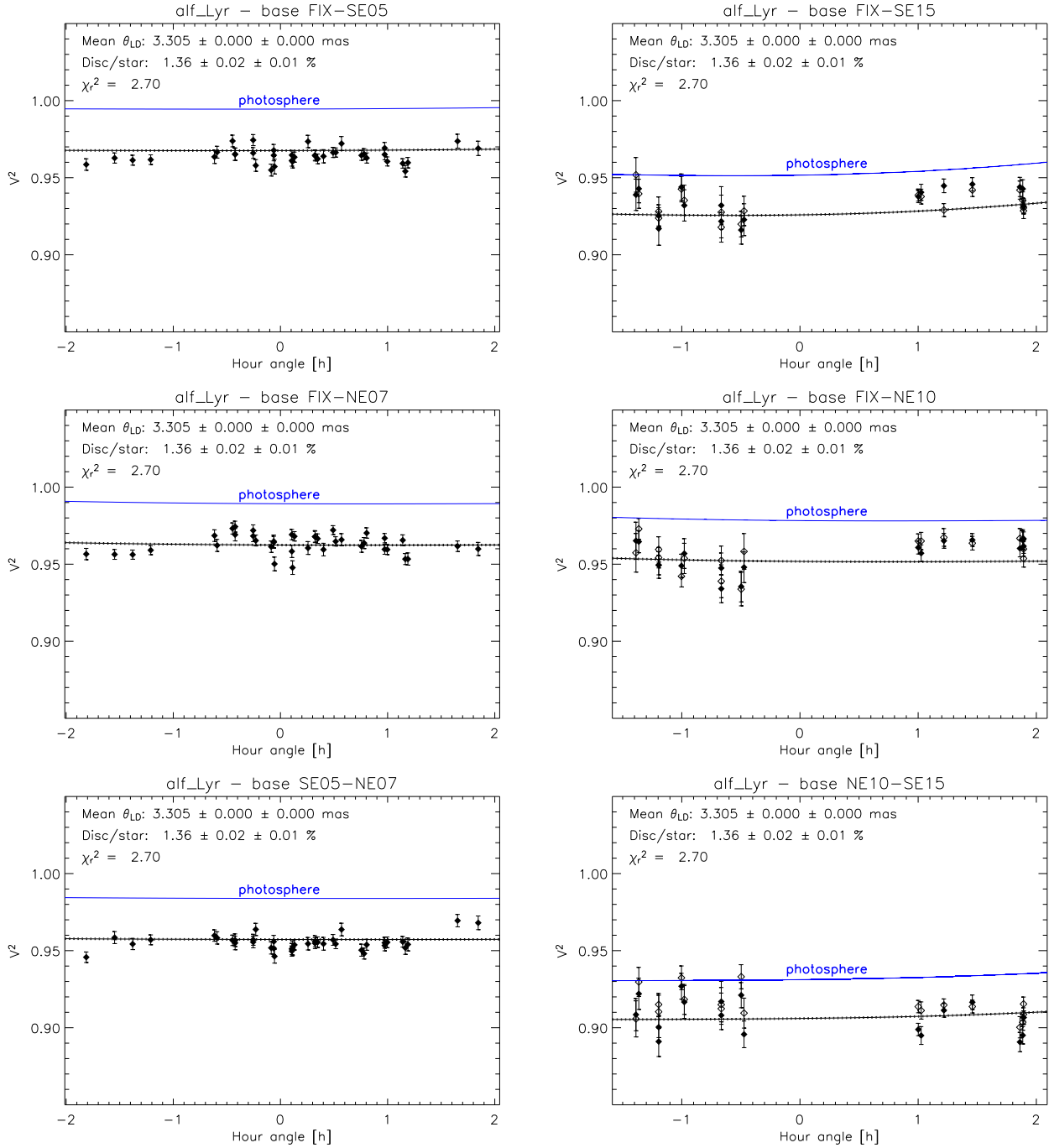


Figure 3.13: Squared visibilities with error bars as a function of hour angle, recorded for Vega on the various IOTA baselines. The blue region represents the 1- σ box defined by the photospheric model. The best-fitted model of a limb darkened photosphere surrounded by a uniform circumstellar emission is represented by the black solid line, while the dotted lines represent the 3- σ statistical uncertainty on the best-fit model. The first polarization is represented by unfilled data points, while the second polarization is represented by filled data points.

science target (uncertainty on the diameter and orientation of the photosphere) and for the calibrator stars (uncertainty on the stellar diameters, which induces a systematic error on the estimation of the interferometric transfer function). The results for Vega and β Leo are discussed separately hereafter:

- For Vega, the fitting procedure gives an H-band flux ratio of $1.36 \pm 0.02 \pm 0.01\%$, with a χ^2_r of 2.70. This confirms the CHARA/FLUOR detection of hot circumstellar emission, which was shown to account for a K-band excess of $1.26 \pm 0.27 \pm 0.06\%$ (Absil et al. 2008b). Even though the H-band flux ratio derived here is very close to the K-band one, its value is somewhat surprising since the model for the exozodiacal dust around Vega predicts a flux ratio much lower (about 0.6%). This result will help us to refine this current model, which is suspected to be mainly composed of sub-micronic highly refractive grains presenting a total mass of $8 \times 10^{-8} M_{\oplus}$ and a fractional luminosity of about 5×10^{-4} .
- For β Leo, the best-fit model gives an H-band flux ratio of $0.42 \pm 0.06 \pm 0.00\%$, with a χ^2_r of 1.65. This relatively small excess in the H-band around this target is very intriguing, since previous K-band observations with CHARA/FLUOR have confirmed the presence of warm dust accounting for $2.4 \pm 1.3\%$ of the stellar flux (Akeson et al. 2009). More recent observations at CHARA/FLUOR show however a somewhat reduced excess with smaller error bars ($0.95 \pm 0.25 \pm 0.06\%$, Absil (in prep.)).

3.4.5 Interpretation of the data

As done in previous similar studies, we will model these IOTA observations with the radiative transfer code originally developed by Augereau et al. (1999) for cold debris discs, and adapted to the case of exozodiacal discs (e.g., Absil et al. 2006b; Di Folco et al. 2007; Absil et al. 2008b, 2009). The model considers a population of dust grains with a parametric surface density profile and size distribution, and calculates the thermal equilibrium temperature of the grains exposed to the stellar radiation. The code handles complex chemical compositions for the grains in order to investigate for instance the fraction of carbonaceous or silicate material contributing to the observed emission. A specific attention is given in the model to the treatment of the exozodiacal disc close to the sublimation radius, to account for the size-dependent position of this radius. The model calculates the thermal and scattered light emissions, and produces both images and spectral energy distributions to combine observations from different instruments (CHARA/FLUOR, Spitzer/IRS, broad-band fluxes). The code allows a broad exploration of the parameter space. These include the disc properties: surface density profile and mass, and the dust properties: size distribution and chemical composition. It allows to go beyond a blackbody approach that poorly constrains the actual location of the dust, and does not permit any discussion of the dust mass nor of the grain properties and dynamics.

The multi-color (H and K bands) interpretation of the data should significantly reduce the possibilities on the dust properties allowed by the fit and based on the sole K band. This work is currently under progress. A Fizeau grant has been attributed to this study and will allow me to spend few weeks at the “Laboratoire d’Astrophysique de l’Observatoire de Grenoble” (LAOG) to work with Jean-Charles Augereau on the dust models for Vega.

3.5 Ongoing work and prospects

3.5.1 Debris disc programme at the CHARA array

Following the pioneering detection of a faint circumstellar dust disc around Vega (Absil et al. 2006a), a survey of near-infrared excesses around bright Vega-type stars has been initiated. The initial goal

was to cover both the northern and southern hemispheres, with CHARA/FLUOR and VLTI/AMBER. However, the analysis of data obtained during three runs of observations with VLTI/AMBER shows that the required precision on the squared visibilities for exozodiacal disc detection (about 1%) cannot be currently achieved¹⁴. The survey was then focused on the observations of the northern hemisphere with CHARA/FLUOR. The target stars were selected through the presence of significant mid- to far-infrared emission in excess to the expected stellar photospheric flux and identified by infrared space missions. One of the main objectives of the survey is to identify new targets with significant near-infrared excess ($\geq 1\%$), which will then be observed in more details at various wavelengths and spatial resolutions, and control a sample consisting of stars with no cold dust detected so far. A detailed model of the discs will then be derived from the available constraints on the SED. With a sufficient sample of targets, it also become possible to constrain the statistics on the hot debris disc phenomenon in order to investigate a possible correlation with either stellar or cold dust population properties. By increasing the statistics, it will be possible to set better constraints on the possible scenarios for the very high on-going dust replenishment rate in the inner part of debris discs (e.g., transient event like a large asteroidal collision, or major dynamical perturbations within the planetary system) can be established. This will already be an indicator of the level of exozodiacal emission that one can expect around nearby main sequence stars, which is of crucial relevance for future life-finding space missions (see chapter 7). On the other hand, the survey has also the objective to look for variability in the near-infrared emission of the hot dust population to identify the dust production mechanisms. For instance, re-observing Vega several years after the discovery observations might provide for the first time the detection of significant fluctuations in the hot dust content, which is predicted by certain scenarios. Recent K-band observations of Vega with the Fiber Nuller¹⁵ are currently under investigation (Hanot and Serabyn in prep.).

The first results of the survey have been reported by Di Folco et al. (2007) and Absil et al. (2008b). Several other stars have been observed since then and a total sample of 30 stars among which 17 with known cold dust have now been observed. The sample consists in 11 A-type stars (8 with cold dust), 10 F-type stars (4 with cold dust) and 9 G- and K-type stars (5 with cold dust). Even though the data are still under analysis, preliminary results indicate some interesting statistical properties (Absil in prep.):

- **Frequency versus spectral type.** Early type stars are more likely to present an infrared excess with 45-64% ($\pm 14\%$) for A-type stars, 20-50% ($\pm 15\%$) for F-type stars and 11% ($\pm 17\%$) for G- and K-type stars. The range of exozodi occurrence depends wether marginal detections are included or not.
- **Frequency versus presence of cold dust.** No significant correlation is presently found in the sample of observations. An infrared excess has been detected around 29-47% ($\pm 11\%$) of stars with cold dust and 21-36% ($\pm 13\%$) with no cold dust.

3.5.2 Prospects with the Keck nullder

The Keck Interferometer Nuller (KIN, see section 4.4.2) has been precisely built to detect and characterize the inner parts of circumstellar discs around nearby stars, providing the appropriate combination of spatial resolution and dynamic range world-wide in the mid-infrared. Whereas the discs discovered so far by CHARA/FLUOR, VLTI/VINCI and IOTA/IONIC are typically a few thousands times more luminous than the solar zodiacal cloud, preliminary results from shared-risk observations and from the 2008-2009 Key Science programs show that the KIN can detect exozodiacal disks with densities around 300 times the solar zodiacal cloud. In this context, modeling N-band observations of KIN in conjunction with K- and H-band data previously obtained with CHARA/FLUOR, VLTI/VINCI and

¹⁴This might partially change with the new version of amdlib 3.0 – TBC.

¹⁵The Fiber Nuller is a so called rotating nulling interferometer developed at the Jet Propulsion Laboratory (JPL/NASA). This transportable instrument is used on the Hale telescope of the Palomar Observatory.

IOTA/IONIC will not only provide a mere flux- (or mass-) scaling of the Solar System zodiacal cloud to an unprecedented level, it will also help to characterize any significant departure from the solar zodiacal dust distribution in these bright debris discs.

Thanks to the resolved N-band observations provided by the KIN, it will be possible to directly constrain the spatial distribution and temperature of the dust grains, by comparing the size and brightness of the disc in K and N bands. This cannot be done based on either K-, H- or N-band observations alone. In addition, obtaining resolved observations at several wavelengths from 8 to $13\mu\text{m}$ will provide a wealth of information to detect silicate dust grains in the discs. Large silicate features would confirm that the grains are small and hot as expected from the K-band observations. In case no silicate features are observed, models with carbonaceous species or large silicate grains will be preferred.

We recently submitted a proposal to observe debris disc stars during the 2010A semester. This programme includes 5 new objects, which have not been observed during the Key Science program, and which are known to have hot inner dust from K-band interferometric measurements.

3.5.3 Further perspectives: Antarctica and space

Assessing the level of circumstellar dust in the habitable zone of nearby main sequence stars is not only relevant for understanding the physics of planetary systems but also of crucial importance for future life-finding space missions. In particular, the detection of habitable terrestrial planets would be seriously hampered for stars presenting warm ($\sim 300\text{ K}$) exozodiacal dust denser than about 10 to 20 times the solar zodiacal disc (see chapter 7). In that respect, substantial efforts have been made in the past few years to achieve the detection of fainter and fainter exozodiacal discs. In addition to KIN, which enables the detection of exozodiacal discs down to a density of a few hundreds zodis, LBTI is expected by 2011 to improve the detection limit down to a few tens of zodis in the northern hemisphere (Hinz et al. 2008b). The ALADDIN project (see Section 4.5.2) is expected to provide similar performances from Antarctica in the southern hemisphere. To go beyond this sensitivity, space-based nulling interferometers are particularly promising to measure the near-infrared emission of exozodiacal discs down to the density of the solar zodiacal cloud. The performance study of space-based nulling interferometers is one of the major topics of this thesis (see chapter 5).

Part III

Debris discs: prospects with infrared nulling interferometry

4

Overview of nulling interferometry

Contents

4.1	Principle of nulling interferometry	75
4.1.1	Instrument response	76
4.1.2	Main noise sources	79
4.1.3	Sensitivity to perturbations	81
4.2	The need for chopping	82
4.3	Instability noise	84
4.4	First ground-based nulling instruments	85
4.4.1	BLINC at the MMT	85
4.4.2	Keck Interferometer Nuller (KIN)	86
4.4.3	Large Binocular Telescope Interferometer (LBTI)	86
4.5	The European projects	87
4.5.1	GENIE	87
4.5.2	ALADDIN	88

*A*fter reporting the major advances in the study of debris discs enabled by infrared stellar interferometry, this chapter introduces the basic principles of a specific promising technique referred to as “nulling interferometry”. In addition to providing the required spatial resolution, this technique offers an improved dynamic range with respect to classical stellar interferometry, and open the path towards the detection of faint circumstellar discs similar to the solar zodiacal disc. After a theoretical introduction, the first ground-based experiments currently under development in the United States are presented with their scientific results. European ground-based projects are also briefly discussed, with a particular attention on the prospects for exozodiacal disc detection with a dedicated Antarctica-based nulling interferometer.

4.1 Principle of nulling interferometry

In addition to the high angular resolution necessary to study extrasolar systems, another major difficulty comes from the luminosity contrast between the science target (e.g., planet, disc) and the host star. For instance, the luminosity contrast between Earth and the Sun is about 10^{-10} in the visible and 10^{-7} in the mid-infrared. Unfortunately, the dynamic range of state-of-the-art stellar interferometers, a few 0.1% (Absil 2006), is not sufficient, and thus only bright debris discs can be investigated.

In this context, Bracewell (1978) proposed nulling interferometry as a solution to directly detect extrasolar planets. The basic principle of nulling interferometry is to combine the beams coming from

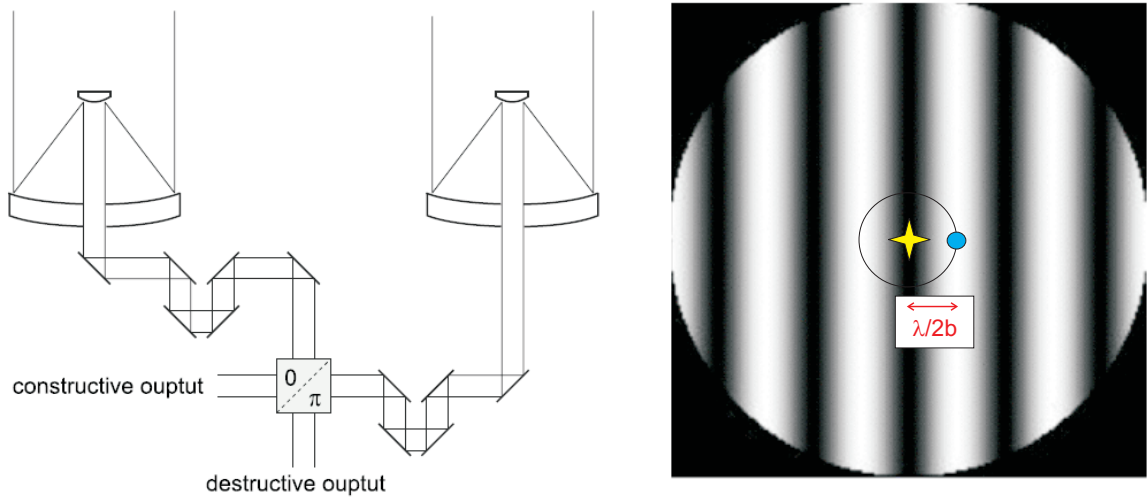


Figure 4.1: Schematic configuration of a Bracewell interferometer (left Figure from Absil 2006) with the corresponding response on the sky (right figure). The beam-combining system produces a destructive interference by applying an achromatic π phase shift to one of the two input beams and by superposing them in a co-axial way. At an angular distance $\lambda/2b$ (λ is the wavelength and b the baseline length) from the line-of-sight, the interference is constructive and the flux from a planet located at this position is fully transmitted.

two telescopes in phase opposition so that a dark fringe appears on the line of sight, which strongly reduces the starlight emission (see Figure 4.1). The response of this simple interferometer on the plane of the sky is a series of sinusoidal fringes, with an angular spacing of λ/b which transmits the light from an off-axis source by adjusting the baseline length (see Figure 4.1, right). As the baseline is rotated in the plane perpendicular to the line of sight, the star remains nulled, and the planet moves through peaks and nulls of the response, giving an output photon rate that is modulated in time. Appropriate demodulation of this output gives the flux of the planet and its position relative to the star. The rationale of Bracewell's proposal was already based on the limited performances of indirect techniques (astrometry, radial velocity) and on the inability of "direct photography" to detect small and faint extrasolar planets around bright stars. The purpose of the initial proposal was the detection of Jupiter-like planets in the far-infrared ($40 \mu\text{m}$) with a moderate interferometer baseline (7.7 m), althought the key features of future missions for Earth-like planet detection were already included. The idea proposed by Bracewell has led to the definition of the so-called "Bracewell" interferometer, meaning a two-telescope nulling interferometer.

4.1.1 Instrument response

The method described in this section to derive the instrument response relies on the full analytical study of Lay (2004). This method has the advantage to be easily applicable to any interferometer configuration, represented in a generic way in Figure 4.2. The final detection of output photons of a nulling interferometer can be performed either in a pupil plane or in an image plane. In the first case, a single-pixel detector is sufficient to record the total flux in the output pupil, coming from all the sources in the diffraction limited field-of-view. In the latter, an image similar to that of a single telescope is formed, except that the relative contribution of each source is affected by the interferometer's intensity response at its location. In any case, no fringe is formed nor recorded, and the final output generally consists of a single value: the total intensity in the diffraction-limited field-of-view. At the output of the

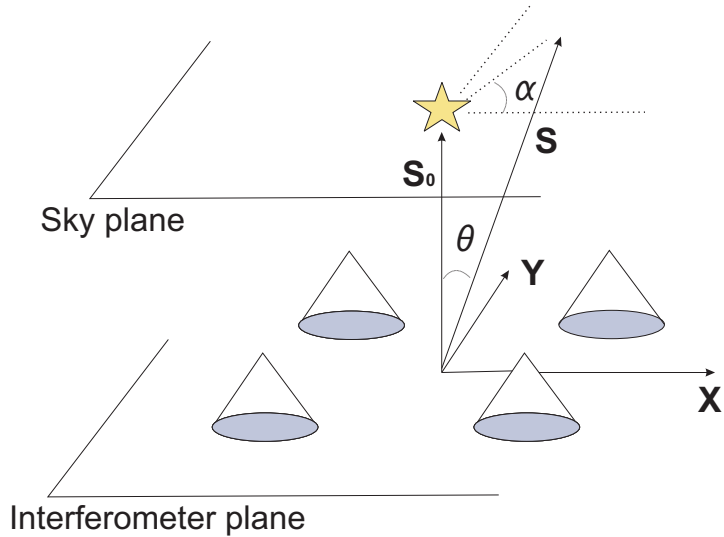


Figure 4.2: Schematic of a generic nulling interferometer and target system. The two angular coordinates (θ, α) denote the position in the sky plane.

interferometer, the total detected photon rate (excluding stray light¹⁶) can be written as:

$$N = \int_{\theta} \int_{\alpha} B_{\text{sky}}(\mathbf{s}) R(\mathbf{s}) P(\mathbf{s}) \theta d\theta d\alpha, \quad (4.1)$$

where B_{sky} is the brightness distribution on the sky for a spectral channel centered on wavelength λ and a bandwidth $\Delta\lambda \ll 1$ (units in photons/s/m²), \mathbf{s} is a unit vector whose direction represents the position on the sky, $P(\mathbf{s})$ is a field-of-view taper function resulting from the size of a collecting aperture and the input response of the single-mode spatial filter (equal to 1 on axis) and $R(\mathbf{s})$ is the intensity response of the interferometer on the sky (excluding the taper), the so-called transmission map.

To deduce the transmission map, the first step is to compute the expression of the electrical field produced by a point source of unit flux at position \mathbf{s} . Due to the linearity of Maxwell equations, the result is simply given by the sum over the contributions from each collector:

$$r(\mathbf{s}) = \sum_j A_j \exp \left[i \left(\phi'_j + \frac{2\pi}{\lambda} \mathbf{x}_j \cdot \mathbf{s} \right) \right], \quad (4.2)$$

where j is the index identifying the collector, i is the imaginary unit, A_j is the electric field amplitude response for collector j , scaled such that A_j^2 represents the detected photon rate from a source with a flux of 1 photon/m² (including the beam combiners), ϕ'_j is the relative phase shift for collector j and x_j the vector position for the center of collector j . The transmission map is then given by:

$$\begin{aligned} R(\mathbf{s}) &= rr^* = \left\{ \sum_j A_j \exp \left[i \left(\phi'_j + \frac{2\pi}{\lambda} \mathbf{x}_j \cdot \mathbf{s} \right) \right] \right\} \times \left\{ \sum_k A_k \exp \left[-i \left(\phi'_k + \frac{2\pi}{\lambda} \mathbf{x}_k \cdot \mathbf{s} \right) \right] \right\} \\ &= \sum_j \sum_k A_j A_k \cos \left(\phi'_j - \phi'_k + \frac{2\pi}{\lambda} (\mathbf{x}_j - \mathbf{x}_k) \cdot \mathbf{s} \right). \end{aligned} \quad (4.3)$$

¹⁶Stray light is made of the photons originating from outside the interferometer and which do not follow the nominal route to the detector. It includes scattered light from the target and thermal photons from the instrument.

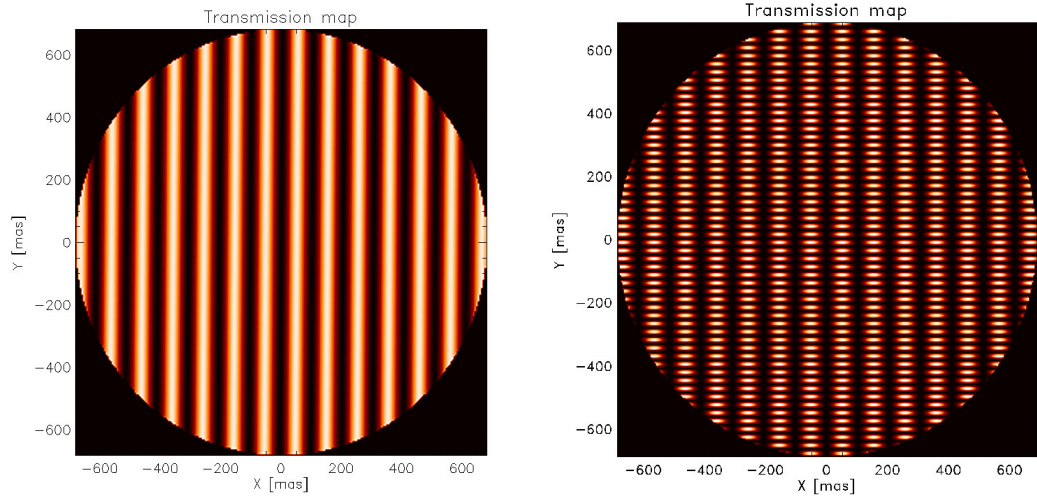


Figure 4.3: *Left:* Monochromatic transmission map for a Bracewell interferometer for a factor λ/b fixed at 5×10^{-7} (corresponding for example to $\lambda = 10 \mu\text{m}$ and a baseline length of 20 m). The transmitted parts of the field are indicated by bright stripes while those that are indicated by dark stripes, including the central dark fringe, indicate the blocked parts. *Right:* Monochromatic transmission map for a 4-telescope nulling interferometer with 2-m mirrors with an aspect ratio of 4 (the long baseline length is 4 times larger than the short one). This configuration is referred to as X-array and is the current configuration for the Darwin mission (see Chapter 7 for more details).

This expression represents the interference pattern and defines which parts of the field-of-view are transmitted by constructive interference, and which are blocked by destructive interference. To be specific, the transmission of a single Bracewell interferometer (2 telescopes, $\phi'_1 = 0$, $\phi'_2 = \pi$, $A_1 = A_2 = A$) writes:

$$R(\theta, \alpha) = 4A^2 \sin^2 \left(\pi \frac{b\theta}{\lambda} \cos \alpha \right), \quad (4.4)$$

taking into account that $(\mathbf{x}_2 - \mathbf{x}_1) \cdot \mathbf{s} = b\theta \cos \alpha$ with b the baseline length and (θ, α) denoting the position in the sky plane. The resulting transmission map is represented in Figure 4.3 (left) for a Bracewell interferometer with 2-m telescopes. The baseline length which would locate a planet (at an angular distance θ_p from its host star) is then given by $b = \lambda/(2\theta_p)$.

The right part of Figure 4.3 shows the transmission map of a 4-telescope nulling interferometer with 2-m mirrors. This configuration is referred to as X-array and is the current baseline configuration for the DARWIN/TPF mission (see Chapter 7 for more details). For both transmission maps, the ratio λ/b has been fixed at 5×10^{-7} representing for example a nulling interferometer working at $10 \mu\text{m}$ with a nulling baseline length of 20 m. In theory, there is no real limitation to the field-of-view of a nulling interferometer, although the crests and troughs of the transmission map wash out for angular distances larger than $\lambda^2/(b\Delta\lambda)$ due to the effect of the finite bandwidth.

Substituting the expression of the transmission map (see Eq. 4.3) in Eq. 4.1, the expression of the output intensity writes:

$$N = \sum_j \sum_k A_j A_k \left\{ \cos(\phi_j - \phi_k) \iint B_{\text{sky,sym}}(\theta, \alpha) P(\theta) \cos \left(\frac{2\pi}{\lambda} [b_{jk} \cos \alpha] \right) \theta d\theta d\alpha \right. \\ \left. - \sin(\phi_j - \phi_k) \iint B_{\text{sky,asym}}(\theta, \alpha) P(\theta) \times \sin \left(\frac{2\pi}{\lambda} [b_{jk} \cos \alpha] \right) \theta d\theta d\alpha \right\}, \quad (4.5)$$

where $b_{jk} = (x_{jk}^2 + y_{jk}^2)^{0.5}$ is the length of the projected baseline between collectors j and k and $B_{\text{sky,sym}}$ (resp. $B_{\text{sky,asym}}$) is the symmetric (resp. asymmetric) part of the sky brightness distribution. The double integrals are two-dimensional Fourier transforms of the sky brightness distribution, including the field-of-view taper, which are denoted by a horizontal bar:

$$N = \sum_j \sum_k A_j A_k [\cos(\phi_j - \phi_k) \bar{B}_{\text{sky,jk,sym}} - \sin(\phi_j - \phi_k) \bar{B}_{\text{sky,jk,asym}}] . \quad (4.6)$$

The total photon rate is therefore a sum over all possible pairs of collectors. If a baseline has a phase difference of $0, \pm \pi$ or $\pm 2\pi$, then its contribution to the photon rate comes entirely from the symmetric brightness distribution while a baseline with a phase difference that is an integer multiple of $\pi/2$ couples entirely to the asymmetric brightness distribution (like a planet). This total output photon rate contains the contributions from the planet (N_p), star (N_*), exo-zodiacal cloud (N_{EZ}), local zodiacal cloud (N_{LZ}), stray light and any solar photons that are scattered into the instrument (N_{stray}), and instrumental thermal emission (N_{thermal}). Therefore, it can also be written as:

$$\begin{aligned} N &= N_p + N_* + N_{EZ} + N_{LZ} + N_{\text{stray}} + N_{\text{thermal}} \\ &= N_o + \delta N , \end{aligned} \quad (4.7)$$

where the second equality indicates that the photon rate at the detector can be written as the sum of the photon rate for an ideal instrument without perturbations (N_o) and the additional photon rate that is due to perturbations (δN , the “perturbation leakage”). These two terms are addressed separately in the following sections.

4.1.2 Main noise sources

Even for an ideal instrument, photons from the different sources leak through the interferometer (as illustrated in Figure 4.4, left). The main sources have characteristic contributions described hereafter:

- The planet can be represented by a point-like δ function in Eq. 4.5 and has both symmetric and asymmetric components:

$$N_p = F_p \sum_j \sum_k A_j A_k \left\{ \cos(\phi_j - \phi_k) \cos\left(\frac{2\pi}{\lambda} [b_{jk} \theta_p \cos \alpha_p]\right) - \sin(\phi_j - \phi_k) \sin\left(\frac{2\pi}{\lambda} [b_{jk} \theta_p \cos \alpha_p]\right) \right\} , \quad (4.8)$$

where F_p is the flux from the planet and (θ_p, α_p) its position on the sky.

- If the star is assumed center symmetric, the stellar contribution to the detected photon rate is given by:

$$N_* \approx \sum_j \sum_k A_j A_k \cos(\phi_j - \phi_k) \bar{B}_{\star jk} . \quad (4.9)$$

Assuming also that the stellar brightness is distributed over a uniform circular disc, the Fourier transform is then given by:

$$\bar{B}_{\star jk} = 2F_* J_1\left(\frac{2\pi b_{jk} \theta_*}{\lambda}\right) \Big/ \frac{2\pi b_{jk} \theta_*}{\lambda} , \quad (4.10)$$

where F_* is the stellar flux at wavelength λ over the bandwidth $\Delta\lambda$, J_1 is the first kind Bessel function and θ_* is the stellar angular diameter.

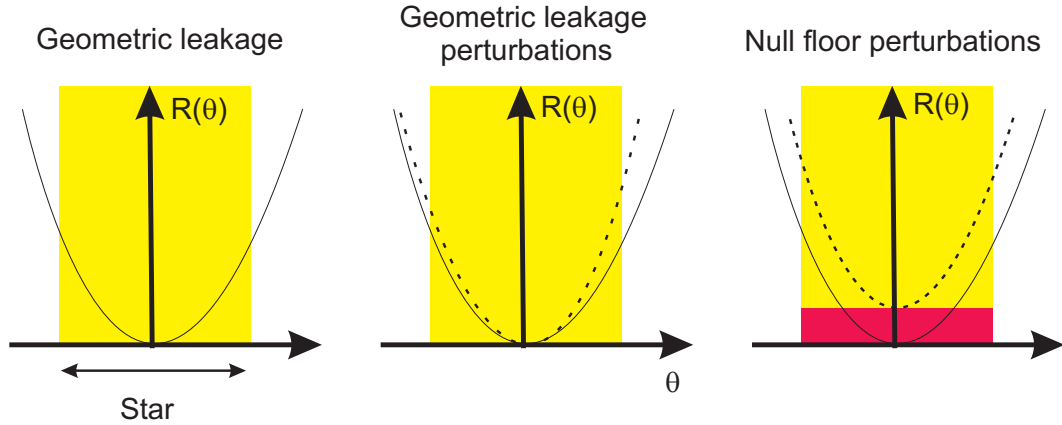


Figure 4.4: Schematic representation of different contributions to the detected photon rate on the output of a nulling interferometer (figure adapted from Lay 2004, see main text for further information).

- The exozodiacal dust emission is several orders of magnitude fainter than the one from the star, but cannot be nulled efficiently since it extends into the habitable zone (HZ). The detected photon rate can be calculated with Eq. 4.6:

$$N_{EZ} \approx \sum_j \sum_k A_j A_k \cos(\phi_j - \phi_k) \bar{B}_{EZjk}. \quad (4.11)$$

assuming here again that the brightness distribution is center symmetric.

- The local zodiacal dust is a uniform and incoherent foreground source of photons. It can be calculated with the symmetric part of Eq. 4.5, leading to:

$$N_{LZ} = B_{LZ} \sum_j A_j^2 \Delta\Omega_j, \quad (4.12)$$

with $\Delta\Omega_j$ being the effective solid angle of the collector beam pattern. For the local zodiacal dust, the photon rate only depends on the amplitudes (no phase or baseline dependence).

Finally, the geometrical leakage (N_g) is defined as the part of the sky brightness distribution that “leaks” through the ideal instrument (except the planetary signal, N_p) and can be derived using Eqs. 4.9, 4.11 and 4.12:

$$\begin{aligned} N_g &= N_o - N_p \\ &= \sum_j \sum_k A_j A_k \cos(\phi_j - \phi_k) (\bar{B}_{*jk} + \bar{B}_{EZjk}) + B_{LZ} \sum_j A_j^2 \Delta\Omega_j. \end{aligned} \quad (4.13)$$

Considering a Bracewell interferometer and assuming that the emissions of the exozodiacal and local zodiacal clouds are negligible with respect to that of the star, the geometrical leakage is given by:

$$N_g = 4F_\star A^2 \left(\frac{2\pi b\theta_\star}{4\lambda} \right)^2, \quad (4.14)$$

taking into account that $J_1(x)/x \simeq 1 - (x/4)^2$ for $x \ll 1$. Useful quantities to characterize a nulling interferometer are the geometric nulling ratio G , defined as the ratio between the transmitted flux and the

initial flux at the input of the beam-combiner (flux coming from both telescopes), and the corresponding rejection factor ρ_g , defined as the inverse of the nulling ratio:

$$G = \frac{N_g}{2F_\star A^2} = \frac{\pi^2}{4} \left(\frac{b\theta_\star}{\lambda} \right)^2 ; \quad \rho_g = \frac{4}{\pi^2} \left(\frac{\lambda/b}{\theta_\star} \right)^2 . \quad (4.15)$$

These quantities depend on two parameters: the wavelength-baseline ratio, which sets the angular resolution of the interferometer, and the angular radius of the star (θ_\star). The rejection factor decreases for longer baselines (or shorter wavelengths) as the stars get more and more resolved.

4.1.3 Sensitivity to perturbations

If the instrument were ideal, the total photon rate on output of a nulling interferometer would be given by the sum of expression 4.13, the geometrical leakage, and expression 4.8. In practice, the photon rate is affected by instrumental perturbations, such as intensity, Optical Path Difference (OPD) and/or pointing errors. For the stellar emission, the contributions of each perturbation can be assessed by deriving Eq. 4.9 to the second order:

$$\begin{aligned} \delta N_\star &\approx \sum_j \left[\frac{\partial N_\star}{\partial A_j} \delta A_j + \frac{\partial N_\star}{\partial \phi_j} \delta \phi_j + \frac{\partial N_\star}{\partial x_j} \delta x_j + \frac{\partial N_\star}{\partial y_j} \delta y_j \right] + \sum_j \sum_k \left[\frac{1}{2} \frac{\partial^2 N_\star}{\partial A_j \partial A_k} \delta A_j \delta A_k \right. \\ &\quad \left. + \frac{\partial^2 N_\star}{\partial A_j \partial \phi_k} \delta A_j \delta \phi_k + \frac{1}{2} \frac{\partial^2 N_\star}{\partial \phi_j \partial \phi_k} \delta \phi_j \delta \phi_k \right] \\ &\approx \sum_j (C_{A_j}^* \delta a_j + C_{\phi_j}^* \delta \phi_j + C_{x_j}^* \delta x_j + C_{y_j}^* \delta y_j) + \sum_j \sum_k [C_{AAjk}^* \delta a_j \delta a_k + C_{A\phi jk}^* \delta a_j \delta \phi_k \\ &\quad + C_{\phi\phi jk}^* \delta \phi_j \delta \phi_k] , \end{aligned} \quad (4.16)$$

defining $\delta a_j = \delta A_j / A_j$ and C^* , the sensitivity coefficients for the star which can be written as:

$$C_{A_j}^* = A_j \frac{\delta N_\star}{\delta A_j} \approx 2A_j \sum_k A_k \cos(\phi_j - \phi_k) \bar{B}_{*jk} , \quad (4.17)$$

$$C_{\phi_j}^* = \frac{\delta N_\star}{\delta \phi_j} \approx -2A_j \sum_{k \neq j} A_k \sin(\phi_j - \phi_k) \bar{B}_{*jk} , \quad (4.18)$$

$$C_{x_j}^* = \frac{\delta N_\star}{\delta x_j} \approx 2 \sum_k A_j A_k \cos(\phi_j - \phi_k) \frac{\partial \bar{B}_{*jk}}{\partial x_j} , \quad (4.19)$$

$$C_{y_j}^* = \frac{\delta N_\star}{\delta y_j} \approx 2 \sum_k A_j A_k \cos(\phi_j - \phi_k) \frac{\partial \bar{B}_{*jk}}{\partial y_j} , \quad (4.20)$$

$$C_{AAjk}^* = \frac{1}{2} A_j A_k \frac{\delta^2 N_\star}{\delta A_j \delta A_k} \approx A_j A_k \cos(\phi_j - \phi_k) \bar{B}_{*jk} , \quad (4.21)$$

$$\begin{aligned} C_{A\phi jk}^* &= A_j \frac{\delta^2 N_\star}{\delta A_j \delta \phi_k} \\ &\approx \begin{cases} 2A_j A_k \sin(\phi_j - \phi_k) \bar{B}_{*jk} & j \neq k \\ -2A_j \sum_l A_l \sin(\phi_j - \phi_l) \bar{B}_{*kl} & j = k \end{cases} \end{aligned} \quad (4.22)$$

$$\begin{aligned} C_{\phi\phi jk}^* &= \frac{1}{2} \frac{\delta^2 N_\star}{\delta \phi_j \delta \phi_k} \\ &\approx \begin{cases} A_j A_k \cos(\phi_j - \phi_k) \bar{B}_{*jk} & j \neq k \\ -A_j \sum_l A_l \cos(\phi_j - \phi_l) \bar{B}_{*kl} & j = k \end{cases} \end{aligned} \quad (4.23)$$

The second order is necessary since the amplitudes and phases are chosen to null the stellar photon contribution, leading to first order derivatives close to 0. Considering the other contributors to the photon rate, the “perturbation leakage” δN is given by

$$\delta N \approx \sum_j (C_{Aj}\delta a_j + C_{\phi j}\delta \phi_j + C_{xj}\delta x_j + C_{yj}\delta y_j) + \sum_j \sum_k [C_{AAjk}\delta a_j \delta a_k + C_{A\phi jk}\delta a_j \delta \phi_k + C_{\phi\phi jk}\delta \phi_j \delta \phi_k], \quad (4.24)$$

where C is the global sensitivity factor, which can be computed similarly for other sources with Eqs. 4.17 to 4.23. As illustrated in Figure 4.4, the perturbations lead to two classes of leakage : “geometric leakage perturbations” and “null-floor leakage”. Geometric leakage perturbations arise from the linear terms in Eq. 4.24 while the null-floor perturbations arise from the nonlinear terms.

Phase chopping techniques (described in the following section) allow for the subtraction of the null-floor leakage, which is the same in the two chop states provided that there is no systematic difference between them. The null floor will therefore contribute only as an additional source of shot noise. On the other hand, most of the instrumental noise is not suppressed by phase chopping, as proven by Lay (2004). This contribution, referred to as instability noise (previously “systematic error” or “variability noise”), is dominated by nonlinear, second order terms related to the perturbations in the amplitudes, phases and polarization angles of the electric fields from each telescope. Instability noise is discussed in more details in Section 4.3, and addressed in the context of DARWIN/TPF in Chapter 7.

4.2 The need for chopping

Even if the stellar emission is sufficiently reduced, it is generally not possible to detect Earth-like planets with a static array configuration, particularly due to the dominant exozodiacal emission. This is the reason why Bracewell proposed to rotate the interferometer such that the planet signal would then be temporally modulated by alternatively crossing high and low transmission regions, while the stellar signal and the background emission remain constant. The planetary signal could then be retrieved by synchronous demodulation. The first array configurations designed to separate the planetary signal from the exozodiacal emission have been proposed by Angel and Woolf (1997) and by Mennesson and Mariotti (1997). The former relied on the strong modulation of the exozodiacal emission at twice the interferometer rotation frequency (due to its symmetry), while the latter suggested to break the central symmetry of the interferometer, for example by using five telescopes regularly located on a circle or on an ellipse. However, since the rotation of the array can not be implemented sufficiently fast, this observing scenario is highly vulnerable to low frequency drifts in the stray light, thermal emission, and detector gain. To perform faster modulation and overcome this problem, the technique of phase chopping has been proposed in 1997 by J.-M. Mariotti (Mennesson et al. 2005). The principle of phase chopping is to synthetise two different transmission maps with the same telescope array, by applying different phase shifts in the beam combination process (see Figure 4.5). By quickly switching between the two different transmission maps, it is possible to modulate the planet signal without modulating the stellar, local zodiacal cloud, exozodiacal cloud, stray light, thermal, or detector gain contributions to the noise. Phase chopping can be implemented in various ways (e.g., inherent and internal modulation, see Absil 2006), and are now an essential part of the future space-based life-searching space missions.

Figure 4 in Section 7.3.2 illustrates the principle of phase chopping. The outputs of two Bracewell interferometers are combined with opposite phase shifts ($\pm \pi/2$) to produce two transmission maps (or “chop states”). Taking the difference of the photon rates obtained in the two chop states gives the chopped response of the array (R_c), given by:

$$R_c(\theta, \alpha) = \frac{1}{2}[R_L(\theta, \alpha) - R_R(\theta, \alpha)], \quad (4.25)$$

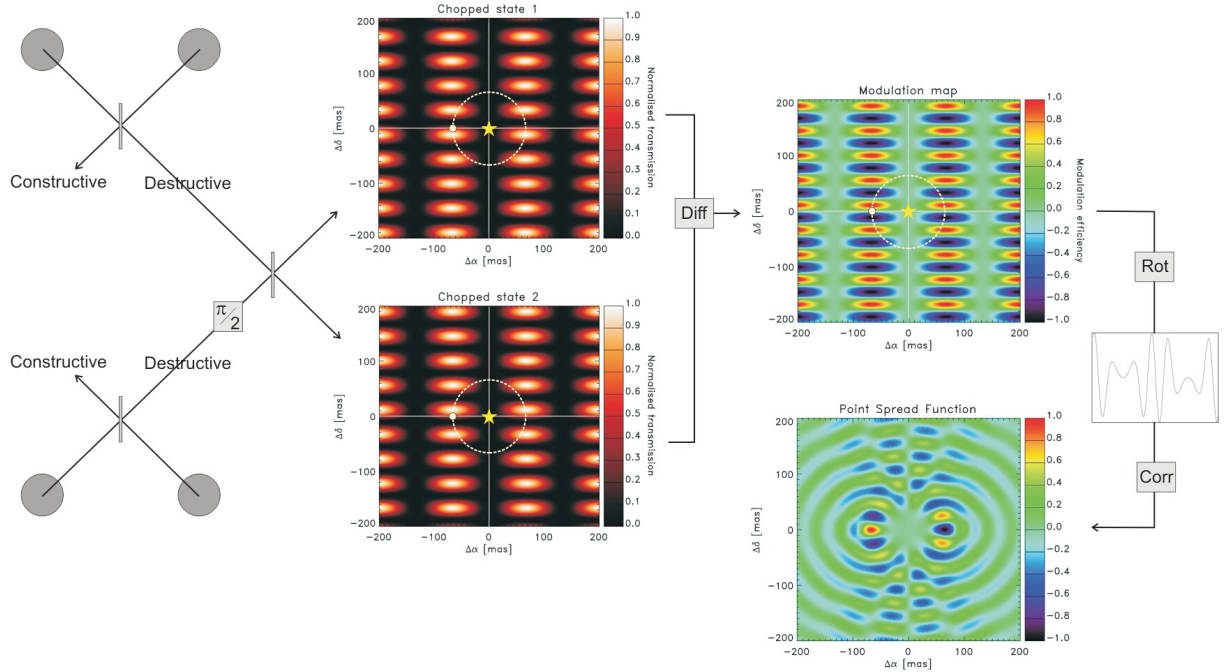


Figure 4.5: Overview of phase chopping for the X-array configuration, the current baseline for the DARWIN/TPF mission (see Chapter 7). Combining the beams with different phases produces two conjugated transmission maps (or chop states), which are used to produce the modulation map. Array rotation then locates the planet by cross-correlation of the modulated chopped signal with a template (Courtesy O. Absil).

where R_L and R_R are the two chop states. The factor $1/2$ accounts for the fact that the instrument spends only half the time in each chop state. The chopped response (R_c) is the so-called modulation map, which can be negative by construction. Since the value of the modulation map varies across the field-of-view, the position of the planet cannot be unambiguously inferred and an additional level of modulation is mandatory. This is provided by the rotation of the interferometer (typically with a period of 1 day). The two levels of modulation (chopping and rotation) allow to define the concept of “rotational modulation efficiency”, which indicates the part of the incoming signal which is actually modulated and thus retrievable by synchronous demodulation. The rotational modulation efficiency for the X-array configuration is about 50%, depending on the radial distance as shown in Figure 4.6 (right). The left part of Figure 4.6 shows the modulation map in polar coordinates, so that each abscissa corresponds to a complete rotation of the interferometer. Note that the rotational modulation efficiency for several array configurations has been investigated by Lay (2005).

The variation of the chopped planet photon rate with the rotation angle of the array appears in Figure 4.6 (right). Finally, the most common approach applied to retrieve the planet is correlation mapping, a technique closely related to the Fourier transform used for standard image synthesis (Lay 2004). The result is a correlation map, displayed for a single point source in the low right part of Figure 4.6. This represents the Point Spread Function (PSF) of the array. This process, illustrated here for a single wavelength, is repeated across the waveband, and the maps are co-added to obtain the net correlation map. The broad range of wavelengths planned for DARWIN/TPF greatly extends the spatial frequency coverage of the array, suppressing the side lobes of the PSF.

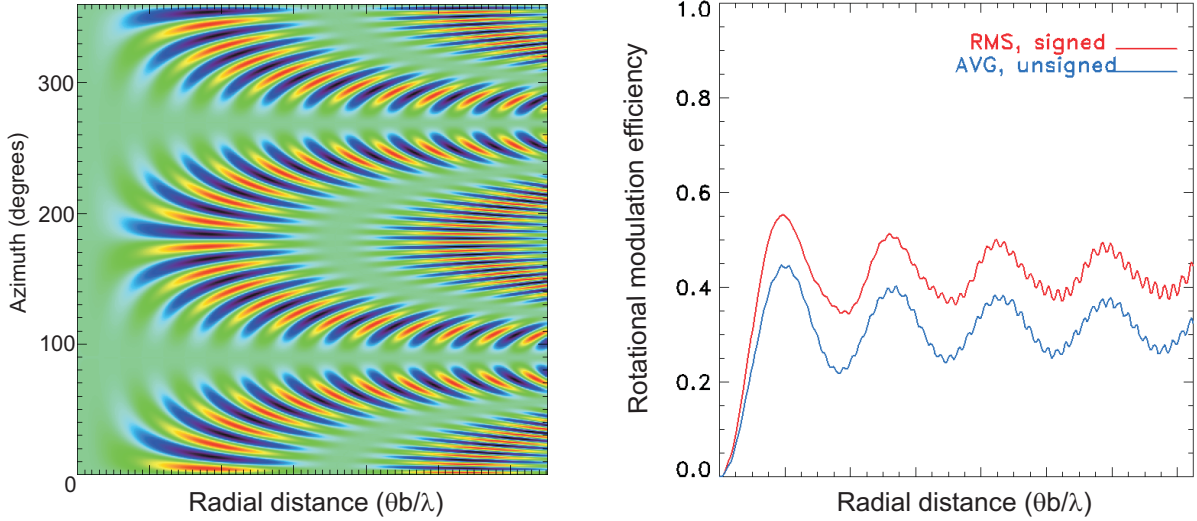


Figure 4.6: *Left:* modulation map of the X-array configuration in polar coordinates. *Right:* Corresponding rotational modulation efficiency (red curve, labelled “rms signed”). The blue curve (labelled “avg unsigned”) indicates the mean value of the modulation map absolute value (see main text for further information).

4.3 Instability noise

Instability noise is defined as the component of the demodulated nulled signal that arises from phase, amplitude and polarization errors (Lay 2004). Telescope vibrations, fringe tracking offset, control noise, longitudinal chromatic dispersion, and birefringence are at the origin of the phase errors whereas tip/tilt, defocus, beam shear, and differential transmission produce amplitude errors. These phase, amplitude and polarization errors induce a time-dependent asymmetry between the two chop states so that the modulation map does not remain centered on the nominal position of the line of sight (i.e. the position of the star). Hence a fraction of the starlight survives the modulation process and mixes with the planet photons. Using Eq. (4.24) and assuming that the perturbations in amplitude and phase for each collector beam train are mutually independent, the variance of the demodulated output is given by:

$$\langle O_{\text{sys}}^2 \rangle = \sum_j C_{Aj}^2 \langle \widehat{\delta a_j}^2 \rangle + \sum_j C_{\phi j}^2 \langle \widehat{\delta \phi_j}^2 \rangle + \sum_j C_{xj}^2 \langle \widehat{\delta x_j}^2 \rangle + \sum_j C_{yj}^2 \langle \widehat{\delta y_j}^2 \rangle + \sum_j \sum_k C_{AAjk}^2 \langle \widehat{\delta a_j \delta a_k}^2 \rangle + \sum_j \sum_k C_{A\phi jk}^2 \langle \widehat{\delta a_j \delta \phi_k}^2 \rangle + \sum_j \sum_k C_{\phi \phi jk}^2 \langle \widehat{\delta \phi_j \delta \phi_k}^2 \rangle, \quad (4.26)$$

where C is the global sensitivity factor defined in Section 4.1.3, and the wide-hat notation designates the demodulated output signal. Using the cross-correlation method, the demodulated output signal is given by

$$\widehat{N_p} = \frac{1}{T} \int_0^T N_p \eta \, dt, \quad (4.27)$$

where η is the template function, which is normalized to have a root-mean square value of one. Instability noise corresponds to the square-root of $\langle O_{\text{sys}}^2 \rangle$. The factors within the angular braces in Eq. 4.26 indicate the extent to which each contributor to instability noise mimics the planet signal. The power spectra of these instrumental effects mix with each other so that perturbations at all frequencies, including DC, have an effect. Although a simple binary phase chop removes a number of these systematic errors, it has no effect on the dominant amplitude-phase cross terms and on the co-phasing errors (Lay 2004).

Four independent studies (Lay 2004; D’Arcio 2005; Chazelas et al. 2006; Defrère et al. in press) have reviewed the instrumental requirements on the DARWIN/TPF mission that reduce the instrumental

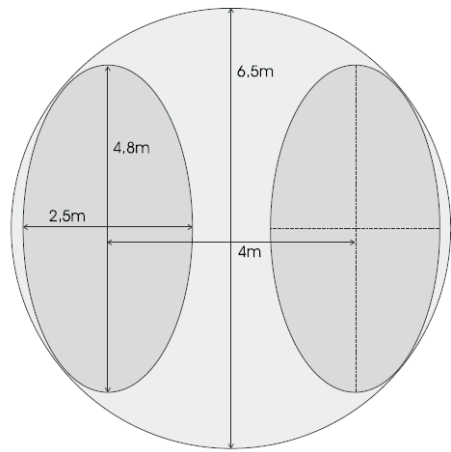


Figure 4.7: *Left:* Picture of the Multi-Mirror Telescope (MMT, Mount Hopkins, Arizona). *Right:* Division of the MMT pupil by the BLINC instrument to artificially produce a baseline of 4 m between two oval sub-pupils and perform destructive beam combination (Figure from Absil 2006).

stellar leakage to a sufficiently low level for Earth-like planet detection. Assuming the presence of 1/f-type noise, these studies showed that the requirements on amplitude and phase control are not driven by the null-floor leakage, but by instability noise. This is discussed in more details in Chapter 7.

4.4 First ground-based nulling instruments

4.4.1 BLINC at the MMT

The Bracewell Infrared Nulling Cryostat (BLINC) is a nulling interferometer installed on the Multi-Mirror Telescope (MMT, Mont Hopkins, Arizona). It was first installed on the segmented version of the MMT, using the beams from two of its 1.8-m segments (Hinz et al. 1998b), and produced first scientific results on late-type giant stars around which dust outflows were detected (Hinz et al. 1998a). After the refurbishment of the MMT in 1999, BLINC was re-installed on the new 6.5-m monolithic telescope (Hinz et al. 2000). It uses the two parts of the MMT's 6.5-m primary mirror to create an interferometer with two elliptical 4.8×2.5 -m sub-apertures and a baseline length of 4 m (see Figure 4.7). These two sub-apertures are overlapped in the pupil plane in order to destructively interfere the central point source in the image plane. Nulling interferometry is implemented in combination with the MMT's adaptive optics (AO) secondary mirror. The addition of AO has benefits for nulling, providing correction of atmospheric wavefront aberrations in the incoming light which allows destructive interference to be precisely tuned for the deepest possible suppression of starlight. However, despite adaptive optics, the performance of BLINC is limited to a few percent in null depth because of mechanical vibrations. The BLINC instrument has obtained interesting results on YSO and Vega-type stars (Liu et al. 2003, 2004, 2005, 2007). Recently, a survey of nearby main sequence stars to search for evidence of exozodiacal dust has been initiated. First results show no evidence of warm debris in the habitable zone of six nearby main sequence stars (α CrB, α Lyr, β Leo, γ Ser, ϵ Eri, and ζ Lep). These results place a 3σ upper limits on dust density of these systems ranging from 220 to 10^4 zodi (Liu et al. 2009). Note that the BLINC instrument has also been used in the southern hemisphere, at the Magellan I (Baade) telescope.

4.4.2 Keck Interferometer Nuller (KIN)

The Keck Interferometer nuller is part of the KI previously described (see Section 2.3). Following laboratory development and testing, the addition to KI of the hardware to implement the nuller mode began in June 2004, and first 10- μm measurements were performed later that year. The first null measurements took place in early 2005, with first stabilized nulls in mid 2005. Shared risk observations began in October 2005 in parallel with continued nuller development. The KIN is implemented as a four-beam system operating at a wavelength of 10 μm . The two Keck telescope apertures are split into left (“primary”) and right (“secondary”) halves at a dual-star module (DSM) at each telescope (Colavita et al. 2008). Accounting for diffraction, the beam size on the sky at 10 μm is approximately 0.45–0.50 arcsec. Two modified Mach-Zehnder nullers combine the light from the left halves and right halves on the 85-m long baseline. The outputs of the two long baseline nullers are combined in a Michelson combiner with a short 4-m effective baseline. The output of the cross combiner feeds the nuller mid-IR camera. Nulling on the long baseline is used to suppress the central star in order to detect surrounding extended emission, while modulation on the short baseline allows fringe detection in the presence of the strong thermal background. Because of the limited control bandwidths achievable with the integration times required to observe faint 10- μm sources, phasing and tilt stabilization rely upon feed-forward from two 2- μm fringe trackers (i.e., phase-referencing, or cophasing), as well as tilt feed-forward from the KI angle tracker operating at 1.2 or 1.6 μm . Laser metrology and accelerometer feed-forward is used to stabilize against non-atmospheric disturbances. A distributed real-time control system checks the various servos and interconnections, aided by high-level sequencers.

The initial objective was to achieve exozodiacal disc detection at the 30-zodi level around G2V stars located at 10 pc. This level of performance requires a deep and stable instrumental null depth of at least 0.1% at 10 μm . First science results with the KIN have been recently reported (Serabyn et al. 2006). In 2007 a series of performance validation tests were completed in preparation for a NASA call for nuller key science teams to participate in an intensive observing programme to be carried out in 2008 and 2009. First results have been published recently: observations of the nova RS Ophiuchi (RS Oph) approximately 3.8 days following the most recent outburst that occurred in 2006, supporting a model in which the dust appears to be present between outbursts and is not created during the outburst event (Barry et al. 2008). Other results are related to the observations of 51 Ophiuchi, a rapidly rotating star located at 131 pc showing a large infrared excess in its spectral energy distribution due to dust emission from a circumstellar disk (Stark et al. 2009).

4.4.3 Large Binocular Telescope Interferometer (LBTI)

The Large Binocular Telescope Interferometer (LBTI) is a ground-based interferometer currently under development by the University of Arizona and located at Mont Graham, Arizona (see Section 2.3.3 for further details). The Nulling Camera (NIC) will present a science channel between 8 and 13 μm . NIC is composed of two different science channels, a long wavelength channel, called the Nulling Optimized Mid-Infrared Camera (NOMIC) and a short wavelength channel, called LMIRcam. The long wavelength channel can be diverted to an intermediate set of optics, called NIL (Nulling Interferometer for the LBT) or relayed directly to NOMIC. The components of NIC are housed within a single cryostat. The design has been optimized to minimize the volume of the cryostat and to allow cooling with a single mechanical cooler. The cryostat also houses a K-band fast readout camera (Phasecam) to sense phase variations between the LBT apertures and carry out closed loop correction. The optical design uses diamond-turned biconical mirrors to realize diffraction-limited performance in a compact space. A range of cryogenic actuators and alignment mechanisms have been developed to carry out a fine alignment of the interferometer and to feed the spectral channels of NIC.

The characterization of habitable environments is the primary goal and key science deliverable of the

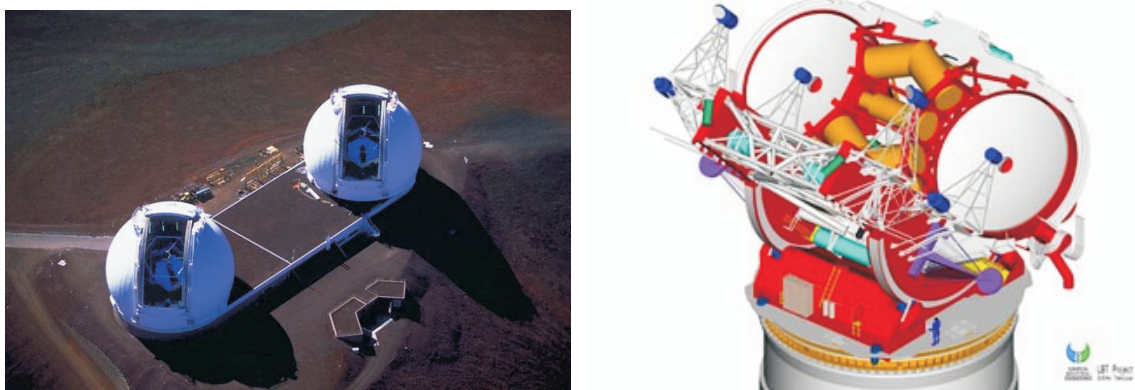


Figure 4.8: *Left:* Picture of the Keck interferometer (Mauna Kea, Hawaii). *Right:* Artist concept of the fully assembled Large Binocular Telescope Interferometer (LBTI, Mount Graham, Arizona).

LBTI project. LBTI will accomplish this in two ways. First, by detecting zodiacal dust, it will probe the HZ of nearby stars to search for exozodiacal dust emission. Secondly, by detecting Jupiter-like planets and characterizing their orbits, LBTI will identify which stars have gas giants similar to those of our solar system and determine whether these planets provide a dynamically stable or unstable HZ. These science objectives are of crucial importance for future searches for Earth-like planets.

4.5 The European projects

4.5.1 GENIE

GENIE (Ground-based European Nulling Interferometer Experiment, Gondoin et al. 2004) is a nulling interferometer conceived as a focal instrument for the VLTI. It has been studied by ESA at the phase A level. GENIE was intended as a scientific and technologic step toward DARWIN/TPF but has been unfortunately put on hold by ESA and ESO. The objectives of the GENIE project were twofold. From a technological and operational point of view, the goal was to advance and mature the experience on designing, manufacturing and operating a nulling interferometer, employing DARWIN/TPF representative concepts and technologies. From a scientific point of view, the objective was to perform a systematic survey of candidate targets for DARWIN/TPF in order to detect bright exozodiacal dust discs around nearby solar type stars. GENIE would have benefitted from the existing VLTI infrastructure including 8-m Unit Telescopes (UT) and 1.8-m Auxiliary Telescopes (AT), adaptive optics, delay lines, fringe sensors and a beam combiner laboratory. The overall capabilities of the instrument heavily depend on the performance of all VLTI sub-systems and in particular on the adaptive optics and co-phasing sub-systems. The GENIE optical bench within the VLTI laboratory would have provided the functions specific to the nulling interferometry technique, namely photometry and amplitude control, polarization matching, phase shifting, beam combination and internal modulation, spatial filtering, spectrometry, detection, electronics and cryogenics.

Considering the DARWIN/TPF targets, GENIE/UT could have detected exozodiacal discs about 100 times as dense as the solar zodiacal cloud (Absil et al. 2006a). Thanks to the shorter available baselines, GENIE/AT would have also been valuable to observe the closest stars for which GENIE/UT is strongly limited by the geometric leakage (see Eq. 4.15). Further information on the capabilities of GENIE is given in Chapter 5, reporting the comparison of performance with other nulling instruments such as ALADDIN which is described hereafter.

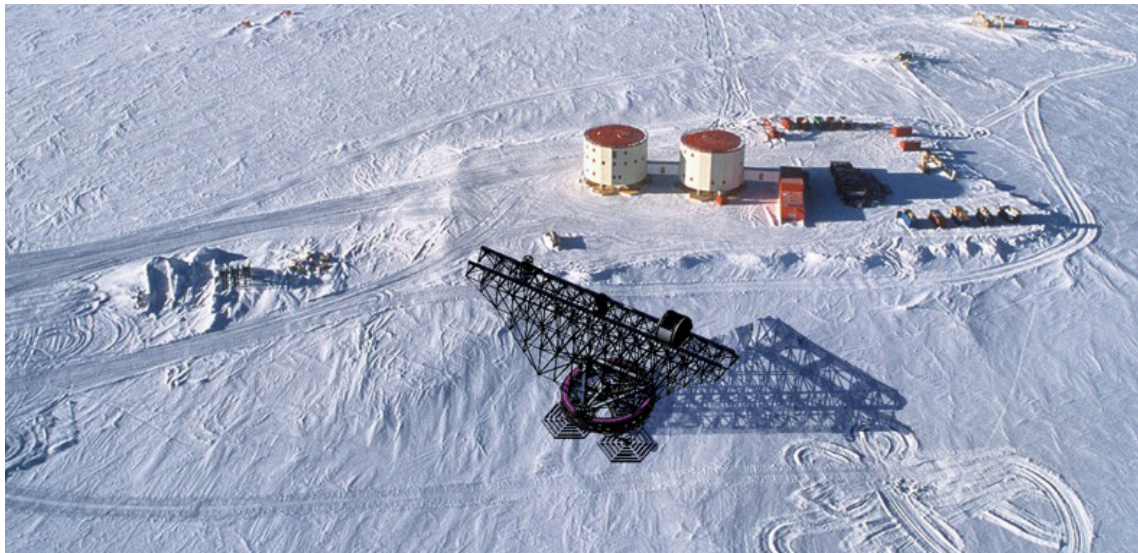


Figure 4.9: Artist impression of the ALADDIN infrastructure installed at Dome C (Antarctica, Courtesy Vincent Coudé du Foresto). A \sim 40-m rotating truss bearing two 1-m diameter telescopes is mounted on a 18-m high structure (© AMOS). The light beams collected by the two telescopes are routed towards the nulling instrument cryostat by fixed relay optics.

4.5.2 ALADDIN

ALADDIN (Antarctic L-band Astrophysics Discovery Demonstrator for Interferometric Nulling, Coudé du Foresto et al. 2006) is a Bracewell interferometer with two 1-m collectors, foreseen to be installed at Dome C (Antarctica, the most favorable ground-based site for high dynamic range infrared interferometry). Dome C offers several interesting features in the context of infrared interferometry:

- An extremely low turbulence above the boundary layer;
- An increased sky transparency, which improves and enlarges the atmospheric windows in the near-to mid-infrared;
- A reduced thermal background, from both the sky and the optical train;
- A reduced water vapour content.

ALADDIN consists of two moveable siderostats are located on a \sim 40-m long rotating truss installed on top of an 18-m tower and are able to move on a circular path to maintain the source at the meridian of the baseline (see Figure 4.9). In that manner, the baseline is always perpendicular to the line of sight so that neither long delay lines nor dispersion correctors are needed. Moreover, polarization issues, which are especially harmful in nulling interferometry, are mitigated by this fully symmetric design. The whole nulling instrument is assumed to be enclosed in a cryostat, in order to improve its overall stability and to mitigate the influence of temperature variations between seasons at the ground level (the mean temperature during the austral summer is about 40 K higher than during winter, while the instrument should be usable during the whole year). The lower temperature of the optics inside the cryostat (77 K) also further decreases the background emission produced by the instrument.

The available baseline lengths range from 4 to 32 m and is optimized for each source to obtain the best compromise between angular resolution and stellar leakage. The baseline can also be reverted for calibration purposes. Operating in the L-band (ranging from 2.8 to 4.2 μ m), ALADDIN provides a maximum angular resolution of 10 mas, which is ideal to probe the inner region of exozodiacal discs,

and study the HZ around DARWIN/TPF-I candidate targets (typically separated by a few 10 mas from their parent star, see Figure 5.2). Thanks to the exceptionally low turbulence of the free air 18 m above the ground, ALADDIN presents an improved sensitivity with respect to GENIE and should be able to detect exozodiacal discs at the level of 30 zodis (Absil et al. 2007). Within one winter-over on the high Antarctic plateau, ALADDIN could identify suitable candidate targets for direct Earth-like planet detection in the southern hemisphere, and allow to tune the design of future space missions to cope with the statistical occurrence of bright exozodiacal discs.

5

Pegase and FKSI: toward the detection of zodiacal cloud analogs

Contents

5.1	Introduction	91
5.2	Instrumental concepts	92
5.2.1	PEGASE	93
5.2.2	The Fourier-Kelvin Stellar Interferometer (FKSI)	94
5.3	Main scientific objectives	95
5.3.1	Circumstellar disc science	95
5.3.2	Sub-stellar objects	97
5.3.3	Additional programmes	98
5.4	Performance for exozodiacal disc detection	98
5.4.1	The GENIEsim software	98
5.4.2	Vibrations in the ambient space environment	100
5.4.3	Real-time correction of spacecraft vibrations	102
5.4.4	Paper: <i>Nulling interferometry: performance comparison between space and ground-based sites for exozodiacal disc detection</i>	102
5.5	Summary	114

PEGASE and FKSI are two projects of space-based Bracewell interferometers conceived as scientific precursors and technological demonstrators for future exo-Earth characterization missions. Their main scientific goals would be to enable the high-angular resolution study of EGPs and exozodiacal discs at infrared wavelengths. Characterization of exozodiacal discs with interferometry has been recently recommended as one of the priorities in the medium term (6-10 years) by the recently completed report of the Exoplanet Task Force (2008). After a brief overview of PEGASE and FKSI, this chapter is dedicated to their performance simulation for exozodiacal disc detection. Comparison with ground-based instruments is also provided.

5.1 Introduction

Characterization of debris discs around nearby stars is an important complement to planet finding for several reasons. Primarily, the existence of planets is intrinsically linked to circumstellar discs and observing them provides an efficient way to study the formation, evolution and dynamics of planetary

systems. Photometric surveys primarily with IRAS, ISO, and Spitzer have revealed the presence of micron-sized grains around a large number of main sequence stars (e.g., Trilling et al. 2008; Hillenbrand et al. 2008). This is interpreted as the presence of planet building material, the production of grains believed (by analogy with the zodiacal cloud in our solar system) to be sustained by asteroid collisions and outgassing of comets in the first tens of AU. Indeed, in a gas-poor disc, debris material is believed to be cleared away through collisional destruction, radiation pressure, or Poynting-Robertson drag on relatively short timescales compared to the planetary system itself (see Section 1.1.2 for further details). Therefore, the presence of dust indicates that larger parent bodies must also be located in the system. Thus, the detection of dust, in tandem with the detection of the massive planets in the system allows the development of a more complete observational picture of the architecture of a planetary system. In fact, information obtained from disc structure can be used to detect planets that would otherwise be too faint or have a mass that is too low to be detected using other techniques. Similarly, the presence of small body populations in a habitable zone could affect habitability through the frequency of large impact events.

In addition, for the ultimate goal of detecting and characterizing an Earth-like extrasolar planet, debris discs can decrease the significance of the detection and hamper the planet detection and characterization. Observing in the infrared (6-20 μm), these missions would enable the spectroscopic characterization of the atmosphere of habitable extrasolar planets orbiting nearby main sequence stars. This ability to study habitable distant planets strongly depends on the density of exozodiacal dust in the inner part of circumstellar discs, where the planets are supposed to be located. In particular, the detection of habitable terrestrial planets would be seriously hampered for stars presenting warm (~ 300 K) exozodiacal dust more than 15 times as dense as our solar zodiacal disc (Defrère et al. in press). Assessing the level of circumstellar dust around nearby main sequence stars is therefore a necessary pre-requisite to prepare the observing programme of DARWIN/TPF by reducing the risk of wasting time on sources for which exozodiacal light prevents Earth-like planet detection.

However, the presence of warm dust can generally not be unequivocally determined from photometric surveys because the typical accuracy on both near-infrared photometric measurements and photospheric flux estimations is a few percent at best, limiting the sensitivity to typically 1000 times the density of our solar zodiacal cloud (Beichman et al. 2006b). Photometric measurements are therefore generally not sufficient to probe the innermost regions of the discs and interferometry is required to separate the starlight from the disc emission. Good examples are given by the detection of hot dust around several nearby main sequence stars with classical interferometry at the CHARA array and VLTI (e.g., Absil et al. 2006b; Di Folco et al. 2007; Absil et al. 2008a; Akeson et al. 2009; Absil et al. 2009).

In that context, the recently completed report by the Exoplanet Task Force (2008) made two recommendations related to dust disc detection. In the near term (1 to 5 years), they recommended that the community to invest in a census of exozodi systems around exoplanet target stars, and in the medium term (6 - 10 years) that the community implement next generation high spatial resolution imaging techniques on ground-based telescopes: AO for direct detection of young, low-mass companions, and interferometry for disc science. This chapter presents the prospects for exozodiacal disc detection with space-based nulling interferometry and compares the results with those expected performance at ground-based sites.

5.2 Instrumental concepts

PEGASE and FKSI are space-based Bracewell interferometers, conceived as scientific and technological precursors to DARWIN/TPF. They present similar architectures, the main difference being that the two telescopes of PEGASE are free-flying while those of FKSI are arranged on a single boom. PEGASE was initially proposed in the framework of the 2004 call for ideas by the French space agency (CNES) for its

Table 5.1: Instrumental parameters for PEGASE and FKSI considered in this study.

Instrumental parameters	PEGASE	FKSI
Baselines [m]	40-500	12.5
Telescope diameter [m]	0.40	0.50
Field of regard	$\pm 30^\circ$	$\pm 20^\circ$
Optics temperature [K]	90	65
Detector temperature [K]	55	35
Science waveband [μm]	1.5-6.0	3.0-8.0
Spectral resolution	60	20
Fringe sensing waveband [μm]	0.8-1.5	0.8-2.5 (80%)
Tip-tilt sensing waveband [μm]	0.6-0.8	0.8-2.5 (20%)

formation flying demonstrator mission. CNES performed a Phase 0 study in 2005 and concluded that the mission is feasible within an 8 to 9 years development plan (Le Duigou et al. 2006). However, the mission was not selected for budgetary reasons. On the US side, FKSI has been initially studied by the Goddard Space Flight Center in preparation for submission as a Discovery-class mission. Several concepts have been considered and the mission was studied to the phase A level based on the two-telescope design described here.

5.2.1 PEGASE

Following the phase 0 study, the optimum instrumental parameters of PEGASE have been determined. The baseline concept for the mission consists in a two-telescope interferometer composed of three free flying spacecraft orbiting around the second Lagrangian point, L2, and pointing in the anti-solar direction within a $\pm 30^\circ$ cone. Thanks to this location, the spacecraft and the focal plane assembly can be passively cooled down to respectively 90 ± 0.1 K and 55 ± 0.1 K. In its nominal configuration, PEGASE consists in two 40-cm siderostats and a beam combiner flying in linear formation (see Figure 1 in Section 5.4.4, right). Visibility measurements and recombination in a nulling mode (Bracewell interferometer) are both possible with a spectral resolution of about 60. The formation flying constraints allow baseline lengths from 40 to 500 m leading to an angular resolution in the range of 0.5-30 mas. The fine-tuning of the optical path difference (OPD) is performed by a dedicated control loop based on a fringe sensor measuring the observed central target in the 0.8-1.5 μm range and an optical delay line. The intensity control is performed by a fine pointing loop using a field relative angle sensor operating in the 0.6-0.8 μm range and fast steering mirrors based on piezoelectric devices. This implementation allows to control the OPD down to a level of 2.5 nm rms and the tip/tilt errors to a value of 30 mas rms, corresponding to a nulling ratio of 10^{-4} stable at the level of 10^{-5} . The instrumental parameters of PEGASE are summarized in Table 5.1.

The optical arrangement is represented in Figure 5.1 with the following elements along the optical path:

- Two afocal telescopes, composed of two mirrors (M_2 and M_3), with an optical magnification which will be a trade-off between dynamics of the tip-tilt errors, the available stroke of the fast steering mirrors, the actuation noise, the mechanical constraints and the polarization limitations. A magnification of the order of 20 is today considered as a good starting value.
- Two fast steering mirrors to correct for the tip-tilt errors. They are placed as close as possible to the afocal telescopes in order to minimize the optical space where the tip-tilt errors are not corrected, and hence reduce differential polarization effects (possible location are M_3 or M_4).

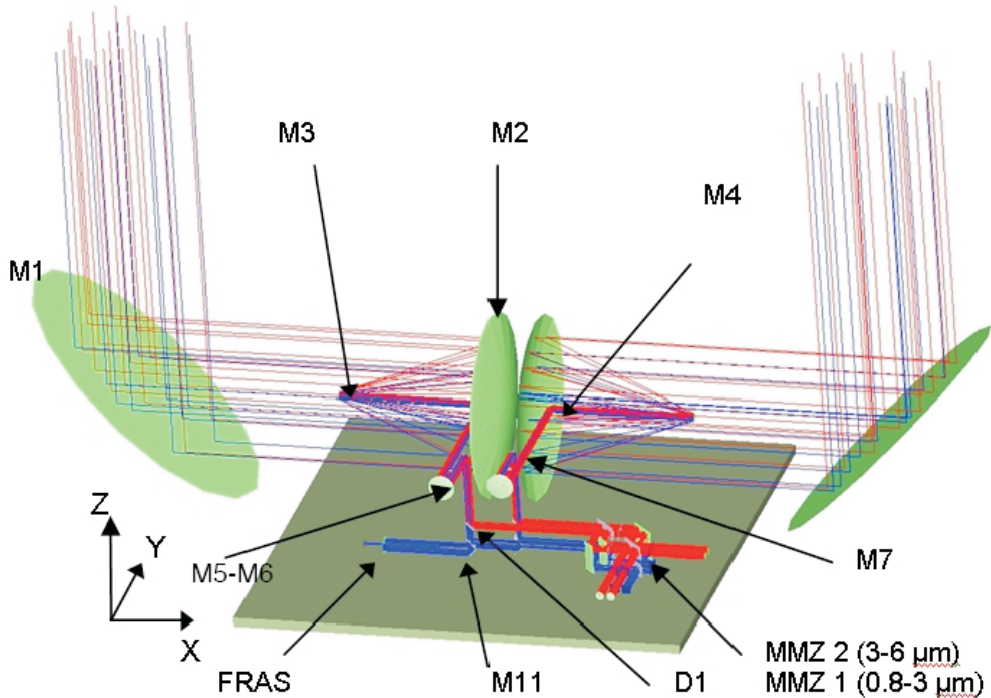


Figure 5.1: Optical layout of the PEGASE nulling interferometer (adapted from Le Duigou et al. 2006).

- Two achromatic π -phase shifters using field reversal by reflections (Serabyn 1999, M₄ and M₁).
- Two optical delay lines placed after the active mirrors to operate in a tip/tilt corrected optical space.
- Dichroic beam splitters which separate the signal between the science wave band and the tip-tilt/OPD sensing wave bands.
- A Modified Mach Zehnder (MMZ) to achieve the combination. Another MMZ might be necessary to cover the full wavelength range, depending on the coating feasibility.
- Small off axis parabolas focus the four outputs of the MMZ into single mode fibres. A fluoride glass fibre can cover the spectral range 1.5-3 μ m. A chalcogenide fibre is required for the spectral range 3-6 μ m.

5.2.2 The Fourier-Kelvin Stellar Interferometer (FKSI)

Resulting from several dedicated studies during the past few years, the FKSI design nowadays consists in two 0.5-m telescopes on a 12.5-m boom. The wavelength band used for science ranges between 3 and 8 μ m, which corresponds to an angular resolution ranging between about 25 and 66 mas (sufficient to probe the habitable zone of nearby stars, see Figure 5.2). The instrument is foreseen to be launched to L2 where it will be passively cooled down to 65 K. The field of regard is somewhat smaller than the one of PEGASE with possible angles of $\pm 20^\circ$ around the anti-solar direction (vs $\pm 30^\circ$ for PEGASE). This value depends on the size of the sunshields considered in the present design and could eventually be increased. The optical arrangement is similar to that of PEGASE and follows the description given in Section 5.2, with some differences explained hereafter. OPD stabilization is performed by a FSU using

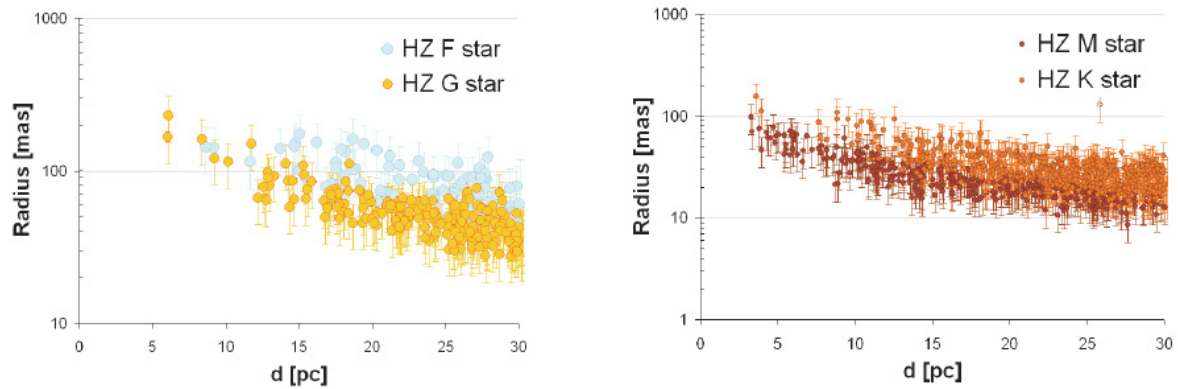


Figure 5.2: The extent of the Habitable Zone for the single main sequence stars (F,G stars on left panel, and M, K stars on right panel) within 30 pc from the Sun (Kaltenegger et al. 2008).

the observed central target in the 0.8-2.5 μm range and feeding an ODL. Unlike PEGASE, tip/tilt control is performed in the same wavelength range as the OPD control. After separation from the science signal with dichroic beam splitters, 80% of the light in the 0.8-2.5 μm range feeds the FSU and 20% the tip/tilt sensor. One hollow-glass fibre is used as modal filter in the 3.0-8.0 μm wavelength range at each of the two destructive outputs of a symmetric Mach Zehnder beam combiner (Barry et al. 2006). The fibre outputs are focused on the science detector, cooled down to a temperature of 35 K. Note that photonic crystal fibres are also considered and provide a promising solution for single mode propagation on a wider spectral band. The instrumental parameters of FKSI are listed in Table 5.1.

5.3 Main scientific objectives

With their high dynamic range, PEGASE and FKSI are particularly well suited to observe faint targets in the proximity of a bright source. They will focus on three main science goals for further study of utmost importance to the direct detection of extrasolar planets in the infrared, namely (1) survey prospective targets for future exo-Earth characterization missions for levels of exozodiacal dust, (2) detect and characterize the atmospheres of nearby extrasolar planets, including those currently known and those that may be discovered by this technique, and (3) measure resonant structures in exozodiacal discs, their flux levels, and the chemical evolution of the material they contain. The survey of brown dwarfs and active galactic nuclei (AGN) is also expected to be very fruitful. These objectives are briefly reviewed hereafter.

5.3.1 Circumstellar disc science

Protoplanetary discs

As discussed in Chapter 1, planets form in a protoplanetary disc well before the parent star reaches the main sequence. The probable migrations of the extrasolar planets from their birth places, probably external to the snow line towards the inner regions, produce wide gaps in the circumstellar discs. Hence, looking for gaps created by transiting planets inside the disc is very important to understand the formation of planetary systems and early dynamics of planets, including migration and orbital interactions. The gaps create a non-uniformity in the disc which can be detected by high accuracy visibility measurements. A Gap can particularly be observed in a bright protoplanetary disc, as it is the case

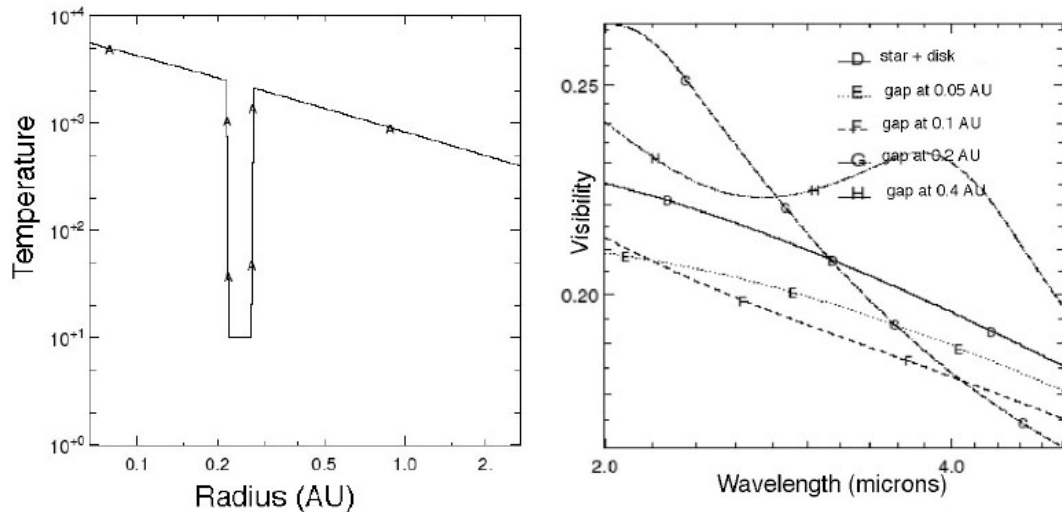


Figure 5.3: Variation of the measured fringe visibility as a function of the gap in a FU Ori disc. The gap is modelled by a break in the temperature distribution. The baseline is equal to 500 m (Herwats, in prep.).

for FU Ori objects¹⁷ due to the (see Figure 5.3). The gap is detected by an accurate measurement of the visibility function. Around Herbig Ae/Be stars, the transition between the photospheric emission of the star and the disc emission can be observed. This observation of the internal part of the disc where the dust grains sublimate (0.1 to 0.4 AU) is relevant to constrain models. Around T Tauri stars, it is possible to constrain the size of the magnetosphere of the star and to observe the inner part of the disc, allowing the study of matter transfer from the internal disc to the stellar surface.

Debris discs

The next step in understanding planetary formation is the study of debris discs. Infrared interferometry is a very appropriate tool as it can provide sub-AU spatial resolution and spatially separate the contribution of the warm dust from that of the stellar photosphere. Indeed, near-infrared (K-band) thermal emission at the $\sim 1\%$ photospheric level has already been isolated in the vicinity of several main sequence stars with ground-based interferometers (Absil et al. 2006b; Di Folco et al. 2007; Absil et al. 2008b; Akeson et al. 2009; Absil et al. 2009). Providing detectability for higher contrast environments (up to 10000:1) and at longer wavelengths, PEGASE/FKSI will be able to probe a much wider range of inner debris discs. Beyond the mere photometry of warm dust, an interferometer can provide very useful information about its spatial distribution. Most of the near-IR flux is expected to be emitted by a thin ring region whose radius corresponds to the sublimation limit of the dust. Measuring the sublimation radius strongly constrains the type of mineralogy of the grains. This, however, requires the capability to address arbitrarily any point in the (u,v) plane, a feature that distinguishes PEGASE from ground-based interferometers. In addition, the presence of planets in a circumstellar disc creates structures (not only gaps but also large scale structures) that can be detected with a high angular resolution, high dynamics instrument. Such observations of debris discs should provide useful information on the existence and major parameters of planets (e.g., mass, orbit, current location) as well as the location of planetesimal belts, comparable to the Kuiper belt.

¹⁷In stellar evolution, FU Ori objects are pre-main sequence stars which display an high accretion rate and an extreme change in magnitude and spectral type.

Exozodiacal light characterization in the context of future exo-Earth characterization missions

The study of the amount and distribution of exozodiacal dust around main sequence stars has a particular relevance in the context of future exo-Earth characterization missions. The emission of dust particles within the HZ around the target stars is a key parameter for the performance of a nulling interferometer, as it is likely to be the brightest component (after the star itself) of an extrasolar system. For example in the solar system, the zodiacal light is two orders of magnitude brighter than Earth at mid-infrared wavelengths. Warm exozodiacal cloud could thus become a dominant source of noise and hamper the detection of faint planets. Irregularities in the dust cloud (such as clumps) may also be confused with a planet. PEGASE and FKSI will have the capability of providing a statistically significant survey of the amount of exozodiacal dust in the HZ around nearby main sequence stars, and its prevalence as a function of other stellar characteristics (e.g., age, spectral type, metallicity, cold debris disc). It will be used to streamline the input source catalogue of future exo-Earth characterization missions (reducing the risk of observing sources for which exozodiacal light prevents Earth-like planet detection) and optimize the mission profile before the launch. The dust density tolerable around nearby main sequence stars for future life-searching nulling interferometry missions is discussed in more detail in Chapter 7.

5.3.2 Sub-stellar objects

Extrasolar planets

The main scientific goal of PEGASE/FKSI, which is also the main design driver, is to perform a spectroscopic characterization of extrasolar planets. With a minimum baseline length of 40 m, PEGASE could directly survey most hot Jupiter-like planets ($M \geq 0.2 M_J$) within 150 pc with a good signal-to-noise ratio (SNR) as well as several favourable hot Uranus-type planets ($0.04 M_J \leq M \leq 0.2 M_J$) with a final SNR ranging between 1 and 6 (Absil 2006). In particular, PEGASE will be able to perform spectroscopy for about 15% of the extrasolar planets known so far within 25 pc, including several planets outside the hot regime (further than 0.1 AU from the host star, Defrère et al. 2007). The working method of FKSI is slightly different from that of PEGASE. Due to its relatively small baseline length (12.5 m), FKSI uses a two-color method (based on the ratio of measurements at two wavelengths) to account for the fact that the planetary signal is likely to fall partly within the central dark fringe (Danchi et al. 2003). Using this method, an earlier version of FKSI would be able to detect at least 25 EGPs, obtain low resolution spectra of their atmosphere and make a precise determination of their orbital parameters (Barry et al. 2006). This previous version of FKSI presented an 8-m boom length, assumed 15 nm rms OPD errors and considered a sample of 140 known extrasolar planets. With the current version of FKSI, as discussed here (12.5-m boom length and \sim 2-nm OPD errors), and considering a much larger available sample of known extrasolar planets (\sim 350), this value should be of the order of 100. Work is in progress to determine how many known extrasolar planets can be characterized with FKSI, as well as the possibility of detecting super-Earths (i.e., \sim 10 M_\oplus). Further details about the capabilities for planet detection are given in Chapter 6.

Brown dwarfs

With moderate baseline lengths, PEGASE/FKSI could also be used to characterize the atmospheres of binary brown dwarf stars by using the nulling mode. Spectroscopic studies of brown dwarfs provide constraints on their surface temperature, radius and the composition of their atmosphere (especially for CH₄ and for the clouds). In addition, observing bounded brown dwarfs has the advantage of giving an accurate estimate of the mass of the companion (thanks to the observation of the companion trajectory and its likely adherence to Kepler's laws) and its age (thanks to the spectroscopic study of the parent

star), compared to free floating objects where these parameters have to be estimated using theoretical models. PEGASE/FKSI would provide the required angular resolution and dynamic range to study bounded brown dwarfs (the contrast between a Sun-like star and a brown dwarf typically ranges between 10^3 and 10^5 for a 1 Gyr-old system). Furthermore, the study of brown dwarfs of various ages will help to constrain evolutionary models of these objects.

5.3.3 Additional programmes

The scientific programmes using the constructive visibility mode have to take into account the instrumental characteristics of PEGASE/FKSI and the main operational constraints. The targets of PEGASE/FKSI are compact sources for which emission peaks in the $1.5\text{-}8\,\mu\text{m}$ spectral range, corresponding to a temperature range from 500 to 3000 K (maximum of the black body emission). In that spectral range, PEGASE/FKSI will get the sensitivity of ISO but with an angular resolution 80 to 1000 times higher for PEGASE (about 0.5 mas, thanks to baseline from 40 to 500 m) and 5 to 20 times higher for FKSI (about 25 mas due to the interferometric baseline of 12.5 m). As a two telescope interferometer, PEGASE/FKSI will not be able to spend a lot of time on imaging complex sources. The astrophysical targets have to be easily characterized by simple models, symmetrical (uniform or Gaussian) or not (binaries). The great advantage of PEGASE/FKSI with respect to other interferometers will be their ability to observe continuously with a stable configuration during a time exceeding the classical 24 hour cycle. The following programs might take advantage of this situation to propose unique science that can be done with PEGASE/FKSI in the future: (1) active galactic nuclei (AGN), (2) resolving images of quasars split by gravitational lens effects, (3) temporal characterization of different classes of rapid radial pulsators, (4) disc formation and evolution of active hot stars.

5.4 Performance for exozodiacal disc detection

In order to assess the performance of PEGASE/FKSI for exozodiacal disc detection, the GENIESim software¹⁸ (Absil et al. 2006b) has been adapted to enable the simulation of a space-based nulling interferometer. In particular, the expected vibrations of the telescopes along the optical path in the ambient space environment have been implemented and all atmospheric effects discarded. The space environment is now fully integrated in GENIESim and space-based nulling interferometers can be simulated by switching the appropriate keywords. After briefly describing the GENIESim software, the modifications necessary to simulate space-based instruments are discussed in Section 5.4.2.

5.4.1 The GENIESim software

GENIESim is an IDL-written code which has originally been designed to simulate the GENIE instrument at the VLTI interferometer (see Section 4.5.1). It has the advantage to benefit from extensive validation efforts by cross-checking with performance estimates carried out by industrial partners during the GENIE phase A study. GENIESim performs end-to-end simulations of ground-based nulling interferometers which include the simulation of astronomical sources (star, circumstellar disc, planets and background emission), atmospheric turbulence (piston, longitudinal dispersion, wavefront errors and scintillation), as well as a realistic implementation of closed-loop compensation of atmospheric effects by means of fringe tracking and wavefront correction systems. It has been thoroughly described elsewhere (see Absil 2003), so that we only give here some important principles of the code for a better understanding of this dissertation.

¹⁸GENIESim is available on request from Olivier Absil (absil@astro.ulg.ac.be).

On input of GENIESim, two text files are required to define the instrument and the science target. These two files contain 170 global parameters which can be classified as:

- The operational parameters, detailing the configuration, the control loops, the atmosphere and the VLTI environment;
- The observational parameters, specifying the target system and relevant observational parameters.

In addition to these two input files, GENIESim is controlled by a set of keyword switches, by which GENIESim is told what are the names of the output files, what atmospheric effects and control loops to take into account in the computation. In the last release of GENIESim, the simulation of a nulling instrument at Cerro Paranal (Chile), Dome C (Antarctica) or located in space can be performed. ALADDIN, PEGASE and FKSI keywords are available for a direct simulation of these instruments.

Based on these inputs, GENIESim produces an instantaneous transmission map of the nulling interferometer (see Eq. 4.3), taking into account all perturbations related to the instrument and its environment. This map is projected on the plane of the sky in order to compute the transmitted flux from all astrophysical sources located within the field-of-view of the instrument. Each individual source is affected by the transmission map differently:

- The residual stellar emission at the destructive output of the instrument is computed in a semi-analytical way by 2D numerical integration. This process gives a very accurate stellar leakage estimate.
- The contribution of the exozodiacal disc is computed by multiplying a disc image, sampled over the field-of-view by a $n \times n$ pixel grid, by a digitised transmission map of the same size. The disc image can be computed with three different packages, depending on the target (optically thin disc, optically thick or the solar zodiacal disc seen from outside the solar system). The size of the image is generally 128×128 pixels but special attention has to be payed for configurations for which the “telescope diameter/baseline length” ratio is low. In this case, the field-of-view is relatively large and it can be necessary to increase the number of pixels in order to avoid undersampling problems, especially when the baseline length is long.
- Potential planets are considered as point-like sources, and are thus only affected by the value of the transmission map at the position of their centre.
- The background emission is assumed to be perfectly incoherent so that the resulting signal can be computed by a simple integration over the field-of-view.

Taking into account all the sources in the field-of-view, GENIESim simulates an observational run by a number of Observation Blocks (OB), which have a duration of typically 10 to 100 seconds. For each OB, the simulator generates time sequences for the random variables, based on their input power spectral densities and on the transfer functions of the control loops. The initialisation of control loops is one of the first actions performed in the time loop on OBs. The coupling efficiency is also computed in real-time as it is affected by random perturbations as well. Finally, the output of the simulator basically consists in time series of photo-electrons recorded by the detector at the two outputs of the nulling combiner (constructive and destructive outputs) as a function of time and wavelength. The overall architecture of the GENIESim software is represented in Figure 5.4.

5.4.2 Vibrations in the ambient space environment

To enable the simulation of a space-based nulling interferometer, only a few modifications were necessary thanks to the versatility of GENIEsim. Discarding all atmospheric effects and the VLTI environment is easily achieved by setting the appropriate keywords. The main modification was to introduce the random sequences of OPD and tip/tilt generated by the vibrations of the telescopes in the ambient space environment.

The vibrations of the spacecraft are a critical issue for nulling interferometry because they induce mismatches in the optical paths and pointing errors which give rise to instability noise (Lay 2004). These vibrations are caused by disturbance forces which can be either internal (due to on-board systems) or external (caused by the ambient space environment). For PEGASE, the internal disturbance forces arise mainly from the thrusters, the Optical Delay Line (ODL), the steering mirrors, and the reaction wheels. The requirements on these on-board systems have been assessed recently by two R&D studies (Villien et al. 2007). The external disturbance forces are mainly caused by particulate impacts, solar radiation pressure and charging effects but these effects are not expected to be dominant at the L2 point. To derive the perturbations in OPD and tip/tilt acting on the spacecraft, two approaches have been considered in this study. The first approach was based on analytical models and is described hereafter. The second approach was based on a R&D study carried out by EADS Astrium and is briefly addressed here with more details given in Section 5.4.4.

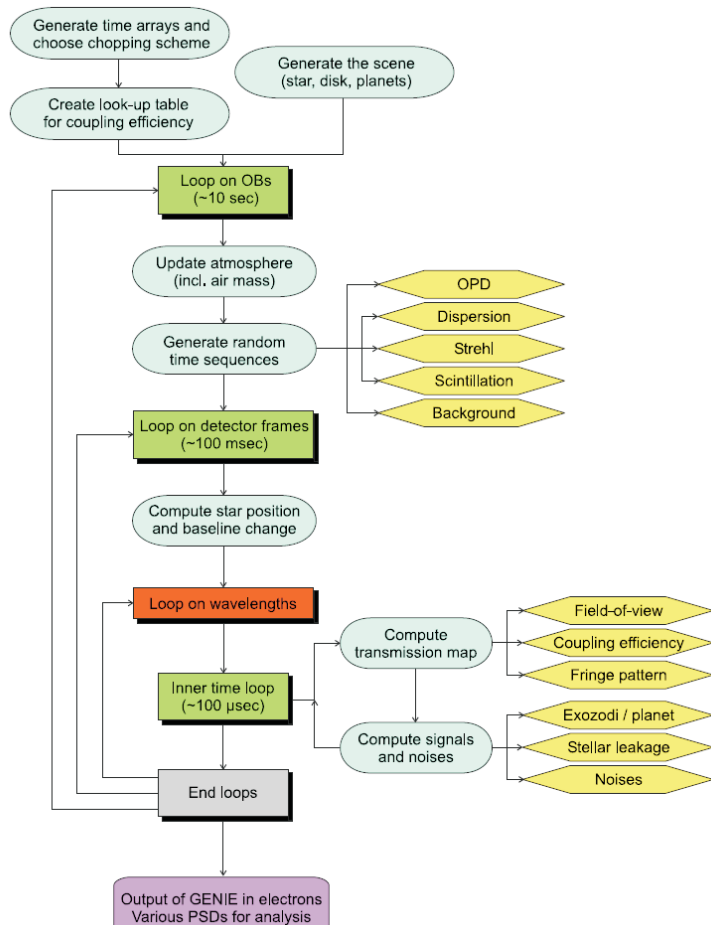


Figure 5.4: Block diagram showing the top-level architecture of the GENIEsim software (Figure from Absil 2006).

First approach

A recent comparative study concludes that the ambient space environment causes OPD no larger than the disturbances induced by on-board equipments for DARWIN/TFP, and its precursor missions (Sterken 2005). The total disturbance force can be related to the induced vibrations from the basic equation of the rigid body motion:

$$S_{\text{vib}} = \frac{1}{16\pi^4 m^2 f^4} S_{\text{in}}, \quad (5.1)$$

where m is the mass of the spacecraft, f the frequency, S_{in} the Power Spectral Density (PSD) of the total disturbance force in N^2/Hz and S_{vib} the PSD of the spacecraft displacement in m^2/Hz . Assessing the shape and magnitude of the input disturbance PSD requires a specific R&D study and is beyond the scope of this dissertation. Following the results about the DARWIN mission (Sterken et al. 2005), we will assume that the global disturbance force is distributed as white noise, so that the PSD of the spacecraft displacement (S_{out}) decays linearly with a slope of -40 dB/dec. The relative displacement induced by internal disturbances (rms_{vib}) should not exceed 1 μm rms as indicated by the PEGASE phase 0 study performed by CNES in 2005. Based on this value, the PSD of the spacecraft tip-tilt before correction (rms_{tt}) can be computed as:

$$\text{rms}_{\text{tt}} = \frac{M}{R} \text{rms}_{\text{vib}}, \quad (5.2)$$

where M is the magnification factor (20 according to the phase 0 study) and R the telescope radius. This gives a rms tip-tilt error of about 35" rms. This value does not take into account an additional noise of $10 \text{ mas}/\sqrt{(\text{Hz})}$ per tip-tilt mirror which has been considered separately in GENIESim as an actuator noise. Finally, one should note that the frequencies at which resonances are present should cause additional peaks in the input vibrations (for instance, due to the sun-shields) but these frequencies have not been considered since they are not yet well defined. Their impact on the residual OPD could however be minimised by the use of an appropriate filtering.

Second approach

An R&D study carried out by EADS Astrium in 2007 in collaboration with CNES has identified the two main sources of perturbations: torque noise and micro-vibrations, both at the reaction wheel level (Villien et al. 2007). The torque noise corresponds to the perturbations around the wheel rotation axis. It is due to the wheel electronics noise, the wheel controller loop, the friction torque and the motor defect. Microvibrations are due to the wheel mechanical defects such as rotor imbalance and ball bearing imperfections. They correspond to harmonic perturbations, which are function of the wheel velocity and generate both torques and forces disturbance. For FKSI, the reaction wheels are also expected to be the main contributor to the vibrational level (Hyde et al. 2004). Another contribution comes from boom deflections induced by thermal changes and producing low frequency OPD. The worst case occurs at the boom resonant frequency which results in a sine wave with an amplitude of 2.4 nm at 5 Hz for the OPD perturbation and a sine wave of 0.2 mas at 5 Hz for the tip/tilt perturbation. The PSDs defined by Astrium and CNES are presented in Section 5.4.4.

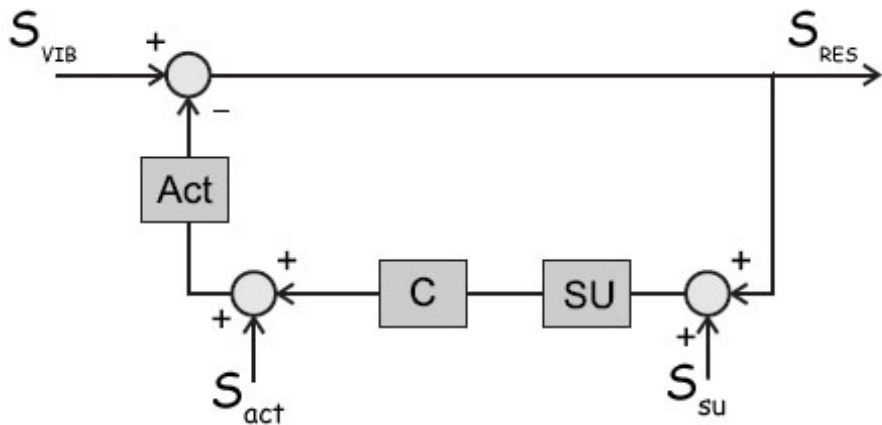


Figure 5.5: Simplified block-diagram of a fringe tracking system (adapted from Absil 2006).

5.4.3 Real-time correction of spacecraft vibrations

As indicated in the previous Section, the level of OPD would be of the order of $1 \mu\text{m}$ rms without an appropriate control loop. This is harmful for exozodiacal disc detection so that a fringe tracker is mandatory to stabilize the OPD to a sufficiently low value. In GENIEsim, the simulation of the control loop is achieved by a simultaneous optimisation of the repetition frequency and of the controller parameters (a simple PID¹⁹). The procedure is based on a description of spacecraft vibrations in terms of its temporal PSD, while the action of control loops is expressed by means of transfer functions in the frequency domain. The general architecture of real-time control loops is illustrated in Figure 5.5. The three main components of the loop are the sensing unit (SU), which provides an estimation of the perturbations to be corrected for (e.g., OPD difference for a fringe tracking loop), the controller (C), which computes the correction applied to cancel the perturbation, and the actuator (Act), which performs the correction (e.g., an optical delay line). Both sensor and actuator produce additional noise in the control process, modelled by their PSDs (S_{su} and S_{act}), which is applied at the input of the associated block. Sensor noise (S_{su}) depends on the number of available photons in each elementary measurement (shot noise and detector noise), while actuator noise (S_{act}) depends on the particular design of the actuator. The input and residual vibrations are described by their PSDs (S_{vib} and S_{res}).

5.4.4 Paper: Nulling interferometry: performance comparison between space and ground-based sites for exozodiacal disc detection

The following article (Defrère et al. 2008) presents a thorough performance comparison between space- and ground-based nulling interferometers for exozodiacal disc detection. Besides their main scientific goal (characterizing hot giant extrasolar planets), the space-based nulling interferometers PEGASE and FKSI would be very efficient to assess the level of circumstellar dust in the habitable zone around nearby main sequence stars down to the density of the solar zodiacal cloud (and thereby outperform any ground-based instrument). These space-based interferometers are complementary to ALADDIN in terms of sky coverage and would be ideal instruments to prepare future life-finding space missions.

¹⁹PID stands for “Proportional, Integral and Differential” which is a basic controller device for closed-loop control

Nulling interferometry: performance comparison between space and ground-based sites for exozodiacal disc detection

D. Defrère¹, O. Absil^{2,*}, V. Coudé du Foresto³, W. C. Danchi⁴, and R. den Hartog⁵

¹ Institut d’Astrophysique et de Géophysique, Université de Liège, 17 Allée du Six Août, 4000 Liège, Belgium
e-mail: defrere@astro.ulg.ac.be

² LAOG-UMR 5571, CNRS and Université Joseph Fourier, BP 53, 38041 Grenoble, France

³ LESIA, Observatoire de Paris-Meudon, CNRS, 5 place Jules Janssen, 92195 Meudon, France

⁴ NASA Goddard Space Flight Center, 8800, Greenbelt Road, Greenbelt, MD 20771, USA

⁵ Science Payloads and Advanced Concepts Office, ESA/ESTEC, postbus 299, 2200 AG Noordwijk, The Netherlands

Received 22 May 2008 / Accepted 11 August 2008

ABSTRACT

Context. Characterising the circumstellar dust around nearby main sequence stars is a necessary step in understanding the planetary formation process and is crucial for future life-finding space missions such as ESA’s DARWIN or NASA’s terrestrial planet finder (TPF). Besides paving the technological way to DARWIN/TPF, the space-based infrared interferometers PEGASE and FKSI (Fourier-Kelvin Stellar Interferometer) will be valuable scientific precursors.

Aims. We investigate the performance of PEGASE and FKSI for exozodiacal disc detection and compare the results with ground-based nulling interferometers.

Methods. We used the GENIESim software (Absil et al. 2006, A&A, 448, 787) which was designed and validated to study the performance of ground-based nulling interferometers. The software has been adapted to simulate the performance of space-based nulling interferometers by disabling all atmospheric effects and by thoroughly implementing the perturbations induced by payload vibrations in the ambient space environment.

Results. Despite using relatively small telescopes (≤ 0.5 m), PEGASE and FKSI are very efficient for exozodiacal disc detection. They are capable of detecting exozodiacal discs 5 and 1 time respectively, as dense as the solar zodiacal cloud, and they outperform any ground-based instrument. Unlike PEGASE, FKSI can achieve this sensitivity for most targets of the DARWIN/TPF catalogue thanks to an appropriate combination of baseline length and observing wavelength. The sensitivity of PEGASE could, however, be significantly boosted by considering a shorter interferometric baseline length.

Conclusions. Besides their main scientific goal (characterising hot giant extrasolar planets), the space-based nulling interferometers PEGASE and FKSI will be very efficient in assessing within a few minutes the level of circumstellar dust in the habitable zone around nearby main sequence stars down to the density of the solar zodiacal cloud. These space-based interferometers would be complementary to Antarctica-based instruments in terms of sky coverage and would be ideal instruments for preparing future life-finding space missions.

Key words. instrumentation: high angular resolution – techniques: interferometric – circumstellar matter

1. Introduction

Nulling interferometry is the core technique of future life-finding space missions such as ESA’s DARWIN (Fridlund et al. 2006) and NASA’s Terrestrial Planet Finder Interferometer (TPF-I, Beichman et al. 2006a). Observing in the mid-infrared (6–20 μ m), these missions would enable the spectroscopic characterisation of the atmosphere of habitable extrasolar planets orbiting nearby main sequence stars. This ability to study habitable distant planets strongly depends on the density of exozodiacal dust in the inner part of circumstellar discs, where the planets are supposed to be located. In particular, the detection of habitable terrestrial planets would be seriously hampered for stars presenting warm (~ 300 K) exozodiacal dust more than 10 to 100 times as dense as our solar zodiacal disc, depending on stellar type, stellar distance and telescope diameter (Beichman et al. 2006b; Defrère et al. 2008). Assessing the level of circumstellar dust around nearby main sequence stars is therefore a necessary pre-requisite for preparing the observing

programme of DARWIN/TPF by reducing the risk of wasting time on sources for which exozodiacal light prevents Earth-like planet detection. In addition, the existence of planets is intrinsically linked to circumstellar discs and observing them provides an efficient way to study the formation, evolution and dynamics of planetary systems. At young ages, essentially all stars are surrounded by protoplanetary discs in which the planetary systems are believed to form (Meyer et al. 2008). In particular, the detection of gaps in these protoplanetary discs is very important for understanding the early dynamics of planets, including migration and orbital interaction. At older ages, photometric surveys primarily with IRAS, ISO, and Spitzer have revealed the presence of micron-sized grains around a large number of main sequence stars (see e.g., Trilling et al. 2008; Hillenbrand et al. 2008). This is interpreted as the sign of planetary activity, as the production of grains is believed (by analogy with the zodiacal cloud in our solar system) to be sustained by asteroid collisions and outgassing of comets in the first tens of astronomical units (AU). However, the presence of warm dust can generally not be unequivocally determined because the typical

* Marie Curie EIF Postdoctoral Fellow.

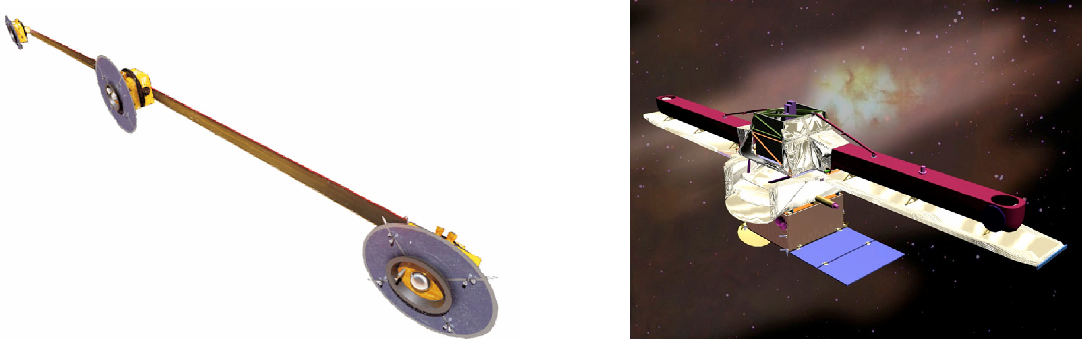


Fig. 1. *Left:* overview of the PEGASE space-based interferometer. Two 0.4-m siderostats are flying in a linear configuration with the beam combiner spacecraft located in the middle of the formation. *Right:* representation of FKSI, showing the two 0.5-m siderostats located on a 12.5-m boom.

accuracy on both near-infrared photometric measurements and photospheric flux estimations is a few percent at best, limiting the sensitivity to typically 1000 times the density of our solar zodiacal cloud (Beichman et al. 2006c). Photometric measurements are therefore generally not sufficient to probe the innermost regions of the discs and interferometry is required to separate the starlight from the disc emission. Good examples are given by the detection of hot dust (~ 1500 K) around Vega and τ Cet with near-infrared interferometry at the CHARA array (Absil et al. 2006b; Di Folco et al. 2007). Nulling interferometry is a quite new technique even though it was initially proposed in 1978 (Bracewell 1978). Several scientific observations using this technique have recently been carried out with the Bracewell Infrared Nulling Cryostat (BLINC, Hinz et al. 2000) instrument at the Multi-Mirror Telescope (MMT, Mount Hopkins, Arizona), with the Keck Interferometer Nuller (KIN, Hawaii, Serabyn et al. 2006; Barry et al. 2008; Serabyn 2008), and are foreseen to begin in 2010 at the Large Binocular Telescope (Mount Graham, Arizona, Hinz et al. 2008). In Europe, ESA has initiated the study of a ground-based demonstrator for DARWIN, the Ground-based European Nulling Interferometer Experiment (GENIE, Gondoin et al. 2004). GENIE is a nulling interferometer conceived as a focal instrument for the VLTI which has been studied by ESA at the phase A level. Another European project is ALADDIN (Antarctic L-band Astrophysics Discovery Demonstrator for Interferometric Nulling, Coudé du Foresto et al. 2006), a nulling interferometer project for Dome C, on the high Antarctic plateau. The performance of GENIE has been studied in detail (Absil et al. 2006a; Wallner et al. 2006) and recently compared to that of ALADDIN (Absil et al. 2007). Using 1-m collectors, ALADDIN would have an improved sensitivity with respect to GENIE working on 8-m telescopes, provided that it is placed above the turbulence boundary layer (about 30 m at Dome C). Circumstellar discs 30 times as dense as our local zodiacal cloud could be detected by ALADDIN around typical DARWIN/TPF targets in an integration time of few hours.

The low atmospheric turbulence on the high Antarctic plateau is a significant advantage with respect to other astronomical sites and one of the main reasons for the very good sensitivity of ALADDIN. However, as for any other ground-based site, the atmosphere effects (turbulence and thermal background) are still major limitations to the performance and active compensation by real-time control systems are mandatory. Observing from space would provide an efficient solution to improve the sensitivity by getting rid of the harmful effect of the atmosphere. Two infrared nulling interferometers could achieve the detection

of circumstellar dust discs from space (see Fig. 1): PEGASE, a two-telescope interferometer based on three free-flying spacecraft (Le Duigou et al. 2006) and the Fourier-Kelvin Stellar interferometer (FKSI), a structurally-connected interferometer also composed of two telescopes (Danchi et al. 2006). These two missions have been initially designed to study hot extrasolar giant planets at high angular resolution in the near- to mid-infrared regime (respectively $1.5\text{--}6.0\,\mu\text{m}$ and $3.0\text{--}8.0\,\mu\text{m}$). Besides their main scientific goal, they could also be particularly well suited for the detection of warm circumstellar dust in the habitable zone around nearby main sequence stars. The objective would be to provide a statistically significant survey of the amount of exozodiacal light in the habitable zone around the DARWIN/TPF targets, and its prevalence as a function of other stellar characteristics (age, spectral type, metallicity, presence of a cold debris disc, etc.). Following our performance studies of ground-based instruments such as GENIE at Cerro Paranal (Absil et al. 2006a, hereafter Paper I) or ALADDIN on the high Antarctic plateau (Absil et al. 2007, hereafter Paper II), the present study addresses the performance of space-based nulling instruments for exozodiacal disc detection. We have limited our comparison to instruments working at similar wavelengths (ranging from 2 to $8\,\mu\text{m}$), and purposely discarded ground-based instruments working in the N -band such as the KIN and the LBTI. The ultimate performance of these two mid-infrared instruments essentially depends on the spatial and temporal fluctuations of the sky and instrumental thermal backgrounds, which are very difficult to model with a sufficient accuracy for our comparative study.

2. PEGASE and FKSI overview

PEGASE and FKSI are space-based Bracewell interferometers, conceived as scientific and technological precursors to DARWIN/TPF. They present similar architectures, the main difference being that the two telescopes of PEGASE are free-flying while those of FKSI are arranged on a single boom. PEGASE was initially proposed in the framework of the 2004 call for ideas by the French space agency (CNES) for its formation flying demonstrator mission. CNES performed a Phase 0 study in 2005 and concluded that the mission is feasible within an 8 to 9 years development plan (Le Duigou et al. 2006). However, the mission was not selected for budgetary reasons. On the US side, FKSI has been initially studied by the Goddard Space Flight Center in preparation for submission as a Discovery-class mission. Several concepts have been considered and the mission was studied to

the phase A level based on the two-telescope design described here.

2.1. Scientific objectives

The main scientific goal of PEGASE and FKSI is to perform the spectroscopy of hot extrasolar giant planets (EGP). With a minimum baseline length of 40 m, PEGASE could directly survey most hot Jupiter-like planets ($M \geq 0.2 M_{\text{Jup}}$) within 150 pc with a good signal-to-noise ratio (S/N) as well as several favourable hot Uranus-type planets ($0.04 M_{\text{Jup}} \leq M \leq 0.2 M_{\text{Jup}}$) with a final S/N ranging between 1 and 6 (Absil 2006). In particular, PEGASE will be able to perform spectroscopy on about 15% of the extrasolar planets known so far within 25 pc, including several planets outside the hot regime (further than 0.1 AU from the host star, Defrère et al. 2007). The working method of FKSI is slightly different from that of PEGASE. Due to its relatively short baseline length (12.5 m), FKSI uses a two-color method (based on the ratio of measurements at two wavelengths) to account for the fact that the planetary signal is likely to fall partly within the central dark fringe (Danchi et al. 2003). Using this method, an earlier version of FKSI was estimated to be able to detect at least 25 EGPs, obtain low resolution spectra of their atmosphere and make precise determination of their orbital parameters (Barry et al. 2006). This previous version of FKSI presented an 8-m boom, assumed 15 nm rms residual OPD error and considered a sample of 140 known extrasolar planets. With the current version of FKSI, as discussed in this paper (12.5-m boom length and 2-nm rms residual OPD errors), and considering a much larger available sample of known extrasolar planets (~ 250), this value should be of the order of 75–100. Work is in progress to determine how many known extrasolar planets can be detected with FKSI, as well as the possibility of detecting super-Earths.

The detection and characterisation of circumstellar discs are also in the core programmes of these two missions but the performance has not yet been carefully assessed. PEGASE and FKSI are expected to be able to provide an accurate estimate of the dust density from the very neighbourhood of the star up to several AUs. They will also help providing maps of the mineralogical composition, with a combination of spectral and spatial information on the discs. Combined with sub-mm observations from the ground providing the gas distribution with a comparable spatial resolution, it will then become possible to study the dust-gas interactions in young systems. Additional programmes on brown dwarfs and active galactic nuclei are also foreseen, but only the primary objective (the study of hot EGPs) drives the design of the instruments.

2.2. The PEGASE instrumental concept

Following the phase 0 study, the baseline configuration of PEGASE consists in a two-aperture near-infrared (1.5–6 μm) interferometer formed of three free flying spacecraft planned to orbit at the Lagrange point L2, where the spacecraft and the focal plane assembly can be passively cooled down to respectively 90 K and 55 K. In its nominal configuration, PEGASE consists in two 40 cm siderostats and a beam combiner flying in linear formation. Visibility measurements and recombination in nulling mode (Bracewell interferometer) are both possible with a spectral resolution of about 60. The interferometric baseline length ranges between 40 m and 500 m giving an angular resolution in the range of 0.5–30 mas. Shorter baseline lengths are not allowed due to the free-flying collision avoidance distance of 20 m. The

Table 1. Instrumental parameters of PEGASE and FKSI considered in this study.

Instrumental parameters	PEGASE	FKSI
Baselines [m]	40–500	12.5
Telescope diameter [m]	0.40	0.50
Field of regard	$\pm 30^\circ$	$\pm 20^\circ$
Optics temperature [K]	90	65
Detector temperature [K]	55	35
Science waveband [μm]	1.5–6.0	3.0–8.0
Spectral resolution	60	20
Fringe sensing waveband [μm]	0.8–1.5	0.8–2.5 (80%)
Tip-tilt sensing waveband [μm]	0.6–0.8	0.8–2.5 (20%)

fine-tuning of the optical path difference (OPD) is performed by a dedicated control loop based on a fringe sensing unit (FSU) using the observed central target in the 0.8–1.5 μm range and an optical delay line (ODL). Intensity control is performed by a fine pointing loop using a field relative angle sensor (FRAS) operating in the 0.6–0.8 μm range and fast steering mirrors based on piezoelectric devices. The instrumental parameters of PEGASE are summarized in Table 1. The optical system architecture is represented by the block diagram in Fig. 2 with the following elements on the optical path:

- two afocal telescopes with an optical magnification which will result from a trade-off between the dynamics of the tip-tilt errors, the available stroke of the fast steering mirrors, the actuation noise, the mechanical constraints and the polarization limitations. A magnification of the order of 20 is considered in the present design;
- two fast steering mirrors to correct the tip-tilt errors. They are placed as close as possible to the afocal telescopes in order to minimize the optical path where the tip-tilt errors are not corrected, and hence reduce differential polarisation effects;
- the achromatic π phase-shift is achieved geometrically, by means of opposite periscopes producing field reversal by reflections (Serabyn 1999);
- two optical delay lines placed after the active mirrors to operate in a tip/tilt corrected optical space;
- dichroic beam splitters which separate the signal between the science wave band and the tip-tilt/OPD sensing wave bands;
- a Modified Mach Zehnder (MMZ, Serabyn & Colavita 2001) to perform beam combination. A second MMZ might be necessary to cover the full wavelength range, depending on the coatings;
- small off axis parabolas to focus the four outputs of the MMZ into single mode fibres. A fluoride glass fibre can cover the spectral range 1.5–3 μm . A chalcogenide fibre is required for the spectral range 3–6 μm ;
- a detection assembly controlled at a temperature of 55 K and connected to the fibres.

2.3. The FKSI instrumental concept

Resulting from several dedicated studies in the past few years, the FKSI design nowadays consists in two 0.5-m telescopes on a 12.5-m boom. The wavelength band used for science ranges from 3 to 8 μm , which gives an angular resolution between about 25 and 66 mas. The instrument is foreseen to be launched to L2 where it will be passively cooled down to 65 K. The field of regard is somewhat smaller than the one of PEGASE with possible angles of $\pm 20^\circ$ around the anti-solar direction (vs. $\pm 30^\circ$ for

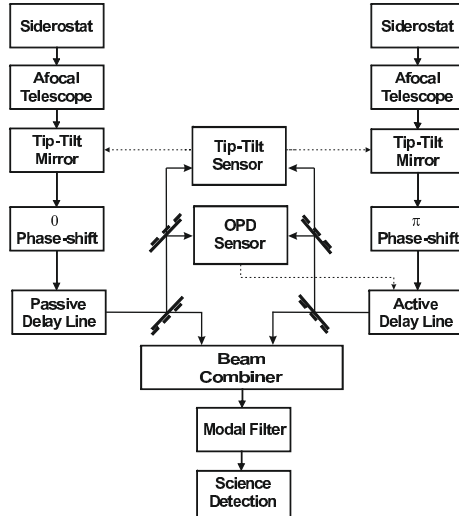


Fig. 2. Block diagram of the PEGASE/FKSI optical layout. Feed-back signals driving the tip-tilt/OPD control are represented by dashed lines.

PEGASE). This value depends on the size of the sunshields considered in the present design and could eventually be increased. The optical arrangement is similar to that of PEGASE and follows the description given in Sect. 2.2, with some differences explained hereafter (see also Fig. 2). OPD stabilization is performed by a FSU using the observed central target in the 0.8–2.5 μm range and feeding an ODL. Unlike PEGASE, tip/tilt control is performed in the same wavelength range as the OPD control. After separation from the science signal with dichroic beam splitters, 80% of the light in the 0.8–2.5 μm range feeds the FSU and 20% the tip/tilt sensor. One hollow-glass fibre is used as modal filter in the 3.0–8.0 μm wavelength range at each of the two destructive outputs of a symmetric Mach Zehnder beam combiner (Barry et al. 2006). The fibres outputs are focused on the science detector, cooled down to a temperature of 35 K. Note that photonic crystal fibres are also considered and are a promising solution for single mode propagation on a wider spectral band. The instrumental parameters of FKSI are listed in Table 1.

3. Nulling performance in space

In order to assess the performance of PEGASE and FKSI for exozodiacal disc detection, the GENIE simulation software (GENIESim, see Paper I) has been used. GENIESim has originally been designed to simulate the GENIE instrument at the VLTI interferometer and has been extensively validated by cross-checking with performance estimates done by industrial partners during the GENIE phase A study. GENIESim performs end-to-end simulations of ground-based nulling interferometers, including the simulation of astronomical sources (star, circumstellar disc, planets, background emission), atmospheric turbulence (piston, longitudinal dispersion, wavefront errors, scintillation), as well as a realistic implementation of closed-loop compensation of atmospheric effects by means of fringe tracking and wavefront correction systems. The output of the simulator basically consists in time series of photo-electrons recorded by the detector at the constructive and destructive outputs of the nulling combiner. To enable the simulation of a space-based nulling interferometer, few modifications were necessary

due to the versatility of GENIESim. Beside disabling all atmospheric effects, the main modification was to introduce the random sequences of OPD and tip/tilt generated by the vibrations of the telescopes in the ambient space environment. This is discussed in the following section.

3.1. Vibrations in space environment

Spacecraft vibrations are critical in nulling interferometry because they induce fluctuations in the differential optical paths and pointing errors, which both give rise to stochastic stellar leakage in the destructive output. These vibrations are caused by disturbance forces which can be either internal (due to on-board systems) or external (caused by the ambient space environment). Internal disturbance forces arise mainly from the thrusters, the optical delay line (ODL), the steering mirrors, the reaction wheels and the boom in the case of structurally connected telescopes. The external disturbance forces are mainly caused by particulate impacts, solar radiation pressure and charging effects but all these effects are not expected to be dominant at the L2 point. A recent comparative study concludes that the ambient space environment causes OPD errors no larger than the disturbances induced by on-board equipment for DARWIN and its precursor missions (Sterken 2005).

In the case of PEGASE, an R&D study carried out by EADS-Astrium in collaboration with CNES (Villien et al. 2007) has identified the two main sources of perturbations: torque noise and micro-vibrations, both at the reaction wheel level. The torque noise corresponds to the perturbations around the wheel rotation axis. It is due to the wheel electronics noise, the wheel controller loop, the friction torque and the motor defect. Micro-vibrations are due to the wheel mechanical defects such as rotor imbalance and ball bearing imperfections. They correspond to harmonic perturbations, function of the wheel velocity and generate both torques and forces disturbances. In the present architecture, the observation is considered to be divided into a succession of 100-s phases of science and control: pulse control phases of 100 s interrupt the science observation during which the constellation is free flying (so that there is no thruster noise during this phase). The power spectral densities (PSD) defined by Astrium and CNES during the R&D study for OPD and tip/tilt have been implemented in GENIESim. The PSD of the OPD in m^2/Hz is represented in Fig. 3 by the solid curve labelled “VIB_{IN}” and defines the vibrational level at the input of the FSU (about 0.18 μm rms). This PSD corresponds to a wheel rotation frequency of 1 Hz, with flexible modes at 20 Hz (due to the sunshield) and 40 Hz (due to the platform structure). Increasing the rotation frequency of the wheel could reduce the torque noise but at the expense of micro-vibrations. The shape of the tip/tilt PSD is similar to that of OPD with a value of about 3.5 rms at the input of the tip/tilt sensor.

For FKSI, the reaction wheels are also expected to be the main contributor to the vibrational level (Hyde et al. 2004). Another contribution comes from boom deflections induced by thermal changes and producing low frequency OPD. The worst case occurs at the boom resonant frequency which results in a sine wave with an amplitude of 2.4 nm at 5 Hz for the OPD perturbation and a sine wave of 0.2 mas at 5 Hz for the tip/tilt perturbation (Tupper Hyde, private communication). Assuming that FKSI will use the same wheels as PEGASE, we can in good approximation use the PSD defined for PEGASE, to which we add the resonant boom contribution at 5 Hz.

Table 2. Control loop performance and optimum repetition frequencies computed on a 100 s observation sequence for a Sun-like G2V star located at 20 pc. The total null is the mean nulling ratio including both the geometric and instrumental leakage contributions. The rms null is the standard deviation of the instrumental nulling ratio for this 100 s sequence. The goal performance for exozodiacal disc detection discussed in Paper I appears in the last column.

	GENIE-UT	ALADDIN	PEGASE	FKSI	Goal
Piston	6.2 nm @ 13 kHz	10 nm @ 2 kHz	1.7 nm @ 60 Hz	2 nm @ 65 Hz	<4nm
Inter-band disp.	4.4 nm @ 300 Hz	7.0 nm @ 0 kHz	0 nm @ 0 kHz	0 nm @ 0 kHz	<4nm
Intra-band disp.	1.0 nm @ 300 Hz	7.4 nm @ 0 Hz	0 nm @ 0 kHz	0 nm @ 0 kHz	<4nm
Tip-tilt	11 mas @ 1 kHz	7 mas @ 1 kHz	15 mas @ 85 Hz	20 mas @ 60 Hz	(see intensity)
Intensity mismatch	4% @ 1 kHz	1.2% @ 0 Hz	0.02% @ 0 kHz	0.04% @ 0 Hz	<1%
Total null	6.2×10^{-4}	2.2×10^{-4}	1.0×10^{-3}	3.0×10^{-5}	$f(b, \lambda)$
Instrumental null	1.5×10^{-4}	1.3×10^{-4}	1.0×10^{-5}	7.0×10^{-6}	10^{-5}
rms null	2.0×10^{-6}	3.5×10^{-6}	1.1×10^{-7}	6.9×10^{-8}	10^{-5}

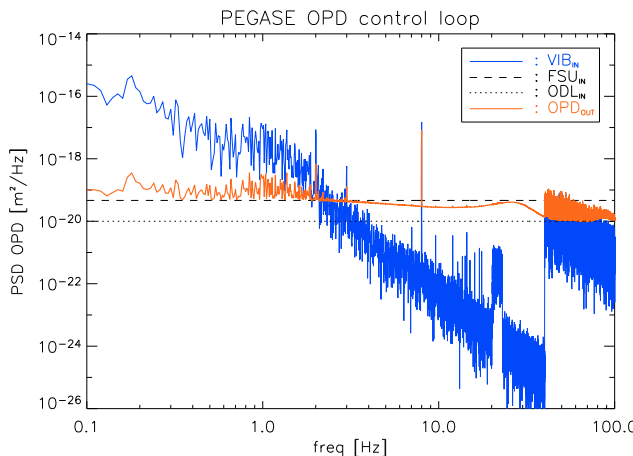


Fig. 3. Power spectral density of OPD errors at the input (VIB_{IN}) and at the output (OPD_{OUT}) of the PEGASE control loop. The PSDs of the fringe sensing unit (FSU_{IN} , dashed curve) and of the ODL (ODL_{IN} , dotted curve) before the OPD control loop are also represented. Similar PSDs are used for FKSI, taking into account in the input OPD perturbations an additional 5-Hz contribution due to the boom.

3.2. Control loop performance

As indicated in the previous section, the level of OPD and tip/tilt would be of the order of $0.18 \mu\text{m}$ and $3''.5$ rms without appropriate correction techniques. This is prohibitive for exozodiacal disc detection and fine control loops are therefore mandatory to stabilise the OPD and the tip-tilt to acceptable values. In GENIEsim, control loops are simulated through their transfer function in the frequency domain. A simultaneous optimisation is performed on the loop repetition frequency and the controller parameters (a simple PID¹) in order to minimise the residual errors, which are computed by integrating the corrected PSD on the frequency domain. The PSDs of the OPD perturbation before and after fringe tracking are shown in Fig. 3 in the case of PEGASE. At the input of the loop, the OPD perturbations come from the wheels (VIB_{IN}), the FSU measurement noise (FSU_{IN}) and the intrinsic ODL noise (ODL_{IN}). The PSD of the FSU noise is computed by considering a standard ABCD algorithm to estimate the phase of the fringe and assuming a read-out noise of 15 electrons rms per pixel. For the ODL, a white PSD of 1 nm rms over a 100 Hz bandpass has been assumed, as suggested by industrial studies (Van Den Tool 2006). The output OPD PSD

indicates the total residue after correction by the FSU, limited at low frequencies (below ~ 2 Hz) by the non-perfect control of the input perturbations, by the noise of the FSU between 2 and 30 Hz and by the ODL noise beyond 30 Hz. The tip/tilt control loop is treated in a similar way, assuming a noise of 10 mas/ $\sqrt{\text{Hz}}$ per tip-tilt mirror. The same assumptions have been considered for FKSI.

The optimised control loop performances are displayed in Table 2 for the GENIE instrument working on the 8-m Unit Telescopes (UT) at the VLTI (results taken from Paper I), the ALADDIN instrument working on 1-m telescopes at Dome C (results taken from Paper II), and the space-based instruments as presented in this paper. The observations are carried out for a Sun-like G2V star located at 20 pc on a 100 s observation sequence using either the 47-m UT2-UT3 baseline at the VLTI (waveband: 3.5–4.1 μm), a baseline length of 20 m for ALADDIN (waveband: 3.1–4.1 μm), a 40-m baseline length for PEGASE (waveband: 1.5–6.0 μm) and the 12.5-m baseline for FKSI (waveband: 3.0–8.0 μm). As in the case of ALADDIN, dispersion and intensity errors are expected to be very low in space and the corresponding control loops have been disabled in GENIEsim for simulating PEGASE and FKSI. This is indicated by a 0 Hz control loop frequency in Table 2. Fringe tracking can be carried out at much lower frequencies than for ground-based instruments (about 60 Hz instead of 2 kHz) and the residual OPD errors are much lower with a typical stability of about 2 nm rms. Pointing errors can also be controlled at lower frequencies (<100 Hz instead of 1 kHz), but the residual tip/tilt is somewhat larger. Globally, the instrumental nulling performance is better by at least a factor 10 with respect to GENIE and ALADDIN because OPD errors remain the dominant perturbations. Taking into account geometric stellar leakage, the overall nulling performance of PEGASE is only about 10^{-3} due to the combined effect of the larger baseline length and the extension of the wavelength range towards shorter wavelengths. Relaxing the collision avoidance requirements of 20 m or flying in triangular formation would enable shorter interferometric baseline lengths and would therefore improve the overall nulling performance of PEGASE (the geometric null is proportional to the baseline length to the square). Another way to improve the overall nulling performance while keeping the linear configuration is to discard the short wavelengths. This is discussed in more details in Sect. 4. With its 12.5-m baseline length and a wavelength range of [3–8] μm , the total null of FKSI is about 3.0×10^{-5} . Note that the results presented for GENIE and ALADDIN assume the “best case scenario”, which takes into account pupil averaging, a physical phenomenon reducing the power spectral density of piston and dispersion at high frequencies (see Paper I for more details).

¹ PID stands for “proportional, integral and differential” which is a basic controller device for closed-loop control.

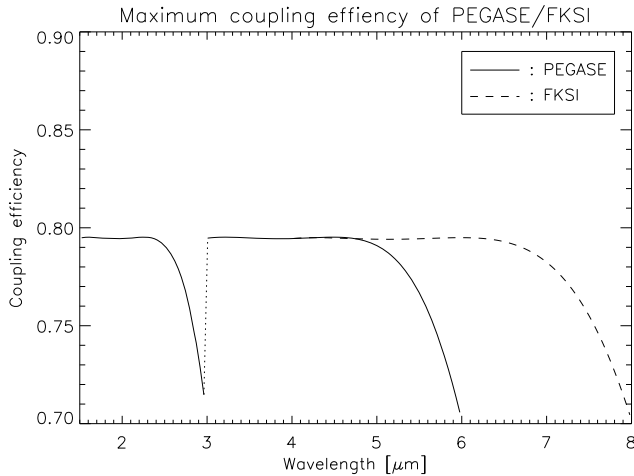


Fig. 4. Maximum coupling efficiency for PEGASE and FKSI with respect to the wavelength. The core radius is chosen so as to stay single-mode on the whole wavelength range and the focal lengths are optimised at wavelengths of $4.5\,\mu\text{m}$ and $6\,\mu\text{m}$, respectively for PEGASE and FKSI.

4. Simulated performance

4.1. Coupling efficiency

The coupling efficiency represents the fraction of incoming light from a point-like source which is transmitted into an optical fibre. It depends on the core radius of the fibre, its numerical aperture, the wavelength, the diameter of the telescope and its focal length (Ruilier & Cassaing 2001). In order to have an efficient correction of wave-front defects, the core radius of the fibres is chosen so as to ensure single-mode propagation over the whole wavelength range. The focal length can then be optimised to give the maximum coupling efficiency at a chosen wavelength and more importantly, to provide a roughly uniformly high coupling efficiency across the whole wavelength band. This is generally achieved by optimising the coupling efficiency in the middle of the wavelength range. However, for fibres covering a wide wavelength range, this procedure can lead to a significant degradation of the coupling efficiency at long wavelengths (where the instruments are most sensitive, see Sect. 4.2). For instance, the coupling efficiency of FKSI would be below 50% in the $[7\text{--}8]\,\mu\text{m}$ band. For PEGASE, the use of two fibres partly solves this issue but the coupling efficiency can be further improved. Optimising the coupling efficiency at wavelengths of $4.5\,\mu\text{m}$ for PEGASE and $6\,\mu\text{m}$ for FKSI is particularly convenient to maximize the coupling efficiency at long wavelengths while keeping a high level at short wavelengths (see Fig. 4). In both cases, the coupling efficiency remains around its maximum (about 80%) over almost the whole wavelength band of each fibre and decreases to a minimum of about 70% at the longest wavelengths. With these assumptions, we obtained optimised focal lengths of $1.1\,\text{m}$ and $1.4\,\text{m}$ respectively for PEGASE and FKSI. Note that in the case of PEGASE, we will discard in the following study the wavelength range corresponding to the first fibre ($1.5\text{--}3.0\,\mu\text{m}$), which is not well suited for exozodiacal disc detection.

4.2. Signal-to-noise ratio analysis

In this section, we present the different sources of noise simulated by GENIEsim and the level at which they contribute to

the final *SNR* in the case of a Sun-like star located at 20 pc. Each source of noise is given on output of GENIEsim in photo-electrons detected per spectral channel. Considering an integration time of 30 min, the detailed noise budget in the highest-*SNR* spectral channel is given in Table 3 for PEGASE and FKSI (first column). The listed sources of signal and noise are briefly discussed hereafter.

- The stellar signal represents the total number of photo-electrons detected in both constructive and destructive outputs.
- The raw instrumental leakage accounts for the stellar photons collected at the destructive output due to the influence of instrumental imperfections such as co-phasing errors, wavefront errors or mismatches in the intensities of the beams.
- The 20-zodi signal is the amount of photo-electrons at the destructive output that come from the circumstellar disc, assumed to be face-on and to follow the same model as in the solar system (Kelsall et al. 1998), except for a global density factor of 20.
- The background signal takes into account the instrumental brightness and the emission of the local zodiacal cloud. In the absence of atmosphere, the latter becomes the main background contributor and overwhelms the instrumental brightness by a factor ~ 1000 at $3.5\,\mu\text{m}$ or ~ 250 at $5.5\,\mu\text{m}$ respectively for PEGASE and FKSI.
- The geometric stellar leakage accounts for the imperfect rejection of the stellar photons due to the finite size of the star. Thanks to the analytical expression of the rejection rate (see Paper I), it can be calibrated. Here, we assume a typical precision ($\Delta\theta_\star$) of 1% on stellar angular diameters so that a calibration accuracy of 2% is reached on geometric stellar leakage.
- The raw instrumental leakage can be decomposed into its mean value and its variability, referred to as “instability noise” (Lay 2004; Chazelas et al. 2006). The mean value can be estimated by observing a calibrator star, provided that the interferometer behaves in the same way during both science observation and calibration. This calibration process is obviously limited by its own geometrical stellar leakage, instability noise, shot noise, detector noise and background noise. Therefore, calibrating the mean instrumental leakage is not necessarily useful for the improvement of the sensitivity. The absence of calibration is indicated by a dash sign in Table 3.
- Shot noise is due to the statistical arrival process of the photons from all sources. It is mainly dominated by stellar leakage and by the emission of the solar zodiacal cloud.
- Detector noise is computed assuming a read-out noise of 15 electrons rms and a typical read-out frequency of $0.01\,\text{Hz}$.
- The background noise stands for the residual background signal in the calibration process. Two off-axis fibres located close to the “science” fibre in the focal plane are used to measure the background emission in real time. Using this technique, the background noise is reduced to the sum of the shot noise contribution from the background itself and of the stellar light coupled into the “background” fibres. Considering fibres located at $40''$ from the axis and telescopes with a central obscuration of 14%, the residual stellar light in the background fibres does not exceed about 10^{-5} of the total stellar flux. More details about this technique can be found in Absil (2006).

Table 3. Expected sensitivity of PEGASE (40-m baseline) and FKSI, given in number of zodis that can be detected around a Sun-like star located at 20 pc in 30 min. For each instrument, the individual contributions are given in photo-electrons in three cases: in the optimum wavelength bin, in the optimised wavelength range and in the whole wavelength range. We assume a 1% precision on stellar diameter knowledge. The dash sign indicates that no calibration is performed.

	PEGASE			FKSI		
Wavelength [μm]	5.96	[5.7–6.0]	[3.0–6.0]	7.83	[6.3–8.0]	[3.0–8.0]
Bandwidth [μm]	0.08	0.3	3.0	0.34	1.7	5.0
Stellar signal [e-]	1.5×10^7	6.6×10^7	1.8×10^9	5.0×10^7	3.5×10^8	3.0×10^9
Raw instr. leakage [e-]	8.3×10^1	3.6×10^2	1.2×10^4	2.7×10^2	1.9×10^3	2.1×10^4
Total stellar leakage [e-]	2.2×10^3	1.0×10^5	6.1×10^5	6.6×10^2	5.4×10^3	1.1×10^5
20-zodi signal [e-]	1.0×10^3	4.1×10^3	4.9×10^4	2.7×10^3	1.4×10^4	2.9×10^4
Background signal [e-]	2.8×10^2	7.3×10^2	9.7×10^2	1.8×10^2	2.5×10^2	2.5×10^2
Calibrated geom. leakage [e-]	4.3×10^1	1.9×10^2	1.2×10^5	8.0×10^0	7.0×10^1	1.8×10^3
Calibrated instr. leakage [e-]	7.2×10^1	2.3×10^2	–	4.4×10^1	1.3×10^2	1.9×10^3
Instability noise [e-]	1.0×10^0	4.3×10^0	1.8×10^2	1.4×10^0	1.2×10^1	1.9×10^2
Shot noise [e-]	4.7×10^1	1.0×10^2	7.8×10^2	2.6×10^1	7.3×10^1	3.4×10^2
Detector noise [e-]	1.8×10^1	3.6×10^1	1.1×10^2	1.8×10^1	4.0×10^1	8.0×10^1
Background noise [e-]	2.7×10^1	4.6×10^1	1.4×10^2	3.0×10^1	6.3×10^1	1.8×10^2
Zodis for $S/N = 5$ (calibrated)	10	7.8	34	2.2	1.3	9.2

The single channel S/N can be improved by adding the signals from different spectral channels, taking into account the possible correlation of the noises between the wavelength bins. In this study, we assume that systematic noises such as geometrical leakage, instrumental leakage and instability noise are perfectly correlated between the wavelength bins so that the noise contributions have to be added linearly. On the other hand, random noises such as shot noise, detector noise and background noise are considered uncorrelated between the spectral channels and are thus added quadratically. Combining spectral channels is efficient to a limited extent and wide band observations give generally poor results. This is illustrated in Table 3 which details the noise budget in the optimum wavelength range (second column) and in the whole wavelength range (third column).

For both PEGASE and FKSI, the highest- S/N wavelength bin corresponds to the longest wavelength of the science waveband with an achievable sensitivity of respectively 10 and 2.2 zodis for a Sun-like star located at 20 pc. This sensitivity is slightly improved by combining the spectral channels in the [5.7–6.0] μm and [6.3–8.0] μm bands respectively for PEGASE and FKSI. Wider wavelength ranges would degrade the sensitivity as illustrated by the whole band sensitivity (respectively 34 and 9.2 zodis). This is because the part of the S/N that is due to systematic noises is not improved by combining spectral channels and both PEGASE and FKSI are largely dominated by geometric stellar leakage at short wavelengths. As a side effect, the calibration of instrumental leakage, which is very efficient for ground-based instruments (see Papers I and II), would impair the performance of PEGASE for observations performed in the whole wavelength range. In the optimum wavelength range of PEGASE, calibrating the instrumental leakage has only a slight influence on the final sensitivity and the geometric stellar leakage remains the dominant noise contributor, indicating that PEGASE would present a better sensitivity with a shorter-baseline configuration (for instance with the three spacecraft flying in triangular formation). For FKSI, geometric stellar leakage is less problematic due to the shorter baseline length but remains one of the main noise contributors. In the optimum wavelength range, the sensitivity of FKSI is also dominated by shot noise in this particular case (a Sun-like star located at 20 pc). In the next section, we will see however that geometric stellar leakage is generally dominant for brighter targets.

Table 4. Simulated sensitivity and optimum wavelength range of PEGASE and FKSI for four representative targets of the DARWIN/TPF catalogue, assuming 1% uncertainty on the stellar angular diameter and an integration time of 30 min.

Targets	PEGASE-12.5 m		PEGASE-40 m		FKSI	
	zodi	λ [μm]	zodi	λ [μm]	zodi	λ [μm]
K0V-05 pc	10	5.9–6.0	40	5.9–6.0	2.6	7.6–8.0
G5V-10 pc	4.2	5.6–6.0	12	5.9–6.0	1.0	7.2–8.0
G0V-20 pc	3.8	5.0–6.0	7.0	5.7–6.0	0.9	6.7–8.0
G0V-30 pc	7.7	4.3–6.0	5.5	5.4–6.0	1.8	6.0–8.0

4.3. Estimated sensitivity

Following the method used for the GENIE and ALADDIN studies (see Papers I and II), the performances of PEGASE and FKSI are presented for 4 hypothetic targets representative of the DARWIN/TPF catalogue (Kaltenegger et al. 2007): a K0V star located at 5 pc, a G5V located at 10 pc, a G0V located at 20 pc and a G0V located at 30 pc. The results of the simulations are presented in Table 4, taking into account the calibration procedures (i.e., background subtraction, geometric leakage calibration and instrumental leakage calibration) when necessary. The detection threshold is set at a global S/N of 5 in the optimised wavelength range. Unless specified otherwise, the integration time has been fixed to 30 min and the accuracy on the stellar angular diameters to 1%.

FKSI is the most sensitive instrument and can detect circumstellar discs with a density down to the level of the solar zodiacal cloud. For the four representative targets of the DARWIN/TPF catalogue, FKSI can detect discs of 2.6, 1.0, 0.9 and 1.8 zodis compared to 40, 12, 7.0 and 5.5 zodis for PEGASE (see Table 4). For both instruments, geometric stellar leakage is the dominant noise in all cases, except for the G0V star located at 30 pc for which FKSI is dominated by the shot and background noises. This explains why the sensitivity decreases for the closest targets, which have a larger angular stellar diameter and therefore produce more geometric stellar leakage for a given baseline length. This also explains why the optimum wavelength range is wider for the distant targets, for which combining the spectral channels is more efficient due to the higher relative contribution of shot noise to the final S/N . Note also that, for the same

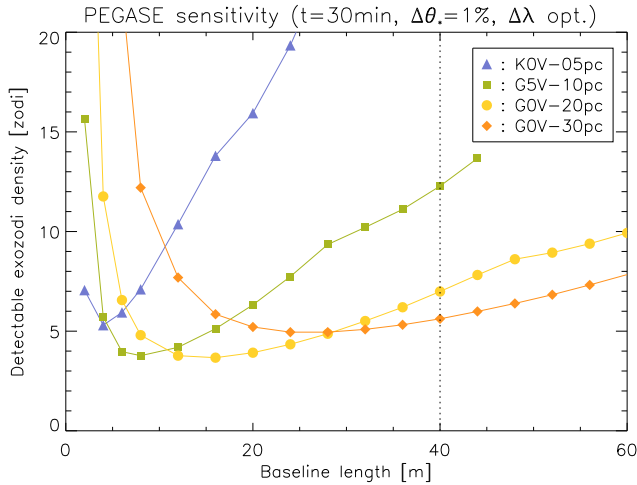


Fig. 5. Simulated performance of PEGASE for four typical DARWIN/TPF targets with respect to the baseline length, assuming 1% uncertainty on stellar angular diameters and an integration time of 30 min.

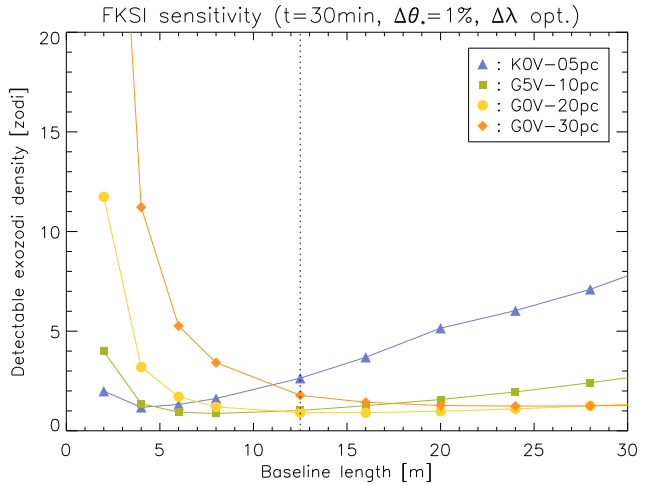


Fig. 6. Simulated performance of FKSI for four typical DARWIN/TPF targets with respect to the baseline length, assuming 1% uncertainty on the stellar angular diameter and an integration time of 30 min.

reason, the optimum wavelength range for a given star is always wider for FKSI than for PEGASE.

The main difference between FKSI and PEGASE is related to the geometric stellar leakage which is much larger in the case of PEGASE due to its 40-m baseline length. Considering the same baseline length for both instruments, the sensitivity of FKSI would however remain better than that of PEGASE due to the longer observing wavelength and the lower thermal background. Indeed, observing at longer wavelengths improves the geometric stellar rejection which is proportional to the squared wavelength. For instance, with a hypothetical baseline length of 12.5 m, PEGASE could detect circumstellar discs of 10, 4.2, 3.8 and 7.7 zodis compared to 2.6, 1.0, 0.9 and 1.8 zodis for FKSI (see Table 4). The feasibility of such a flight configuration is however beyond the scope of this paper and will not be addressed.

The estimated sensitivity is represented as a function of baseline length in Fig. 5 for PEGASE and in Fig. 6 for FKSI, where the wavelength range is optimised separately for each baseline length. As already suggested, the sensitivity at long baseline lengths is dominated by geometric stellar leakage, especially for the closest targets which have a larger stellar angular diameter. By reducing the baseline length, the starlight rejection improves and the sensitivity curves decrease towards a minimum, indicating the optimum baseline length. It is interesting to note that the 12.5-m interferometric baseline of FKSI is a good compromise for most stars in the DARWIN/TPF catalogue. The decrease in performance towards longer baselines lengths is stronger for PEGASE than for FKSI since it observes at shorter wavelengths. At short baseline lengths, background noise becomes dominant due to the decrease of the exozodiacal disc transmission and the sensitivity curves rise again. The slight inflection in the sensitivity curves of Fig. 5 (e.g., at a baseline length of 15 m for the K0V star) indicates the baseline lengths at which the instrumental leakage calibration becomes useless and would not improve the sensitivity. The difference in sensitivity between PEGASE and FKSI decreases with the target distance since the optimum baseline length of PEGASE is getting closer to 40 m.

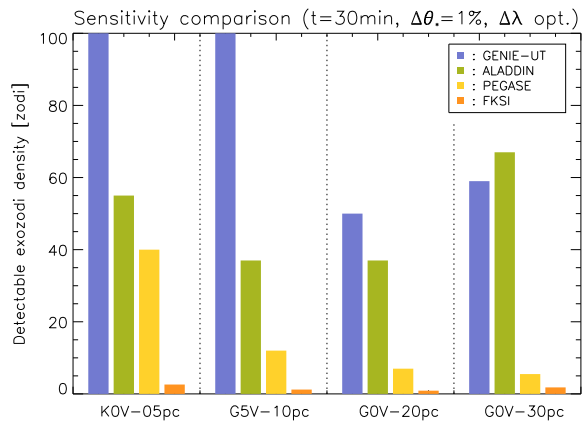


Fig. 7. Expected performance for PEGASE and FKSI compared to the ground-based instruments (for 30 min integration time and 1% uncertainty on the stellar angular diameters).

5. Discussion

5.1. Comparison with ground-based sites

In order to provide a fair comparison between ground- and space-based nulling interferometers, we use the performance estimations of GENIE and ALADDIN obtained with GENIESim for the 4 representative targets of the DARWIN/TPF catalogue (from Papers I and II). The detectable exozodiacal dust densities for GENIE on the unit telescopes (UT – 8 m diameter), ALADDIN, PEGASE and FKSI are represented in Fig. 7, considering an integration time of 30 min and an uncertainty on the stellar angular diameters of 1%. For all target stars, the space-based nulling interferometers are the most sensitive instruments. PEGASE (resp. FKSI) outperforms ALADDIN by a factor ranging from about 1.5 (resp. 20) for the K0V star located at 5 pc to a factor of about 10 (resp. 30) for the G0V star located at 30 pc. This better sensitivity of space-based instruments is mainly due to the lower thermal background and geometric stellar leakage, which are the dominant noises for GENIE and ALADDIN.

Table 5. Performance comparison between GENIE, ALADDIN, PEGASE and FKSI expressed in detectable exozodiacal disc densities as compared to the solar zodiacal disc (for different uncertainties on the stellar angular diameter and an integration time of 30 min).

Star	0.25%	0.5%	1%	1.5%	Instrument
K0V-05pc	110	230	450	680	GENIE-UT
	20	33	55	79	ALADDIN
	12	21	40	60	PEGASE
	0.9	1.4	2.6	3.9	FKSI
G5V-10pc	30	59	120	180	GENIE-UT
	15	24	37	51	ALADDIN
	4.7	8.3	12	17	PEGASE
	0.5	0.7	1.0	1.4	FKSI
G0V-20pc	21	29	50	73	GENIE-UT
	19	25	37	48	ALADDIN
	2.8	4.2	7.0	9.5	PEGASE
	0.7	0.8	0.9	1.1	FKSI
G0V-30pc	36	46	59	71	GENIE-UT
	62	63	67	72	ALADDIN
	3.1	3.9	5.5	7.3	PEGASE
	1.7	1.7	1.8	1.9	FKSI

While the absence of atmosphere in space and the cooler optics explain the lower thermal background, the longer observing wavelength improves the geometric stellar rejection, which is proportional to the squared wavelength.

As discussed in the previous sections, PEGASE and FKSI are generally limited by geometric stellar leakage. Reducing the baseline length to improve the sensitivity is not possible either due to the free-flying constraints for PEGASE or due to the fixed boom on FKSI. Besides reducing the interferometric baseline length, another way to minimize the geometric stellar leakage is to improve the knowledge on stellar angular diameters. Considering the four targets representative of the DARWIN/TPF catalogue, Table 5 gives the sensitivity to exozodiacal discs of PEGASE and FKSI for different uncertainties on the stellar angular diameter. The results of GENIE on the unit telescopes (UT = 8 m diameter) and ALADDIN are also presented for comparison. Unlike the other instruments, FKSI is relatively insensitive to the uncertainty on the stellar angular diameter, with a sensitivity below 4 zodis even for a knowledge of the stellar angular diameter of 1.5%.

5.2. Influence of integration time

Increasing the integration time has different influences on the individual noise sources. For instance, shot noise, detector noise and instability noise (to the first order) have the classical $t^{1/2}$ dependence and their relative impact on the final S/N decreases for longer integration times. On the other hand, the imperfect calibration of geometric and instrumental stellar leakage is proportional to time, so that increasing the integration time has no influence on the associated S/N . Since geometric stellar leakage is generally dominant, increasing the integration time does not improve significantly the sensitivity to exozodiacal discs. The sensitivity as a function of the integration time is represented in Fig. 8, using the optimum wavelength range. With a 40-m baseline length, PEGASE is dominated by geometric stellar leakage for the four targets and reducing the integration time to five minutes has almost no influence. For FKSI, geometric stellar leakage is not dominant for the G0V star located at 30 pc and increasing the integration time improves slightly the sensitivity (1.4-zodi disc detectable in 60 min instead of 1.8-zodi disc in 30 min). For

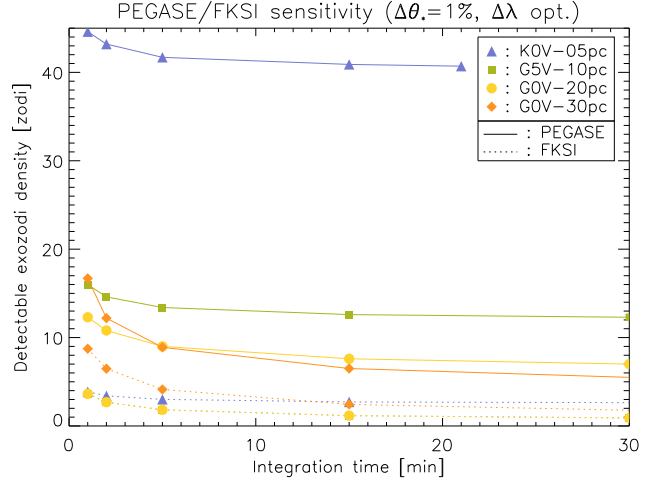


Fig. 8. Simulated performance of PEGASE and FKSI in terms of exozodiacal disc detection with respect to the integration time, for an uncertainty on the stellar angular diameter of 1% and in the optimised wavelength range.

the other three targets, geometric stellar leakage is dominant and integration times longer than 30 min have no significant influence on the sensitivity. Like PEGASE, an integration time of five minutes is already sufficient to reach the maximum sensitivity for most targets. For comparison, ALADDIN could reach a sensitivity of 30 zodis after about 8 h of integration time for G0V stars located between 20 and 30 pc (see Paper II). Due to the low thermal background, PEGASE and FKSI achieve their maximum sensitivity much faster than ground-based nulling instruments.

5.3. Influence of telescope diameter

Similarly to integration time, increasing the telescope diameter has different influences on the individual noise sources. Since the geometric nulling ratio does not depend on the aperture size, the component of the S/N which is due to geometric stellar leakage is not improved by increasing the telescope diameter. Since the geometric stellar leakage is generally dominant for an integration time of 30 min, different pupil sizes have therefore little influence on the final sensitivity. In order to clearly show the impact of different pupil sizes, we consider in this section an integration time of 5 min which is generally sufficient to reach the maximum sensitivity (see previous section). Considering an uncertainty on the stellar angular diameter of 1% and 5 min of integration time, the sensitivities of PEGASE (solid lines) and FKSI (dashed lines) for different pupil diameters are presented in Fig. 9. As expected, the sensitivity varies more significantly for the faintest targets, which are more dominated by shot noise. For PEGASE, the sensitivity is already close to the maximum with the 40-cm diameter apertures and increasing the telescope diameter has only a slight impact for the faintest target (G0V star located at 30 pc). For FKSI, the sensitivity remains practically unchanged for telescopes with a diameter larger than 30 cm, except for the G0V star located at 30 pc. In practice, the final choice of the pupil diameter will result from a trade-off between integration time, feasibility and performance.

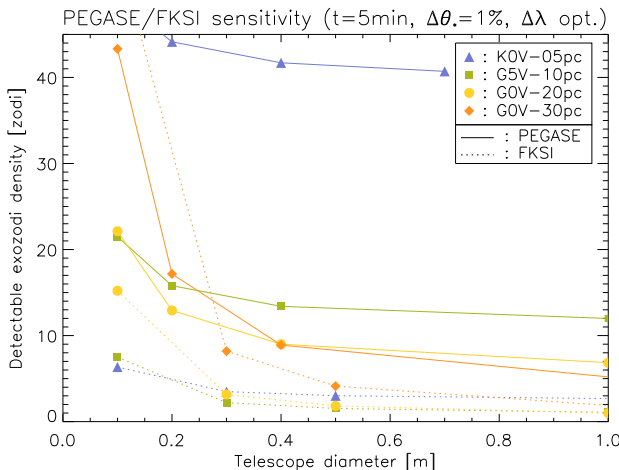


Fig. 9. Simulated performance of PEGASE and FKSI in terms of exozodiacal disc detection for different pupil diameters, considering an uncertainty on the stellar angular diameter of 1% ($\Delta\theta_*$) and 5 min of integration.

5.4. Sky coverage

In the context of DARWIN/TPF preparatory activities, another relevant issue is the sky coverage, i.e., the part of the celestial sphere accessible by each instrument. A representative way to assess the sky coverage is to determine how many stars of the DARWIN/TPF all sky target catalogue (Kaltenegger et al. 2007) can be observed by each instrument. This value depends on the combination of two parameters: the location of the instrument and its pointing direction ability. For the ground-based instruments, we assume that the zenith distance can not be larger than 60° . For space-based instruments, the pointing direction covers the part of the sky with an ecliptic latitude between $\pm 30^\circ$ for PEGASE and $\pm 20^\circ$ for FKSI (after 1 year of observation).

Considering the 1354 single target stars of the DARWIN/TPF catalogue (106 F, 251 G, 497 K and 500 M stars), the results are presented in Fig. 10 for GENIE (dark frame), ALADDIN (light frame) and PEGASE (shaded area). The sky coverage of FKSI is not represented for the sake of clarity but is similar to that of PEGASE with an extension in declination of 40° instead of 60° . The stars enclosed in a specified frame are observable by the corresponding instrument in a 1-year observation window. Counting the stars in each frame, GENIE can observe 1069 targets (90 F, 191 G, 405 K, 383 M stars), ALADDIN 514 (52 F, 98 G, 204 K, 160 M stars), PEGASE 677 (53 F, 125 G, 244 K and 255 M stars) and FKSI 443 (28 F, 74 G, 164 K and 177 M stars). These values correspond to about 80%, 40%, 50% and 30% of the targets, respectively for GENIE, ALADDIN, PEGASE and FKSI. Note that ALADDIN and the space-based instruments cover complementary regions of the sky and are able to survey most of the targets with a declination lower than 50° .

6. Conclusions

Nulling interferometry is a promising technique to assess the level of circumstellar dust in the habitable zone around nearby main sequence stars. From the ground, instruments like GENIE (VLT nuller, using two 8-m telescopes) and ALADDIN (Antarctic nuller, using two dedicated 1-m telescopes) could achieve the detection of exozodiacal discs with a density of several tens of zodis. The high Antarctic plateau is a particularly

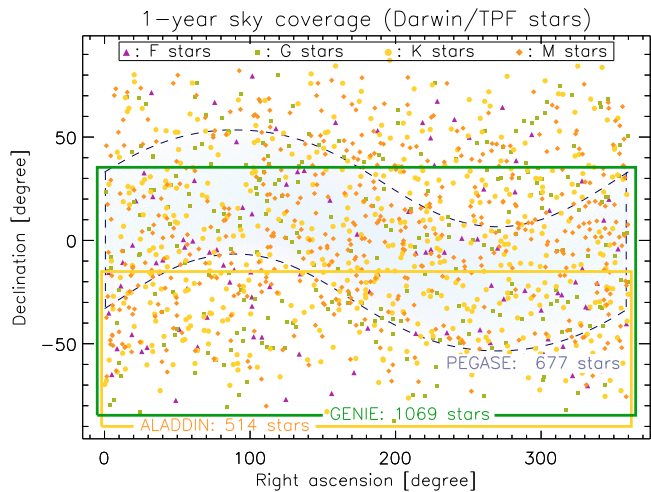


Fig. 10. Sky coverage after 1 year of observation of GENIE (dark frame), ALADDIN (light frame) and PEGASE (shaded area) shown with the DARWIN/TPF all sky target catalogue. The blue-shaded area shows the sky coverage of a space-based instrument with an ecliptic latitude in the $[-30^\circ, 30^\circ]$ range (such as PEGASE). The sky coverage of FKSI is similar to that of PEGASE with an extension of 40° instead of 60° .

well suited site in that context, so that ALADDIN is expected to achieve the best sensitivity (down to 30 zodis in few hours of integration time). Observing from space provides the solution to go beyond this sensitivity by getting rid of the high thermal background constraining ground-based observations. In this paper, we have investigated the performance of two space-based nulling interferometers which have been intensively studied during the past few years (namely PEGASE and FKSI). Even though they have been initially designed for the characterisation of hot extra-solar giant planets, PEGASE and FKSI would be very efficient to probe the inner region of circumstellar discs where terrestrial habitable planets are supposed to be located. Within a few minutes, PEGASE (resp. FKSI) could detect exozodiacal discs around nearby main sequence stars down to a density level of 5 (resp. 1) times our solar zodiacal cloud and thereby outperform any ground-based instrument. FKSI can achieve this sensitivity for most targets of the DARWIN/TPF catalogue while PEGASE becomes less sensitive for the closest targets with detectable density levels of about 40 times the solar zodiacal cloud. This outstanding and uniform sensitivity of FKSI over the DARWIN/TPF catalogue is a direct consequence of the short baseline length (12.5 m) used in combination with an appropriate observing wavelength of about $8 \mu\text{m}$, which is ideal for exozodiacal disc detection. Another advantage of FKSI is to be relatively insensitive to the uncertainty on stellar angular diameters, which is a crucial parameter driving the performance of other nulling interferometers. In terms of sky coverage, we show that these space-based instruments are able to survey about 50% of the DARWIN/TPF target stars. The sky coverage reaches 80% if they are used in combination with ALADDIN, which provides a complementary sky coverage. Beyond the technical demonstration of nulling interferometry in space, the present study indicates that PEGASE and FKSI would be ideal instruments to prepare future life-finding space missions such as DARWIN/TPF.

Acknowledgements. The authors are grateful to Lisa Kaltenegger (Harvard-Smithsonian Center for Astrophysics) for providing the updated DARWIN catalogue, Jean Surdej (IAGL), Amaud Magette (IAGL), Pierre Riaud (Paris observatory), Tupper Hyde (NASA/GSFC), Pierre-Yves Guidotti (CNES) and

Julien Morand (EADS-Astrium) for their support and contribution. The authors also thank Richard Barry (NASA/GSFC) for a careful reading of the manuscript. The first author acknowledges the support of the Belgian National Science Foundation ("FRIA"). O.A. acknowledges the financial support from the European Commission's Sixth Framework Program as a Marie Curie Intra-European Fellow (EIF).

References

Absil, O. 2006, Ph.D. Thesis, Liège University, Liège, Belgium

Absil, O., den Hartog, R., Gondoin, P., et al. 2006a, *A&A*, 448, 787 (Paper I)

Absil, O., di Folco, E., Mérand, A., et al. 2006b, *A&A*, 452, 237

Absil, O., Coudé Du Foresto, V., Barillot, M., & Swain, M. R. 2007, *A&A*, 475, 1185 (Paper II)

Barry, R. K., Danchi, W. C., Deming, L. D., et al. 2006, in Proc. SPIE, 6265

Barry, R. K., Danchi, W. C., Traub, W. A., et al. 2008, *ApJ*, 677, 1253

Beichman, C., Lawson, P., Lay, O., et al. 2006a, in Proc. SPIE, 6268

Beichman, C. A., Bryden, G., Stapelfeldt, K. R., et al. 2006b, *ApJ*, 652, 1674

Beichman, C. A., Tanner, A., Bryden, G., et al. 2006c, *ApJ*, 639, 1166

Bracewell, R. N. 1978, *Nature*, 274, 780

Chazelas, B., Brachet, F., Bordé, P., et al. 2006, *Appl. Opt.*, 45, 984

Coudé du Foresto, V., Absil, O., Swain, M., Vakili, F., & Barillot, M. 2006, in Proc. SPIE, 6268

Danchi, W. C., Deming, D., Kuchner, M. J., & Seager, S. 2003, *ApJ*, 597, L57

Danchi, W. C., Barry, R. K., Deming, D., et al. 2006, in Proc. SPIE, 6268

Defrère, D., Absil, O., Hanot, C., & Fridlund, M. 2007, in Proc. SPIE, 6693, 53

Defrère, D., Lay, O., den Hartog, R., & Absil, O. 2008, in Proc. SPIE, 7013, in press

di Folco, E., Absil, O., Augereau, J.-C., et al. 2007, *A&A*, 475, 243

Fridlund, C. V. M., d'Arcio, L., den Hartog, R., & Karlsson, A. 2006, in Proc. SPIE, 6268

Gondoin, P. A., Absil, O., den Hartog, R. H., et al. 2004, in Proc. SPIE 5491, ed. W. A. Traub, 775

Hillenbrand, L. A., Carpenter, J. M., Kim, J. S., et al. 2008, *ApJ*, 677, 630

Hinz, P. M., Angel, J. R. P., Woolf, N. J., Hoffmann, W. F., & McCarthy, D. W. 2000, in Proc. SPIE, ed. P. J. Lena, & A. Quirrenbach, 4006, 349

Hinz, P. M., Angel, J. R. P., Woolf, N. J., Hoffmann, W. F., & McCarthy, D. W. 2008, in Proc. SPIE, ed. P. J. Lena, & A. Quirrenbach, 7013, in press

Hyde, T. T., Liu, K.-C., Blaurock, C., et al. 2004, in Proc. SPIE 5497, ed. S. C. Craig, & M. J. Cullum, 553

Kaltenegger, L., Eiroa, C., & Fridlund, M. 2007, *A&A*, submitted

Kelsall, T., Weiland, J. L., Franz, B. A., et al. 1998, *ApJ*, 508, 44

Lay, O. P. 2004, *Appl. Opt.*, 43, 6100

Le Duigou, J. M., Olivier, M., Léger, A., et al. 2006, in Proc. SPIE, 6265

Meyer, M. R., Carpenter, J. M., Mamajek, E. E., et al. 2008, *ApJ*, 673, L181

Ruillier, C., & Cassaing, F. 2001, *J. Opt. Soc. Am. A*, 18, 143

Serabyn, E. 1999, *Appl. Opt.*, 38, 4213

Serabyn, E. 2008, in Proc. SPIE, 7013

Serabyn, E., & Colavita, M. M. 2001, *Appl. Opt.*, 40, 1668

Serabyn, E., Booth, A., Colavita, M. M., et al. 2006, in Proc. SPIE, 6268

Sterken, V. 2005, Master's thesis, Delft University of Technology

Trilling, D. E., Bryden, G., Beichman, C. A., et al. 2008, *ApJ*, 674, 1086

Van Den Tool, T. 2006, in Proc. ICSO 2006 conference, Noordwijk

Villien, A., Morand, J., Delpech, M., & Guidotti, P. 2007, in 17th IFAC Symposium on Automatic Control in Aerospace

Wallner, O., Flatscher, R., & Ergenzinger, K. 2006, *Appl. Opt.*, 45, 4404

5.5 Summary

Studying the inner part of debris discs is of prime importance to characterize the global architecture of planetary systems, and to prepare future exo-Earth characterization missions. In this chapter, we investigate the performance of two infrared space-based Bracewell interferometers (namely PEGASE and FKSI), that have been intensively studied the past few years, for exozodiacal dust cloud detection. Even though they have been initially designed for the characterization of hot extrasolar giant planets, we show that PEGASE and FKSI would be very efficient to probe the inner region of circumstellar discs, where terrestrial habitable planets are supposed to be located. In few minutes, PEGASE (resp. FKSI) could detect exozodiacal discs around nearby main sequence stars down to a density level of 5 (resp. 1) times our solar zodiacal cloud to outperform any ground-based instrument. FKSI can achieve this sensitivity for most nearby F-, G-, K- and M-type main sequence stars, while PEGASE becomes less sensitive for the closest targets with detectable density levels of about 40 times the solar zodiacal cloud. In terms of sky coverage, PEGASE and FKSI are complementary to ALADDIN and would be able to survey about 50% of nearby F-, G-, K- and M-type main sequence stars. The sky coverage reaches 80% if they are used in combination with ALADDIN. Beyond the technical demonstration of nulling interferometry in space, these results suggest that PEGASE and FKSI would be ideal instruments to prepare future life-finding space missions. Indeed, we will see in Chapter 7 that the characterization of habitable terrestrial planets would be seriously jeopardized for stars presenting warm exozodiacal dust more than about 15 times as dense as our solar zodiacal dust cloud.

Part IV

Unveiling hidden worlds with space-based nulling interferometry

6

Prospects for single infrared Bracewell interferometers

Contents

6.1 Science case	118
6.1.1 Hot extrasolar giant planets	118
6.1.2 Super-Earth extrasolar planets	118
6.2 PEGASUS: an enhanced version of PEGASE	120
6.2.1 Concept overview	120
6.2.2 The split-pupil technique	121
6.2.3 The OPD modulation technique	122
6.3 Performance predictions for PEGASE and PEGASUS	123
6.3.1 The simulation software	124
6.3.2 Paper: <i>Potential of space-based infrared Bracewell interferometers for planet detection</i>	127
6.3.3 Complementary results	141
6.4 Performance predictions for FKSI	143
6.4.1 Detection of known super-Earths	143
6.4.2 General sensitivity	145
6.4.3 An enhanced version of FKSI	146
6.5 Summary	147

PEGASE and FKSI are space-based Bracewell interferometer projects dedicated to the exploration of the faint environment (including habitable zone) around nearby main sequence stars in the infrared. After the detailed analysis of the performance for exozodiacal disc detection in the previous part of this thesis, this chapter is dedicated to the detection and characterization of extrasolar planets. In addition to PEGASE and FKSI, two ambitious Bracewell interferometers are discussed and investigated: an enhanced version of PEGASE (namely PEGASUS) and an upgraded version of FKSI. Compared to PEGASE and FKSI, these enhanced concepts are particularly efficient to extend the search zone for super-Earth extrasolar planets in the habitable zone of nearby main sequence stars.

6.1 Science case

6.1.1 Hot extrasolar giant planets

The original goal of PEGASE/FKSI, which was also their main design driver, was to perform a spectroscopic characterization of hot EGPs. Such planets generally consist in Jupiter-mass gaseous bodies orbiting close to their parent stars (0.02 to 0.1 AU, i.e., orbital periods shorter than 10 days). Up to now, about 55 hot EGPs have been detected in our neighbourhood (≤ 150 pc), generally by means of radial velocity surveys, which allow the characterization of orbital parameters of the companion planet and the estimation of its mass through the product $M_p \sin i$. About 15 of these planets have also been characterised by the observation of the photometric drop as the planet transits in front of the stellar photosphere, giving an unambiguous access to the mass and radius of these planets. From this additional piece of information, one can constrain their nature, their evolution and some of their atmospheric properties (see section 1.1.3). For a few cases, the detections of the secondary eclipse has even provided some limited information on the thermal emission of these planets (e.g., Charbonneau et al. 2005; Deming et al. 2005). Similar results have been obtained on several other giant planets detected by photometric transits farther out in the galaxy, at about 1500 pc from our solar system by the OGLE survey (e.g., Udalski et al. 2004). However, very few spectral observations with a resolution of several tens has been obtained so far. In order to improve our understanding of the physics of hot EGPs and to test atmospheric models, a spectroscopic study of their thermal and/or reflected radiation is mandatory.

Studying the physics of hot EGPs is of particular interest because these objects have no equivalent in the solar system and no theory had predicted their existence before their discovery. These hot and highly irradiated objects ($T_{\text{eff}} \sim 1000$ to 2000 K) are nowadays thought to have formed far from their central star, and to have migrated inward (see section 1.1.2), where their rotation is now synchronously locked with their revolution period. This means that the same face of the planet is permanently irradiated, leading to a complex circulation within the atmosphere. Even though all the models describe hot EGPs as giant gaseous objects, the role of aerosols and potential clouds of dust, the level of thermalization between irradiated and dark hemispheres of the planet and the potential existence of winds between the hemispheres are strongly discussed. Figures 6.1 and 6.2 show three alternative models with and without clouds leading to a strong difference in the spectral features depth. A spectral analysis of the objects with a spectral resolution of several tens in the near-infrared (1-5 μm) would strongly constrain the atmospheric models. Performing spectroscopy in the near infrared has several advantages to study hot EGPs. This spectral range contains molecular species such as CH_4 , CO (whose depth is a tracer of cloud thickness) and especially H_2O at 2.6 μm , difficult to detect from the ground. Collision-induced absorption by H_2 can also potentially be detected between 2.5 and 3.0 μm . Moreover, this wavelength regime gives access to an almost unperturbed part of the continuum in the thermal emission, between roughly 3.5 and 4.3 μm , which allows good estimates of the planetary equilibrium temperature.

6.1.2 Super-Earth extrasolar planets

Super-Earth is a term generally used for rocky planets with masses in the range of a few to 10 Earth masses, depending on the author (Valencia et al. 2007; Fortney et al. 2007). Already a few planets with masses smaller than 10 M_{\oplus} have been detected. In 1992, two planets with masses of 2.8 and 3.4 M_{\oplus} orbiting a pulsar in almost perfect circular orbits have been discovered from precise timing measurements (Wolszczan and Frail 1992). The microlensing technique has also demonstrated its potential to detect low-mass planets with two detections announced: a planet of about 5.5 M_{\oplus} orbiting a low-mass star (Beaulieu et al. 2006), and a still less massive object, of only 3.3 M_{\oplus} , probably gravitationally bound to a brown dwarf (Bennett et al. 2008). The first super-Earth detected around a main sequence star was discovered in 2005, orbiting a M4V star named GJ 876 (Rivera et al. 2005). Its estimated mass is $7.5 \pm 0.7 M_{\oplus}$ and it has an orbital period of 1.94 days. It is close to the host star, and the surface

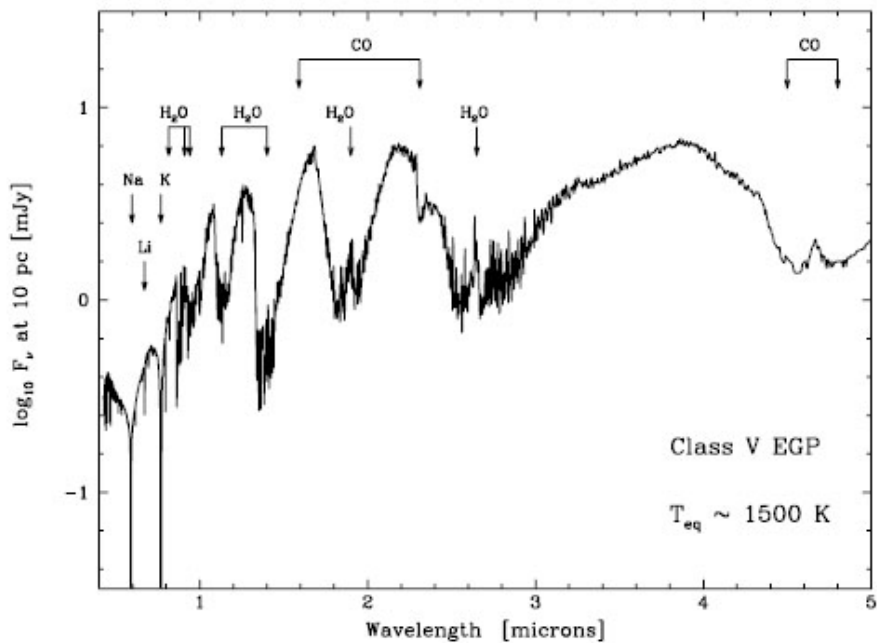


Figure 6.1: Example of a synthetic spectrum for a hot Jupiter located at 0.1 AU from its parent star and heated up to 1000 K (applicable to *51 Peg*, Sudarsky et al. 2003). For the sake of comparison, a Sun located at the distance of *51 Peg* would have a flux of about 8 Jy at 3 μ m.

temperature is calculated to lie between 430 and 650 K. Doppler spectroscopy also revealed three other planets with a minimum mass less than $10 M_{\oplus}$: GJ 581c and d, with minimum masses of 5.1 and $8.2 M_{\oplus}$ respectively (Udry et al. 2007) and HD 181433b with a maximum mass of $7.5 M_{\oplus}$ (Bouchy et al. 2009). GJ 581 is a M3V star while HD 181433 and HD 40307 are both K dwarfs. A recent radial velocity survey suggests that at least $30 \pm 10\%$ of G and K dwarfs have Neptune or super-Earth companions in the narrow range of periods shorter than 50 days (Mayor et al. 2009b). Note that the first transiting super-Earth may have been discovered very recently by CoRoT (Leger et al. 2009). Corot-Exo7b is a $1.68-R_{\oplus}$ planet orbiting at 0.017 AU around a K0V star located at 140 pc.

The scientific interest of these planets lies in the fact that super-Earth planets share common geo-physical attributes with the Earth, like oceans/continents, plate tectonics, volcanism and habitability. Active volcanoes produce large quantities of gases, primarily H_2O , CO_2 , and SO_2 , which have spectral bands in the infrared. Although water vapor is the dominant constituent of volcanic gases, substantial quantities of carbon dioxide and sulfur dioxide are emitted. For example, at the hot spot at the Kilauea Summit (Hawaii, USA), the concentrations by volume percentage are: 37% of H_2O , 49% of CO_2 , 12% of SO_2 . Trace amounts of molecular hydrogen gas, carbon monoxide, hydrogen sulfide, and hydrochloric acid are also present. Sulfur dioxide has fundamental vibrational lines at wavelengths of 7.34, 8.68, and $19.30 \mu m$, which should be observable if sufficient quantities of atmospheric SO_2 exist. Interestingly, emission rates vary enormously for volcanoes on Earth, from as little as about 20 tons per day to over 10 million tons per day. Non-equilibrium chemistry of H_2O , CH_4 , CO , and CO_2 in an exoplanet atmosphere could also be indicative of volcanism. Transitory non-equilibrium atmospheric chemistry associated with exoplanet volcanism may, in some cases, be detectable with a sensitive, high angular resolution system such as PEGASE/FKSI.

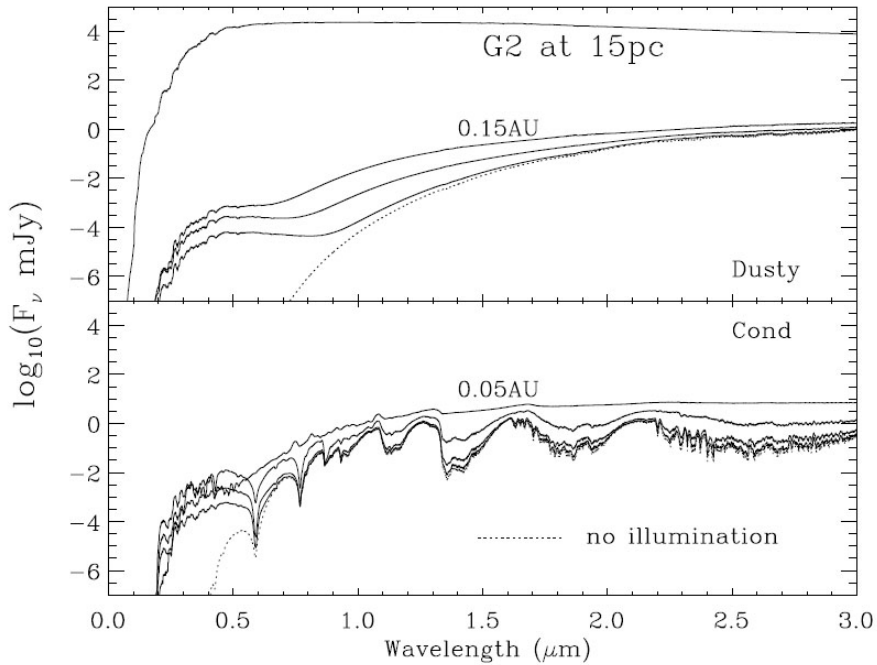


Figure 6.2: Example of synthetic spectra for hot EGPs using different atmospheric models (Barman et al. 2001). In the top figure, the dust is supposed to have entirely settled, leaving “clear skies”. In the bottom figure, settling is ignored so that the dust contributes to the opacity. The planets have been placed respectively at 0.15, 0.25 and 0.5 AU from the star in the top figure and at 0.05, 0.1 and 0.25 AU in the bottom figure.

6.2 PEGASUS: an enhanced version of PEGASE

PEGASUS was initially referred to as “DARWIN Lite” or “Super-Pegase” and is a Bracewell interferometer built on the PEGASE mission. It has been studied to assess the relevance of a down-scoped DARWIN for the Cosmic Vision 2015-2025 programme. The idea was to study the single Bracewell concept to assess which of DARWIN/TPF objectives could be achieved. This has been done first by optimising the PEGASE specifications for the detection of Earth-like planets, which requires larger telescopes, cooler optics and an optimised wavelength range. The analysis was then extended to planets with different orbits to give a general overview of the instrument capabilities. One of the major challenges in detecting an Earth-like planet is to extract its signal from the emission of the exozodiacal cloud, which cannot be subtracted by internal modulation, as in the case of DARWIN/TPF. Specific methods for Bracewell interferometers, such as split-pupil and OPD modulation, have been investigated. The study was performed in the framework of the present thesis in partnership with ESA/ESTEC.

6.2.1 Concept overview

PEGASUS consists in two 1-m diameter telescopes and one beam combiner spacecraft, free flying at least 20 m away from each other (20 m is the minimum distance to avoid the collision of the spacecraft). The linear configuration of PEGASE with a central beam combiner is not convenient for PEGASUS since the optimum baseline length for most of the targets in the DARWIN/TPF catalogue is shorter than 40 m when focusing on the habitable zone of nearby stars (at 10 μm , see Figure 6.3). This is particularly important for the closest targets of each spectral type which are the targets requiring the shorter integration time.

PEGASUS is therefore better configured as being triangular, which makes baseline lengths shorter

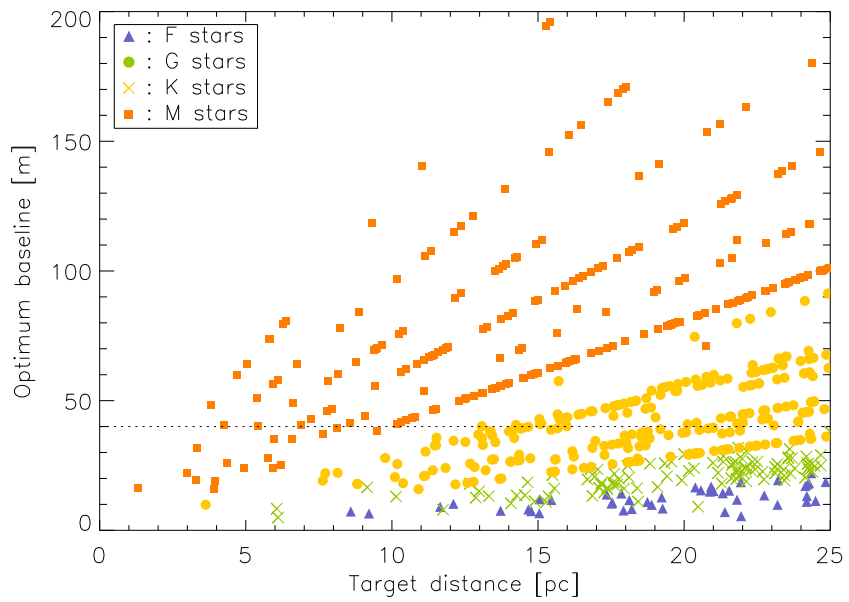


Figure 6.3: Optimum baseline length to observe the habitable zone of DARWIN targets with respect to the target distance (at $10\mu\text{m}$).

than 40 m available (see Figure 1 in the paper presented in section 6.3.2). According to CNES, it is conceivable to consider a minimal baseline reduced to 20 m if a triangular configuration is adopted, with the beam combiner at one angle. In that case, the payload has to be designed with an angle of 120° between the incoming beams instead of the 180° in the linear case. The waveband ranges from 9 to $13\mu\text{m}$ with a spectral resolution of 60. In the nulling mode, control loops have to stabilise the OPD to an rms value of 1 nm and the pointing accuracy to 20 mas (instead of 2.5 nm and 30 mas respectively for PEGASE). An rms OPD error of 1 nm is very challenging but should be realistic in the near-term future (Lawson 2006). At $10\mu\text{m}$, the main challenge to detect an Earth-like planet is nevertheless the exozodiacal emission, which can be up to 400 times brighter than an Earth located at 1 AU. Internal modulation used in the case of DARWIN/TPF is not appropriate since it requires at least 3 telescopes. On the other hand, modulation by rotation of the interferometer can generally not be implemented sufficiently fast and the planet signal is easily corrupted by long term drifts and $1/f$ noise. The solution to remove the exozodiacal emission (at least partially) with a single Bracewell interferometer is rather to use one of the specific techniques described hereafter.

6.2.2 The split-pupil technique

Pupil division is a technique developed for the KIN (Serabyn et al. 2006) to perform phase modulation with only two telescopes. In this configuration, both telescope pupils are spatially divided into two parts, creating two independent Bracewell interferometers (see Figure 6.4). The outputs of these two interferometers are then combined with a time-varying phase shift ($\varphi(t)$). Assuming that the final beam combination is done in a co-axial way on a beam combiner, the same background flux will be measured in both outputs of the beam splitter, simultaneously in time, allowing in theory a perfect background subtraction. A review of this technique in the context of the DARWIN mission has been presented by Hanot (2005).

There are two ways to perform the phase modulation, corresponding to two possibilities for the modulation function $\varphi(t)$:

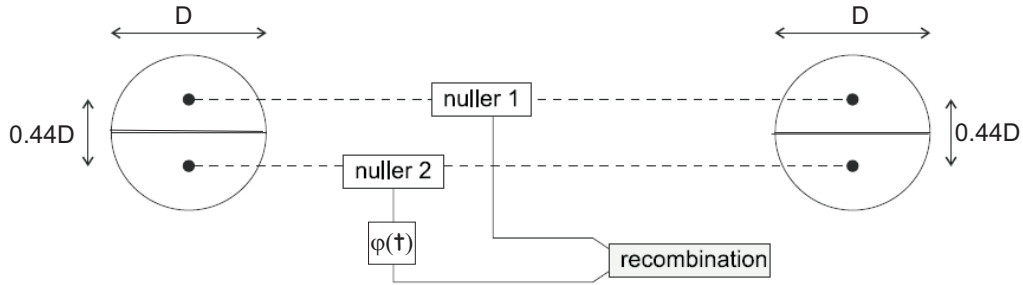


Figure 6.4: Principle of the pupil division technique (“split-pupil Bracewell”). The corresponding transmission maps are given in Figure 6.5.

- **Discrete phase modulation.** In this method, an achromatic phase shift is applied to one of the two nulled beams before the final combination so that the half pupils are put out of phase. In this condition, all coherent signals will be directed to only one of the two outputs of the beam splitter. A simple subtraction of the two detected fluxes will thus be sufficient to single out the coherent signals. In order to avoid potential systematic errors, the role of the two outputs should be repeatedly changed by putting the phase shift alternately in one or the other nulled beam. The transmission maps of the total instrument are illustrated in Figure 6.5, where the left top figure corresponds to a phase shift of $\pi/2$ and the right top figure to a phase shift of $3\pi/2$ between the semi-pupils.
- **Continuous phase modulation.** Phase modulation can also be implemented as a variation of the OPD in one arm of the interferometer (chromatic phase modulation). In this configuration, the background subtraction can benefit both from the variation of coherent signals in each output and from the fact that two complementary outputs are available.

The modulation map, proportional to the difference between the transmission maps (see Eq. 4.25), is shown in the bottom row of Figure 6.5, displaying a maximum rotational modulation efficiency of about 50%. Although splitting the pupil provides theoretically a perfect background subtraction, it also introduces significant additional complexity: instead of having only one nullder, this configuration requires two nullers and an additional beam combiner. Most of the hardware will thus be duplicated, including the control sub-systems, such as required for fringe tracking and intensity control.

6.2.3 The OPD modulation technique

The principle of OPD modulation is to scan back and forth the dark fringe of the transmission map by modulating the path length in one arm of the interferometer. In this way, all centro-symmetric sources are modulated at twice the modulation frequency. The principle of this technique is illustrated in Figure 6.6. Starting from a situation where the minimum of the transmission map (null) is centered on the star, any shift either to the left or the right will increase the stellar leakage. By placing the planet in between a crest and a valley (i.e. on the grey fringe), a shift of the transmission map to the right will decrease the planetary transmission while a shift to the left will increase it. As a result, the stellar leakage is modulated at twice the frequency as for any other symmetric source such as the exozodiacal cloud whereas the planetary signal is modulated at the modulation frequency (see Figure 6.6). Hence both signals can be separated in the frequency space, using synchronous coherent demodulation.

In principle, fast planet modulation could be implemented with only a little increase of the system complexity: a simple sinusoidal offset to the zero point setting of the OPD controller. However, OPD modulation is chromatic, i.e. the phase modulation amplitude varies as the inverse of the wavelength.

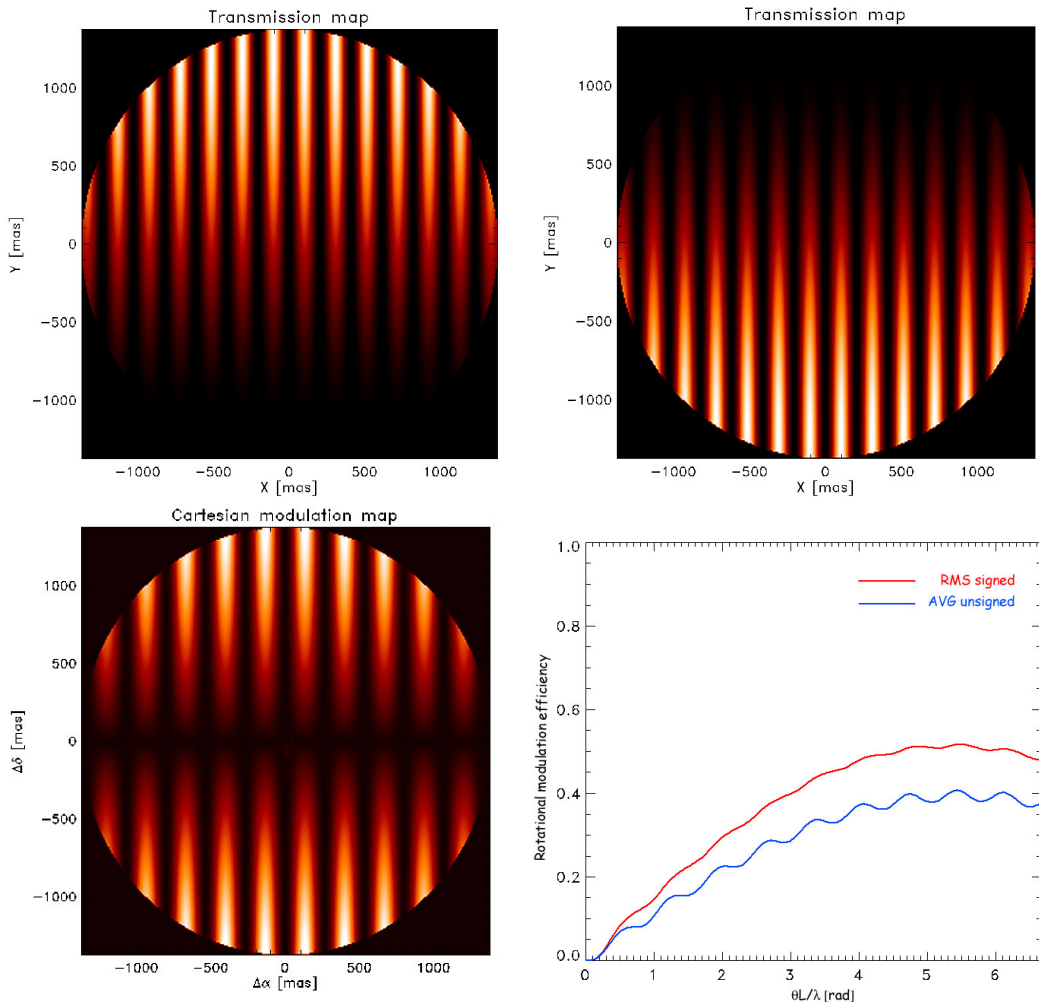


Figure 6.5: Top row: monochromatic transmission maps of a split pupil interferometer with 2-m collectors for a factor λ/b fixed at 2×10^{-6} (corresponding for example to $\lambda = 10 \mu\text{m}$ and a baseline length of 5 m). The left figure corresponds to $\varphi(t) = \pi/2$ while the right figure to $\varphi(t) = 3\pi/2$. Bottom row: corresponding modulation map (left) and rotational modulation efficiency (right).

The nominal response over the full bandwidth could be restored by modulating the phase of the beams, instead of their optical path length. At least one of the Achromatic Phase Shifter (APS) devices developed for DARWIN/TPF could operate as an achromatic phase modulator over the required range of ± 0.5 radian. Unfortunately, in presence of instrumental errors, the planetary signal is not the only signal to be modulated at the modulation frequency. If the null in the transmission map is not exactly centered on the star (e.g., due to a systematic offset or quasi-static residuals in the OPD between the arms), the part of the stellar disc that is asymmetric with respect to the modulation of the transmission map will start to act as a pseudo-planet. The instrumental errors are a severe limitation to this technique (D'Arcio et al. 2004).

6.3 Performance predictions for PEGASE and PEGASUS

Although GENIEsim is now able to simulate the performance of PEGASE and PEGASUS for planet detection, the results presented in this section have been obtained with another simulator. The main reason is because this study has been conducted before the adaptation of GENIEsim to space-based

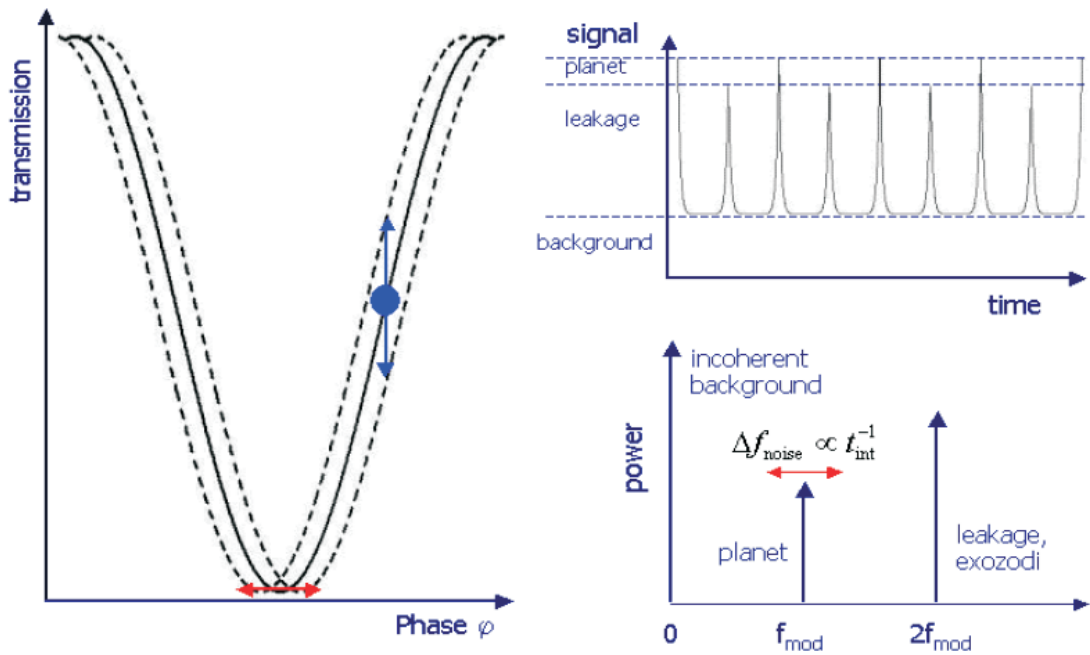


Figure 6.6: Principle of OPD modulation. By locating the planet on a grey fringe, any excursion of phase (OPD) induces a maximum change of the planetary signal, whereby in the illustrated case an increase of phase induces a decrease of planetary signal and vice versa. Provided the null in the transmission map is centered on the star, any phase excursion will only induce an increase in the stellar leakage. When the phase is modulated with a frequency f_{mod} , the stellar leakage is therefore modulated at twice this frequency, allowing a separation of the planetary signal from the leakage in frequency space. The more modulation cycles are present in the data, the sharper the lines in the frequency space will become (figure from den Hartog et al. 2004).

nulling interferometers. The simulation software used is built on excel work-sheets in combination with Visual Basic for Applications (VBA). It comes from a top-level performance prediction tool developed by O. Absil for PEGASE (Absil 2006) and several routines of the DARWIN science simulator, DARWINsim (see section 7.3.1 for more details, den Hartog 2005b). It can be considered as an approximation of GENIESim, with several simplifying assumptions. In particular, the most restrictive assumption is relative to the instability noise, only computed at the first order. This is a major limitation to the performance assessment since it has been shown that second order effects of the instability noise are the dominant noise contributors (Lay 2004). Performance comparisons with the GENIESim software indicate however similar results.

6.3.1 The simulation software

The initial simulation tool was a static excel worksheet, similar to the one described in Table 6.1, showing the output of the software for PEGASE and for 5 representative targets (τ Boo b, 55 Cnc b, 51 Peg b, 55 Cnc e and Gl 876 d). Any modification in the instrumental configuration or in the data of the target system results in an immediate update of the individual SNRs. The way to compute each cell value is thoroughly discussed in the thesis of Absil (2006) and briefly reminded in the paper hereafter (see section 6.3.2). In the following paragraphs, we give some details on the content of Table 6.1 necessary for the understanding of the table. Each group of lines is related to one specific aspect of the SNR computation:

- The “instrument” block describes the interferometer with its fundamental parameters such as collector diameter, baseline length, observing wavelength, spectral resolution, etc. The baseline length is always optimised so as to provide an optimum SNR at the optimum wavelength (in the PEGASE waveband in the present case). Note that the actual optimum baseline is smaller than the baseline which would locate the planet on a maximum of the transmission map (see the planetary transmission line). This is due to the fact that the planetary transmission does not significantly decrease when increasing the baseline, while stellar leakage is much more sensitive to the baseline length (see section 6.3.3 for more details). The values given for the total throughput and total emissivity both take into account the detector quantum efficiency. The instrumental rejection ratio is deduced from the contributions of OPD and tip-tilt errors, characterised by their standard deviation.
- The target star data come from the extrasolar planet encyclopedia (Schneider 2009) when available and otherwise from the DARWIN full extrasolar planet catalogue (Stankov 2005). The flux of the star is computed with a blackbody model. The total stellar flux on output is computed by considering both the geometric and the instrumental rejection ratios. The geometric rejection (the inverse of the nulling ratio) is computed using Eq. 4.15 while the instrumental rejection is computed using Eqs. 1 and 2 in the paper presented in section 6.3.2.
- The planetary parameters come also from the extrasolar planet encyclopedia (Schneider 2009) and the thermal and reflected emissions are computed according to Eq. 6 in the paper presented in section 6.3.2.
- The “background” block considers the emissions of the local zodiacal dust, computed using the model of Kelsall et al. (1998), and of the instrumental background, computed as a grey body with an emissivity given in the instrument block of the table. The background fluctuation is the standard deviation of the instrumental background and is only related to the temperature fluctuations of the payload. The output flux is computed by multiplying these contributions by the effective field-of-view area, i.e. $0.772(\lambda/D)^2$. The emission of the exozodiacal cloud is taken into account when necessary. This is the case for PEGASUS which works at longer wavelengths for which the exozodiacal emission becomes dominant. A specific routine (“exo_zodi.pro”) of DARWINsim has been used to assess the level of exozodiacal emission.
- The “individual” noise block summarizes the contribution of each source as a function of time. Due to its Poisson statistics, shot noise increases as the square root of time. Read-out noise shows the same time behaviour because the individual noise realisations produced in successive read-outs add up quadratically. The three other sources of noise are all proportional to the time. These contributions are in fact biases, i.e. the residues of imperfect calibration or subtraction processes. Instrumental nulling noise and stellar leakage calibration noise are both proportional to the stellar signal, while the background fluctuation noise is proportional to the background signal. The knowledge of the stellar diameter is assumed to be equal to 1% which gives a calibration accuracy for geometric stellar leakage of 2%. In addition to the new specifications of PEGASE, this explains the discrepancy with the previous performance assessment of PEGASE (Absil 2006).
- Using the integration time specified in the first line of this block, the individual signal-to-noise ratios are computed for the four noise sources. Shot noise and read-out noise are taken into account jointly in the detection SNR. While the latter increases as the square root of time, the three others remain the same whatever the integration time. It must be noted that, with an integration time of 10 hours, the detection SNR is already comfortably larger than the instrumental SNR for most targets. Longer integration times would thus only marginally improve the final SNR.
- The final SNR has been computed from the combination of the individual SNRs, assuming that the three biases, respectively related to calibration, instrumental errors and background fluctuations, add up linearly. Adding them quadratically as totally uncorrelated noise sources would be too

Table 6.1: Details of the computation of the final signal-to-noise ratio for five extrasolar planets. Full results are given in Section 6.3.3.

	<i>Tau Boo b</i>	<i>55 Cnc b</i>	<i>51 Peg b</i>	<i>55 Cnc e</i>	<i>Gl 876 d</i>
Instrument					
Diameter [m]	0.4	0.4	0.4	0.4	0.4
Optimum baseline [m]	70	50	61	89	59
Wavelength [μm]	4.5	5.5	5	5	5.5
Spectral resolution	60	60	60	60	60
Total throughput	0.042	0.042	0.042	0.042	0.042
Total emissivity	0.25	0.25	0.25	0.25	0.25
Calib. accuracy	0.02	0.02	0.02	0.02	0.02
Instrument temp. [K]	90	90	90	90	90
Rms temp. fluct. [K]	0.1	0.1	0.1	0.1	0.1
Rms OPD error [nm]	2.5	2.5	2.5	2.5	2.5
Rms pointing error [mas]	30	30	30	30	30
Instrumental nulling	323761	485855	400754	400754	485855
Star					
Distance [pc]	15.0	13.4	15.4	13.4	4.7
Spectral type	F7V	G8 V	G2 IV	G8 V	M4 V
Radius [R_\odot]	0.84	0.6	1.17	0.6	0.36
Angular radius [mas]	0.26	0.21	0.35	0.21	0.36
Effective temperature [K]	6309	5243	5770	5243	3500
Flux [Jy]	3.31	1.18	4.56	1.39	2.01
Geometric nulling	1039.8	4886.6	927.8	1244.5	1173.7
Total stellar nulling	1036.5	4838.0	925.6	1240.7	1170.9
Output flux [Jy]	1.3E-04	1.0E-05	2.1E-04	4.7E-05	7.2E-05
Output flux [ph-el/s]	8.48	0.65	13.07	2.98	4.56
Planet					
Semi-major axis [AU]	0.05	0.12	0.05	0.04	0.02
Mass $\times \sin(i)$ [M_J]	3.90	0.78	0.47	0.05	0.02
Radius [R_J]	1.6	0.9	0.8	0.4	0.3
Bond albedo	0.1	0.1	0.1	0.1	0.1
Equilibrium temp. [K]	1266.5	562.6	1285.7	978.7	683.9
Thermal flux [Jy]	7.1E-03	1.8E-04	1.6E-03	2.1E-04	2.8E-04
Reflected flux [Jy]	4.4E-05	8.7E-07	1.2E-05	1.4E-06	3.6E-06
Star/planet contrast	467	6394	2768	6565	7120
Interf. transmission	0.42	0.81	0.33	0.46	0.42
Output flux [Jy]	1.3E-04	6.3E-06	2.3E-05	4.1E-06	5.0E-06
Output flux [ph-el/s]	7.96	0.40	1.43	0.26	0.31
Background					
Local zodi [Jy/sr]	1.8E+05	6.7E+05	3.5E+05	3.5E+05	6.7E+05
Exo zodi [Jy/sr]	1.2E+05	1.1E+05	1.6E+05	1.1E+05	1.8E+05
Instr. brightness [Jy/sr]	4.1E+01	1.4E+04	1.0E+03	1.0E+03	1.4E+04
Rms bckg fluctuations [Jy/sr]	1.6E+00	4.6E+02	3.7E+01	3.7E+01	4.6E+02
Output flux [Jy]	6.2E-07	4.0E-06	1.4E-06	1.4E-06	4.1E-06
Output flux [ph-el/s]	2.0E-02	1.3E-01	4.5E-02	4.5E-02	1.3E-01
Individual noises					
Shot noise [ph-el/s $^{0.5}$]	4.1E+00	1.1E+00	3.8E+00	1.8E+00	2.2E+00
Detector noise [ph-el/s $^{0.5}$]	1	1	1	1	1
Instr. leakage noise [ph-el/s]	2.7E-02	6.5E-03	3.0E-02	9.2E-03	1.1E-02
Leakage calib. noise [ph-el/s]	1.7E-01	1.3E-02	2.6E-01	6.0E-02	9.1E-02
Bckg fluct. noise [ph-el/s]	6.0E-06	2.6E-03	1.7E-04	1.7E-04	2.6E-03
Individual SNRs					
Integration time [hours]	10	10	10	10	10
Detection SNR	361.4	51.3	68.8	23.9	24.3
Instrumental SNR	293.1	61.6	47.4	28.2	28.5
Calibration SNR	46.9	30.7	5.5	4.4	3.4
Bckg fluctuation SNR	1.3E+06	1.6E+02	8.4E+03	1.5E+03	1.2E+02
Final SNR	36.4	13.4	4.6	3.3	2.7

optimistic because the stellar calibration noise is expected to be correlated with instrumental leakage, which is itself correlated with the background subtraction noise through the instrumental temperature fluctuations (which also produce OPD and tip-tilt errors). The final SNR should thus be regarded as a minimum SNR.

This static worksheet is not convenient for optimisation purposes because it requires several attempts by trial and error, as well as an expert eye. For this reason, the corresponding software has been updated using Visual Basic for Application (VBA). The software now automatically performs various optimisations (e.g., wavelength, baseline length). For each wavelength, the optimum baseline length is computed. The software then compares the results at different wavelengths to give the optimum wavelength-baseline pair. This process can be executed on the whole list of known extrasolar planets as well as on the DARWIN/TPF catalogue. After the optimisation phase, the targets are sorted by ascending integration time, either in the optimum wavelength element (for spectroscopy) or on the full wavelength range (for detection). Considering 50% downtime and that each system has to be surveyed three times in order to reach a good confidence in case of non detection, the sorted list is cut off where the cumulative integration time exceeds the nominal survey period. The resulting list defines the number of targets that can be surveyed. Several other outputs are given such as the number of targets of a given spectral type which can be surveyed in a given time, the list of planets sorted by increasing integration time, decreasing SNR, etc.

6.3.2 Paper: *Potential of space-based infrared Bracewell interferometers for planet detection*

The following paper (Defrère et al. 2007) presents a performance study of space-based Bracewell interferometers. In particular, PEGASE and PEGASUS are addressed and their sensitivity for the detection of known extrasolar planets compared. The performance of PEGASUS to survey the HZ of nearby main sequence stars is also thoroughly addressed.

Potential of space-based infrared Bracewell interferometers for planet detection

D. Defrère^{*a}, O. Absil^b, C. Hanot^a and M. Fridlund^c

^a Institut d’Astrophysique et de Géophysique de Liège (IAGL), Université de Liège, Belgium

^b Laboratoire d’Astrophysique de l’Observatoire de Grenoble, France

^c Astrophysics Mission Division, ESA (ESTEC), The Netherlands

ABSTRACT

The Darwin and TPF-I space missions will be able to study the atmosphere of distant worlds similar to the Earth. Flying these space-based interferometers will however be an extraordinary technological challenge and a first step could be taken by a smaller mission. Several proposals have already been made in this context, using the simplest nulling scheme composed of two collectors, i.e., the original Bracewell interferometer. Two of these projects, viz. Pegase and the Fourier-Kelvin Space Interferometer, show very good perspectives for the characterisation of hot extra-solar giant planets (i.e., Jupiter-size planets orbiting close to their parent star). In this paper, we build on these concepts and try to optimise a Bracewell interferometer for the detection of Earth-like planets. The major challenge is to efficiently subtract the emission of the exo-zodiacal cloud which cannot be suppressed by classical phase chopping techniques as in the case of multi-telescopes nulling interferometers. We investigate the potential performance of split-pupil configurations with phase chopping and of OPD modulation techniques, which are good candidates for such a mitigation. Finally, we give a general overview of the performance to be expected from space-based Bracewell interferometers for the detection of extra-solar planets. In particular, the prospects for known extra-solar planets are presented.

Keywords: Nulling interferometry, space-based mission, extra-solar planets.

1. INTRODUCTION

Nulling interferometry is one of the most promising techniques to study extra-solar planets. The simplest way to implement it is to use a Bracewell interferometer.¹ The principle is to combine the beams coming from two telescopes in phase opposition so that a dark fringe appears on the line of sight, which strongly reduces the starlight emission while letting through the light from an off-axis source by adjusting the baseline length. This concept is used in several space mission projects, like Pegase² and the Fourier-Kelvin Stellar Interferometer,³ aiming at studying extra-solar giant planets (EGP) located close to their parent star. The detection of Earth-like planets is much more challenging due to the higher star/planet contrast. It requires a higher nulling stability over a longer period and specific methods of modulation to suppress the emissions of the local and exo-zodiacal clouds. This should be achieved by the Darwin⁴ and TPF-I⁵ projects, which are based on a more complex scheme of nulling using at least three collectors. These missions will achieve direct detection and atmospheric characterization of Earth-like planets orbiting in the habitable zone (HZ) of nearby main sequence stars (within ~ 30 pc). They will be fantastic tools to search for biological signatures in our vicinity.⁶ Beyond these ambitious objectives, the scientific goals of these missions also include the origin of the planetary systems, its evolutionary history and its future development. The study of hot EGP with Pegase or the Fourier-Kelvin Space Interferometer (FKSI) would already be very fruitful in that respect, but it would be interesting to know what could be achieved with a more advanced Bracewell concept. Improving the specifications of these missions, such as the size of the telescopes, could increase the sensitivity and give additional information on smaller planets. The goal of this study is to assess the performance of such a mission.

* E-mail: defrere@astro.ulg.ac.be, Telephone: 003243669713

2. INSTRUMENTAL CONCEPT

2.1 Overview of the Pegase design

This study considers the CNES formation flying demonstrator Pegase as a baseline.² Pegase consists in a two 40-cm diameter apertures interferometer observing in the near-infrared (2.5-5 μm) and formed of three free flying spacecrafsts orbiting at the Lagrange point L2. Thanks to this location, the spacecrafsts and the focal plane assembly can be passively cooled down to respectively $90 \pm 1 \text{ K}$ and $55 \pm 0.1 \text{ K}$. Visibility measurements and recombination in nulling mode are both possible with a spectral resolution of about 60. The formation flying constraints allow baseline lengths from 40 m to 500 m giving an angular resolution in the range of 0.5 mas to 30 mas. The fine-tuning of the optical path difference (OPD in the following) is performed by a dedicated control loop based on a fringe sensor measuring the observed central target in the 0.8-1.5 μm range and an optical delay line. The intensity control is performed by a fine pointing loop using a field relative angle sensor operating in the 0.6-0.8 μm range. This implementation allows to control the OPD down to a level of 2.5 nm rms and the tip/tilt errors to a value of 30 mas rms, corresponding to a nulling ratio of 10^{-4} stable at the level of 10^{-5} .²

2.2 Modifying Pegase

If Pegase was pointed towards a Solar system located at 20 pc, it would be inefficient for Earth-like planet detection for several reasons. The main show-stopper is the starlight cancellation which is not sufficiently stable and requires a better control of the OPD. Of minor relevance when observing hot EGPs, the local and exo-zodiacal clouds become very problematic for Earth-like planets and will be major sources of noise in the final budget. A way to improve the sensitivity of the instrument is to optimise the wavelength range of observation. Since Earth-like planets are cooler than hot EGPs, their maximum brightness is shifted toward longer wavelengths. For example, at 10 μm , the emission of an Earth is about 30 times larger than at 2.5 μm while the flux of the exo-zodiacal cloud increases only by a factor 4. In addition, the stellar flux decreases and is 10 times lower at 10 μm than at 2.5 μm . Nevertheless, increasing the observation wavelength is limited by the thermal emission of the instrument which becomes dominant at long wavelengths. The thermal specifications of Pegase would cause overwhelming background fluctuations for Earth-like planets detection. To reach this objective, the instrument has to be cooled down and more thermally stable. This is part of the optimisation presented in this study. The parameters used in our simulations are listed in Table 1.

Spectral	
Wavelength	10 μm
Resolution	60
Target system	
Distance	20 pc
Star radius	$1 R_{\text{Sun}}$
Star eff. temperature	5770 K
Star flux	0.56 Jy
Planet radius	$1 R_{\text{Earth}}$
Planet angular offset	50 mas
Planet eff. temperature	265 K
Planet flux	6.00E-8 Jy
Exo-zodi dust	1 solar system zodi
Local zodi brightness	1.13E+7 Jy/sr
Bracewell specifications	
Telescope diameter	1 m
Baseline length	20 m
Throughput	7%

Table 1. Parameters used in this study

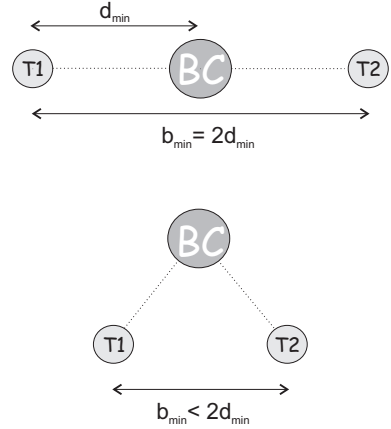


Figure 1. Above: nominal linear flying configuration of Pegase with a central beam combiner. Bottom: modified flying configuration of Pegase allowing a shorter interferometric baseline length.

The observing scenario is based on the one of Pegase. Since the inclination and the position angle of the planetary orbit are unknown, three observations with baselines separated by 60° will be obtained on each target. By consequence, the bright fringe will be closer than 30° from the actual planet position angle for at least one observation and the planet flux will be reduced by a maximum of 5% in the worst case. In addition, since the ephemeris of the planet is unknown, 3 different sets of observations along the orbit are necessary to reach a high level of confidence in case of non detection. A duty cycle of 50% is also considered.

Finally, assuming a minimum anti-collision baseline length of 20 m (d_{\min}), the linear configuration of Pegase with a central beam combiner is not convenient to survey the habitable zone of most F and G stars of the Darwin catalogue^{7,8} which require baselines shorter than 40 m at $10 \mu\text{m}$. To solve this problem, a triangular flying configuration is considered, with the beam combiner spacecraft at equal distance from collector spacecrafs (see Figure 1).

3. SIGNALS AND NOISES IN SPACED-BASED INTERFEROMETRY

3.1 Instrumental stellar leakage

In nulling interferometry, a key quantity is the null depth which determines the level of on-axis stellar rejection. This null depth undergoes fluctuations due to instrumental imperfections such as co-phasing errors, wavefront errors or mismatches in the intensities of the beams. The influence of all these contributions is called instrumental leakage, which acts both as bias, by introducing an additional amount of unwanted signal in the nulled output, and as a noise through its instability. Assuming that the instrument behaves in the same way during the three successive observations of the same system, the average instrumental stellar leakage can be calibrated and only instability noise (including long-term drifts) and shot noise associated to the mean stellar leakage have to be considered in the total noise budget.

Leakage due to the OPD

Since the actual power spectral densities of instrumental perturbations are not available, the estimation of instability noise will be made assuming that the rms leakage is equal to its mean value. This assumption is supported by the results obtained on the GENIE and ALADDIN studies.^{9,10} The contribution of the residual OPD error to the stellar leakage can be estimated using the following formula:¹¹

$$\sigma_{\text{OPD}} \leq \frac{\lambda}{\pi} \sqrt{N_i}, \quad (1)$$

where N_i is the required stability for the instrumental nulling ratio. This means that a stability at the level of $\sigma_{\text{OPD}} \leq 1 \text{ nm}$ is required to cancel the star emission by a factor of 10^7 at an observing wavelength of $10 \mu\text{m}$. Very encouraging results have been obtained recently with the adaptive nuller¹² at Jet Propulsion Laboratory with the demonstration of a broadband null of 1.2×10^{-5} over a 32% bandwidth centered in the $8\text{-}12 \mu\text{m}$ band*. Reaching a stability of 1 nm at $10 \mu\text{m}$ is still challenging but should be realistic in the near-term future.¹³ This value will be considered in this study. Note however that Eq. 1 is a first order estimation and does not take into account the non-linear second order error terms which are expected to dominate the instrumental leakage.¹⁴

Leakage due to tip/tilt errors

The other major contributors to the stellar leakage are the wavefront errors and the intensity mismatch between the beams. Because modal filtering is used, wave front errors will be traded against intensity errors which are less severe source of instrumental leakage and add to the true intensity mismatch. In fact, true intensity errors are not expected to be a significant source of intensity mismatch and will be neglected in the following discussion. The instrumental nulling ratio N_i due to the tip-tilt error can be estimated with the following formula, taking into account the modal filtering process:¹⁵

$$N_i = \frac{(\pi D \sigma_\theta)^4}{64 \lambda^4}, \quad (2)$$

*see the adaptive nuller website: <http://planetquest.jpl.nasa.gov/TPF-I/adaptiveNullerTestbed.cfm>

where D is the telescope diameter and σ_θ the residual tip/tilt error. The tip-tilt control device which will be implemented in Pegase should reach a typical residual of 30 mas rms.² At 10 μm and for 1-m size telescopes, a tip/tilt residual below 22 mas rms is necessary to get an SNR of 5 for an Earth located at 20 pc. The use of larger telescopes in combination with a two-stage control loop implementation will improve the pointing accuracy with respect to the Pegase nominal value (30 mas rms). Without an appropriate system study, it is difficult to give an accurate estimation of this value but a tip/tilt residual of 20 mas rms should not be too optimistic and will be assumed in this study.

3.2 Geometric stellar leakage

Because of the finite size of the target star, a residual stellar flux appears in the nulled output. This deterministic part of the stellar leakage is called the geometric leakage and is given by:¹⁰

$$N = \frac{\pi^2}{4} \left(\frac{b\theta_*}{\lambda} \right)^2, \quad (3)$$

where b is the baseline length and θ_* the stellar angular radius. At 10 μm , the contribution of geometric leakage for a Sun-like star located at 20 pc is about 125 times larger than the flux of the planet in the nulled output. To reveal the hypothetic planetary companion, the most straightforward method relies on the knowledge of the target star angular radius, which is the only unknown parameter in Eq. 3. The angular radii of Darwin target stars can be determined with a typical accuracy of 1% which gives a precision of 2% on the estimation of the stellar leakage.¹⁶ This level of calibration is however not sufficient to get a SNR of 5 for an Earth located at 20 pc.

3.3 The thermal background and its fluctuations

Exo-zodiacal dust emission

An exo-zodiacal cloud similar to the local zodiacal disk is much brighter than an Earth-like planet with an integrated flux about 400 times larger at 10 μm . Filtered through the interferometer transmission map, the residual contribution does not exceed 30% of the total flux for a disk located at 20 pc. In addition, since several observations of the same system will be performed, the morphology of the dust cloud can be constrained and model-fitted. Taking into account both contributions, a conservative value of 10% is assumed in this study for the residual exo-zodiacal emission. To go further, fast modulation techniques have been developed in the context of Darwin/TPF but they require the use of at least 3 collectors.^{1,17} More specific methods such as the split-pupil configuration and the OPD modulation have to be used for a single Bracewell.^{18,19} These good candidates are reviewed by Hanot²⁰ and briefly discussed in section 5.3.

Local zodiacal dust emission

The local zodiacal dust cloud produces a foreground through which the interferometer will observe. Its thermal emission is estimated by the zodiacal disk model of Kelsall.²¹ The model takes into account the dust in the line of sight of the interferometer located at the Lagrange point L2 and pointing in the anti solar direction. At 10 μm , the total background emission associated with the local zodiacal disk is about 2×10^{-4} times larger than the flux coming from an Earth at 20 pc and received by an 1-m telescope. This emission presents a slow variation with typical periods of 13, 27, 36, 47, 52, and 72 days²¹ which are very problematic for long integration times. However, for integration times of the order of some hours, the variation of this emission can be considered as negligible²² and remains below the residual contribution of the exo-zodiacal cloud.

Instrumental background

The thermal emission of the instrument is modelled as a grey body emission, i.e. a black-body emission multiplied by a constant emissivity factor related to the optical train. The mean value of the instrumental background can be removed with the three inclined observations and only the fluctuations remain. In order not to induce significant variations of the background emission, a high thermal stability is therefore required. To detect at 10 μm an Earth located at 20 pc (SNR of 5), the thermal stability has to be as low as 0.1 K rms for an instrument cool down to 45 K.

4. ANALYSIS FOR AN EARTH AT 20 PC

Following the previous discussion, Table 2 shows the different requirements on a 1-m Bracewell to achieve at 10 μm an SNR of 5 when observing an Earth located at 20 pc. It also shows the specifications considered for this study and the minimum size of the planet (located in the middle of the HZ) detectable with it.

	Req.	Spec.	R_{Earth}
OPD [nm]	0.47	1	2.1
Tip/tilt [mas]	22	20	0.8
Stellar radius knowledge [%]	0.8	1	3.6
Exo-zodiacal subtraction [%]	0.05	10	11.2
Instrument temperature [K]	45.3	45	1
Integration time [days]	3000		
20 surveys/year [h]	-	24	5.7
50 surveys/year [h]	-	10	7.2
100 surveys/year [h]	-	5	8.5

Table 2. First column: requirements on an 1-m Bracewell to detect an Earth-like planet located at 20 pc at 10 μm . Second column: specifications of the 1-m Bracewell considered in this study. Third column: minimum radius of the planet detectable with it. The shot and detector noises impose a lower limit on the integration time and the three last rows give the minimum radius of the planet detectable in 5, 10 or 24 hours (corresponding respectively to 100, 50 or 20 systems surveyed per year).

Due to the limited suppression of the exo-zodiacal emission, a 1-m aperture single Bracewell could not detect planets smaller than Jupiter (about 11 R_{Earth}) and orbiting in the middle of the HZ of a Sun located at 20 pc. With an appropriate method to subtract the exo-zodiacal emission, 7 Earth-radii planets would be possible to detect in 10 hours which corresponds to 50 systems surveyed per year. In 24 hours, the detection of 6 Earth-radii planets could be achieved and potentially 4 Earth-radii planets for a longer integration time. The reason is that the limitation coming from the integration time is due to the shot and detector noises which can be minimized by a sufficiently long integration time as shown by Eq. 4, giving the SNR per spectral channel:

$$\text{SNR}_n = \frac{F_p \cdot t}{\sqrt{(N_s^2 + N_d^2)t + (\sigma_i + \sigma_c + \sigma_b)t}}, \quad (4)$$

where F_p is the planet's flux, N_s the shot noise, N_d the detector noise, σ_i the instrumental nulling noise, σ_c the instrumental calibration noise, σ_b the background fluctuation noise and t the integration time. Shot noise is dominated mainly by the stellar leakage and the contribution from the local zodiacal cloud. The detection unit features a Si:As focal plane array with a read out noise assumed to amount to 10 electrons per pixel. Dark current is supposed to be negligible by cooling down the detector to an appropriate temperature (a few K). The SNR per spectral element is represented by the solid line in Figure 2 with respect to the wavelength.

Figure 2 shows that the optimum wavelength is effectively near 10 μm and that the exo-zodiacal emission is dominant in the 5-12 μm band. In order to improve the detection capability, one can combine the spectral channels, using Eq. 5:¹⁴

$$\text{SNR}_{\text{tot}} = \left[\sum_{n_{\text{indep}}} \text{SNR}_n^2 \right]^{1/2}, \quad (5)$$

where the sum is performed over the noise independent spectral channels. Determining their number would require a full analysis and is beyond the scope of this paper (some clues are given in the paper of Lay¹⁴). For the time being, with a spectral resolution of 60, the spectral channels are narrow at 10 μm (about 0.16 μm wide) and we will assume than only 10% of the channels are noise independent (about 1.6 μm wide). The percentage of noise independent spectral channels is denoted η in the following.

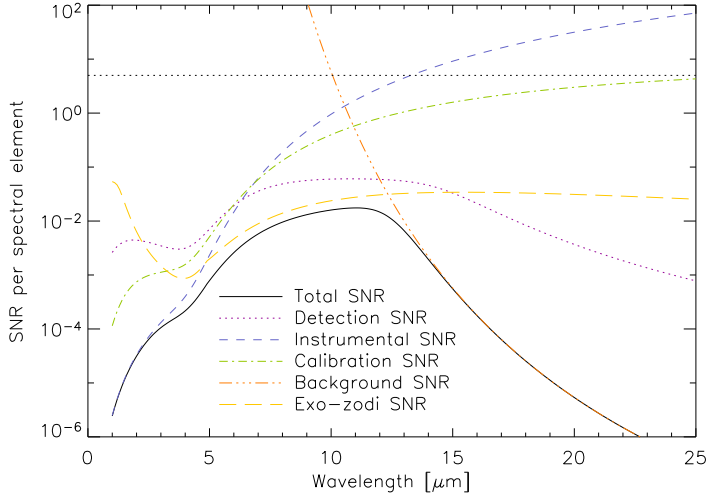


Figure 2. Individual SNRs contributing to the total SNR (solid line) for an Earth-like planet located at 20pc with respect to the wavelength, after 10 hours of integration and 1-m diameter collectors.

5. DETECTION THRESHOLD

5.1 Planet signal

In good approximation, the flux emitted by an extra-solar planet and detected by an Earth-based observer writes:¹⁶

$$F_p(\lambda) = A_b \frac{\pi R_\star^2}{d^2} B_\lambda(T_\star) \Phi(\Theta) \frac{R_p^2}{4a^2} + \frac{\pi R_p^2}{d^2} f(\Theta) B_\lambda(T_p), \quad (6)$$

where $B_\lambda(T)$ represents the surface brightness per wavelength unit for a blackbody at temperature T , d is the distance to the target star, a the semi-major axis of the planetary orbit and R_p the planetary radius. $\Phi(\Theta)$ and $f(\Theta)$ are the phase function affecting respectively the reflected and the emitted emissions. A_b is the Bond albedo, defined as the ratio between the total reflected and total incident powers. The first term in Eq. 6 represents the reflected part of the stellar spectrum while the second term represents the thermal emission of the planet. T_p is the equilibrium temperature of the planet and can be calculated by the following formula:¹⁶

$$T_p = T_\star (1 - A_b)^{1/4} \left(\frac{R_\star}{2a} \right)^{1/2}. \quad (7)$$

The Bond albedo used to compute the equilibrium temperature depends on several parameters such as the chemical composition of the planet's atmosphere and surface. The results presented in this paper assume a Bond albedo of 0.306 for rocky planets by analogy to the Earth's albedo, although the surface and the potential atmosphere are probably not the same. This value has also the advantage to be intermediate among the Bond albedos of the Solar system rocky planets (0.119 for Mercur and 0.750 for Venus). For the giants planets, a value of 0.10 is assumed as derived by Baraffe²³ for hot EGPs instead of Jupiter's classical value of 0.342, since the regions close to the star will mostly be investigated. Finally, following the simulations of core accretion reported by Ida,²⁴ the limit between gaseous and rocky planets will be considered around 15 Earth masses.

5.2 Results for a Sun at 20 pc

The purpose of this section is to extend the analysis presented in the previous sections by considering planets with different orbits. This general approach requires numerical simulations which have been done by adapting a top-level performance prediction tool developed by O. Absil for Pegase¹⁶ and using several routines from the Darwin science simulator, DARWINsim.²⁵ A crucial parameter in the performance assessment is the distance

between the planet and its parent star. In accordance with Eq. 6 and Eq. 7, the closer the planet is to its parent star the brighter it is, which improves also the contrast with the background sources. The optimum wavelength is also modified since the planet becomes hotter. Optimizing the wavelength in agreement with the semi-major axis of the planet's orbit, the detection threshold, i.e. the minimum size of the planet detectable, is represented in Figure 3 for a Sun-like star located at 20 pc (the detection threshold for detection is set at a global SNR of 5). For practical reasons (it is difficult to cover the full wavelength range with one set of glasses and single-mode spatial filters), the width of the total wavelength band has been set to 4 μm .

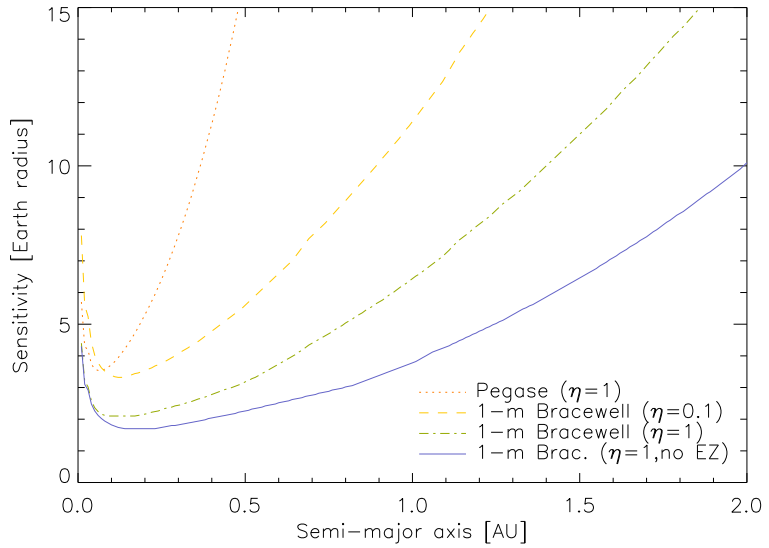


Figure 3. Sensitivity of Pegase (dotted), 1-m Bracewell with respectively 10% (dashed) and 100% (dash-dot) independent spectral channels and without exo-zodiacal cloud (solid) for 10 hours integration time and observing a Sun-like star located at 20 pc. For each semi-major axis, the sensitivity is computed in the optimum 4- μm wide wavelength band.

Each curve represents the detection threshold for an integration time of 10 hours (about 50 surveys per year). The dotted curve shows the sensitivity domain of Pegase assuming a perfect combination of the spectral channels ($\eta=1$) in the 2.5-5 μm wavelength range. The best sensitivity arises for planets located very close to the star with 4 Earth-radii planets detectable at about 0.05 AU and Jupiter-size planets detectable till 0.4 AU. Including the exo-zodiacal emission, the dash-dot curve shows the improvement of the capabilities by considering a 1-m Bracewell working at 10 μm . Jupiter-size planets are detectable till about 1.6 AU while in the middle of the HZ, Neptune-size planets could be detected. Rocky planets are detectable in the close vicinity of the star (~ 0.1 AU). Going further, the solid curve shows the potential of the concept on the basis of 10 hours integration time, assuming a perfect subtraction of the exo-zodiacal emission in addition to the perfect combination of the spectral channels ($\eta = 1$). Small Neptune-like planets orbiting around a Sun located at 20 pc are detectable within 10 hours in the middle of the HZ. Shot noise is now the limiting factor and a longer integration time is required to improve the sensitivity.

Finally, a more realistic assessment of the capabilities is given by the dashed curve, plotted considering that only 10% of the spectral channels are independent. This curve gives also an approximation of the minimum size of planets for which spectroscopy can be performed. As expected from the previous section, the performance would be limited to Jupiter-size planets in the middle of the HZ.

5.3 Removing the exo-zodiacal emission

As shown by Table 2, the residual of the exo-zodiacal emission is the main limiting factor. The level of performance could be considerably improved (4 Earth-radii instead of Jupiter-size planets detectable) by removing it from the nulled output. The basic method to modulate the planet signal against the exo-zodiacal emission is to

rotate the interferometer along the line of sight but this can generally not be performed sufficiently fast and the planet signal is easily corrupted by long term drifts. Fast modulation can be implemented with the split-pupil configuration¹⁸ or with OPD modulation.¹⁹ In the case of split-pupil, both telescopes are divided in two parts, creating two independent Bracewell interferometers. The outputs of these two interferometers are then combined with a time-varying phase shift which allows to remove all point-symmetric emissions (in the ideal case). The division of the pupil introduces however significant additional complexity.¹⁶ The principle of OPD modulation is to sweep back and forth the dark fringe of the transmission map by modulating the pathlength in one arm of the interferometer.¹⁹ In that manner, all centro-symmetric sources are modulated at twice the modulation frequency. If the baseline length is chosen such as the planet locates on a grey fringe, the planet signal will be modulated at the modulation frequency and can be retrieved by using synchronous coherent demodulation. In principle, OPD modulation could be implemented at little increase of the system complexity. For both methods, only 50% of the planet signal is generally retrieved which reduces the actual performance. In his master thesis, Hanot shows that the split-pupil technique leads to better SNRs than the OPD modulation but remains pessimistic about the ability of both methods to reveal Earth-like planets in presence of instrumental errors and typical asymmetries of the cloud.²⁰ A full investigation of these techniques will be the object of an upcoming paper.

5.4 Study of the habitable zone: application to the Darwin catalogue

The application to the Darwin catalogue^{7,8} allows to extend the study to stars of different spectral types. The prime targets of the catalogue, i.e. the single star systems, amount to 628 stars (43 F, 100 G, 244 K and 241 M stars), in our close neighbourhood (≤ 25 pc). Around each of these stars, a planet is supposed to be present in the middle of the HZ. Expressed in AU, the position of the HZ is given in good approximation by the following formula:²⁶

$$r_{\text{HZ}} = \left(\frac{T_{\star}}{T_{\odot}} \right)^2 \frac{R_{\star}}{R_{\odot}}, \quad (8)$$

which corresponds to 2.3, 1.3, 0.7 and 0.2 AU for F0V, G0V, K0V and M0V stars respectively. To estimate the performance of a 1-m Bracewell, the integration time required to reach an SNR of 5 for each target of the Darwin catalogue is computed. The SNRs are computed with the assumption that there is no exo-zodiacal emission so that the full potential of methods described in section 5.3 can be reached. The spectral channels are combined in the optimum 4- μm wide wavelength range with $\eta=1$. Note that according to Eq. 4, only the part of the SNR due to the shot and detector noises can be improved by increasing the integration time. Targets for which $\sigma_i + \sigma_c + \sigma_b > 5F_p$ cannot reach an SNR of 5 and are thus not considered. The integration times of the remaining targets are then sorted by increasing values and added till the sum reaches the mission lifetime. The results are presented in Figure 4 which indicates the number of stars around which a planet of a given radius can be detected during the mission lifetime.

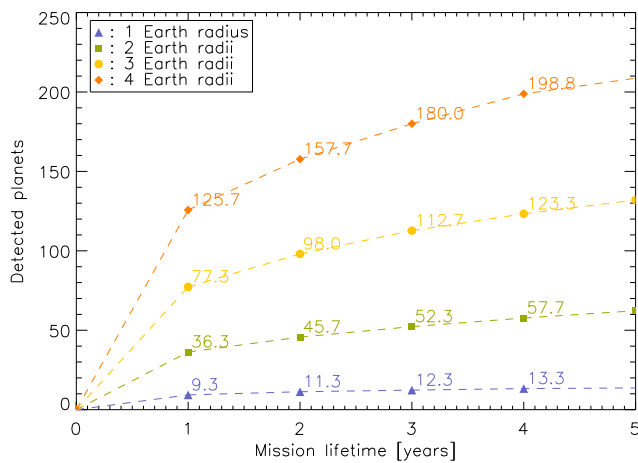


Figure 4. Number of stars around which a planet of a given radius can be detected with respect to the mission lifetime.

During the first year of the mission, about 9 Earth-like or 36 two Earth-radii planets could be detected. A planet is considered detected when a total SNR of 5 is reached for at least one of the three observations for each position on the orbit. The gain by increasing the mission lifetime is not significative, particularly for the smallest planets. These detected planets are mainly around M stars as illustrated in Figure 5, showing the total integrated SNR for a rocky planet of 2 Earth radii and an integration time of 10 hours.

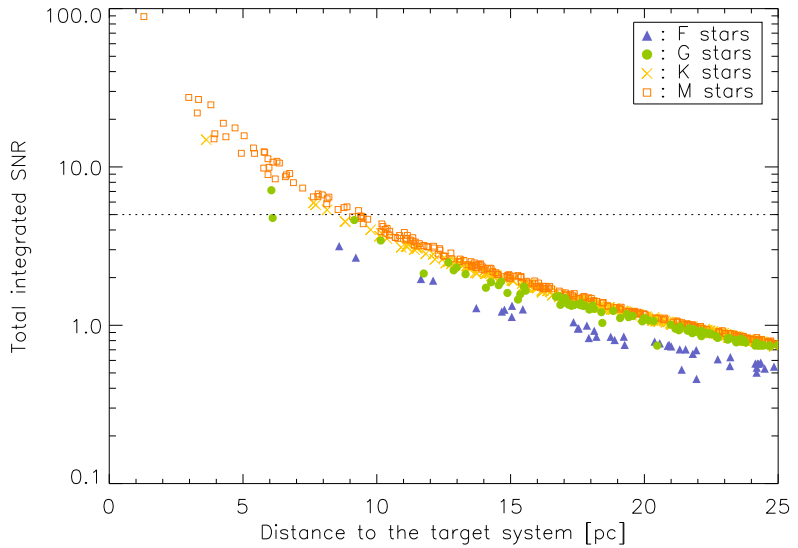


Figure 5. Total SNR for a two Earth-radii planet orbiting in the middle of the HZ of Darwin targets and for an integration time of 10 hours (assuming no exo-zodiacal cloud).

While an SNR of 5 is out of reach for F stars, all M-star planets within \sim 10 pc could be detected as well as several K-star and 1 G-star planets. M stars have been identified as relevant targets for future HZ planet search programs²⁷ and would therefore be very good candidates to survey. Note also that all 2 Earth-radii planets located beyond 10 pc would not be detectable. In conclusion, the Bracewell interferometer presented in this study would be a convenient instrument to search M stars located within 10 pc for planets of 2 Earth-radii. Some K and G stars might also be added to the target list.

5.5 Application to known extra-solar planets

Whereas 246 extra-solar planets have been discovered so far[†], only 61 of them are in our close vicinity (closer than 25 pc). Considering a sample of these 61 favorable targets, Table 3 gives the SNRs achievable by Pegase, the classic Bracewell with 1-m diameter telescopes including the noise contribution of the exo-zodiacal emission (1-m Bracewell) or not (1-m+ configuration), in the optimum spectral element and for an integration time of 10 hours. By definition, the 1-m+ configuration gives upper limits on the actual SNRs that we could expect from the split-pupil configuration and the OPD modulation technique.

Defining the good candidates for spectroscopy as those for which an SNR of 5 can be achieved in the optimum spectral element, Pegase could perform spectroscopy on 9 of the 61 targets (about 15%), including 3 planets in the hot regime (closer than 0.1 AU from its parent star, see for instance τ Boo *b* and 51 Peg *b* in Table 3) and 6 cooler planets like 70 Vir *b* and 55 Cnc *b*. These results suggest that the Pegase target list could be extended to a significant number of planets outside the hot regime (see the master thesis of Defrère²⁸ for the SNRs of the full target list).

[†] see <http://exoplanet.eu/catalog.php> or <http://exoplanets.org/> for an up-to-date list.

	Star			Planet			SNR		
	spectral type	dist. [pc]	eclipt. lat.	s-maj. axis [AU]	Min. mass [M _{Jup}]	T _{eq} [K]	Peg.	1-m	1-m+
Ups And b	F8V	13.5	28.9	0.06	0.69	1570	2	3	4
Ups And c	F8V	13.5	28.9	0.83	1.98	420	2	18	41
Ups And d	F8V	13.5	28.9	2.53	3.95	240	0	4	14
Tau Boo b	F7V	15.6	26.5	0.05	3.90	1270	36	79	85
55 Cnc b	G8V	13.4	10.4	0.12	0.78	560	13	47	76
55 Cnc c	G8V	13.4	10.4	0.24	0.22	390	1	10	22
55 Cnc d	G8V	13.4	10.4	5.26	4.00	80	0	0	0
55 Cnc e	G8V	13.4	10.4	0.04	0.05	980	3	7	8
70 Vir b	G5V	18.1	21.3	0.48	7.44	500	6	39	59
51 Peg b	G2V	15.4	25.2	0.05	0.47	1290	5	8	9
HD 69830 b	K0V	12.6	-0.55	0.08	0.03	830	2	4	5
HD 69830 c	K0V	12.6	-0.55	0.19	0.04	540	1	5	7
HD 69830 d	K0V	12.6	-0.55	0.63	0.06	290	0	2	3
GI 581 b	M3	6.26	10.26	0.04	0.05	675	3	13	18
GI 581 c	M3	6.26	10.26	0.07	0.02	510	0	4	7
GI 581 d	M3	6.26	10.26	0.25	0.02	205	0	0	1
Gliese 876 b	M4V	4.7	-6.6	0.21	1.93	220	0	18	47
Gliese 876 c	M4V	4.7	-6.6	0.13	0.56	270	1	22	53
Gliese 876 d	M4V	4.7	-6.6	0.02	0.02	680	3	7	9

Table 3. Sample of known extra-solar planets located within 25 pc from our solar system given with the SNRs achievable by Pegase, the classic 1-m Bracewell and the 1-m Bracewell without exo-zodiacal cloud (1-m+). The SNRs are given per spectral element at the optimum wavelength and for an integration time of 10 hours.

The use of the 1-m classic Bracewell allows to go up to 27 of the 61 targets (about 45%), including 5 of the 9 remaining planets in the hot regime (see for instance *55 Cnc e*, the hot-Neptune *Gliese 876 d* and *GI 581 b* in Table 3). Finally, with the 1-m+ configuration, spectroscopy can be performed on 38 targets, which represents about 60% of known extra-solar planets within 25 pc. The achievable SNRs can also be much better as illustrated by the *Ups And* system. More interesting, a SNR of 7 could be achieved in 10 hours on the recently discovered planet orbiting close to the HZ of its star, *GI 581 c*. Since the values given for the 1-m+ configuration are only upper limits, a realistic assessment of the capabilities of split-pupil/OPD modulation techniques would be the ability to do spectroscopy on 45 to 60% of all known extra-solar planets within 25 pc.

6. SUMMARY AND CONCLUSION

Infrared nulling interferometry is the core technique of several projects dedicated to the study of extra-solar planets. The most promising in terms of scientific return is undoubtedly the Darwin/TPF missions which should enable the spectroscopy of Earth-like planets in our close vicinity (within 30 pc). The achievement of this objective requires a complex scheme of nulling using at least 3 beam collectors. In this paper, we assess the capabilities of a simpler version of Darwin/TPF, which apart from consisting in only two 1-m diameter telescopes, presents Darwin-like specifications. The study is based on the infrared Bracewell interferometer Pegase, aimed at studying known hot Jupiters located within 150 pc. The main challenge to detect an Earth-like planet is the exo-zodiacal cloud which is 400 times brighter than an Earth located at 20 pc (at 10 μm). Specific methods to mitigate the exo-zodiacal emission in the case of Bracewell interferometers (viz. OPD modulation and split-pupil configuration) are addressed and results are given separately from those of the classic scheme (without the implementation of these methods).

Around a Sun located at 20 pc, the Bracewell interferometer presented in this study could detect in one year about 50 Neptune-like planets ($M \sim 0.05 \text{ M}_{\text{Jup}}$) orbiting in the middle of the habitable zone. The application to the Darwin catalogue has shown that smaller planets could be detected, with about 40 two Earth-radii planets detectable the first year of the mission. In particular, this “upgraded” Pegase or “down-scoped” Darwin would

be a very efficient instrument to search M stars located within 10 pc for planets of 2 Earth-radii. Finally, 45% of the 61 known extra-solar planets in the close vicinity of the solar system (within 25 pc) could be surveyed for spectroscopy instead of 15% with Pegase. This value reaches 60% if the exo-zodiacal emission is efficiently subtracted. These preliminary results need to be confirmed by detailed simulations, taking particularly into account the continuous rotation of the array and second order effects of the instability noise.

ACKNOWLEDGMENTS

The authors would like to thank R. den Hartog for his expert advice. Thanks also to J. Surdej, P. Riaud, D. Mawet and A. Magette for their contribution to the work presented in this paper. The first author acknowledges the financial support from the Belgian National Science Foundation (“FRIA”).

REFERENCES

1. R. N. Bracewell, “Detecting nonsolar planets by spinning infrared interferometer,” *Nature* **274**, pp. 780–+, Aug. 1978.
2. J. M. Le Duigou, M. Ollivier, A. Léger, F. Cassaing, B. Sorrente, B. Fleury, G. Rousset, O. Absil, D. Mourard, Y. Rabbia, L. Escarrat, F. Malbet, D. Rouan, R. Clédassou, M. Delpech, P. Duchon, B. Meyssignac, P.-Y. Guidotti, and N. Goriüs, “Pegase: a space-based nulling interferometer,” *Presented at the Society of Photo-Optical Instrumentation Engineers (SPIE) Conference 6265*, July 2006.
3. R. K. Barry, W. C. Danchi, L. D. Deming, L. J. Richardson, M. J. Kuchner, S. Seager, B. J. Frey, A. J. Martino, K. A. Lee, M. Zuray, J. Rajagopal, T. T. Hyde, R. Millan-Gabete, J. D. Monnier, R. J. Allen, and W. A. Traub, “The Fourier-Kelvin stellar interferometer: a low-complexity low-cost space mission for high-resolution astronomy and direct exoplanet detection,” *Presented at the Society of Photo-Optical Instrumentation Engineers (SPIE) Conference 6265*, July 2006.
4. C. V. M. Fridlund, L. d’Arcio, R. den Hartog, and A. Karlsson, “Status and recent progress of the Darwin mission in the Cosmic Vision program,” *Presented at the Society of Photo-Optical Instrumentation Engineers (SPIE) Conference 6268*, July 2006.
5. C. Beichman, P. Lawson, O. Lay, A. Ahmed, S. Unwin, and K. Johnston, “Status of the terrestrial planet finder interferometer (TPF-I),” *Presented at the Society of Photo-Optical Instrumentation Engineers (SPIE) Conference 6268*, July 2006.
6. L. Kaltenegger, W. A. Traub, and K. W. Jucks, “Spectral Evolution of an Earth-like Planet,” *ApJ* **658**, pp. 598–616, Mar. 2007.
7. A. Stankov, “All sky target stars catalogue - no limit in ecliptic latitude,” 2005.
8. L. Kaltenegger, C. Eiroa, A. Stankov, and M. Fridlund, “Nearby Stellar sample for the search for terrestrial planets. Target star catalogue for the Darwin Mission Study,” *A&A* , 2007 (submitted).
9. O. Absil, V. Coudé du Foresto, M. Barillot, and M. Swain, “Nulling interferometry: comparison of performances between Antarctica and other ground-based sites,” *A&A* , 2007 (submitted).
10. O. Absil, R. den Hartog, P. Gondoin, P. Fabry, R. Wilhelm, P. Gitton, and F. Puech, “Performance study of ground-based infrared Bracewell interferometers. Application to the detection of exozodiacal dust disks with GENIE,” *A&A* **448**, pp. 787–800, Mar. 2006.
11. M. Ollivier, *Contribution à la recherche d’exoplanètes coronographie interférentielle pour la mission Darwin*. PhD thesis, Université Paris-Sud, Paris, France, 1999.
12. R. D. Peters, O. P. Lay, A. Hirai, and M. Jeganathan, “Adaptive nulling for the Terrestrial Planet Finder Interferometer,” *Presented at the Society of Photo-Optical Instrumentation Engineers (SPIE) Conference 6268*, July 2006.
13. P. Lawson, “Results of Laboratory Experiments Kin Nulling Interferometry (1998-2006),” in *the proceedings of the TPF/Darwin 2006 conference*, 2006.
14. O. P. Lay, “Systematic Errors in Nulling Interferometers,” *Appl. Opt.* **43**, pp. 6100–6123, Nov. 2004.
15. B. Mennesson, M. Ollivier, and C. Ruillier, “Use of single-mode waveguides to correct the optical defects of a nulling interferometer,” *Journal of the Optical Society of America A* **19**, pp. 596–602, Mar. 2002.

16. O. Absil, *Astophysical studies of extrasolar planetary systems using infrared interferometric techniques*. PhD thesis, Liège University, Liège, Belgium, 2006.
17. O. Absil, A. Karlsson, and L. Kaltenegger, “Inherent modulation: a fast chopping method for nulling interferometry,” in *Interferometry in Space. Proceedings of the SPIE, Volume 4852*, M. Shao, ed., pp. 431–442, Feb. 2003.
18. E. Serabyn, “An overview of the Keck Interferometer Nuller,” in *ESA SP-539: Earths: DARWIN/TPF and the Search for Extrasolar Terrestrial Planets*, M. Fridlund, T. Henning, and H. Lacoste, eds., pp. 91–98, Oct. 2003.
19. L. L. D’Arcio, A. L. Karlsson, and P. A. Gondoin, “Use of OPD modulation techniques in nulling interferometry,” in *New Frontiers in Stellar Interferometry, Proceedings of SPIE Volume 5491*, W. A. Traub, ed., pp. 851–+, Oct. 2004.
20. C. Hanot, “Investigation of a down scoped version of the darwin mission,” Master’s thesis, Liège University, Liège, Belgium, 2005.
21. T. Kelsall, J. L. Weiland, B. A. Franz, W. T. Reach, R. G. Arendt, E. Dwek, H. T. Freudenreich, M. G. Hauser, S. H. Moseley, N. P. Odegard, R. F. Silverberg, and E. L. Wright, “The COBE Diffuse Infrared Background Experiment Search for the Cosmic Infrared Background. II. Model of the Interplanetary Dust Cloud,” *ApJ* **508**, pp. 44–73, Nov. 1998.
22. C. Leinert, S. Bowyer, L. K. Haikala, M. S. Hanner, M. G. Hauser, A.-C. Levasseur-Regourd, I. Mann, K. Mattila, W. T. Reach, W. Schlosser, H. J. Staude, G. N. Toller, J. L. Weiland, J. L. Weinberg, and A. N. Witt, “The 1997 reference of diffuse night sky brightness,” *A&AS* **127**, pp. 1–99, Jan. 1998.
23. I. Baraffe, G. Chabrier, T. S. Barman, F. Allard, and P. H. Hauschildt, “Evolutionary models for cool brown dwarfs and extrasolar giant planets. The case of HD 209458,” *A&A* **402**, pp. 701–712, May 2003.
24. S. Ida and D. N. C. Lin, “Toward a Deterministic Model of Planetary Formation. I. A Desert in the Mass and Semimajor Axis Distributions of Extrasolar Planets,” *Astrophysical Journal of Physics* **604**, pp. 388–413, Mar. 2004.
25. R. den Hartog, “The DARWINsim science simulator,” Tech. Rep. Issue 1, ESA (SCI-A/297), May 2005.
26. J. F. Kasting, D. P. Whitmire, and R. T. Reynolds, “Habitable Zones around Main Sequence Stars,” *Icarus* **101**, pp. 108–128, Jan. 1993.
27. J. Scalo, L. Kaltenegger, A. G. Segura, M. Fridlund, I. Ribas, Y. N. Kulikov, J. L. Grenfell, H. Rauer, P. Odert, M. Leitzinger, F. Selsis, M. L. Khodachenko, C. Eiroa, J. Kasting, and H. Lammer, “M Stars as Targets for Terrestrial Exoplanet Searches And Biosignature Detection,” *Astrobiology* **7**, pp. 85–166, Feb. 2007.
28. D. Defrère, “Performance study of spaced-based infrared nulling interferometers,” Master’s thesis, Liège University, Liège, Belgium, 2007.

6.3.3 Complementary results

More detailed results

In the paper presented in the previous section, the results are given for a representative sample of known extrasolar planets. In order to provide a more complete performance overview, Table 6.2 hereafter lists all the extrasolar planets known within 25 pc (in September 2007) and gives the expected SNRs at the optimum wavelength and for the different instrumental configurations. Note that several targets located

	Star			Planet			SNR		
	spectral type	dist. [pc]	eclipt. lat.	s-maj. axis [AU]	Min. mass [M _J]	T _{eq} [K]	Peg.	1-m	1-m+
HD 33564b	F6 V	21.0	-	1.10	9.10	294	1	13	45
Tau Boo b	F7V	15.0	7.55°	0.05	3.90	1267	36	79	85
Ups And b	F8V	13.5	-34.3°	0.06	0.69	1567	2	3	4
Ups And c	F8V	13.5	15.1°	0.83	1.98	418	2	18	41
Ups And d	F8V	13.5	-44.7°	2.53	3.95	239	0	4	14
HD 10647b	F8V	17.4	35.4°	2.10	0.91	205	0	1	2
HD 19994b	F8V	22.4	24.9°	1.30	2.00	222	0	1	4
HD 210277b	G0	21.3	-54.7°	1.10	1.23	268	0	3	7
47 Uma b	G0V	13.7	-30.7°	2.11	2.60	212	0	2	7
47 Uma c	G0V	13.7	-47.5°	7.73	1.34	111	0	0	0
HR 810b	G0V	15.5	-61.0°	0.91	1.94	402	1	17	30
HD 39091b	G1IV	20.6	-76.0°	3.29	10.35	221	0	4	9
HD 142b	G1IV	20.6	-44.5°	0.98	1.00	272	0	3	8
51 Peg b	G2IV	15.4	-19.8°	0.05	0.47	1286	5	8	9
rho CrB b	G2V	17.4	43.3°	0.22	1.04	680	7	20	31
HD 160691e	G3IV-V	15.3	-28.4°	0.92	0.52	311	0	5	11
HD 195019b	G3IV-V	20.0	36.6°	0.14	3.70	865	15	43	49
HD 147513b	G3/G5V	12.9	-43.6°	1.26	1.00	239	0	4	9
HD 160691d	G3V	15.3	-49.3°	0.09	0.04	994	1	2	3
HD 160691b	G3V	15.3	47.2°	1.50	1.67	243	0	4	10
HD 160691c	G3V	15.3	56.9°	4.17	3.10	146	0	0	0
70 Vir b	G4V	22.0	57.9°	0.48	7.44	502	6	39	59
HD 4308b	G5V	21.9	-60.2°	0.11	0.05	747	1	5	6
HD 134987b	G V	25.0	-7.09°	0.78	1.58	324	0	9	14
16 Cyg b	G5V	21.4	7.56°	1.67	1.68	269	0	4	8
HD 190360b	G6IV	15.9	48.9°	3.92	1.50	203	0	1	2
HD 190360c	G6IV	15.9	48.9°	0.13	0.06	1125	0	1	1
GJ 3021b	G6V	17.6	-43.1°	0.49	3.32	363	2	18	60
55 Cnc b	G8V	13.4	10.4°	0.12	0.78	563	13	47	76
55 Cnc c	G8V	13.4	10.4°	0.24	0.22	389	1	10	22
55 Cnc d	G8V	13.4	10.4°	5.26	3.92	83	0	0	0
55 Cnc e	G8V	13.4	10.4°	0.04	0.05	979	3	7	8
HD 114783b	K0	22.0	-20.8°	1.20	0.99	199	0	1	1
HD 128311b	K0	16.6	-28.3°	1.01	2.18	210	0	3	5
HD 128311c	K0	16.6	-9.18°	1.76	3.21	159	0	1	1

	Star			Planet			SNR		
	spectral type	dist. [pc]	eclipt. lat.	s-maj. axis [AU]	Min. mass [MJ]	T _{eq} [K]	Peg.	1-m	1-m+
HD 62509b	K0IIIb	10.3	-	1.69	2.90	500	0	2	2
HD 3651b	K0V	11.1	-19.6°	0.28	0.20	439	1	12	20
Gl 86 b	K0V	10.9	-53.3°	0.11	4.01	679	34	52	139
14 Her b	K0V	18.1	31.7°	2.80	4.64	141	0	0	0
HD 69830b	K0V	12.6	4.72°	0.08	0.03	833	2	4	5
HD 69830c	K0V	12.6	4.72°	0.19	0.04	541	1	5	7
HD 69830d	K0V	12.6	4.72°	0.63	0.06	294	0	2	3
HD 164922b	K0V	21.9	-	2.11	0.36	165	0	0	0
HD 189733b	K1-K2	19.3	-	0.03	1.15	1143	12	28	30
HD 27442b	K2 IV	18.1	-76.3°	1.18	1.28	528	0	2	2
Gam Cep b	K2V	11.8	64.7°	2.04	1.60	393	0	3	3
Eps Eri b	K2V	3.2	-5.95°	3.39	1.55	123	0	1	1
HD 99492b	K2V	18.0	33.0°	0.12	0.11	594	2	9	11
HD 192263b	K2V	19.9	4.72°	0.15	0.72	522	6	22	37
GJ 674b	M2.5	4.5	-	0.04	0.04	492	3	17	23
GJ 436b	M3	10.2	-23.5°	0.03	0.07	619	3	8	13
Gl 581b	M3	6.3	-	0.04	0.05	506	3	13	18
Gl 581c	M3	6.3	-	0.07	0.02	379	0	4	7
Gl 581d	M3	6.3	-	0.25	0.02	205	0	0	1
GJ 849b	M3.5	8.8	-	2.35	0.82	78	0	0	0
GJ 317b	M3.5	9.2	-	0.95	1.20	105	0	0	0
GJ 317c	M3.5	9.2	-	0.95	0.83	105	0	0	0
Gliese 876b	M4V	4.7	-70.5°	0.21	1.94	216	0	18	47
Gliese 876c	M4V	4.7	-63.6°	0.13	0.56	274	1	22	53
Gliese 876d	M4V	4.7	-37.1°	0.02	0.02	684	3	7	9
SCR 1845b	M8.5 V	3.9	-	4.50	8.50	33	0	0	0

Table 6.2: Known extrasolar planets located within 25 pc from the solar system given with the SNRs achievable by PEGASE, PEGASUS (“1-m” row) and PEGASUS in the absence of exozodiacal clouds (“1-m+” row). The SNRs are given per spectral element at the optimum wavelength and for an integration time of 10 hours.

beyond 25 pc could also be surveyed by PEGASE and PEGASUS (as shown by Absil 2006).

The results of Table 6.2 are discussed in Section 5.5 of the paper presented in section 6.3.2. In order to have a global overview of the capabilities of each instrument, Figure 6.7 gives the SNR achievable by PEGASE (left) and PEGASUS (right) with respect to the minimum mass and the semi-major axis of each planet. PEGASE (resp. PEGASUS) could achieve SNRs larger than 10 for 5 targets (resp. 15). Unlike PEGASE, PEGASUS could also achieve SNRs larger than 1 for most targets.

Optimum baseline

Figure 6.8 shows the simulated signal-to-noise ratio as a function of the baseline length for three different wavelength (1.5 μ m, 3 μ m and 5 μ m), and for the observation of the hot giant planet 51 Peg b (a total integration time of 10 hours has been considered). Since the maximum angular separation between 51

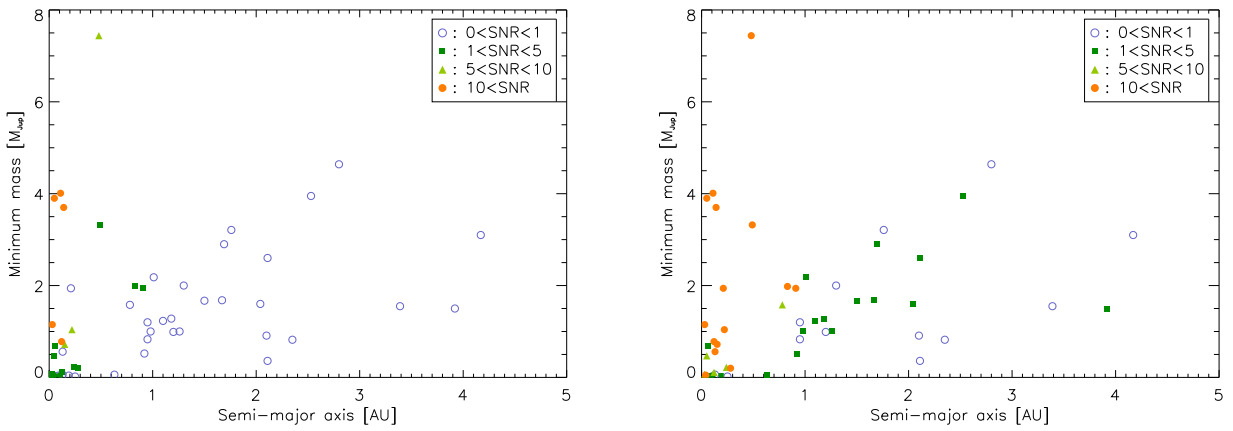


Figure 6.7: Expected SNR at the optimum wavelength for PEGASE (left) and PEGASUS (right), given with respect to the planetary semi-major axes and minimum masses.

Peg b and its host star is 3.385 mas, the baseline lengths which locate 51 Peg b on a maximum of each transmission map should be 46 m, 91 m and 152 m, respectively at $1.5 \mu\text{m}$, $3 \mu\text{m}$ and $5 \mu\text{m}$ (according to Eq. 4.4). However, as illustrated in Figure 6.8, the optimum baseline lengths are smaller and correspond to interferometric transmissions not necessarily close to 1 (see Table 6.1). This behaviour is due to the fact that the planetary transmission does not significantly decrease when increasing the baseline, while stellar leakage is much more sensitive to the baseline length (see the discussions on the stellar leakage in Chapter 4). This conclusion supports and reinforces the relevance of shorter-baseline configurations, as for the detection of exozodiacal discs (see section 5.4).

6.4 Performance predictions for FKSI

In this section, the performances of FKSI for super-Earth extrasolar planet detection and characterization are investigated. We consider FKSI in its nominal architecture, i.e. a structurally-connected Bracewell interferometer with 0.5-m aperture telescopes located 12.5 m from each other and operating in the infrared regime ($3\text{-}8 \mu\text{m}$, see a detailed description of FKSI in section 5.2.2). Unlike the previous performance predictions computed for PEGASE and PEGASUS, we use the GENIESim software (Absil et al. 2006a) which has been adapted to simulate space-based Bracewell interferometers and used to investigate the performance of PEGASE/FKSI for exozodiacal disc detection (Defrère et al. 2008).

6.4.1 Detection of known super-Earths

Among the known super-Earths, we have chosen a representative sample of 4 planets for which we have computed the signal-to-noise ratio (SNR). The first three planets belong to the same system and orbit HD 40307, a K2.5V star located at 13 pc. HD 40307b, HD 40307c and HD 40307d present masses of 4.2, 6.9 and $9.2 M_{\oplus}$ and semi-major axes of 0.047, 0.081 and 0.134 AU (Mayor et al. 2009b). The fourth extrasolar planet (HD 285968b) orbits at 0.066 AU around a M2.5V star located at 9.4 pc and has a mass of $8.4 M_{\oplus}$ (Forveille et al. 2009). We assume that each planetary system is seen face-on and presents an exozodiacal cloud with the same density as the solar zodiacal cloud. The typical orbital period is a few days so that the planet moves significantly across the transmission map during the integration time. To cope with that, we consider two modes of observation: staring and rotating. For a staring interferometer, the telescopes follow the orbital motion of the planet so that the signal remains at the same position on the transmission map during the observation. This has the advantage to maintain

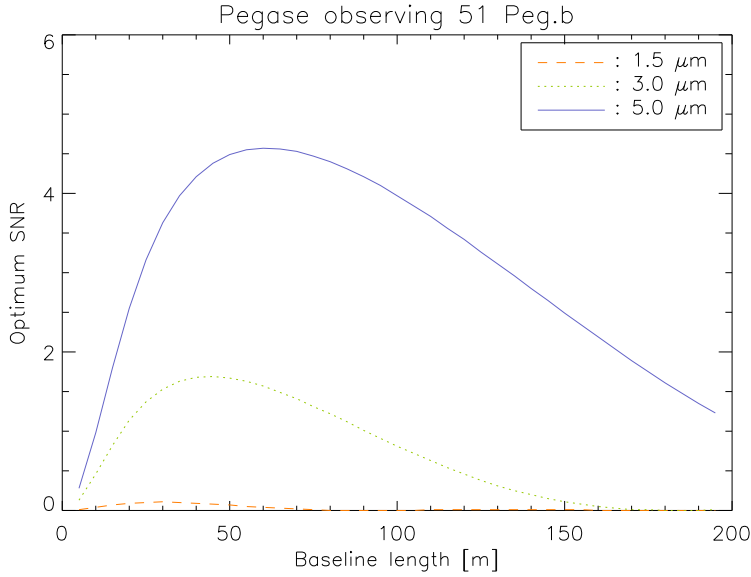


Figure 6.8: Simulated signal-to-noise ratio as a function of the baseline length of PEGASUS for three different wavelengths ($1.5\text{ }\mu\text{m}$, $3\text{ }\mu\text{m}$ and $5\text{ }\mu\text{m}$), and for the observation of the hot giant planet $51\text{ Peg }b$. A total integration time of 10 hours has been considered.

an optimum transmission of the planetary signal during the observation. On the other hand, this has the disadvantage to be sensitive to geometric stellar leakage, mean instrumental leakage, background noise and exozodiacal dust emission. Several calibration procedures have been proposed to mitigate the impact of these noise contributors, but they come with their own precision. Techniques such as OPD modulation (D'Arcio et al. 2004) could be useful but will not be addressed here. For a rotating array, the telescope array moves around the beam combiner so that the planet signal is modulated as it crosses bright and dark fringes of the transmission map. The advantage of rotating FKSI is that geometric leakage, mean instrumental leakage, background noise and exozodiacal dust emission are constant during the observation and hence not modulated. The different calibration procedures used in the case of the staring interferometer are therefore not necessary and the planet signal is retrieved at the end by synchronous demodulation. The results of our simulations are shown in Figure 6.9 for a staring (left) and a rotating (right) interferometer.

For both staring and rotating FKSI, the SNR remains below 5 for all targets and all wavelengths for an integration time of 24 hours (corresponding typically to a full rotation of the interferometer). For the staring case, increasing the integration time would have basically no influence on the SNR which is dominated by the non-perfect calibration of the geometric leakage at short wavelengths and by the exozodiacal cloud emission at long wavelengths. For the rotating FKSI, increasing the integration time would improve the SNR since the shot noise is dominant for all targets and all wavelengths. Stellar leakage dominates the shot noise at short wavelengths while the exozodiacal dust emission and the detector noise dominate at long wavelengths. To get an SNR of 5 for the most favorable target (HD 40307d) across the whole wavelength range, the integration time has to be increased by a factor 5^2 , which gives 25 days of observation. Another advantage of rotating the interferometer is that the SNR is likely dominated by shot noise so that combining the spectral channels improves the SNR. For instance, combining the spectral channels over the whole wavelength range gives SNRs of about 3, 7, 10 and 4 for HD 40307b, HD 40307c, HD 40307d and HD 285968b respectively.

Due to the fixed baseline, the planet signal falls mostly into the null rather than on the maximum of the transmission map for these known super-Earth extrasolar planets. Consequently, only a few percents of the planetary signal make it to the nulled output. For instance, the maximum transmission is only

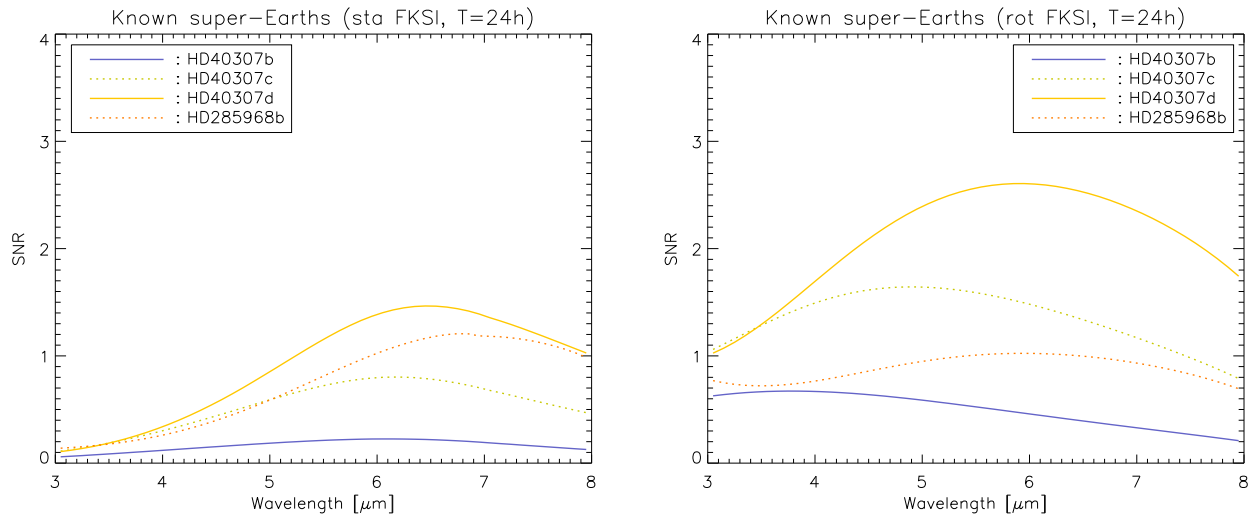


Figure 6.9: Signal-to-noise ratio provide by FKSI with respect to wavelength for 4 known super-Earth extrasolar planets and an integration time of 24 hours. Left and right figures show the results for a staring and a rotating interferometer respectively.

Table 6.3: Comparison between the position of the maximum transmission ($3 \leq \lambda \leq 8 \mu\text{m}$) and the characteristic position of the habitable zone of the target systems.

	Max. trans.	Pos. HZ	Max. FKSI
	[AU]	[AU]	[AU]
M0V-05pc	0.12-0.33	0.09	<0.05
K0V-08pc	0.20-0.53	0.68	0.05
G0V-10pc	0.25-0.66	1.16	0.1
F0V-15pc	0.37-0.99	2.33	0.2

of about 1%, 4%, 12% and 6% for HD 40307a, HD 40307c, HD 40307d, and HD 285968b respectively. The modulation efficiency, indicating the part of the signal which is retrievable by synchronous demodulation, is also very weak (about 0.5%, 1.3%, 3.3% and 1.2% for HD 40307b, HD 40307c, HD 40307d, and HD 285968b respectively). The maximum transmission and the modulation efficiency are obviously better for planets with a larger semi-major axis. However, the improvement is addressed by the lower planetary emission at larger star-planet distances. We discuss this issue in the next section.

6.4.2 General sensitivity

In this section, we investigate the sensitivity of FKSI in the rotating mode for a hypothetical 2-R_\oplus super-Earth planet orbiting around 4 different targets: a M0V star located at 5 pc, a K0V star at 8 pc, a G0V star at 10 pc and a F0V star at 15 pc. These fiducial targets have been chosen to cover the 4 spectral types present in the DARWIN/TPF catalogue (Kaltenegger et al. 2008) and at distances favorable for our purpose. The results are shown in Figure 6.10, which gives the integrated SNR with respect to the semi-major axis of the planet for an integration time of 24 hours.

Considering an SNR of 5 as the criterion of detection, FKSI could detect within 24 hours all the 2-R_\oplus extrasolar planets orbiting closer than about 0.3, 0.5 and 0.7 AU from the K0V star located at 8 pc, the G0V star at 10 pc and the F0V star at 15 pc respectively. The shape of the sensitivity curves is driven by the decrease of the modulation efficiency at short semi-major axes and the decrease of the planetary temperature at long semi-major axes. The maximum of the sensitivity curve shifts towards longer semi-

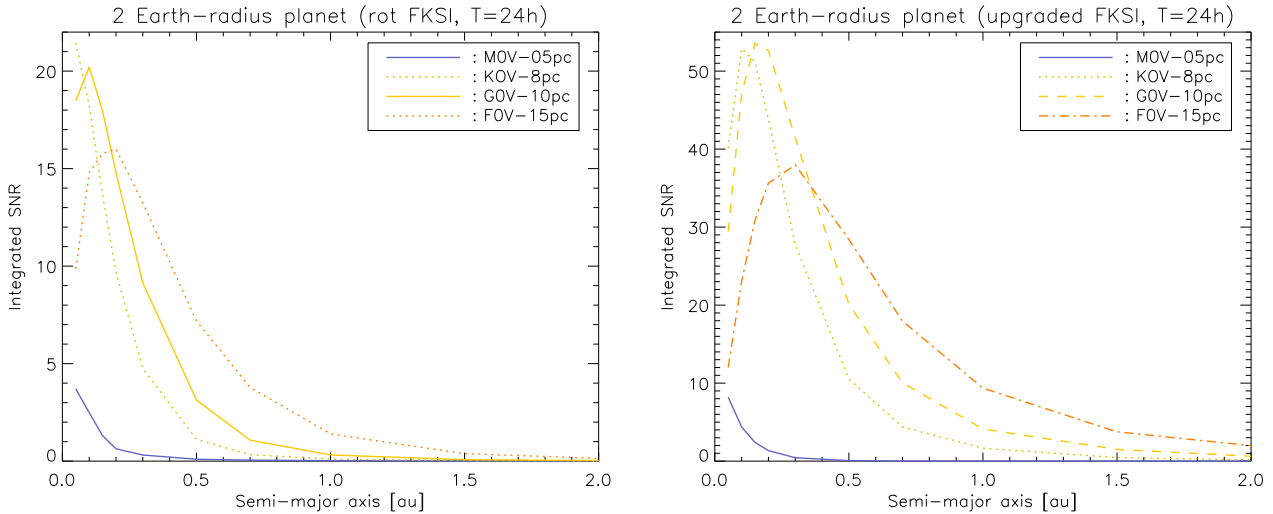


Figure 6.10: *Left:* Signal-to-noise ratio with respect to the semi-major axis for a $2-R_{\oplus}$ planet orbiting each of the 4 fiducial stars. *Right:* Same figure computed for the upgraded FKSI.

major axes with the stellar temperature since the planet becomes brighter for a given position. The maximum SNR is however smaller for hotter stars due to the higher geometric stellar leakage. In all cases, the SNR is maximum for semi-major axes shorter than the region where the response of the interferometer is optimum (see Table 6.3). A trade-off with the increase of the geometric leakage has to be made to define the optimum baseline length.

Considering the characteristic position of the habitable zone (HZ²⁰, see Table 6.3), the left part of Figure 6.10 shows that the SNR is about 2 for the M0V star located at 5 pc, and well below 1 for the three others fiducial targets. To detect $2-R_{\oplus}$ planets in the middle of the habitable zone, longer integration times are necessary: 4 days for the M0V star located at 5 pc and more than 100 days for the three other targets. To reduce this integration time, there are several possibilities. The most efficient ways are to consider larger aperture telescopes and a wavelength range extended to $10\ \mu\text{m}$, where the planet brightness peaks for Earth-like planets located in the middle of the habitable zone. Increasing the baseline length, on the other hand, would have a negative impact on the integration time for planets located in the middle of the habitable zone. This is because the geometric leakage increases with the baseline length and the modulation efficiency does not vary significantly beyond the first bright fringe (the HZ is likely located at larger distances than the position of the first bright fringe, see Table 6.3). These results are in agreement with a previous study reporting that a 1-m aperture Bracewell interferometer operating at $10\ \mu\text{m}$ would be efficient to detect $2-R_{\oplus}$ extrasolar planets around M stars located within 10 pc (Defrère et al. 2007).

6.4.3 An enhanced version of FKSI

The Goddard Space Flight Center (GSFC) is currently studying an enhanced FKSI mission concept with 1-2 m class telescopes (see Fig. 6.11) to increase the sensitivity to low-mass extrasolar planets located in the habitable zone of nearby main sequence stars. This enhanced FKSI would be passively cooled down to 40 K so that the system could operate at longer wavelengths (5-15 μm). Using GENIESim, the performance of this enhanced version of FKSI (1-m telescopes, 40 K, 20-m baseline and 5-15 μm wavelength range) has been investigated. The results are presented in the right part of Figure 6.10.

²⁰According to Kasting et al. (1993), the position of the habitable zone expressed in AU is given in good approximation by $r_{\text{HZ}} = (T_{\star}/T_{\odot})^2 R_{\star}/R_{\odot}$.

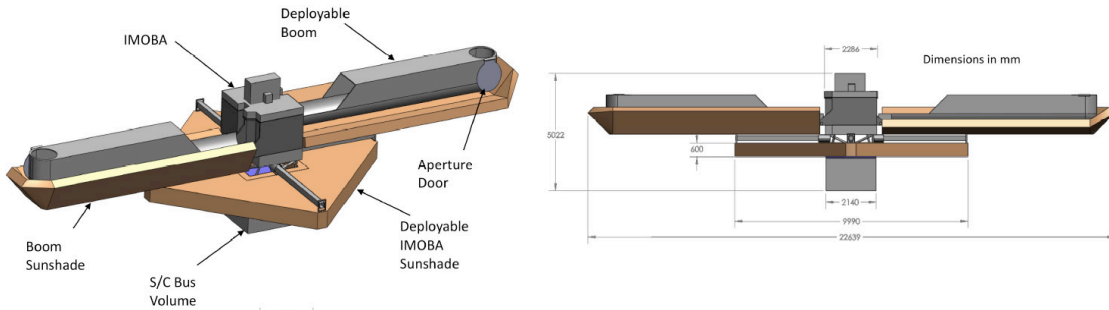


Figure 6.11: Overview of the enhanced version of FKSI, presenting two 1.2 m class telescopes located 20 m from each other on a boom (Courtesy Richard Barry).

Figure 6.10 shows that the enhanced FKSI can detect (with $\text{SNR} > 5$) $2-R_{\oplus}$ planets at semi-major axes less than 0.1, 0.7, 1.0, and 1.4 AU for an M0V star at 5 pc, a K0V star at 8 pc, a G0V star at 10 pc, and an F0V star at 15 pc. Compared to the nominal FKSI (see the left part of Figure 6.10), the maximum SNR is higher and shifted towards longer semi-major axes so that the sensitivity for extrasolar planets located in the habitable zone is largely improved. Note however, that we have assumed a perfect modulation by rotation, i.e. rotation sufficiently fast to get rid of the low-frequency instrumental leakage. At this point, we need a better model for OPD perturbations than the one provided by CNES for 0.4-m apertures. Using this model with 1-m telescopes, GENIEsim computes a very optimistic residual RMS OPD error of 0.8 nm so that instrumental leakage is underestimated. Further investigations are necessary in that respect.

6.5 Summary

After the performance study for exozodiacal dust cloud detection reported in Chapter 5, we investigate in this chapter the performance for planet detection of PEGASE and FKSI. Considering the nominal mission designs, we show that these space-based Bracewell interferometers would be able to study most extrasolar planets known so far. In a second step, we investigate the performance of enhanced versions of PEGASE and FKSI, which have been specifically tuned to probe the habitable zone of nearby main sequence stars. We show that these enhanced concepts would be very efficient to study “super-Earth” extrasolar planets ($\sim 2 - 10 M_{\oplus}$) orbiting M stars located within 10 pc. Performance improvements are also considered by addressing specific modulation techniques (namely the split-pupil and OPD modulation techniques) to mitigate the harmful exozodiacal emission. In order to enable the spectroscopic characterization of Earth-like extrasolar planets around F-, G- and K-type stars, more complex nulling interferometers have been defined. We report in the next chapter a performance study of such an instrument.

The exo-Earth characterization missions

Contents

7.1	The DARWIN/TPF mission	149
7.1.1	Instrumental concept	149
7.1.2	Scientific objectives	151
7.2	Instability noise	152
7.3	Science performance predictions	155
7.3.1	DARWINsim, the DARWIN science simulator	155
7.3.2	Paper: <i>Nulling interferometry: Impact of exozodiacal clouds on the performance of future life-finding space missions</i>	157
7.4	Summary	176

*E*arth-sized planets around nearby stars are now being detected by ground-based radial velocity and space-based transit surveys. In order to detect directly the light from these planets, both ESA and NASA have identified nulling interferometry as one of the most promising techniques. Based on the recent convergence between ESA and NASA on the mission architecture, a concept comprising 4 telescopes has emerged (Emma X-array). This nulling interferometer will operate in the mid-infrared regime (from 6 to $20\mu\text{m}$), where the star/planet contrast (10^7) is more favourable than in the visible (10^{10}), and where suitable atmospheric signatures (CO_2 , H_2O , O_3) can be found to assess the presence of biological activity on the detected planets. After a brief introduction of the instrumental concept, this chapter presents the simulated performance for Earth-like planet detection and characterization. The impact of exozodiacal cloud on the mission performance is specifically addressed.

7.1 The DARWIN/TPF mission

7.1.1 Instrumental concept

Considerable efforts have been carried out in the past decade by both ESA and NASA to define a mission design that provides excellent scientific performance while minimizing cost and technical risks. After the investigations of several interferometer architectures, these efforts culminated in 2005-2006 with two parallel assessment studies of the DARWIN mission, carried out by EADS Astrium and Alcatel-Alenia Space. Two array architectures have been thoroughly investigated during these industrial studies: the four-telescope X-array (Leger et al. 2009) and the Three-Telescope Nuller (TTN, Karlsson et al. 2004). These studies included the launch requirements, payload spacecraft, and the ground segment during which the actual mission science would be executed. Almost simultaneously, NASA/JPL initiated a

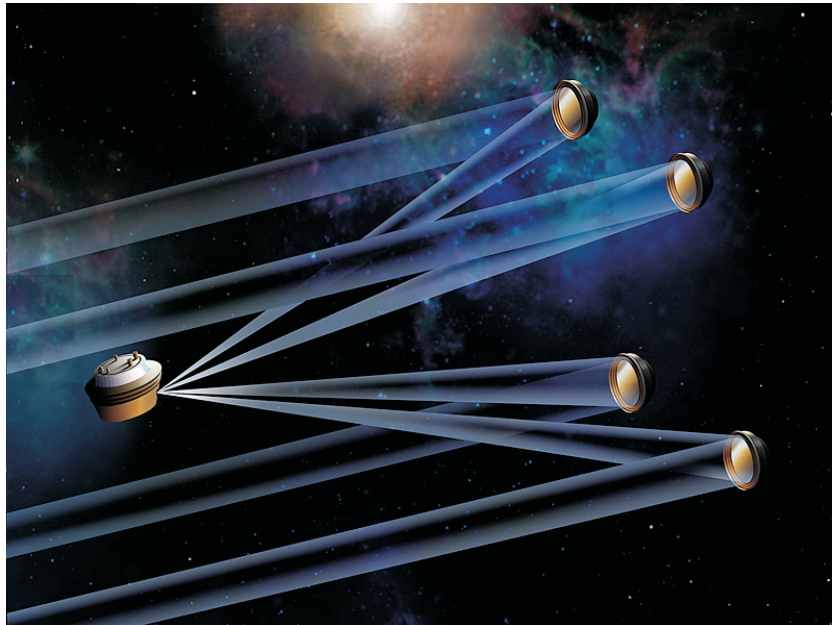


Figure 7.1: Artist impression of the DARWIN/TPF space interferometer in its “Emma X-array” baseline configuration. It presents 4 telescopes and a beam combiner spacecraft, deployed and observing at the Sun-Earth Lagrange point L2 (Courtesy P. Lawson).

similar study for the Terrestrial Planet Finder Interferometer (TPF-I). These efforts on both sides of the Atlantic have finally resulted in a convergence and consensus on mission architecture, the so-called non-coplanar or Emma-type X-array (represented in Figure 7.1). The baseline design consists in four 2-m aperture collector spacecraft, flying in rectangular formation and feeding light to the beam combiner spacecraft located approximately 1200 m above the array. This arrangement makes available baselines up to 170 m for nulling measurements and up to 500 m for the general astrophysics programme (constructive imaging). Note that the size of the collecting apertures has not yet been fixed and will depend mainly on the final cost of the mission.

The optical layout of the X-array configuration separates the nulling and imaging functions, the shortest baselines being used for nulling while the longest are dedicated to imaging. This configuration has the advantage to allow optimal tuning of the shorter dimension of the array for starlight suppression while keeping a relatively longer dimension to resolve the planet. The X-array design is also appropriate to consider techniques for removing instability noise, a key limit to the sensitivity of DARWIN (see appendix of the paper given in Section 7.3.2). Beam combination takes place on a series of optical benches arranged within the beam combiner spacecraft. The necessary optical processing includes:

- Transfer optics and spacecraft metrology;
- Correction and modulation, including optical delay lines, tip-tilt, deformable mirrors;
- Mirrors, wavefront sensors and beam switching;
- Spectral separation, if necessary, to feed the science photons into 2 separate channels;
- Phase shifting, beam mixing;
- Recombination, spectral dispersion and detection.

DARWIN/TPF is foreseen to be placed at the second Lagrange point (L2) by an Ariane 5 ECA vehicle (the total mass is significantly less than 6.6 tons, the launcher capability for delivery to L2).

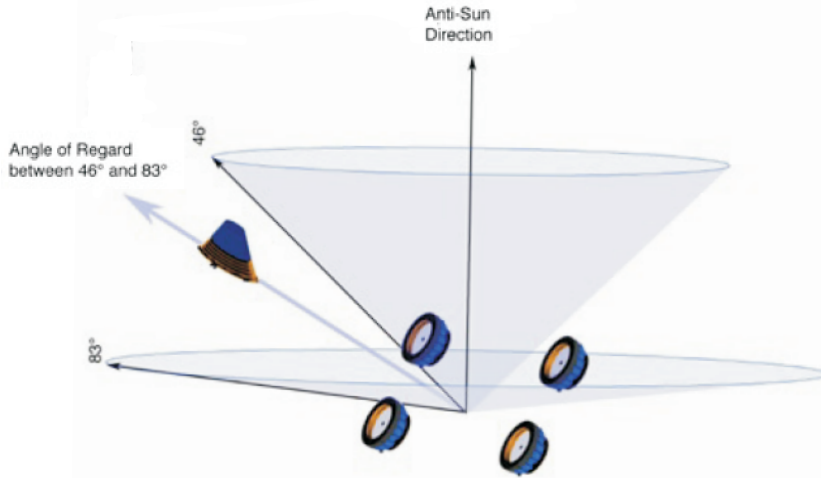


Figure 7.2: Observational constraints of the Emma X-array. At any given time, it can observe an annular region on the sky between 46° and 83° from the anti-Sun direction. During one Earth year, this annulus executes a complete circle, giving access to almost all regions of the celestial sphere.

This placement at L2 is ideal to achieve passive cooling below 50 K of the collector and beam combiner spacecraft by means of sunshades. An additional refrigerator within the beam combiner spacecraft cools the detector assembly to below 10 K. Due to the configuration of the array and the need for solar avoidance, the instantaneous sky access is limited to an annulus with inner and outer half-angles of 46° and 83° centred on the anti-sun vector (Carle 2005, see Figure 7.2). This annulus transits the entire ecliptic circle during one year, giving access to almost the entire sky (see Section 7.3).

7.1.2 Scientific objectives

The main scientific objectives of DARWIN/TPF are the detection of rocky planets similar to Earth and performing the spectroscopic analysis of their atmosphere at mid-infrared wavelengths (6 - 20 μm , Fridlund et al. 2006). In addition to presenting the most advantageous star/planet contrast, this wavelength range holds several spectral features relevant for the search of biological activity (CO_2 , H_2O , CH_4 , O_3 , see Section 1.1.4 and Figure 1.8). The observing scenario of DARWIN/TPF consists in two phases, detection and spectral characterization, whose relative duration can be adjusted to optimise the scientific return. During the detection phase of the mission (nominally 2 years), DARWIN/TPF will examine nearby stars for evidence of terrestrial planets. A duration of 3 years is foreseen for the spectroscopy phase, for a total nominal mission lifetime of 5 years. An extension to 10 years is possible and will depend on the results obtained during the 5 first years. Such an extension could be valuable to observe more M stars, only 10% of the baseline time being attributed to them, search for big planets around a significantly larger sample of stars, and additional measurements on the most interesting targets already studied.

The target star list has been generated from the Hipparcos catalogue, considering several criteria: the distance (< 25 pc), the brightness (< 12 V-mag), the spectral type (F, G, K, M main sequence stars), and the multiplicity (no companion within $1''$). The corresponding star catalogue contains 758 targets, including 54 F stars, 114 G stars, 240 K stars and 350 M stars (Kaltenegger et al. 2007a). Some features of these stars are shown in Figure 7.3. The survey of the target stars and the possible

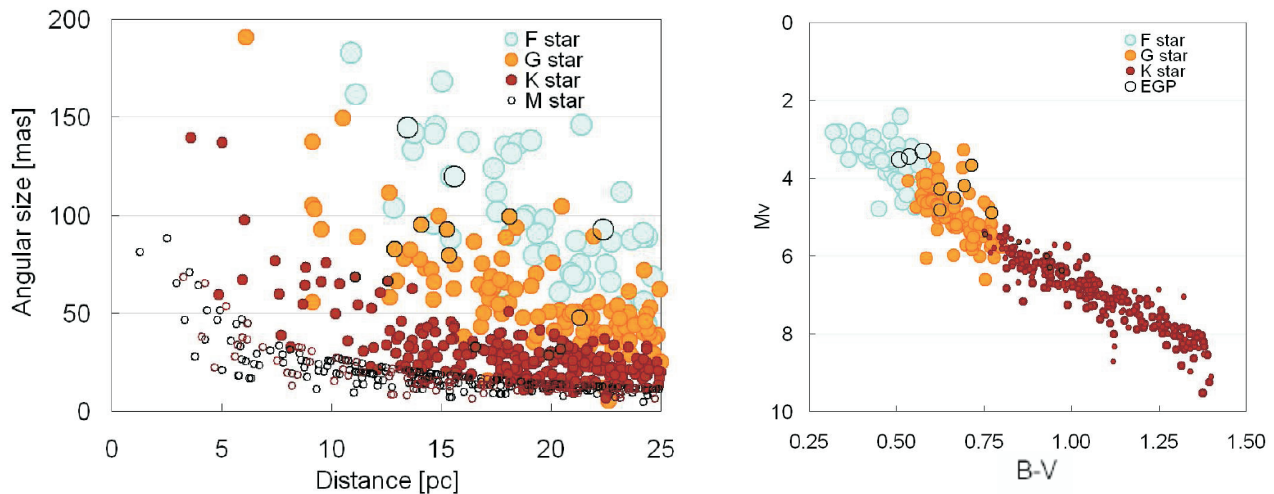


Figure 7.3: Size of the habitable zone for the different spectral types of DARWIN/TPF target (left), and color-magnitude diagram for the same stars (right). Dark circles indicate the stars hosting EGPs (Figures from Kaltenegger et al. 2007a).

detection of terrestrial planets will open a new era of comparative planetology, especially by studying the relationship between habitability and stellar characteristics (e.g., spectral type, metallicity, age), planetary system characteristics (e.g., orbit), and atmospheric composition.

In addition to its primary goals, DARWIN/TPF could provide a wealth of information on the following topics:

- **Planetary formation.** DARWIN/TPF will be able to spatially resolve structures below 1 AU in nearby star forming regions, allowing to witness directly the formation of terrestrial planets in the thermal infrared (see Figure 7.4 for an overview of the imaging capabilities of DARWIN/TPF with respect to JWST). In particular, DARWIN/TPF will be very efficient at studying gaps and determining if the clearing is due to the influence of already-formed giant planets or to another mechanism (e.g., viscous evolution, photo-evaporation).
- **Formation, evolution, and growth of massive black holes.** DARWIN/TPF will be able to probe the immediate environments of very different black holes (BH), ranging from very massive BH in different types of Active Galactic Nuclei (AGN), to the massive black hole at the centre of the Milky Way, down to BH associated with stellar remnants.
- **Galaxy formation and evolution.** With its high angular resolution, DARWIN/TPF will be able to measure the detailed spatial structure of very distant galaxies, which places essential constraints on galaxy formation models.

7.2 Instability noise

Instability noise is defined as the component of the demodulated nulled signal that arises from phase, amplitude and polarisation errors (see Section 4.3). The power spectra of these instrumental effects mix with each other so that perturbations at all frequencies, including DC, have an effect. Spacecraft vibrations, fringe tracking offset, control noise, longitudinal chromatic dispersion, and birefringence are at the origin of the phase errors whereas tip/tilt, defocus, beam shear, and differential transmission produce

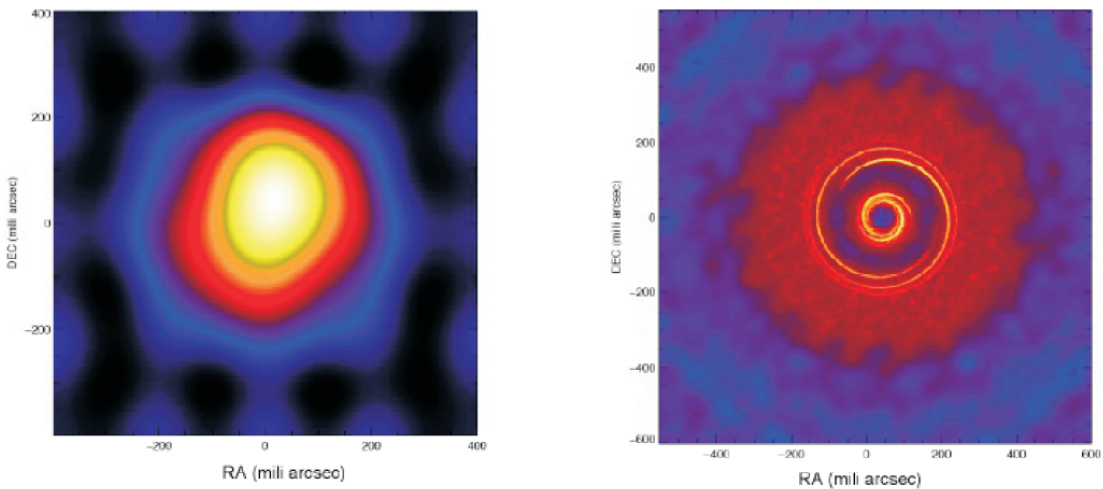


Figure 7.4: Simulation of a hot accretion disc in Taurus (140 pc) as seen by JWST (left) and DARWIN/TPF in its imaging mode (Right). Simulated JWST and DARWIN/TPF images are based on scaled models by D’Angelo et al. (2006) for the formation of a planet of one Jupiter mass at 5.2 AU, orbiting a solar type star. The most prominent features in the model are a gap along the planet’s path and spiral wave patterns emanating from the Lagrangian point, only visible with DARWIN/TPF (courtesy C. de Vries).

amplitude errors. These phase and amplitude errors induce a time-dependent asymmetry between the two chop states so that the modulation map does not remain centered on the nominal position of the line of sight (i.e. the position of the star). Hence a fraction of the starlight survives the modulation process and mixes with the planet photons. Although a simple binary phase chop removes a number of these systematic errors, it has no effect on the dominant amplitude-phase cross terms and on the co-phasing errors (Lay 2004).

Four independent studies (Lay 2004; D’Arcio 2005; Chazelas et al. 2006; Defrère et al. in press) have reviewed the instrumental requirements on the DARWIN/TPF mission that reduce the instrumental stellar leakage to a sufficiently low level for Earth-like planet detection. Assuming the presence of 1/f-type noise, these studies showed that the requirements on amplitude and phase control are not driven by the null-floor leakage, but by instability noise. Considering a Dual-Chopped Bracewell (DCB) with 4-m aperture telescopes operating at $10\text{ }\mu\text{m}$, Lay (2004) shows that a null depth of $\sim 10^{-5}$ is generally sufficient to control the level of shot noise from the stellar leakage, but that a null depth of $\sim 10^{-6}$ is required to prevent instability noise from becoming the dominant source of noise²¹. In particular, a 10^{-6} null requires rms path control to within about 1.5 nm, and rms amplitude control of about 0.1%.

Since instability noise is directly proportional to the stellar flux (see Eq. 4.26), the constraints on the instrument stability is expected to be even more stringent at wavelengths downwards $10\text{ }\mu\text{m}$. In that respect, we applied the analytical method of (Lay 2004) to the new baseline design of DARWIN/TPF (an Emma X-array as described in the previous section), and derived the constraints on the instrument stability such that instability noise is dominated by shot noise by a factor 5 at $7\text{ }\mu\text{m}$ over one rotation period (t_{rot}) of 50000 seconds (with a spectral resolution of 20). Considering 1/f-type PSDs, we showed that this corresponds to residuals rms OPD and amplitude errors of about 1.5 nm and 0.05% respectively (see Section 7.3.2). Although our computation has been done at $7\text{ }\mu\text{m}$ where instability noise is much higher than at $10\text{ }\mu\text{m}$, these constraints are not far from the values derived by Lay (2004) for two reasons. First, the telescopes considered here are smaller so that shot noise is relatively more dominant than in the previous analyses (shot noise is proportional to the square root of the stellar flux while the planetary

²¹The current state-of-the-art for broadband nulling experiments is a 10^{-5} null which has been recently demonstrated at $10\text{ }\mu\text{m}$ ($\Delta\lambda/\lambda=34\%$) with the adaptive nuller (Peters. et al. 2009).

signal and instability noise are directly proportional to the stellar flux). Secondly, the interferometer configuration is stretched by comparison with the DCB so that the planetary signal is modulated at higher frequencies, where the instability noise is lower assuming 1/f-type PSDs.

In order to relax these very stringent requirements, several techniques have been investigated and are briefly discussed hereafter:

- A first solution, proposed by Lay (2006), consists in stretching the array and applying a low-order polynomial fit to the instability noise (as a function of wavelength). By stretching the array, i.e. increasing the imaging baseline of the X-array, the interference pattern orthogonal to the nulling pattern shrinks. As the modulation map scales with wavelength, the planetary signal transmitted by the interferometer will then be a rapidly oscillation function of wavelength. On the other hand, instability noise is shown to be a low-order polynomial of the optical frequency ($1/\lambda$). Therefore, by removing a low-order polynomial fit to the detected signal as a function of wavelength, the instability noise contribution is efficiently subtracted while preserving most of the planetary signal. This operation can actually be performed directly in the cross-correlation, by using a modified planet template where the polynomial components have been removed. Because this method strongly relies on the separation of the nulling and imaging baselines, it can only be efficiently applied with the X-array architecture.
- Another solution, based on the coherence properties of starlight, has been proposed by Lane et al. (2006) to separate the contributions from the planet and the instrumental leakage. The idea is to mix the electric fields of the leakage with that of a separate reference beam, also from the star, in order to form fringes (as long as the relative path delays are maintained within the coherence length). The light from the planet, being not coherent with the starlight, will not form fringes. Using as reference beam the bright output of a pair-wise nulling beam combiner, the amplitude and phase mismatches in the input beams can be extracted from the fringe pattern, allowing the reconstruction of the stellar leakage.
- A third solution has recently been proposed and tested at IAS (Gabor et al. 2008). The principle is to successively apply two ($< \lambda/2$) opposite OPD offsets to one of the beams in order to derive the actual position of the minimum in the transmission map. In this way, one feeds back the actual OPD errors to the delay line and prevents drifts from appearing. The same principle can be used to avoid amplitude drifts, by either blocking all but one beam to measure its actual amplitude or by modulating its amplitude as in the case of the OPD. The frequency at which this process is carried out depends on the input power spectra of the noise sources. It has been demonstrated experimentally in the lab that this process efficiently suppresses the 1/f-type noise generally present in the stellar contribution at the output of a Bracewell interferometer. This technique can theoretically be applied to any nulling configuration, but its efficiency decreases as the number of beams increases.

Others possible approaches (e.g. application of closure phase techniques, new chopping processes, exploiting correlations between measurements taken at different wavelength bins) have been suggested but still need to be investigated. However, these very stringent requirements have been derived with the assumption that the instability noise present an 1/f-type power spectrum. In fact, the shape of the instability noise spectrum strongly depends on the input spectrum of noise fluctuations. Pure 1/f noise might in fact turn out to be a very pessimistic assumption. Given that the DARWIN/TPF system is designed to have three levels of control loops that manage the OPD, and two control loop levels for tip/tilt, the resulting residual phase and intensity fluctuations that are responsible for the instability noise are most likely to have a flat input spectrum. This has a strong influence on the magnitude of the phase-amplitude cross terms, which are the main contributor to instability noise. In particular at low frequencies, where the planetary signal is modulated and the instability noise arises, the 1/f spectrum

diverges, while the flat spectrum increases linearly. In practice, the situation might even be better, as predictive or Kalman filtering may be used to remove low-frequency power. A complication, in particular for the micro Hz domain, is that zero point drifts of the control loops, e.g. related to electronic drifts in the sensors, remain undetected, and thus uncorrected. They will result in a low-frequency 1/f component. A simple solution is to switch the incoming beams with respect to the control loops. The reason why this could work is that the extremely high precision required for DARWIN/TPF is only on relative quantities, namely, the phase and amplitude differences between any two beams. Absolute offsets of phase and amplitude, that apply to all three beams simultaneously, do not contribute to the instability noise, since they do not affect the null. The beams must be switched with respect to the control inputs with a time constant over which the drift can be considered constant. In summary, even though at present a post-processing method has not been identified, it is highly likely that clever and careful engineering may already reduce instability noise to harmless levels.

7.3 Science performance predictions

7.3.1 DARWINsim, the DARWIN science simulator

The DARWINsim science simulation tool is an IDL-written code developed at ESA/ESTEC by R. den Hartog to assess the scientific return of the DARWIN/TPF mission (den Hartog 2005b). For given instrumental configuration and target catalogue, DARWINsim computes the number of stars that can be surveyed for the presence of habitable planets and the number of possible follow-up spectroscopic observations during a nominal mission time.

The basic calculation in DARWINsim consists in an assessment of the required integration times for each individual target to fulfil user-specified SNR values for detection and for different spectroscopy scenarios. Note that the catalogue used in DARWINsim at the time of the simulations presented in Section 7.3 is larger than the new DARWIN/TPF target list (Kaltenegger et al. 2007a) as it contains 1132 stars (114 F, 200 G, 417 K and 401 M stars). In accordance with the interferometer architecture, DARWINsim first selects the stars which are observable during one year. For instance, among the 1132 stars of the catalogue, 625 are observable by the Emma X-array (43 F, 100 G, 241 K and 241 M stars). This constitutes significantly more targets than with a planar configuration (about 440 stars observable during one year). For each of these observable stars, the baseline length is optimised to obtain the minimum integration time for a given SNR, taking into account shot noise contributions from stellar leakage, local and exozodiacal clouds, and instrumental infra-red foreground. The instability noise is also thoroughly implemented using the analytical method of Lay (Lay 2004, see Section 4.1.1 for a brief overview of the method). All these noise contributors are described in detail in the documentation of DARWINsim (den Hartog 2005b).

Detection phase

The observational strategy implemented in DARWINsim is different from the one discussed in Section 6.3.1 for PEGASE (3 observations, assuming that the planet is located in the middle of the HZ and at maximum elongation). Since the location of the planet inside the HZ is a priori unknown, three independent detections are necessary and each integration time is multiplied by three. For the same reason, the integration time (for one of the three observations) is computed from the requirement that it should be long enough to ensure the detection of a planet at 90% of the possible locations. As a first step, the probability distribution for finding a planet at a certain angular distance from the star has to be computed (see Figure 7.5). Note that it is necessary to consider a non-uniform distribution of orbit inclinations in order to get a uniform distribution of orbital axes on the celestial sphere (edge-on systems are more probable). For each position the maximum SNR is then computed, obtained by the

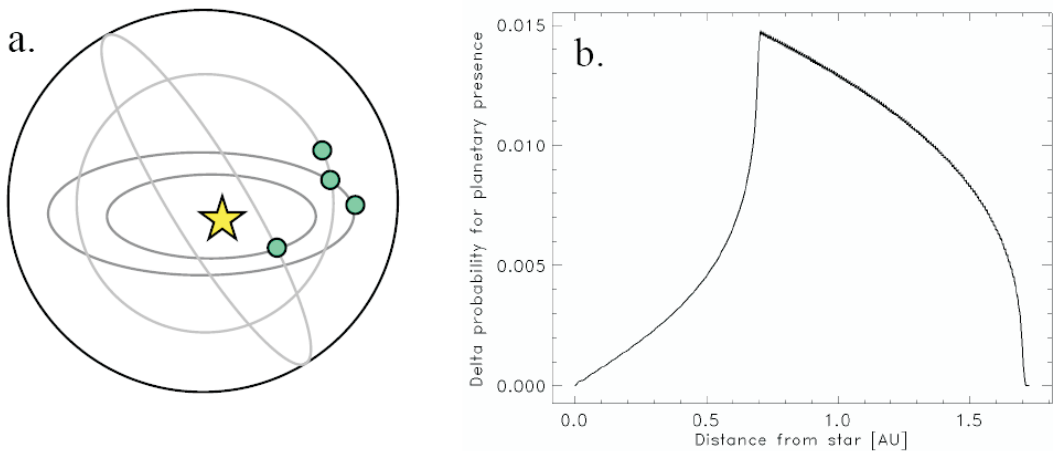


Figure 7.5: *Left*, a planet orbiting in the HZ of its host star can present various apparent distances, because the inclinations and phases of the orbits are a priori unknown. *Right*, probability distribution with respect to the apparent planet-star distance (Figures from den Hartog 2005a).

simultaneous optimisation of the baseline length and the wavelength range. Note that tests performed by R. den Hartog indicate that a reconfiguration to other baselines to perform two or more shorter integrations is never advantageous compared to one single optimised baseline.

After the initial integration time assessment for detection, the targets are sorted by ascending integration time, removing from the list the targets for which the total integration time exceeds the total time during which they are visible from L2. Considering a slew time for re-targeting (nominally 6 hours) and some efficiency for the remaining observing time (nominally 70%), the sorted list is cut off where the cumulative integration time exceeds the nominal survey period. The resulting list defines the number of targets that can be surveyed.

Spectroscopy phase

The number of targets which can be surveyed for spectroscopy in a given time is computed similarly to the method described in the previous section for the detection phase. The only difference is that the integration times for spectroscopy are computed for the most likely position of the planet, which corresponds to circular orbits at random inclination. Then, the total integration time is determined by the requirement to detect the absorption lines of O₃, CO₂ and H₂O to a specified SNR. For the spectroscopy of CO₂ and O₃ (without H₂O), an SNR of 5 would actually be sufficient for a secure detection (Fridlund 2005); the spectroscopy of H₂O is relatively more complex. Recent results suggest that, using a spectral resolution greater than 20, an SNR of 10 from 7.2 to 20 μ m would be sufficient for H₂O, CO₂, and O₃ spectroscopy (private communication with F. Selsis, L. Kaltenegger and J. Paillet). In particular, the H₂O located below 7.2 μ m, which is much more constraining than the H₂O band beyond 17.2 μ m, could be discarded.

DARWINsim considers two types of spectroscopy: the staring spectroscopy, where the array is kept in a position such that the planet resides on a peak of the modulation map and the rotating spectroscopy, where the array keeps on rotating with respect to the target system such as the planet moves in and out of the peaks of the modulation map. Staring spectroscopy is more efficient in terms of signal acquisition, but requires an accurate knowledge of the planetary orbit. As for the detection phase, the total spectroscopy integration time should not exceed the total time during which the target is visible during the characterization phase. Accounting again for a certain fraction of overhead loss, the targets

are sorted on ascending integration time, terminated where the cumulative time exceeds the length of nominal characterization period.

7.3.2 Paper: *Nulling interferometry: Impact of exozodiacal clouds on the performance of future life-finding space missions*

The following paper presents the detailed performance simulations for DARWIN/TPF, and has been accepted for publication in A&A (Defrère et al. in press). The first part of the paper is dedicated to the nominal performance for planet detection and spectroscopic characterization. The second part is focused on the impact of exozodiacal clouds on the performance of the mission. Whereas the disc brightness only affects the integration time, the presence of clumps is more problematic and can seriously hamper the planet detection. Considering modeled resonant structures created by an Earth-like planet orbiting at 1 AU a Sun-like star, we show that this tolerable dust density goes down to about 15 times the solar zodiacal density for face-on systems and decreases with the disc inclination. Observing in advance circumstellar discs around nearby main sequence stars is therefore mandatory in order to prepare future exo-Earth characterization missions. Note that new constraints on instrumental stability are derived in the appendix. These new constraints have been specifically computed to enable the 7- μ m spectroscopy of Earth-like extrasolar planets with the Emma X-array configuration.

Nulling interferometry: impact of exozodiacal clouds on the performance of future life-finding space missions

D. Defrère¹, O. Absil¹, R. den Hartog², C. Hanot¹, and C. Stark³

¹ Institut d'Astrophysique et de Géophysique, Université de Liège, 17 Allée du Six Août, B-4000 Liège, Belgium
e-mail: defrere@astro.ulg.ac.be

² Netherlands Institute for Space Research, SRON, Sorbonnelaan 2, 3584 CA, Utrecht, The Netherlands

³ Department of Physics, University of Maryland, Box 197, 082 Regents Drive, College Park, MD 20742-4111, USA

Received 23 July 2009; accepted 05 October 2009

ABSTRACT

Context. Earth-sized planets around nearby stars are being detected for the first time by ground-based radial velocity and space-based transit surveys. This milestone is opening the path toward the definition of missions able to directly detect the light from these planets, with the identification of bio-signatures as one of the main objectives. In that respect, both the European Space Agency (ESA) and the National Aeronautics and Space Administration (NASA) have identified nulling interferometry as one of the most promising techniques. The ability to study distant planets will however depend on the amount of exozodiacal dust in the habitable zone of the target stars.

Aims. We assess the impact of exozodiacal clouds on the performance of an infrared nulling interferometer in the Emma X-array configuration. The first part of the study is dedicated to the effect of the disc brightness on the number of targets that can be surveyed and studied by spectroscopy during the mission lifetime. In the second part, we address the impact of asymmetric structures in the discs such as clumps and offset which can potentially mimic the planetary signal.

Methods. We use the *DarwinSIM* software which was designed and validated to study the performance of space-based nulling interferometers. The software has been adapted to handle images of exozodiacal discs and to compute the corresponding demodulated signal.

Results. For the nominal mission architecture with 2-m aperture telescopes, centrally symmetric exozodiacal dust discs about 100 times denser than the solar zodiacal cloud can be tolerated in order to survey at least 150 targets during the mission lifetime. Considering modeled resonant structures created by an Earth-like planet orbiting at 1 AU around a Sun-like star, we show that this tolerable dust density goes down to about 15 times the solar zodiacal density for face-on systems and decreases with the disc inclination.

Conclusions. Whereas the disc brightness only affects the integration time, the presence of clumps or offset are more problematic and can seriously hamper the planet detection. The upper limits on the tolerable exozodiacal dust density derived in this paper must be considered as rather pessimistic, but still give a realistic estimation of the typical sensitivity that we will need to reach on exozodiacal discs in order to prepare the scientific programme of future Earth-like planet characterisation missions.

Key words. Instrumentation: high angular resolution – techniques: interferometric – circumstellar matter

1. Introduction

The possibility of identifying habitable worlds and even biosignatures from extrasolar planets currently contributes to the growing interest about their nature and properties. Since the first planet discovered around another solar-type star in 1995 (Mayor & Queloz 1995), nearly 370 extrasolar planets have been detected and many more are expected to be unveiled by ongoing or future search programmes. Most extrasolar planets detected so far have been identified from the ground by indirect techniques, which rely on observable effects induced by the planet on its parent star. From the ground, radial velocity measurements are currently limited to the detection of planets about 2 times as massive as the Earth in orbits around Sun-like and low-mass stars (Mayor et al. 2009) while the transit method is limited to Neptune-sized planets (Gillon et al. 2007). Thanks to the very high precision photometry enabled by the stable space environment, the first space-based dedicated missions (namely CoRoT and Kepler) are now expected to reveal Earth-sized extrasolar planets by transit measurements as well. Launched in 2006, CoRoT (Convection Rotation and planetary Transits) has detected its first extrasolar

planets (e.g., Barge et al. 2008; Alonso et al. 2008; Léger et al. subm.) and is expected to unveil about 100 transiting planets down to a size of $2 R_{\oplus}$ around G0V stars and $1.1 R_{\oplus}$ around M0V stars over its entire lifetime for short orbital periods (Moutou et al. 2005). Launched in 2009, Kepler will extend the survey to Earth-sized planets located in the habitable zone of about 10^5 main sequence stars (Borucki et al. 2007). After 4 years, Kepler should have discovered several hundred of terrestrial planets with periods between one day and 400 days. After this initial reconnaissance by CoRoT and Kepler, the Space Interferometry Mission (SIM PlanetQuest) might provide unambiguously the mass of Earth-sized extrasolar planets orbiting in the habitable zone of nearby stars by precise astrometric measurements. With CoRoT and Kepler, we will have a large census of Earth-sized extrasolar planets and their occurrence rate as a function of various stellar properties. However, even though the composition of the upper atmosphere of transiting extrasolar planets can be probed in favorable cases (e.g., Richardson et al. 2007), none of these missions will directly detect the photons emitted by the

planets which are required to study the planet atmospheres and eventually reveal the signature of biological activity.

Detecting the light from an Earth-like extrasolar planet is very challenging due to the high contrast ($\sim 10^7$ in the mid-IR, $\sim 10^{10}$ in the visible) and the small angular separation ($\sim 0.5 \mu\text{rad}$ for an Earth-Sun system located at 10 pc) between the planet and its host star. A technique that has been proposed to overcome these difficulties is nulling interferometry (Bracewell 1978). The basic principle is to combine the beams coming from two telescopes in phase opposition so that a dark fringe appears on the line of sight, which strongly reduces the stellar emission. Considering the two-telescope interferometer initially proposed by Bracewell, the response on the plane of the sky is a series of sinusoidal fringes, with angular spacing of λ/b . By adjusting the baseline length (b) and orientation, the transmission of the off-axis planetary companion can then be maximised. However, even when the stellar emission is sufficiently reduced, it is generally not possible to detect Earth-like planets with a static array configuration, because their emission is dominated by the thermal contribution of warm dust in our solar system as well as around the target stars (exozodiacal cloud). This is the reason why Bracewell proposed to rotate the interferometer so that the planetary signal is modulated by alternatively crossing high and low transmission regions, while the stellar signal and the background emission remain constant. The planetary signal can then be retrieved by synchronous demodulation. However, a rapid rotation of the array would be difficult to implement and as a result the detection is highly vulnerable to low frequency drifts in the stray light, thermal emission, and detector gain. A number of interferometer configurations with more than two collectors have then been proposed to perform faster modulation and overcome this problem by using phase chopping (Angel & Woolf 1997; Mennesson & Mariotti 1997; Absil 2001). The principle of phase chopping is to synthesize two different transmission maps with the same telescope array, by applying different phase shifts in the beam combination process. By differencing two different transmission maps, it is possible to isolate the planetary signal from the contributions of the star, local zodiacal cloud, exozodiacal cloud, stray light, thermal, or detector gain. Phase chopping can be implemented in various ways (e.g. inherent and internal modulation, Absil 2006), and are now an essential part of future space-based life-finding nulling interferometry missions such as ESA's DARWIN (Fridlund et al. 2006) and NASA's Terrestrial Planet Finder (TPF, Lawson et al. 2008). The purpose of this paper is to assess the impact of exozodiacal dust discs on the performance of these missions. After describing the nominal performance of DARWIN/TPF, the first part of the study is dedicated to centrally symmetric exozodiacal discs which are suppressed by phase chopping and only contribute through their shot noise. If they are too bright, exozodiacal discs can drive the integration time and we investigate the corresponding impact on the number of planets that can be surveyed during the mission lifetime. In the second part, we address the impact of asymmetric structures in the discs (such as clumps and offset) which are not canceled by phase chopping and can seriously hamper the planet detection process.

2. DARWIN/TPF overview

Considerable effort have been expended in the past decade by both ESA and NASA to design a mission that provides the required scientific performance while minimizing cost and technical risks. After the investigation of several interferometer architectures, these efforts culminated in 2005-2006 with two parallel

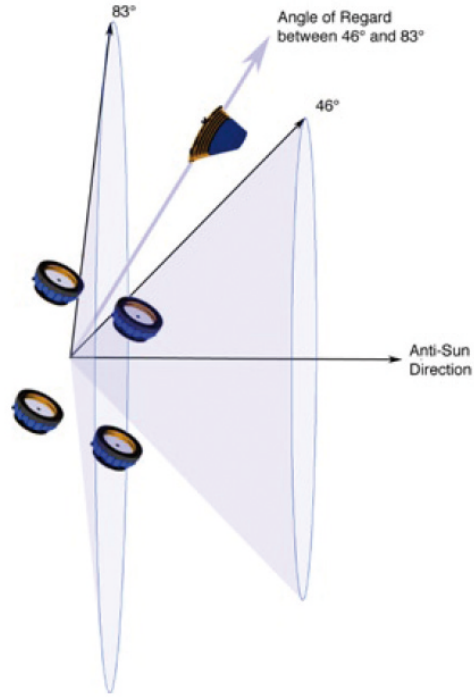


Fig. 1. Representation of the DARWIN/TPF space interferometer in its baseline "Emma X-array" configuration (Léger & Herbst 2007). It includes 4 telescopes and a beam combiner spacecraft, deployed and observing at the Sun-Earth Lagrange point L2. At any given time, it can observe an annular region on the sky between 46° and 83° from the anti-solar direction. During one Earth year, this annulus rotates and gives access to almost all regions of the celestial sphere.

assessment studies of the DARWIN mission, carried out by EADS Astrium and Alcatel-Alenia Space. Two array architectures have been thoroughly investigated during these industrial studies: the four-telescope X-array and the Three-Telescope Nuller (TTN Karlsson et al. 2004). These studies included the launch requirements, payload spacecraft, and the ground segment during which the actual mission science would be executed. Almost simultaneously, NASA/JPL initiated a similar study for the Terrestrial Planet Finder Interferometer (TPF-I, Lawson et al. 2008). These efforts on both sides of the Atlantic have finally resulted in a convergence and consensus on mission architecture, the so-called non-coplanar or Emma-type X-array (represented in Fig. 1).

2.1. Instrumental concept

The baseline design consists of four 2-m aperture collector spacecraft, flying in rectangular formation and feeding light to the beam combiner spacecraft located approximately 1200 m above the array. This arrangement makes available baselines up to 70 m for nulling measurements and up to 400 m for the general astrophysics programme (constructive imaging). Note that the size of the collecting apertures has not yet been fixed and will influence the final cost of the mission. The optical layout separates the nulling and imaging functions, the shortest baselines being used for nulling and the longest ones for imaging. This configuration has the advantage of allowing optimal tuning of the shorter dimension of the array for starlight suppression

Table 1. Instrumental parameters considered in this study for DARWIN/TPF.

Instrumental parameters	Emma X-Array Design
Max. baselines [m]	400×67
Telescope diameter [m]	2.0
Field of regard	46° to 83°
Optics temperature [K]	40
Detector temperature [K]	8
Quantum efficiency	70%
Instrument throughput ^a	10%
Science waveband [μm]	6.0-20.0
Modal filtering [μm] ^b	6.0-11.5/11.5-20.0
Spectral resolution	60
Instrumental stability ^c	
- rms OPD error [nm]	1.5
- rms amplitude error	0.05%

^a excluding ideal beam combiner losses and coupling efficiency.

^b see section 3.2.

^c see section 3.4.

while keeping a significantly longer dimension to provide a rapid modulation of the planet signal as the array rotates. The X-array design is also appropriate to implement various techniques for removing instability noise, which is one of the dominant noise contributor (see appendix A). The assessment studies settled on an imaging to nulling baseline ratio of 3:1, based on scientific and instrument design constraints. A larger ratio of 6:1 could nonetheless improve performance by simplifying noise reduction in the post-processing of science images (Lay 2006). The optical system architecture is represented by the block diagram in Fig. 2 with the following elements in the optical path:

- four spherical primary mirrors located on a virtual paraboloid and focusing the beam at the paraboloid's focal point. The virtual parabola focal length has been set to 1200 m, resulting from a trade-off between differential polarisation effects and inter spacecraft metrology capability, as well as to enable the implementation of longer baselines for an imaging mode;
- transfer optics consist of all the equipment needed to collect and redirect the incoming beams towards fixed directions whatever the interferometer configuration. This includes mainly tip-tilt mirrors to handle array reconfiguration, a derotator to handle the array rotation and a common two or three mirror telescope to achieve beam collimation;
- optical delay lines (ODL) to adjust the optical path differences (OPD);
- fast steering mirrors to correct for tip-tilt errors;
- deformable mirrors to compensate for quasi-static errors such as defocus and astigmatism which are due to the use of spherical mirrors;
- achromatic π phase shifters to produce the destructive interference of on-axis stellar light (using Fresnel Rhombs for instance, Mawet et al. 2007);
- dichroic beam splitters to separate the signals between the science waveband and the waveband used for metrology;
- a Modified Mach Zehnder (MMZ, Serabyn & Colavita 2001) beam combiner;
- coupling optics to focus the outputs of the cross-combiner into single mode fibres. Chalcogenide fibres can cover successfully the wavelength range 6.0-12 μm (Ksendlzov et al. 2007) and silver halide fibres can be used for modal filtering in at least the 10.5-17.5 μm spectral range (further investiga-

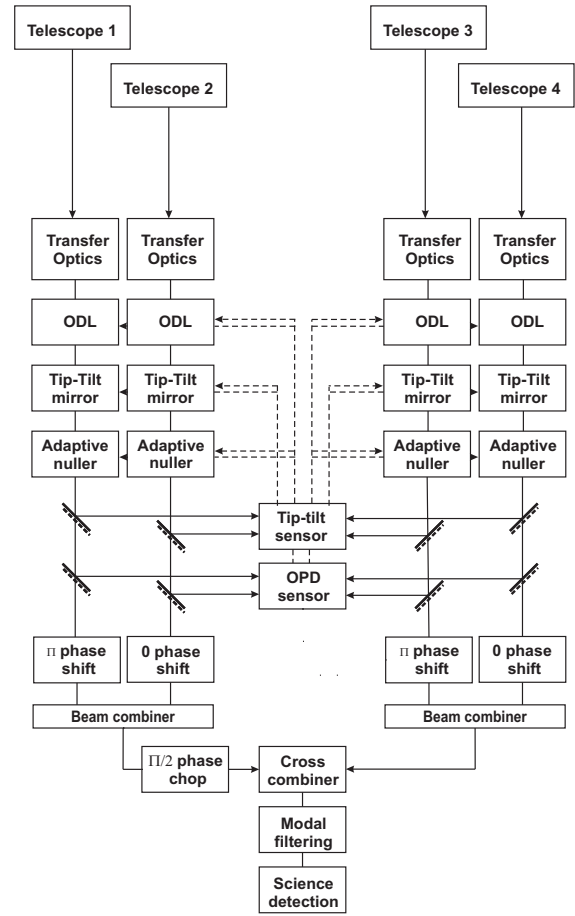


Fig. 2. Block diagram of the DARWIN/TPF optical layout. Feed-back signals driving the tip-tilt/OPD control are represented by dashed lines.

tions are however necessary to demonstrate that they are usable in the 17.5-20.0 μm wavelength range, Ksendlzov et al. 2008);

- a detection assembly controlled at a temperature of 8 K and connected to the fibres.

DARWIN/TPF would be placed around the second Lagrange point (L2) by an Ariane 5 ECA vehicle. L2 is optimal to achieve passive cooling of the collector and beam combiner spacecraft down to 40 K by means of sunshades. An additional refrigerator within the beam combiner spacecraft cools the detector assembly to 8 K. Due to the configuration of the array and the need for solar avoidance, the instantaneous sky access is limited to an annulus with inner and outer half-angles of 46° and 83° centred on the anti-sun vector (see Fig. 1, Carle 2005). This annulus transits the entire ecliptic circle during one year, giving access to almost the entire sky.

2.2. Scientific objectives

The main scientific objectives of DARWIN/TPF are the detection of rocky planets similar to Earth and the spectroscopic analysis of their atmospheres at mid-infrared wavelengths (6 - 20 μm). In addition to presenting an advantageous star/planet contrast, this wavelength range holds several spectral features relevant for the search of biological activity (CO_2 , H_2O , and O_3). The ob-

Table 2. Parameters adopted for the performance simulations.

Parameter	
Configuration	Emma X-Array Design with a 6:1 aspect ratio (see Table 1)
Planet	Earth-sized planet with a constant temperature of 265 K across the habitable zone
Exozodiacal density	Three times our solar system, based on Kelsall model (Kelsall et al. 1998)
Mission duration	5 years (2 years for survey and 3 years for characterisation)
Retargeting time	6 hours
Integration efficiency	70% (accounting for overhead loss)
Target stars	Darwin All Sky Survey Catalogue (DASCC, Kaltenegger et al. 2008)
Earth-like planet per star (η_{\oplus})	1
Habitable zone	0.7 - 1.5 AU scaled with $L_{\star}^{1/2}$
Time allocation	10% F, 50% G, 30% K and 10% M stars
Array rotation period	50000 seconds (not scaled with the array baseline length)
SNR threshold for detection	5
SNR threshold for spectroscopy	5 (CO_2, O_3) and 10 ($\text{CO}_2, \text{O}_3, \text{H}_2\text{O}$)

serving scenario of DARWIN/TPF consists of two phases, detection and spectral characterisation, whose relative duration can be adjusted to optimise the scientific return¹. During the detection phase of the mission (nominally 2 years), DARWIN/TPF will examine nearby stars for evidence of terrestrial planets. A duration of 3 years is foreseen for the spectroscopy phase, for a total nominal mission lifetime of 5 years. An extension to 10 years is possible and will depend on the results obtained during the 5 first years. Such an extension could be valuable to observe more M stars (only 10% of the baseline time being attributed to them), search for big planets around a significantly larger sample of stars, and additional measurements on the most interesting targets already studied.

The DARWIN/TPF target star list has been generated from the Hipparcos catalogue, considering several criteria: the distance (< 30 pc), the brightness (< 12 V-mag), the spectral type (F, G, K, M main sequence stars), and the multiplicity (no companions within 1''). The corresponding star catalogue contains 1229 single main sequence stars of which 107 are F, 235 are G, 536 are K, and 351 are M type (Kaltenegger et al. 2008). The survey of the DARWIN/TPF stars and the possible detection of terrestrial planets will start a new era of comparative planetology, especially by studying the relationship between habitability and stellar characteristics (e.g. spectral type, metallicity, age), planetary system characteristics (e.g. orbit), and atmospheric composition.

3. Simulated performance

3.1. The science simulator

The performance predictions presented in this paper have been computed using the DARWIN science SIMulator developed at ESA/ESTEC (*DarwinSIM*, den Hartog 2005b). This simulator has been subject to extensive validation the past few years and its performance predictions were recently reconciled with a similar mission simulator developed independently at NASA/JPL for the TPF mission (Lay et al. 2007). The two simulation tools have shown a very good agreement in SNR, giving similar integration times for all the Darwin/TPF targets with a discrepancy lower than 10% in average (Defr  re et al. 2008b). These two simulators have the same basic purpose. For a given instrumental configuration and target catalogue, they assess the number of terrestrial planets that can be detected in the habitable zone of nearby main sequence stars and the number of possible follow-up spectroscopic observations during a nominal mission time.

¹ The detection phase might not be necessary if the targets are identified in advance by radial velocity or astrometric surveys.

The duration of detection and spectroscopy phases can be adjusted to optimise the scientific return and is nominally set to 2 and 3 years respectively. The parameters and assumptions used are summarized in Table 2.

3.1.1. Detection phase

The starting point of the simulations is the target star catalogue. Given a specific interferometer architecture, the simulator first identifies the stars which are observable from L2. For each of these observable stars, the basic calculation consists of an assessment of the required integration times to achieve an user-specified SNR for broad-band detection of a hypothetical Earth-like planet located inside the habitable zone. The habitable zone is assumed to be located between 0.7 and 1.5 AU for a G2V star and is scaled with the square root of the stellar luminosity ($L_{\star}^{1/2}$). Since the location of the planet around the star is a priori unknown, the integration time is computed from the requirement that it should ensure the detection of a planet for at least 90% of the possible locations in the habitable zone. Assuming planets uniformly distributed along habitable orbits, this requires the computation of the probability distribution for finding a planet at a certain angular distance from the star. For each planetary position, the maximum SNR is computed by optimisation of the baseline length. The thermal flux of the habitable planet is assumed to be identical to that of Earth irrespective of the distance to the star. The exozodiacal clouds are simulated by assuming a nominal dust density 3 times larger than that in the solar system and a dust sublimation temperature of 1500 K. Under the assumption that the exozodiacal emission is symmetric around the target star, it will be suppressed by phase chopping, and therefore only contributes to shot noise. The noise sources included are the shot noise contributions from stellar leakage, local and exozodiacal clouds, and instrumental infrared background. Instability noise is also present and is partly mitigated by phase chopping. A complete list can be found in Table 3.

After the initial integration time assessment for detection, the targets are sorted by ascending integration time, removing from the list the targets for which the total integration time exceeds the total time during which they are visible from L2. Considering a slew time for re-targeting (nominally 6 hours) and an efficiency for the remaining observing time of 70%, the sorted list is cut off at the moment when the cumulative integration time exceeds the nominal survey period. Accounting for a specific time allocation for each spectral type (10% F, 50% G, 30% K and 10% M stars), the resulting list defines the number of targets that can be surveyed during the detection phase. The actual number of plan-

ets found will then depend on the number of terrestrial planets present in the habitable zone of target stars (η_{\oplus}).

3.1.2. Spectroscopy phase

The number of targets which can be characterised by spectroscopy in a given time is computed similarly. The difference with the detection phase is that the integration times are computed for a given position in the habitable zone. The proper procedure would be to take into account all possible positions for the planet in a similar way to the detection phase but this would be far too time consuming. The strategy is then to consider only the most likely angular separation. Then, the total integration time is determined by the requirement to detect the absorption lines of O_3 , CO_2 and H_2O to a specified SNR. For the spectroscopy of CO_2 and O_3 (without H_2O), an SNR of 5 would actually be sufficient for a secure detection (Fridlund 2005). Considering the spectroscopy of H_2O is relatively more complex. Recent results suggest that, using a spectral resolution greater than 20, an SNR of 10 from 7.2 to 20 μm would be sufficient for H_2O , CO_2 , and O_3 spectroscopy (private communication with F. Selsis, L. Kaltenegger and J. Paillet). In particular, these results suggest that the H_2O band located below 7.2 μm , which is much more time-consuming than the H_2O band beyond 17.2 μm , could be discarded.

Two types of spectroscopic analysis are considered: the staring spectroscopy, where the array is kept in a position such that the planet resides on a peak of the modulation map, and the rotating spectroscopy, where the array keeps on rotating with respect to the target system so that the planet moves in and out of the peaks of the modulation map. Staring spectroscopy is more efficient in terms of signal acquisition, but requires an accurate knowledge of the planetary orbit. As for the detection phase, the total spectroscopy integration time should not exceed the total time during which the target is visible during the characterisation phase. Accounting again for a given fraction of overhead loss, the targets are sorted with respect to ascending integration time, terminated where the cumulative time exceeds the length of the nominal characterisation period. The number of planets that can be characterised is then given with the assumption that there is one terrestrial planet in the habitable zone of each target star ($\eta_{\oplus}=1$).

3.2. Coupling efficiency

Coupling the optical beams into optical fibers is an essential part of the wavefront correction process, which is required for deep nulling. The theoretical efficiency of light injection into an optical fiber depends on several parameters: the core radius of the fiber, its numerical aperture, the wavelength, the diameter of the telescope and its focal length (Ruilier & Cassaing 2001). The method used in the simulator consists in choosing first the core radius of the fiber so as to ensure single-mode propagation over the whole wavelength range. The f-number of the coupling optics can then be optimised to give the maximum coupling efficiency at a chosen wavelength and more importantly, to provide a roughly uniformly high coupling efficiency across the whole wavelength band. The coverage of the full science band of DARWIN/TPF with one optical fiber is generally prohibited since the coupling efficiency drops rapidly with respect to the wavelength. Increasing the number of fibers improves the coupling efficiency but at the expense of complexity. In particular, it has been shown that the loss of targets for detection and spec-

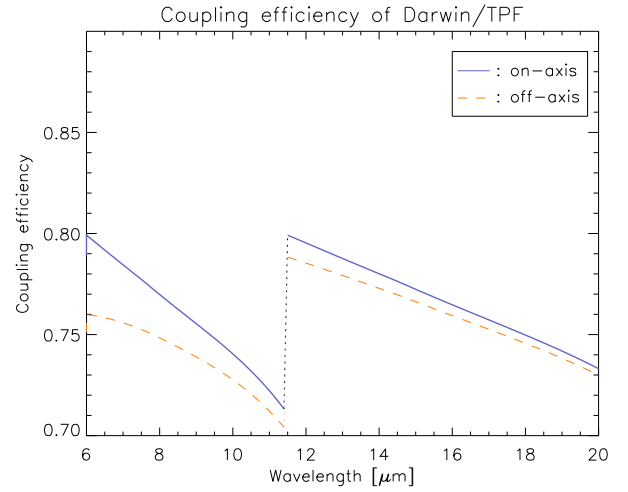


Fig. 3. Coupling efficiency for DARWIN/TPF with respect to the wavelength for an on-axis source and for a source with a fixed off-axis angle, corresponding to an Earth orbit around a Sun at 10 pc. The core radius is chosen so as to stay single-mode on the whole wavelength.

troscopy is about 5% between the optimised 2-band and 3-band cases (den Hartog 2005a). Considering the use of two fibers (respectively on the 6.0-12 μm and 12-20 μm wavelength ranges), Fig. 3 shows the coupling efficiency for an on-axis source and for a source with a fixed off-axis angle, corresponding to an Earth orbit around a Sun at 10 pc. The coupling efficiency remains above 70% over the whole wavelength band of each fiber.

3.3. Modulation efficiency

The modulation of the planetary signal during the observation is a direct consequence of the chopping process which is mandatory to get rid of background noise sources such as exozodiacal and local zodiacal cloud emission. For the X-array configuration, the outputs of two Bracewell interferometers are combined with opposite phase shifts ($\pm \pi/2$) to produce two transmission maps (or “chop states”). Differencing the two transmission maps gives the chopped response of the interferometer, the so-called modulation map, which contains positive and negative values by construction (see Fig. 4). Since the value of the modulation map varies across the field-of-view, the position and flux of the planet cannot be unambiguously inferred and an additional level of modulation is mandatory. This is provided by the rotation of the interferometer (typically with a period of 1 day). The planetary signal is therefore modulated as shown on the right part of Fig. 4. In order to retrieve the planetary signal, the most common approach is correlation mapping, a technique closely related to the Fourier transform used for standard image synthesis (Lay 2005). The result is a correlation map, displayed for a single point source in the lower right part of Fig. 4. This represents the Point Spread Function (PSF) of the array. This process, illustrated here for a single wavelength, is repeated across the wavelength range, and the maps are co-added to obtain the net correlation map. The broad range of wavelengths planned for DARWIN/TPF greatly extends the spatial frequency coverage of the array, suppressing the side lobes of the PSF.

After chopping and rotation, the part of the incoming signal which is actually modulated and retrievable by synchronous

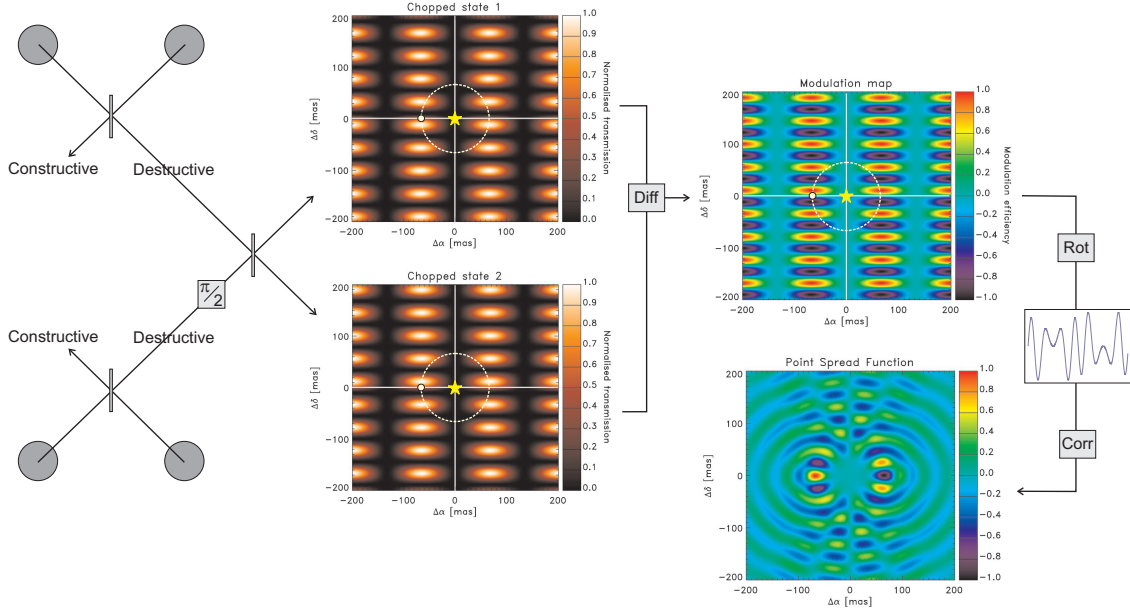


Fig. 4. Overview of phase chopping for the X-array configuration. Combining the beams with different phases produces two conjugated transmission maps (or chop states), which are used to produce the chopped response. Array rotation then locates the planet by cross-correlation of the modulated chopped signal with a template function.

demodulation is proportional to the “rotational modulation efficiency”. It is shown for the X-array configuration in Fig. 5. It depends on the radial distance from the star and reaches a peak value of 0.56 with an asymptotic value of 0.44. Since the planet position inside the habitable zone is a priori unknown, it is desirable that the effective modulation efficiency is as uniform as possible across the habitable zone to avoid too many reconfigurations of the interferometric array. Note that the rotational modulation efficiency for several array configurations has been investigated by Lay (2005).

3.4. Instability noise

Instability noise is defined as the component of the demodulated nulled signal that arises from phase, amplitude and polarisation errors (Lay 2004). The power spectra of these instrumental effects mix with each other so that perturbations at all frequencies, including DC, have an effect. Spacecraft vibrations, fringe tracking offset, control noise, longitudinal chromatic dispersion, and birefringence are at the origin of the phase errors whereas tip/tilt, defocus, beam shear, and differential transmission produce amplitude errors. These phase and amplitude errors induce a time-dependent asymmetry between the two chop states so that the modulation map does not remain centered on the nominal position of the line of sight (i.e. the position of the star). Hence a fraction of the starlight survives the modulation process and mixes with the planet photons. Although a simple binary phase chop removes a number of these systematic errors, it has no effect on the dominant amplitude-phase cross terms and on the co-phasing errors. There is no phase chopping scheme that can remove the systematic errors without also removing the planetary signal. Three independent studies (Lay 2004; d’Arcio 2005; Chazelas et al. 2006) have reviewed the instrumental requirements on the DARWIN/TPF mission that reduce the instrumental stellar leakage to a sufficiently low level for Earth-like planet

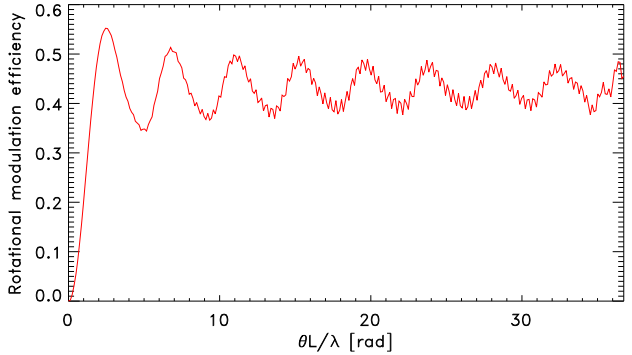


Fig. 5. Rotational modulation efficiency for the Emma X-array with a 6:1 aspect ratio.

detection. Assuming the presence of 1/f-type noise, these studies showed that the requirements on amplitude and phase control are not driven by the null-floor leakage, but by instability noise. Considering a Dual-Chopped Bracewell (DCB, Lay 2004) with 4-m aperture telescopes operating at $10\mu\text{m}$, the different analyses show that a null depth of $\sim 10^{-5}$ is generally sufficient to control the level of shot noise from the stellar leakage, but that a null depth of $\sim 10^{-6}$ is required to prevent instability noise from becoming the dominant source of noise². In particular, a 10^{-6} null requires rms path control to within about 1.5 nm, and rms amplitude control of about 0.1%.

In order to relax these very stringent requirements, several techniques have been investigated (Lay 2005; Lane et al. 2006;

² The current state-of-the-art for broadband nulling experiments is a 10^{-5} null which has been recently demonstrated at $10\mu\text{m}$ ($\Delta\lambda/\lambda=34\%$) with the adaptive nuller (Peters. et al. 2009).

Table 3. Detailed view of the various contributors to the noise budget, given in photo-electrons per second over the 6-20 μm wavelength range for DARWIN/TPF in the Emma X-array configuration. The final SNRs are computed over a single rotation of 50000 s and for four targets representative of the target catalogue (see main text for further information).

	M0V - 05pc	K0V - 10pc	G2V - 15pc	F0V - 20pc
Optimum baseline [m]	25	22	22	11
Planetary modulation efficiency	0.57	0.58	0.58	0.58
Planetary coupling efficiency	0.76	0.76	0.76	0.75
Stellar signal [e-/s]	2.6×10^7	2.1×10^7	1.3×10^7	2.1×10^7
Planetary signal [e-/s]	5.52	1.39	0.62	0.35
Photon noise [e-/s]	0.459	0.388	0.358	0.365
- Geometric leakage [e-/s]	0.304	0.179	0.101	0.078
- Null-floor leakage [e-/s]	0.019	0.017	0.013	0.017
- 3-zodi signal [e-/s]	0.077	0.078	0.075	0.121
- Local zodiacal signal [e-/s]	0.260	0.260	0.260	0.260
- Detected thermal [e-/s]	0.101	0.101	0.101	0.101
- Detected stray light [e-/s]	0.166	0.166	0.166	0.166
Dark current [e-/s]	0.063	0.063	0.063	0.063
Detector noise [e-/s]	0.063	0.063	0.063	0.063
Instability noise [e-/s]	0.025	0.014	0.008	0.012
- First order phase term [e-/s]	0.021	0.008	0.002	0.001
- Second order phase-amplitude [e-/s]	0.014	0.012	0.007	0.012
Total noise [e-/s]	0.460	0.388	0.358	0.365
Integrated SNR (one rotation)	16.0	4.4	2.1	1.1
Integration time for SNR=5 [h]	1.36	17.9	81.8	285

Gabor et al. 2008). Discussion of these mitigation techniques is beyond the scope of this paper, where we assume that instability noise is sufficiently low to ensure the H₂O spectroscopy at 7 μm of an Earth-like planet orbiting around a Sun located at 15 pc. Applying the analytical method of (Lay 2004) to the Emma X-array with the parameters listed in Table 1, we derive the constraints on the instrument stability such that instability noise is dominated by shot noise by a factor 5 at 7 μm over one rotation period (t_{rot}) of 50000 seconds (with a spectral resolution of 20). Considering 1/f-type PSDs defined on the $[1/t_{\text{rot}}, 10^4]$ Hz range, this corresponds to residuals rms OPD and amplitude errors of about 1.5 nm and 0.05% respectively. These values will be used thorough this study (see appendix A for further details). Although our computation has been done at 7 μm where instability noise is much higher than at 10 μm , these constraints are not far from the values derived by Lay (2004) for two reasons. First, the telescopes considered here are smaller so that shot noise is relatively more dominant than in the previous analyses (shot noise is proportional to the square root of the stellar flux while the planetary signal and instability noise are directly proportional to the stellar flux). Secondly, the interferometer configuration is stretched by comparison with the DCB so that the planetary signal is modulated at higher frequencies, where the instability noise is lower assuming 1/f-type PSDs.

3.5. Signal-to-noise analysis

In this section, we present the different sources of noise simulated by *DarwinSIM* and the level at which they contribute to the final SNR for four targets representative of the DARWIN/TPF catalogue: an M0V star located at 5 pc, a K0V star at 10 pc, a G2V star at 15 pc and an F0V star at 20 pc. The noise budget of each source is shown in Table 3 for a single rotation of 50000 s and for the optimum baseline length (computed by minimizing the integration time). The different contributors are described hereafter.

- The stellar signal represents the total number of photo-electrons that are generated by stellar photons detected in both constructive and destructive outputs.
- The planetary signal is the demodulated amount of photo-electrons that come from an Earth-like planet located at 1 AU from the star.
- Shot noise is due to the statistical arrival process of the photons from all sources. It comes from the contributions from stellar leakage, the exozodiacal dust, the local zodiacal cloud, the thermal emission from the telescopes, and the stray light.
- Geometric stellar leakage accounts for the imperfect rejection of the stellar photons due to the finite size of the star and the non-null response of the interferometer for small off-axis angles.
- Null-floor leakage accounts for the stellar photons that leak through the output of the interferometer due to the influence of instrumental imperfections such as co-phasing errors, wavefront errors or mismatches in the intensities of the beams.
- The 3-zodi signal is the shot noise contribution from the circumstellar disc, assumed to be face-on and to follow the same model as in the solar system (Kelsall et al. 1998), except for a global density factor of 3.
- Local zodiacal signal is the shot noise contribution from the solar zodiacal cloud, taking into account the spacecraft location at L2 and the pointing direction.
- Thermal background accounts for the emission of the telescopes.
- Stray light is made of the photons originating from outside the interferometer and which do not follow the nominal route to the detector. It includes scattered light from the target star, thermal photons from the instrument and any solar photon that are scattered into the instrument. We assume a nominal value of 10 photons per second and per spectral channel.
- Dark current is the constant response produced by the detector when it is not actively being exposed to light. We consider a nominal value of of 4 electrons rms per read and per spectral channel.

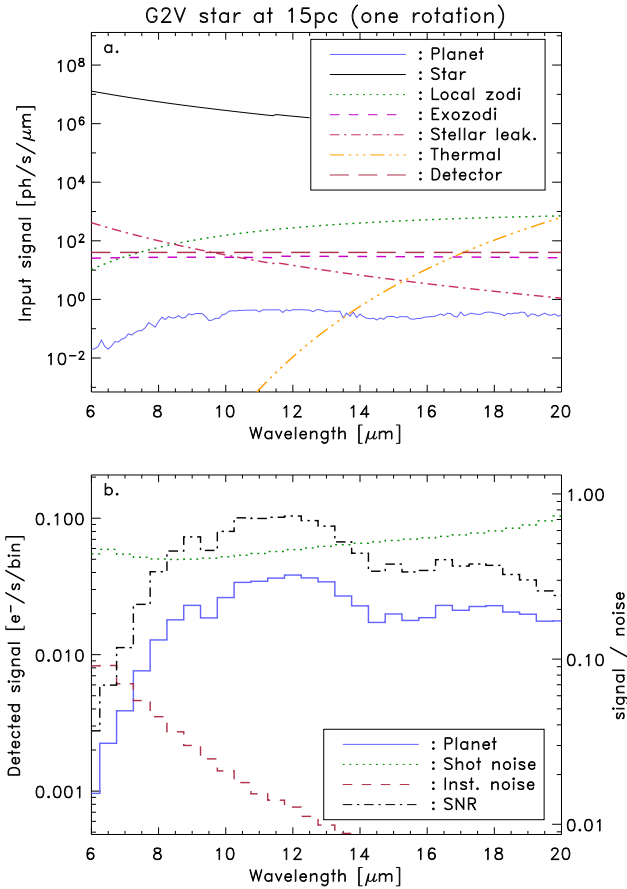


Fig. 6. Input (a) and detected (b) signals for an Earth-like planet orbiting 1 AU around a G2V star located at 15 pc. The demodulated signals are computed over a single rotation of 50000 s.

- Detector noise is computed assuming a read-out noise of 4 electrons rms and a typical read-out frequency of 1 Hz.
- Instability noise has been discussed in section 3.4. It is computed for rms OPD and amplitude errors of 1.5 nm and 0.05% respectively (and defined on 1/f-type power spectra).

As expected, shot noise is the dominant contributor for all targets (we have derived the constraints on the instrument stability so that instability noise is not dominant in section 3.4). The emission of the local zodiacal cloud is generally the dominant source of shot noise but geometric stellar leakage and the exozodiacal dust also produce a significant part of it. Instability noise is dominated by second order phase-amplitude cross terms as pointed out by Lay (2004) and contributes weakly to the integrated SNR. The dependence on the wavelength is shown in Fig. 6 for the G2V star located at 15 pc. The upper figure represents the different input signals, showing that stellar leakage dominates at short wavelengths while the local zodiacal cloud emission is dominant at long wavelengths. The lower figure represents shot noise, instability noise and the detected signal from the planet. The SNR is also represented and measured on the right-hand side vertical axis. It is maximum around $10\mu\text{m}$, where the planetary signal peaks, and decreases rapidly toward short wavelengths, suggesting that the spectroscopy at these wavelengths would be the most time-consuming. Integrating the

Table 4. Expected performance in terms of number of stars surveyed and planets characterised during the nominal 5-year mission for various telescope diameters and planet radii. All stars are assumed to host a planet in the habitable zone and to be surrounded by an exozodiacal cloud 3 times denser than in the solar system.

Telescope diameter	1-m	2-m	4-m	2-m	2-m
Planet radius [R_{\oplus}]	1	1	1	1.5	2
Detection					
Surveyed (5 years)	89	303	813	590	921
Surveyed (2 years)	58	189	497	370	564
# F stars	3	10	35	27	46
# G stars	11	43	136	96	164
# K stars	14	61	183	130	206
# M stars	30	75	143	117	148
Spectroscopy					
Staring (CO_2, O_3)	20	64	199	132	234
Rotating (CO_2, O_3)	20	43	127	89	159
# F stars	0	2	5	4	8
# G stars	2	7	25	17	36
# K stars	2	10	40	24	46
# M stars	16	24	67	44	69
Staring (H_2O)	15	32	101	71	121
Rotating (H_2O)	11	21	60	48	83
# F stars	0	1	2	2	4
# G stars	0	4	11	8	16
# K stars	2	5	18	11	22
# M stars	9	11	39	27	41

signal and noise sources from 6 to $20\mu\text{m}$ gives an SNR of about 2 (see table 3) so that about 6 rotations of the interferometric array would be necessary to achieve the detection of the planet with an SNR of 5. For spectroscopy, the integration time has to be much longer since the individual SNR in each spectral channel is significantly lower. For instance, about 150 rotations of the interferometric array would be necessary to achieve an SNR of 10 at $10\mu\text{m}$.

3.6. Expected performance

Considering the assumptions given in Table 2, the simulated performance of DARWIN/TPF is shown in Table 4 for various aperture sizes and planet radii. Considering Earth-radius planets within the habitable zone, about 200 stars, well spread among the four selected spectral types, can be surveyed during the nominal 2-year detection phase. This number reaches about 500 with 4-m aperture telescopes. DARWIN/TPF will thus provide statistically meaningful results on nearby planetary systems. As already indicated by Table 3, nearby K and M dwarfs are the best-suited targets in terms of Earth-like planet detection capabilities.

For the spectroscopy phase, a required SNR of 5 has been assumed for the detection of CO_2 and O_3 , as discussed in section 3.1. For the full characterisation (i.e. searching for the presence of H_2O , CO_2 , and O_3), the required SNR has been fixed to 10 on the $7.2\text{-}20\mu\text{m}$ wavelength range. With these assumptions, CO_2 and O_3 could be searched for about 40 planets (resp. 60) with rotational spectroscopy (resp. staring spectroscopy) while H_2O could potentially be detected on 20 (resp. 30) planets during the 3-year characterisation phase. These values would be roughly halved for 1-m aperture telescopes. Although staring spectroscopy presents (as expected) better results, rotational spectroscopy is more secure since it does not rely on an accurate localisation of the planet. It is also interesting to note that in the case of planets with radii 1.5 times as large as that of Earth,

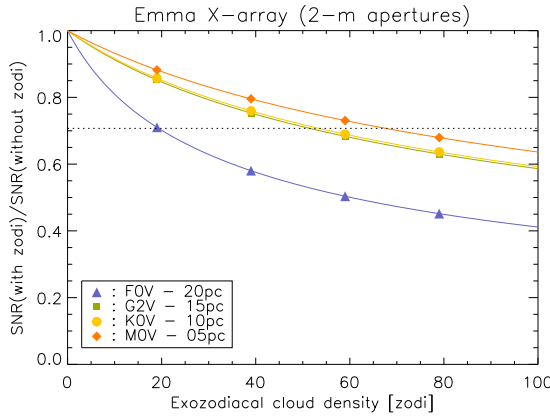


Fig. 7. Impact of the exozodiacal dust density on the SNR for different target stars. The exozodiacal disc is assumed to follow the Kelsall model (Kelsall et al. 1998) and to be seen in face-on orientation. The horizontal dotted line corresponds to an increase of integration time by a factor 2 with respect to the 0-zodi case.

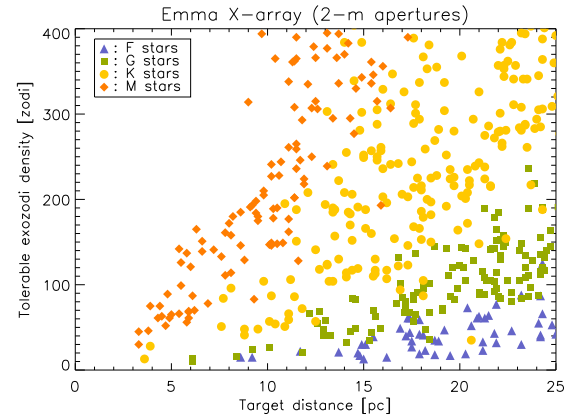


Fig. 8. Maximum number of zodis with respect to the target distance for the DARWIN/TPF target stars. The maximum number of zodis corresponds to an increase of integration time by a factor two with respect to the 0-zodi case.

the number of planets for which H_2O spectroscopy could be performed is doubled.

4. Impact of the exozodiacal cloud density

The amount of exozodiacal dust in the habitable zone of nearby main sequence stars is one of the main design drivers for the DARWIN/TPF mission. Depending on their morphology and brightness, exozodiacal dust clouds can seriously hamper the capability of a nulling interferometer to detect and characterise habitable terrestrial planets. Under the assumption that it is centrally symmetric around the target star, the exozodiacal cloud is suppressed by the chopping process, and therefore only contributes to shot noise. An exozodiacal cloud similar to the local zodiacal disc emits 350 times as much flux at $10\mu\text{m}$ than an Earth-like planet, so that it generally drives the integration time as the disc becomes a few times denser than the local zodiacal cloud. A previous study performed for the DCB with 3-m aperture telescopes observing a G2V star located at 10 pc has led to the conclusion that detecting Earth-like planets around a star for which the exozodiacal cloud density is larger than 20 zodis would be difficult (Beichman et al. 2006). Nevertheless, the tolerable amount of dust around a nearby main sequence star highly depends on several parameters such as the telescope size, the target distance and spectral type. Another parameter which can affect the performance of the interferometer is the presence of asymmetric structures in the exozodiacal disc such as clumps or offset due to the presence of planets. These asymmetries have a different impact on the mission performance because they introduce a signal which is not perfectly suppressed by phase chopping and can mimic the planetary signal. This section is focused on the impact of the exozodiacal dust density on the integration time and the consequence on the number of targets that can be surveyed during the mission lifetime. The impact of asymmetric structures is discussed in section 5.

4.1. Analysis per individual target

Currently, very little is known about the amount of exozodiacal dust in the habitable zone of nearby main sequence stars.

First results have been obtained only very recently using classical infrared interferometry at the CHARA array (Mount Wilson, USA) and at the VLTI (Cerro Paranal, Chile). These instruments have revealed the presence of hot dust in the inner part of planetary systems around a few nearby main sequence stars with a sensitivity of approximately one thousand zodis (Absil et al. 2006; Di Folco et al. 2007; Absil et al. 2008b, 2009; Akeson et al. 2009). Recent observations using ground-based nulling interferometry at the Keck observatory (Mauna Kea, USA) have shown improved sensitivity to exozodiacal dust clouds of a few hundred zodis (Stark et al. 2009). Given the lack of information on exozodiacal clouds with densities of a few zodis, we investigate in this section the impact of exozodiacal dust density on the performance of DARWIN/TPF.

Considering centrally symmetric face-on exozodiacal discs, Fig. 7 shows the SNR (normalised to the SNR for no exozodiacal cloud) integrated over the $6-20\mu\text{m}$ wavelength range as a function of the exozodiacal dust density for the 4 typical target stars used in section 3.5. We consider the normalised SNR because it does not depend on the integration time (the planetary signal is removed from the equation) which has the advantage to provide a common basis to compare the different target stars. Looking at Fig. 7, the impact of the exozodiacal dust density on the normalised SNR is particularly harmful for the hottest target stars which present the brightest exozodiacal discs. For the F0V star located at 20 pc, the normalised SNR is reduced by a factor of about 2.5 between the 0 and 100-zodi cases while for the M0V star located at 5 pc it is only reduced by a factor of about 1.5. Assuming that the integration time should not be twice longer than in the 0-zodi case (see the horizontal dotted curve), the maximum number of zodis are about 70, 50, 50 and 20 respectively for the M0V star located at 5 pc, the K0V star at 10 pc, the G2V star at 15 pc and the F0V star at 20 pc.

The distance of the star also plays an important role. As the distance to the target system increases, the flux collected from the exozodiacal cloud decreases while the flux collected from the local zodiacal cloud remains the same for all targets. The contribution of the exozodiacal dust cloud to the noise level becomes therefore relatively less important so that a higher dust density can be tolerated around the target. This explains why the curves of the G2V star and the K0V star almost coincide despite

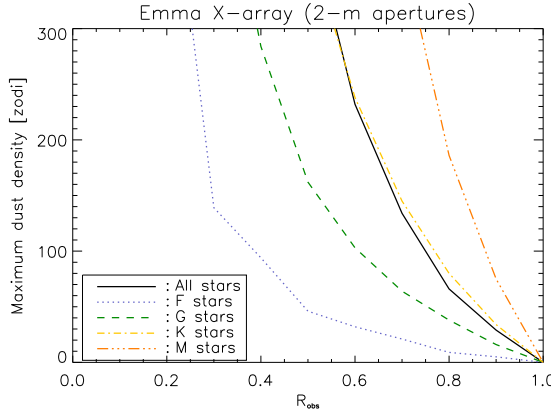


Fig. 9. Tolerable exozodiacal dust density as a function of the number of targets that can be observed during the mission lifetime normalised to the zodi-free case (R_{obs}), accounting for overheads and a specific time allocation for each spectral type (10% F, 50% G, 30% K and 10% M).

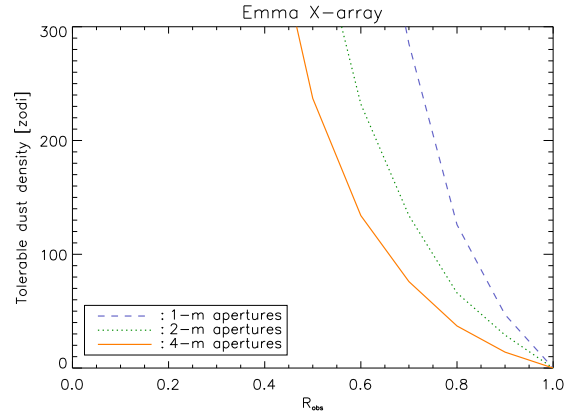


Fig. 10. Tolerable exozodiacal dust density for different aperture sizes as a function of the number of targets that can be observed during the mission lifetime normalised to the zodi-free case (R_{obs}). The results are computed for the nominal mission lifetime accounting for overheads and a specific time allocation for each spectral type (10% F, 50% G, 30% K and 10% M).

the fact that the G2V star is hotter. This behavior is illustrated in Fig. 8, showing the maximum number of zodis with respect to the target distance for the whole DARWIN/TPF catalogue. This maximum number of zodis corresponds to an increase of integration time by a factor two with respect to the 0-zodi case. It depends on the target distance and spectral type, and can take a value from few zodis up to several hundred zodis for the most distant stars. For a given distance to the target system, the maximum number of zodis increases with the stellar temperature, the zodi constraint being more severe on F stars than on M stars, while for a given spectral type, the zodi tolerance increases with the target distance.

4.2. Tolerable dust density

So far we have examined the maximum exozodiacal dust density for each target which corresponds to an integration time per target equal to twice the zero-zodi integration time. However, this does not tell us anything about the total number of stars that could be observed over the survey time of the mission. Here we derive the exozodiacal dust density that can be tolerated around nearby main sequence stars so that a given number of stars can be observed during the nominal mission lifetime.

To calculate the total number of targets that can be surveyed during the mission lifetime, we compute the integration time for each observable target as a function of the exozodiacal dust density and add them in ascending order as described in section 3.1. Considering a slew time of 6 hours and an efficiency for the remaining observing time of 70%, the list is cut off when the cumulative integration time exceeds the nominal survey period. Applying this procedure to each spectral type (with the corresponding time allocation, see Table 2) and to the whole target list, Fig. 9 shows the tolerable dust density as a function of R_{obs} , the ratio of the number of targets that can be observed during the mission lifetime in the presence of exozodiacal clouds of the given density to the number of targets that can be observed during the mission lifetime in the absence of exozodiacal clouds. The corresponding number of target stars that can be observed can easily be computed using Table 4.

As exozodiacal discs become denser, R_{obs} decreases so that the tolerable dust density depends on the goal of the mission in

terms of the number of stars that have to be observed. In order to survey approximately 50% of the stars that could be observed in the absence of exozodiacal discs, a dust density as high as 400 zodis can be tolerated, while only 30 zodis are tolerable to observe 90% of the stars. Considering that at least 150 targets³ have to be observed during the mission lifetime (about 75% of the stars), exozodiacal discs with a density of about 100 zodis can be tolerated around the targets stars. This tolerable dust density is computed for the whole catalogue assuming that the time allocation on each spectral type is maintained. In practice, the effect of exozodiacal dust is more pronounced for early type stars. This behavior is illustrated in Fig. 9 for each spectral type. For a dust density of 100 zodis, about 40%, 60%, 80% and 90% of the F, G, K and M stars respectively can still be surveyed. Conversely, in order to survey at least 75% of the stars, the tolerable dust densities are about 10, 50, 100 and 300 zodis for F, G, K and M stars respectively.

These results show how important it is to observe in advance the DARWIN/TPF targets in order to maximize the number of stars that can be surveyed during the mission lifetime. Ground-based nulling instruments like LBTI (“Large Binocular Telescope Interferometer”, Hinz et al. 2008) and ALADDIN (“Antarctic L-band Astrophysics Discovery Demonstrator for Interferometric Nulling”, Absil et al. 2008a) would be ideal to reach the detection of 50-zodi exozodiacal discs with a sky coverage sufficient to observe almost the entire DARWIN/TPF catalogue.

4.3. Influence of the telescope size

Increasing the telescope diameter has different influences on the individual signal and noise sources. The planetary signal increases as D^2 while the shot noise contributions from geometric leakage and exozodiacal cloud increase as D . The relative contribution from the local zodiacal cloud to shot noise is reduced for larger aperture telescopes, due to the smaller field-of-view. Since the local zodiacal cloud emission is generally one of the

³ Detecting 150 targets has been defined by both ESA and NASA as the minimum mission requirement for DARWIN/TPF-I.

dominant noise sources, the relative impact of the exozodiacal cloud density on the SNR becomes therefore more significant for larger telescopes. Using the assumptions of Table 2, this behavior is illustrated in Fig. 10, which shows the tolerable exozodiacal dust density with respect to R_{obs} for different aperture sizes.

For a given dust density, the loss of observable targets during the mission lifetime with respect to the case without exozodiacal disc is more important for larger aperture telescopes. For instance, the tolerable densities are 50, 30 and 15 zodis respectively for 1-m, 2-m and 4-m apertures telescopes in order to survey at least 90% of the nominal targets. These values become 200, 100 and 60 zodis if 75% of the targets have to be surveyed. Considering again that 150 targets have to be observed during the mission lifetime, dust densities as high as 100 and 600 zodis can be tolerated around the target stars for 2-m and 4-m apertures telescopes respectively (150 targets being not detectable within the survey time with 1-m aperture telescopes). Due to the better nominal performance achieved with 4-m aperture telescopes (about 500 targets surveyed during the survey time, see Table 4), the maximum dust density to survey 150 targets (600 zodis) is higher than for 2-m aperture telescopes (100 zodis) but the corresponding loss of surveyed targets with respect to the nominal case is much more important (R_{obs} of 30% vs 75%). In practice, larger aperture telescopes would obviously be better to maximize the scientific performance but the final choice will also result from a trade-off with cost and feasibility.

5. Impact of the exozodiacal cloud morphology

The previous results have been obtained assuming that the exozodiacal dust emission is centrally symmetric around the target star so that it is suppressed by phase chopping (and therefore only contributes to shot noise). However, exozodiacal discs are likely to show resonant structures or an offset with respect to the central star due to the gravitational influence of embedded planets. These resonant structures have been predicted by theoretical studies (Roques et al. 1994; Liou & Zook 1999; Ozeroy et al. 2000), and similar structures have been observed in few cases around nearby main-sequence stars (e.g., Wilner et al. 2002; Greaves et al. 2005; Kalas et al. 2005; Schneider et al. 2009). The most well-studied example of an asymmetric disc is the solar zodiacal cloud, which exhibits several structures interpreted as the dynamical signature of planets (Dermott et al. 1985, 1994; Reach et al. 1995). This trend suggests that exozodiacal clouds may be full of rings, clumps, and other asymmetries induced by the presence of embedded planets. These asymmetric structures around the target star are not perfectly canceled by the phase chopping process and part of the exozodi signal can then mimic the planetary signal. If the demodulated contribution from the exozodiacal disc is significantly higher than that of the planet, it would be difficult to isolate the planetary signal, whatever the integration time. As mentioned by Lay (2004), asymmetric inhomogeneities at the 0.1% level of the total exozodiacal flux can be confused with a planetary signal. The problem becomes even more serious as the dust density increases: a 10-zodi exozodiacal disc must be smooth at the 0.01% level, in the region to be searched for planets. Considering asymmetric exozodiacal discs, we derive in this section the tolerable dust density in order to ensure the detection of Earth-like planets with DARWIN/TPF.

5.1. Methodology

At the output of the interferometer, the total detected photon rate (excluding stray light) can be written as (Lay 2004):

$$N = \int_{\theta} \int_{\alpha} B_{\text{sky}}(\mathbf{s}) R(\mathbf{s}) P(\mathbf{s}) \theta d\theta d\alpha, \quad (1)$$

where B_{sky} is the brightness distribution on the sky for a spectral channel centered on wavelength λ and a bandwidth $\Delta\lambda \ll \lambda$ (units in photons/s/m²), \mathbf{s} is a unit vector whose direction represents position on the sky, $P(\mathbf{s})$ is a field-of-view taper function resulting from the size of a collecting aperture and from the response of the single-mode spatial filter, and $R(\mathbf{s})$ is the intensity response of the interferometer on the sky (excluding the taper), the so-called transmission map. Expression 1 can be written as a function of the double Fourier transform of the sky brightness, including the field-of-view taper, which are denoted by a horizontal bar:

$$N = \sum_j \sum_k A_j A_k [\cos(\phi_j - \phi_k) \bar{B}_{\text{sky},jk,\text{sym}} - \sin(\phi_j - \phi_k) \bar{B}_{\text{sky},jk,\text{asym}}], \quad (2)$$

where $B_{\text{sky},\text{sym}}$ (resp. $B_{\text{sky},\text{asym}}$) is the symmetric (resp. asymmetric) part of the sky brightness distribution and ϕ_j the phase response of the telescope j . The total photon rate is therefore a sum over all possible pairs of collectors. The baselines with a phase difference that is an integer multiple of π ($0, \pm\pi, \pm2\pi$) couple entirely to the symmetric brightness distribution (star, local zodiacal cloud, exozodiacal disc). Any asymmetric brightness distribution couples entirely to baselines with a phase difference that is an odd multiple of $\pi/2$ (e.g., planet, clump). From Eq. 2, the detected photon rate from the exozodiacal disc is simply given by:

$$N_{\text{EZ}} = \sum_j \sum_k A_j A_k [\cos(\phi_j - \phi_k) \bar{B}_{\text{EZ},jk,\text{sym}} - \sin(\phi_j - \phi_k) \bar{B}_{\text{EZ},jk,\text{asym}}], \quad (3)$$

The demodulated signal from the exozodiacal disc can then be obtained (after combination of the two chop states):

$$O_{\text{EZ}} = \frac{1}{T} \int_0^T (N_{\text{EZ}}^L - N_{\text{EZ}}^R) \eta dt, \quad (4)$$

where T is the integration time, N_{EZ}^L (resp. N_{EZ}^R) the contribution of the exozodiacal disc at the output of the left (resp. right) chop state and η the demodulation template function. This template function is used to extract the planetary signal by cross-correlation (Angel & Woolf 1997). It represents the time series (normalized to have a rms value of one) that would be obtained, should a planet be present at a given position. Taking into account that the phase response of the interferometer is such that $\phi_i^L = -\phi_i^R$ with the ϕ_i^L equal to $(\pi/2, 0, \pi, 3\pi/2)$, Eq. 3 and 4 give:

$$O_{\text{EZ}} = \frac{2}{T} \sum_j \sum_k A_j A_k \sin(\phi_j - \phi_k) \int_0^T \bar{B}_{\text{EZ},jk,\text{asym}} \eta dt, \quad (5)$$

which shows that only asymmetric components of the brightness distribution contribute to the demodulated signal. More specifically, only the baselines with a “fractional- π ” phase difference can produce a demodulated signal. Such baselines are mandatory

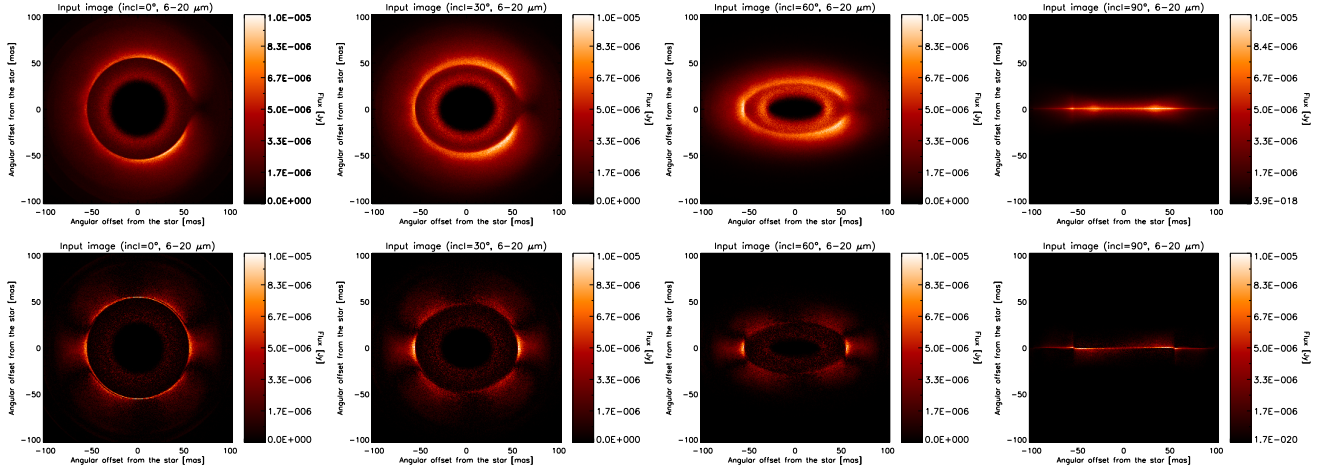


Fig. 11. *Upper:* Thermal flux ($6-20\mu\text{m}$) produced by a 10-zodi exozodiacal dust cloud around a G2V star for four different disc inclinations (0° , 30° , 60° and 90°) and assuming a Dohnanyi distribution of particle sizes (Dohnanyi 1969). The images have been simulated assuming a Earth-mass planet located at 1 AU on the x-axis (90 degrees clockwise from vertical, Stark & Kuchner 2008). *Lower:* Corresponding asymmetric brightness distributions obtained by subtracting to each pixel its centrally symmetric counterpart.

in order to generate odd harmonics of the rotation frequency. A solution to mitigate the influence of the asymmetric structures in the disc is to have long imaging (“fractional- π ”) baselines that resolve out the more spatially extended emission from the exozodi variations, leaving only the point like emission from planets.

5.2. Impact of clumps

The origin of some asymmetric clumpy structures, i.e. local density enhancements, in exozodiacal discs may be attributed to the gravitational influence of planets on the small dust grains. After their release from parent bodies via collisions or outgassing, dust grains experience different paths in the stellar system, depending on their effective size. Whereas the smallest particles are ejected from the planetary systems by radiation pressure in a dynamical time, larger particles slowly spiral inward due to Pointing-Robertson drag (Robertson 1937). While spiraling toward their host star, dust particles may become temporarily trapped in mean motion resonance with planets, extending their lifetimes. This trapping locally enhances the particle density, creating structures, originally described for the solar zodiacal cloud as circumstellar rings, bands, and clumps (e.g., Kelsall et al. 1998).

In order to address the impact of such structures on the performance of *DARWIN/TPF*, we use the results of Stark & Kuchner (2008), who synthesized images of circumstellar discs with resonant rings structures due to embedded terrestrial-mass planets. Among the studies that have examined the geometry of these resonant signatures (e.g., Kuchner & Holman 2003; Moro-Martín & Malhotra 2005; Reche et al. 2008; Stark & Kuchner 2008), these images are particularly convenient for our study since they include enough particles to overcome the limitations of previous simulations, which were often dominated by various sources of Poisson noise, and allow for quantitative study of the modeled ring structures. In addition, these images are geared toward terrestrial-mass planets at a few AU from the star, whereas most other studies concern more massive planets located much far-

ther from the star. We used the Stark & Kuchner (2008) models to produce thermal emission images of inclined discs (0° , 30° , 60° and 90°) with resonant ring structures. We investigated disc models for a system with an Earth-mass planet on a circular orbit at 1 AU around a G2V star located at 15 pc and for a Dohnanyi distribution ranging in size from the blowout size up to $120\mu\text{m}$ (Dohnanyi 1969). The thermal emission produced by such exozodiacal discs are given in the upper part of Fig. 11 in a wavelength range of $6-20\mu\text{m}$.

The images given in Fig. 11 can be thought of as upper-limits to the brightness of structures due to an Earth-like planet. Stark & Kuchner (2008) ignored dust from parent bodies with large inclinations and eccentricities, such as comets, which would tend to wash out any resonant structure. Additionally, these models ignore the effects of collisions, which smooth out overdense regions of the disc and reduce azimuthal asymmetries (Stark & Kuchner 2009). In every simulation, the parent bodies were initially distributed from 3.5 to 4.5 AU in an asteroid belt-like ring. The Earth-mass planet is oriented along the x-axis (located at 66 mas on the x-axis) with a noticeable gap in the ring at its position. The models are truncated at half the semi-major axis of the planet, resulting in the inner holes in the images of Fig. 11. In reality, the dust density distribution should continue inward to the dust sublimation radius in the absence of additional perturbers. This “missing” inner disc should however not affect our results, since the inner disc would be centrally symmetric so that it does not contribute to the detected signal.

Introducing these images into *DarwinSIM*, we compute the chopped photon rate from the exozodiacal disc as a function of the array rotation angle. This is represented in the upper part of Fig. 12 for two different disc inclinations (0° and 60°) at $10\mu\text{m}$ (left figures) and for broadband detection ($6-20\mu\text{m}$, right figures). The density of the disc has been scaled up to 10 zodis and the chopped planetary signal represented for comparison (dashed curve). In all cases, it is dominated by the chopped signal from the exozodiacal disc (solid curve) and particularly for high disc inclinations. To disentangle the planetary signal from the disc signal, it is necessary to apply the cross-correlation

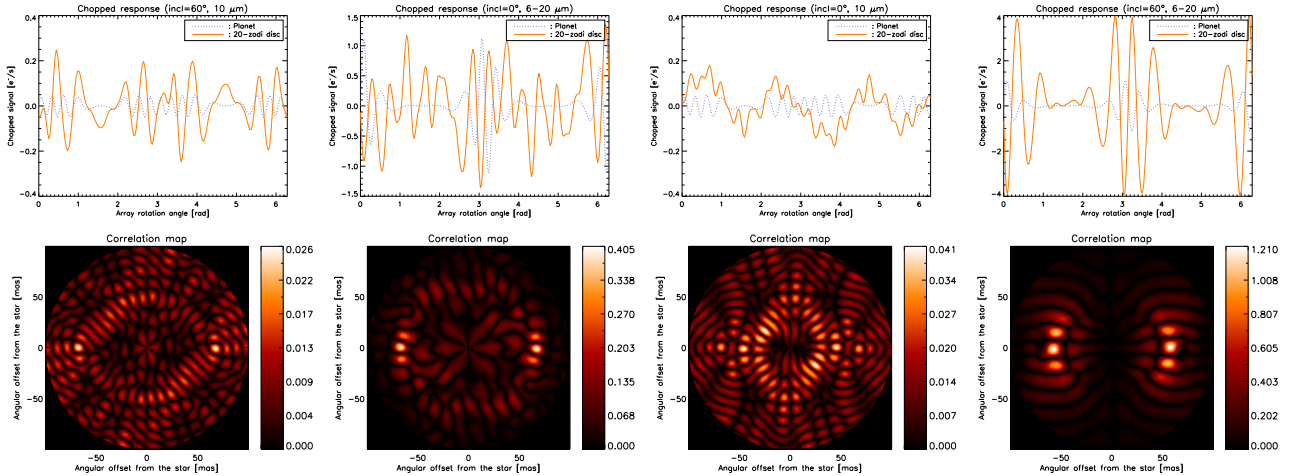


Fig. 12. *Upper:* Chopped photon rate from an Earth-like planet and a 10-zodi asymmetric disc with respect to the rotation angle for two disc inclinations (0° and 60°) and different wavelength ranges (at $10\,\mu\text{m}$ and in the full wavelength range). *Lower:* Corresponding dirty map formed from the cross correlation of the measured signal with templates of the signal expected from a point source at each location on the sky.

method to build the so-called *dirty map*. Applying cross correlation of the measured signal (disc + planet) with templates of the signal expected from a point source at each location on the sky (computed using Eq. 5), the dirty maps represented in the lower part of Fig. 12 are obtained. This process transforms the rotationally modulated signal into a map of the sky by cross-correlation, which is equivalent to the Fourier transform used in standard synthesis imaging. The planet is located at 66 mas on the x-axis and presents a demodulated signal of about $0.028\,\text{e}^-/\text{s}$ at $10\,\mu\text{m}$ and about $0.62\,\text{e}^-/\text{s}$ for broadband detection. The total demodulated signal at the planet position is however lower due to the negative contribution from the exozodiacal disc which presents a hole near the planet. The demodulation of the exozodiacal discs also produces main peaks which are maximum around 30-50 mas from the host star (in agreement with the asymmetric brightness distribution in the initial images, see the lower part of Fig. 11). Fortunately, the high angular resolution provided by the long imaging baseline is sufficient to spatially distinguish these components from the planetary signal and only the contribution from the hole around the planet significantly contributes to the noise level.

In order to ensure the planet detection, we adopt a criterion commonly used in AO imaging (Macintosh et al. 2003; Hinkley et al. 2007; Serabyn 2009). The noise level is taken to be the rms deviation of the pixel counts within an annulus of width equal to the size of the PSF at half maximum. Considering a detection threshold of 5, the results are given in Table 5 for different wavelengths and disc inclinations. The tolerable disc density ranges between about 1 and 15 zodis, depending on the disc inclination. The detection is particularly difficult for highly inclined discs for which the asymmetric components are more dominant and at long wavelengths where the planetary signal is weaker. Combining the spectral channels to obtain a broadband correlation map (see Fig. 12) reduces the impact of sidelobes associated with each main peak but does not significantly improve the results. This is because the performance are limited by the main peak induced by the hole near the planet rather than by sidelobes. Note that this hole generally induces a response 2 to 4 times larger the rms deviation of the pixel counts within the annulus so that it might be marginally interpreted as a planet detection

(a “false positive”). However, it could also be seen as an indirect way to detect the presence of a planet within the hole since such compact structure is expected to be created by a planet.

In order to relax these stringent constraints on the exozodiacal dust density, more sophisticated techniques of data processing could be useful (e.g., Thiebaut & Mugnier 2006). The capability of these techniques still needs to be investigated and is beyond the scope of this paper. The only secure way to ensure the detection and characterization of Earth-like planets with DARWIN/TPF-like missions is to observe in advance the nearby main-sequence stars in order to remove from the target list the stars with a too high inclined/bright exozodiacal disc. To achieve this goal, a space-based nulling interferometer such as FKSI (“Fourier-Kelvin Stellar Interferometer”) would be ideal with a sensitivity sufficient to detect exozodiacal discs down to 1 zodi (Defrère et al. 2008a).

5.3. Impact of the disc offset

An offset between the center of symmetry of a dust cloud and its host star is a natural consequence of the gravitational interaction with planets. In the solar system, the center of the zodiacal cloud is shifted by about 0.013 AU from the Sun due mostly to Jupiter (Landgraf & Jehn 2001). The offset can be much larger, as shown in the case of the Fomalhaut system with an offset of 15 AU (Kalas et al. 2005). Even when inhomogeneities such as clumps are not present, an offset cloud produces an asymmetric brightness distribution such that a part of the exozodiacal disc signal survives the chopping process. Using the zodipic package⁴, we produce images of solar-like zodiacal discs with a given offset and use them to compute the demodulated signal at the output of the interferometer. The results are presented in Fig. 13, showing the tolerable dust density with respect to the disc offset for a G2V star located at 15 pc and for different wavelengths. The disc is assumed to be seen face-on.

As the distance between the host star and the center of symmetry of the exozodiacal disc increases, the tolerable dust density to detect an Earth-like planet located at 1 AU becomes more

⁴ <http://asd.gsfc.nasa.gov/Marc.Kuchner/home.html>

Table 5. Tolerable exozodiacal dust density for different disc inclinations and wavelengths. The detection threshold is taken to be 5 times the rms deviation of the pixel counts within an annulus of width equal to the size of the PSF at half maximum.

Disc incl.	8 μm	10 μm	16 μm	Wide
0°	12.2	15.3	7.0	14.0
30°	9.1	15.0	6.9	13.8
60°	6.1	6.8	2.1	3.8
90°	1.1	1.4	1.0	2.6

severe and reaches less than 5 zodis for an offset of 1 AU. For individual spectral channels, the tolerable dust density rapidly decreases to reach the value of 20 zodis at 0.05, 0.15 and 0.25 AU respectively at 8 μm , 10 μm and 16 μm . The results for broadband detection are much better with a tolerable dust density of 20 zodis only for a disc presenting an offset larger than 0.6 AU. Considering a tolerable exozodiacal dust density of 100 zodis, the offset between the host star and the center of symmetry of the exozodiacal disc can be as high as 0.4 AU in order to ensure the planet detection. For an offset similar to that of the solar zodiacal cloud (about 0.013 AU), this tolerable dust density is even much higher (few thousand zodis).

6. Conclusions

Infrared nulling interferometry is the core technique of future life-finding space missions such as ESA's DARWIN and NASA's Terrestrial Planet Finder (TPF). Observing in the infrared (6-20 μm), these missions will be able to characterise the atmosphere of habitable extrasolar planets orbiting around nearby main sequence stars. This ability to study distant planets strongly depends on exozodiacal clouds around the stars, which can hamper the planet detection. Considering the nominal mission architecture with 2-m aperture telescopes, we show that centrally symmetric exozodiacal dust discs about 100 times denser than the solar zodiacal cloud can be tolerated in order to survey at least 150 targets during the mission lifetime. The actual number of planet detections will then depend on the number of terrestrial planets in the habitable zone of target systems.

The presence of asymmetric structures in exozodiacal discs (e.g., clumps or offset) may be more problematic. While the cloud brightness drives the integration time necessary to disentangle the planetary photons from the background noise, the emission from inhomogeneities are not perfectly subtracted by phase chopping so that a part of the disc signal can mimic the planet. To address this issue, we consider modeled resonant structures produced by an Earth-like planet and introduce the corresponding image into *DarwinSIM*, the mission science simulator. Even for exozodiacal discs a few times brighter than the solar zodiacal cloud, the contribution of these asymmetric structures can be much larger than the planetary signal at the output of the interferometer. Fortunately, the high angular resolution provided by the long imaging baseline of DARWIN/TPF in the X-array configuration is sufficient to spatially distinguish most of the extended exozodi emission from the planetary signal and only the hole in the dust distribution near the planet significantly contributes to the noise level. Considering the full wavelength range of DARWIN/TPF, we show that the tolerable dust density is about 15 times the solar zodiacal density for face-on systems and decreases with the disc inclination. In practice, this constraint might be relaxed since we examined a resonant ring model that does not include dust from highly eccentric or inclined parent bodies, the effects of grain-grain collisions, or perturbations by

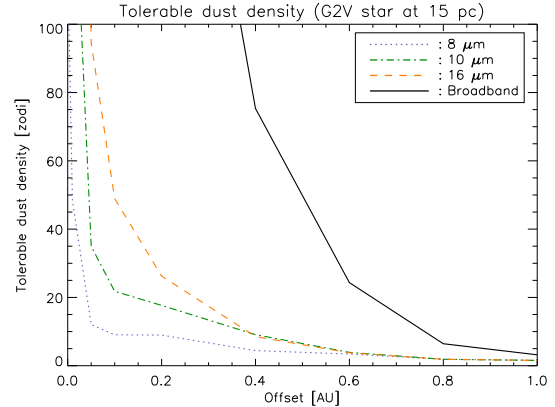


Fig. 13. Tolerable exozodiacal dust density with respect to the offset between the center of symmetry of the exozodiacal disc and the central star (a G2V star located at 15 pc). The disc is assumed to be seen in face-on orientation.

additional planets, all of which can reduce the contrast of the resonant ring and improve the tolerance to the exozodiacal dust density.

These results show that asymmetric structures in exozodiacal discs around nearby main sequence stars are one of the main noise sources for future exo-Earth characterization missions. A first solution to get around this issue is to have a long imaging baseline architecture which resolves out the more spatially extended emission of the exozodiacal cloud from the point-like emission of planets. The stretched X-array configuration is particularly convenient in that respect. The second solution is to observe in advance the nearby main sequence stars and remove from the DARWIN/TPF target list those presenting a too high dust density or disc inclination. The FSKI nulling interferometer would be ideal in that respect with the possibility to detect exozodiacal discs down to the density of the solar zodiacal cloud. Ground-based nulling instruments like LBTI and ALADDIN would also be particularly valuable.

Appendix A: Deriving instability noise constraints

We address here the instability noise and derive the constraints on the instrument stability required to detect an Earth-like planet orbiting at 1 AU around a G2V star located at 15 pc. The analysis follows the analytical method of Lay (2004) which was originally applied to the DCB configuration at 10 μm . The goal is to extend the study to the X-array architecture and to short wavelengths where instability noise is the most dominant. We define the limiting rms OPD and amplitude errors such that instability noise is dominated by a factor 5 by shot noise over a single rotation of 50000 s. Assuming that instability noise is totally uncorrelated with the rotation angle, this factor stays unchanged over multiple rotations. In practice, instability noise can be correlated with the rotation angle due to perturbations such as solar heating effects but it should be possible to remove them by measuring and correcting the amplitudes and phases at intervals during the rotation.

For sake of comparison with Lay (2004), we consider first 4-m aperture telescopes operating at 10 μm and extend the results to 2-m aperture telescopes operating at 7 μm in Table A.1. Assuming a spectral resolution of 20, Fig. A.1 shows instabil-

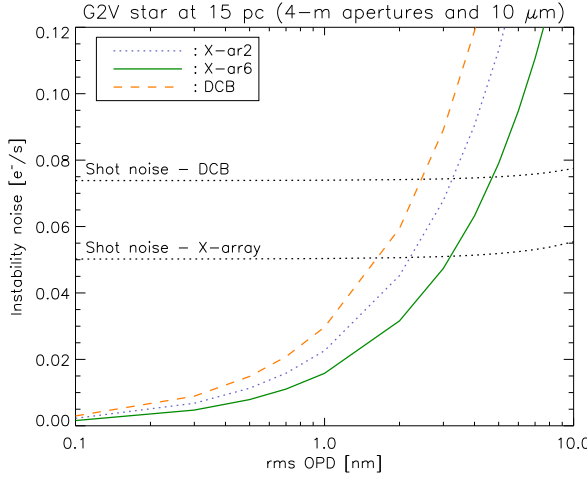


Fig. A.1. Instability noise with respect to the rms OPD errors for different array architectures assuming 1/f-type PSDs and a rms amplitude mismatch of 0.1% (defined on the 0– 10^4 Hz frequency range). The level of shot noise is represented by dotted curves for each configuration. The figure has been plotted for 4-m aperture telescopes operating at 10 μm and a G2V star located at 15 pc (surrounded by an exozodiacal cloud of 1 zodi).

ity noise with respect to the rms OPD error for three different configurations: the DCB as defined in Lay (2004), the X-array with a 1:2 aspect ratio (X-ar2) and the X-array with a 1:6 aspect ratio (X-ar6). These curves have been computed assuming 1/f-type PSDs for amplitude and OPD errors with rms values defined on a frequency range from $1/t_{\text{rot}}$ to 10^4 Hz, where t_{rot} is the rotation period, and a G2V star located at 15 pc. Shot noise is represented by dotted curves. It is higher for the DCB due to geometrical leakage (the nulling baseline is twice larger than for the X-array) and presents a slight increase for large rms OPD errors due to instrumental leakage. Instability noise is also higher for the DCB than for the X-array. This is because the planetary signal is mostly modulated at lower frequencies where the instability noise is higher for 1/f-type noises. This is illustrated in Fig. A.2 showing the chopped planet detection rate with respect to the rotation angle of the array (upper figure) and the corresponding Fourier amplitudes (lower figure).

Fig. A.1 shows that shot noise dominates instability noise by a factor 5 for rms OPD errors of about 0.5 nm, 0.5 nm and 0.6 nm respectively for the DCB, X-ar2 and X-ar6. The slight discrepancy that can be mentioned with Lay (2004) is due to two factors. In addition to the instrument throughput of 10% used in Lay (2004), our study accounts for the coupling efficiency (about 72% for the on-axis light) and for the quantum efficiency of the detectors (70%). We also combine the two chop states whereas the results of Lay (2004) are given for only one. Although instability noise is higher for the DCB configuration than for the X-array, the limiting rms opd error is of the same order due to the higher shot noise. Because instability noise is directly proportional to the stellar flux, the constraints are even more stringent at 7- μm where the star is brighter and the level of shot noise basically the same than at 10 μm (see Table A.1). Considering an rms amplitude mismatch of 0.1%, the OPD has to be controlled to a level of 0.3 nm rms for the three considered configurations. These constraints are slightly relaxed for 2-m aperture telescopes because shot noise is relatively more dominant (shot noise is pro-

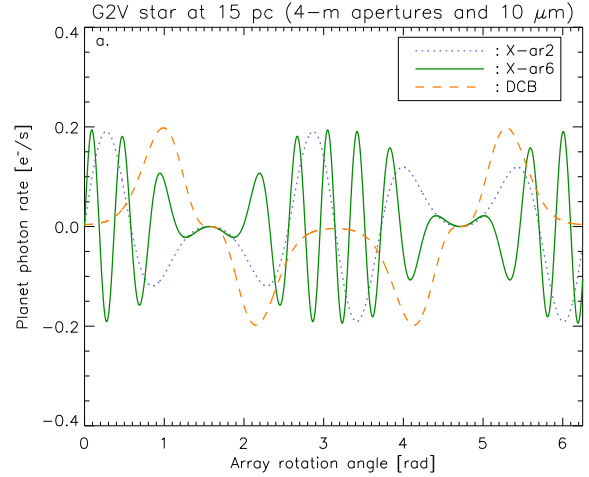


Fig. A.2. *Upper:* Chopped planet detected photon rate as a function of array rotation angle for the different architectures. The planet is assumed to be located at 47 mas from a G2V star located at 15 pc. *Lower:* Corresponding Fourier amplitudes. Only odd harmonics are present because of phase chopping.

portional to the squared root of the stellar flux while instability is directly proportional to the stellar flux). For the results at 7 μm , we use the same baseline length of 20 m with the same rotation period of 50000 s. These requirements are very stringent and are only marginally compliant with state-of-the-art active control, so that potential ways to mitigate the harmful effect of instability noise have been investigated.

– A first solution, proposed by Lay (2006), consists in stretching the array and applying a low-order polynomial fit to the instability noise (as a function of wavelength). By stretching the array, i.e. increasing the imaging baseline of the X-array, the interference pattern orthogonal to the nulling pattern shrinks. As the modulation map scales with wavelength, the planetary signal transmitted by the interferometer will then be a rapidly oscillation function of wavelength. On the other hand, instability noise is shown to be a low-order polynomial of the optical frequency ($1/\lambda$). Therefore, by removing a low-order polynomial fit to the detected signal as a function of wavelength, the instability noise contribution is efficiently subtracted while preserving most of the planetary signal. This operation can actually be performed directly in the cross-correlation, by using a modified planet template where the polynomial components have been removed. Because this method strongly relies on the separation of the nulling and imaging baselines, it can only be efficiently applied with the X-array architecture.

Table A.1. Limiting rms OPD values computed for a G2V star located at 15 pc such that shot noise dominates instability noise by a factor 5. The results are given at $7\text{ }\mu\text{m}$ and $10\text{ }\mu\text{m}$, assuming a spectral resolution of 20, for different rms amplitude mismatches and shapes of the instability noise power spectrum. Three configurations are shown, the X-array with an aspect ratio of 2 (X-ar2), the X-array with an aspect ratio of 6 (X-ar6) and the Dual Chopped Bracewell (DCB, configuration used in Lay 2004).

σ_{OPD} [nm]		2-m apertures						4-m apertures					
σ_{amp}		$\lambda=7\text{ }\mu\text{m}$			$\lambda=10\text{ }\mu\text{m}$			$\lambda=7\text{ }\mu\text{m}$			$\lambda=10\text{ }\mu\text{m}$		
		DCB	X-ar2	X-ar6	DCB	X-ar2	X-ar6	DCB	X-ar2	X-ar6	DCB	X-ar2	X-ar6
White noise ^a	0.1%	46	17	17	97	95	95	10	5.5	5.5	19	14	14
	0.5%	4.3	2.6	2.6	8.7	7.2	7.2	2.1	1.2	1.2	3.3	2.4	2.4
	1.0%	2.3	1.5	1.5	4.5	3.8	3.8	1.1	0.6	0.6	1.8	1.4	1.4
1/f noise ^b	0.01%	0.7	2.6	4.2	2.8	13	19	0.4	1.1	1.9	1.1	3.6	5.6
	0.05%	0.7	0.9	1.5	2.0	2.9	4.1	0.3	0.4	0.6	0.8	0.9	1.4
	0.10%	0.5	0.5	0.7	1.5	1.6	2.0	0.3	0.3	0.3	0.5	0.5	0.6

^a rms values is defined on the [0-10 Hz] wavelength range

^b rms values is defined on the [$1/t_{\text{rot}} \cdot 10^4$ Hz] wavelength range

- Another solution, based on the coherence properties of starlight, has been proposed by Lane et al. (2006) to separate the contributions from the planet and the instrumental leakage. The idea is to mix the electric fields of the leakage with that of a separate reference beam, also from the star, in order to form fringes (as long as the relative path delays are maintained within the coherence length). The light from the planet, being not coherent with the starlight, will not form fringes. Using as reference beam the bright output of a pairwise nulling beam combiner, the amplitude and phase mismatches in the input beams can be extracted from the fringe pattern, allowing the reconstruction of the the stellar leakage.
- A third solution has recently been proposed and tested at IAS (Gabor et al. 2008). The principle is to successively apply two ($< \lambda/2$) opposite OPD offsets to one of the beams in order to derive the actual position of the minimum in the transmission map. In this way, one feeds back the actual OPD errors to the delay line and prevents drifts from appearing. The same principle can be used to avoid amplitude drifts, by either blocking all but one beam to measure its actual amplitude or by modulating its amplitude as in the case of the OPD. The frequency at which this process is carried out depends on the input power spectra of the noise sources. It has been demonstrated experimentally in the lab that this process efficiently suppresses the 1/f-type noise generally present in the stellar contribution at the output of a Bracewell interferometer. This technique can theoretically be applied to any nulling configuration, but its efficiency decreases as the number of beams increases.

Others possible approaches (e.g. application of closure phase techniques, new chopping processes, exploiting correlations between measurements taken at different wavelength bins) have been suggested but still need to be investigated. However, these very stringent requirements have been derived with the assumption that the instability noise present an 1/f-type power spectrum. In fact, the shape of the instability noise spectrum strongly depends on the input spectrum of noise fluctuations. Pure 1/f noise might in fact turn out to be a very pessimistic assumption. Given that the DARWIN/TPF system is designed to have three levels of control loops that manage the OPD, and two control loop levels for tip/tilt, the resulting residual phase and intensity fluctuations that are responsible for the instability noise are most likely to have a flat input spectrum. This has a strong influence on the magnitude of the phase-amplitude cross terms, which are the main contributor to instability noise. For instance, the tol-

erable rms OPD errors for a white spectrum defined on the [0-10 Hz] frequency range are significantly relaxed as indicated in Table A.1. In particular at low frequencies, where the planetary signal is modulated and the instability noise arises, the 1/f spectrum diverges, while the flat spectrum increases linearly. In practice, the situation might even be better, as predictive or Kalman filtering may be used to remove low-frequency power. A complication, in particular for the micro Hz domain, is that zero point drifts of the control loops, e.g. related to electronic drifts in the sensors, remain undetected, and thus uncorrected. They will result in a low-frequency 1/f component. A simple solution is to switch the incoming beams with respect to the control loops. The reason why this could work is that the extremely high precision required for DARWIN/TPF is only on relative quantities, namely, the phase and amplitude differences between any two beams. Absolute offsets of phase and amplitude, that apply to all three beams simultaneously, do not contribute to the instability noise, since they do not affect the null. The beams must be switched with respect to the control inputs with a time constant over which the drift can be considered constant. In summary, even though at present a post-processing method has not been identified, it is highly likely that clever and careful engineering may already reduce instability noise to harmless levels.

Acknowledgements. The authors are grateful to Lisa Kaltenegger (Harvard-Smithsonian Center for Astrophysics) for providing the updated DARWIN catalogue, Jean Surdej (IAGL), Arnaud Magette (IAGL), Dimitri Mawet (NASA/JPL), Peter Lawson (NASA/JPL), Oliver Lay (NASA/JPL), Pierre Riaud (IAGL) and Virginie Chantry (IAGL). This research was supported by the International Space Science Institute (ISSI) in Bern, Switzerland (“Exozodiacal Dust discs and Darwin” working group, <http://www.issibern.ch/teams/exodust/>). DD and CH acknowledge the support of the Belgian National Science Foundation (“FRIA”). OA acknowledges the support from a F.R.S.-FNRS Postdoctoral Fellowship. DD and OA acknowledge support from the Communauté française de Belgique - Actions de recherche concertées - Académie universitaire Wallonie-Europe.

References

Absil, O. 2001, Master’s thesis, Liège University, Liège, Belgium, <http://www.aeos.ulg.ac.be/>
 Absil, O. 2006, PhD thesis, Liège University, Liège, Belgium
 Absil, O., Defrère, D., Coudé du Foresto, V., et al. 2008a, in Proc. SPIE, Vol. 7013
 Absil, O., di Folco, E., Mérard, A., et al. 2006, A&A, 452, 237
 Absil, O., di Folco, E., Mérard, A., et al. 2008b, A&A, 487, 1041
 Absil, O., Mennesson, B., Le Bouquin, J.-B., et al. 2009, ArXiv e-prints
 Akeson, R. L., Ciardi, D. R., Millan-Gabet, R., et al. 2009, ApJ, 691, 1896
 Alonso, R., Auvergne, M., Baglin, A., et al. 2008, A&A, 482
 Angel, J. R. P. & Woolf, N. J. 1997, ApJ, 475, 373

Barge, P., Baglin, A., Auvergne, M., et al. 2008, *A&A*, 482

Beichman, C. A., Bryden, G., Stapelfeldt, K. R., et al. 2006, *ApJ*, 652, 1674

Borucki, W. J., Koch, D. G., Lissauer, J., et al. 2007, in *Astronomical Society of the Pacific Conference Series*, Vol. 366, *Transiting Extrapolar Planets Workshop*, ed. C. Afonso, D. Weldrake, & T. Henning, 309–+

Bracewell, R. N. 1978, *Nature*, 274, 780

Carle, E. 2005, EMMA configuration: evaluation of optical performances, *Tech. Rep. Issue 1, ESA (SCI-A/279)*

Chazelas, B., Brachet, F., Bordé, P., et al. 2006, *Appl. Opt.*, 45, 984

d'Arcio, L. 2005

Defrère, D., Absil, O., Coudé Du Foresto, V., Danchi, W. C., & den Hartog, R. 2008a, *A&A*, 490, 435

Defrère, D., Lay, O., den Hartog, R., & Absil, O. 2008b, in *Proc. SPIE*, Vol. 7013

den Hartog, R. 2005a, DARWIN science performance prediction, *Tech. Rep. Issue 1, ESA (SCI-A/300)*

den Hartog, R. 2005b, The DARWINsim science simulator, *Tech. Rep. Issue 1, ESA (SCI-A/297)*

Dermott, S. F., Jayaraman, S., Xu, Y. L., Gustafson, B. A. S., & Liou, J. C. 1994, in , 719–723

Dermott, S. F., Nicholson, P. D., Burns, J. A., & Houck, J. R. 1985, in *Astrophysics and Space Science Library*, Vol. 119, *IAU Colloq. 85: Properties and Interactions of Interplanetary Dust*, ed. R. H. Giese & P. Lamy, 395–409

Di Folco, E., Absil, O., Augereau, J.-C., et al. 2007, *A&A*, 475, 243

Dohnanyi, J. S. 1969, *J. Geophys. Res.*, 74, 2531

Fridlund, C. V. M., d'Arcio, L., den Hartog, R., & Karlsson, A. 2006, in *Proc. SPIE*, Vol. 6268

Fridlund, M. 2005, Darwin Science Requirements Document, *Tech. Rep. Issue 5, ESA (SCI-A)*

Gabor, P., Chazelas, B., Brachet, F., et al. 2008, *A&A*, 483

Gillon, M., Pont, F., Demory, B.-O., et al. 2007, *A&A*, 472, L13

Greaves, J. S., Holland, W. S., Wyatt, M. C., et al. 2005, *ApJ*, 619, L187

Hinkley, S., Oppenheimer, B. R., Soummer, R., et al. 2007, *ApJ*, 654, 633

Hinz, P. M., Bippert-Plymate, T., Breuninger, A., et al. 2008, in *Proc. SPIE*, Vol. 7013

Kalas, P., Graham, J. R., & Clampin, M. 2005, in , 1067–1070

Kaltenegger, L., Eiroa, C., & Fridlund, C. V. M. 2008, *ArXiv e-prints*

Karlsson, A. L., Wallner, O., Perdigues Armengol, J. M., & Absil, O. 2004, in *Proc. SPIE*, ed. W. A. Traub, Vol. 5491, 831–+

Kelsall, T., Weiland, J. L., Franz, B. A., et al. 1998, *ApJ*, 508, 44

Ksendzov, A., Lay, O., Martin, S., et al. 2007, *Appl. Opt.*, 46, 7957

Ksendzov, A., Lay, O., Martin, S., et al. 2008, *Appl. Opt.*, 46, 7957

Kuchner, M. J. & Holman, M. J. 2003, *ApJ*, 588, 1110

Landgraf, M. & Jehn, R. 2001, *Ap&SS*, 278, 357

Lane, B. F., Muterspaugh, M. W., & Shao, M. 2006, *ApJ*, 648, 1276

Lawson, P. R., Lay, O. P., Martin, S. R., et al. 2008, in *Proc. SPIE*, Vol. 7013

Lay, O. P. 2004, *Appl. Opt.*, 43, 6100

Lay, O. P. 2005, *Appl. Opt.*, 44, 5859

Lay, O. P. 2006, in *Proc. SPIE*, Vol. 6268

Lay, O. P., Martin, S. R., & L., H. S. 2007, in *Proc. SPIE*, Vol. 6693

Léger, A. & Herbst, T. 2007, *ArXiv e-prints*, 707

Léger, A., Rouan, D., Schneider, J., Alonso, B., & Samuel, E. subm., *A&A*

Liou, J.-C. & Zook, H. A. 1999, *AJ*, 118, 580

Macintosh, B. A., Becklin, E. E., Kaisler, D., Konopacky, Q., & Zuckerman, B. 2003, *ApJ*, 594, 538

Mawet, D., Hanot, C., Lenaers, C., et al. 2007, *Optics Express*, 15, 12850

Mayor, M., Bonfils, X., Forveille, T., et al. 2009, *A&A*, in press

Mayor, M. & Queloz, D. 1995, *Nature*, 378, 355

Mennesson, B. & Mariotti, J. M. 1997, *Icarus*, 128, 202

Moro-Martín, A. & Malhotra, R. 2005, *ApJ*, 633, 1150

Moutou, C., Pont, F., Barge, P., et al. 2005, *A&A*, 437, 355

Orzernoy, L. M., Gorkavyi, N. N., Mather, J. C., & Taidakova, T. A. 2000, *ApJ*, 537, L147

Peters, R., Gappinger, R., Lawson, P., & Lay, O. 2009, *JPL Document D-60326*

Reach, W. T., Franz, B. A., Weiland, J. L., et al. 1995, *Nature*, 374, 521

Reche, R., Beust, H., Augereau, J.-C., & Absil, O. 2008, *A&A*, 480, 551

Richardson, L. J., Deming, D., Horning, K., Seager, S., & Harrington, J. 2007, *Nature*, 445, 892

Robertson, H. P. 1937, *MNRAS*, 97, 423

Roques, F., Scholl, H., Sicardy, B., & Smith, B. A. 1994, *Icarus*, 108, 37

Ruillier, C. & Cassaing, F. 2001, *Journal of the Optical Society of America A*, 18, 143

Schneider, G., Weinberger, A. J., Becklin, E. E., Debes, J. H., & Smith, B. A. 2009, *AJ*, 137, 53

Serabyn, E. 2009, *ApJ*, 697, 1334

Serabyn, E. & Colavita, M. M. 2001, *Appl. Opt.*, 40, 1668

Stark, C. C. & Kuchner, M. J. 2008, *ApJ*, 686, 637

Stark, C. C. & Kuchner, M. J. 2009, *ArXiv e-prints*

Stark, C. C., Kuchner, M. J., Traub, W. A., et al. 2009, 41, 501

Thiebaut, E. & Mugnier, L. 2006, in *IAU Colloq. 200: Direct Imaging of Exoplanets: Science and Techniques*, 547–552

Wilner, D. J., Holman, M. J., Kuchner, M. J., & Ho, P. T. P. 2002, *ApJ*, 569, L115

7.4 Summary

In this last chapter, we investigated the performance of future life-finding nulling interferometry missions, and address in particular two major noise sources: exozodiacal dust and instability noise. Considering a space-based infrared nulling interferometer in the Emma X-array configuration, we derived an upper limit on the tolerable exozodiacal dust density, and reviewed the constraints on the instrument stability. Using modeled resonant structures created by an Earth-like planet orbiting at 1 AU around a Sun-like star, we showed in particular that the tolerable dust density is about 15 times the solar zodiacal dust density. Finally, we concluded this study by reporting the science performance predictions, and showed that a 4-telescope space-based nulling interferometer would be able to detect about 200 Earth-like planets, among which 25 could be characterized by spectroscopy within a five year mission.

Conclusion

Objectives and results

The study of extrasolar planetary systems is nowadays among the most rapidly evolving topics in astrophysics. Since the discovery of the first extrasolar planet orbiting a solar-type star (Mayor and Queloz 1995), about 400 extrasolar planets have been detected. The possibility to identify habitable worlds and even life among them largely contributes to the growing interest about their nature and properties. Whereas Earth-size extrasolar planets are currently being detected for the first time by ongoing ground-based radial velocity and space-based transit surveys, the characterization of their atmosphere, mandatory to search for biological signatures, is much more challenging since it requires both a very high dynamic range and a high angular resolution. During the past decade, a large effort has been carried out to define the shortest pathway toward the discovery of Earth-like planets. In that context, infrared interferometry is a very promising technique, since it provides the required angular resolution to separate the emission of a star from that of its environment.

During the last few years, infrared interferometry has enabled the detection of circumstellar dust in the inner parts of debris discs, the extrasolar counterparts of our zodiacal dust cloud. In addition to be of prime importance to characterize the global architecture of planetary systems, the presence of large quantities of warm dust around nearby main sequence stars could seriously jeopardize the ability of future space missions to characterize Earth-like planets. In this dissertation, we contributed to the ongoing effort to characterize exozodiacal dust around nearby main sequence stars with observations using state-of-the-art infrared interferometers, performance studies for next generation space-based instruments, and a detailed analysis about the impact of exozodiacal dust on future exo-Earth characterization missions.

As a first contribution, we reported the detection of warm dust in the first few astronomical units around two A-type stars (Vega and β Leo) with the IOTA infrared stellar interferometer. Unlike previous studies of these two stars, the observations have been carried out in the H band. The multi-color interpretation of the data is currently under progress, and should significantly reduce the possibilities on the dust properties previously established on the sole K band.

As the sensitivity of state-of-the-art stellar interferometers is currently limited to the detection of exozodiacal discs about 1000 times denser than our zodiacal dust cloud, a specific technique of interferometry, referred to as *nulling interferometry*, has emerged to improve the dynamic range capabilities. The second part of this dissertation is dedicated to the performance study of two space-based nulling interferometers that have been intensively studied during the past few years (namely PEGASE and FKSI). We showed that PEGASE and FKSI would be very efficient to probe the inner region of circumstellar discs, with the sensitivity to detect exozodiacal discs down to the density level of our solar zodiacal cloud, and thereby outperform any ground-based instrument.

Another contribution of this dissertation is the investigation of the performance for planet detection of various space-based nulling interferometers. As a first step, we showed that PEGASE and FKSI would be able to characterize most extrasolar planets known so far. In addition, we addressed enhanced versions of these interferometers, which have been tuned to probe the habitable zone of nearby main sequence

stars. We showed that these concepts would be very efficient to characterize “super-Earth” extrasolar planets ($\sim 2 - 10 M_{\oplus}$) orbiting in the habitable zone of M stars located within 10 pc.

Finally, we investigated the performance of future exo-Earth characterization missions and address in particular two major noise sources: exozodiacal dust and instability noise. Considering a space-based infrared nulling interferometer in the Emma X-array configuration, we derived an upper limit on the tolerable exozodiacal dust density, and reviewed the constraints on the instrument stability. For exozodiacal discs not brighter than about 15 times our solar zodiacal cloud and an instrument sufficiently stable, we showed that a 4-telescope space-based nulling interferometer would be able to detect about 200 Earth-like planets, and perform the spectroscopic analysis of the atmosphere for 25 of them within a five year mission.

Prospects

The characterization of Earth-like extrasolar planets orbiting nearby main sequence stars, and the search for biosignatures in their atmosphere are among top-priority objectives in the long-term science plan of both ESA and NASA. In that respect, infrared nulling interferometry has been clearly identified as one of the most promising techniques, and both agencies are currently pursuing a roadmap toward ambitious space-based interferometers by funding many R&D activities. The present dissertation contributes directly to this roadmap, both from scientific and technological point of views. The ongoing survey of nearby debris discs, using state-of-the-art ground-based interferometers, is currently providing important results about the dust properties, and first statistical information on the occurrence of warm dust around nearby main sequence stars. The future generation of ground-based infrared interferometers will complement these results with observations at other wavelengths, and the ability to detect fainter exozodiacal dust clouds. Within the next decades, space-based nulling interferometers are expected to enable the characterization of Earth-like extrasolar planets around nearby stars. The quest for other habitable worlds is just beginning.

Notations and acronyms

Atmospheric windows

Y band	from 0.95 to 1.1 μm
J band	from 1.15 to 1.4 μm
H band	from 1.5 to 1.8 μm
K band	from 2.0 to 2.4 μm
L band	from 2.8 to 4.2 μm
N band	from 8 to 13 μm

Units

arcmin (or ')	minute of arc (2.90888×10^{-4} radian)
arcsec (or '')	second of arc (4.848137×10^{-5} radian)
mas	milli-arcsec (10^{-3} arcsec)
μas	micro-arcsec (10^{-6} arcsec)
AU	Astronomical Unit (1.495978×10^{11} m)
pc	parsec (3.085678×10^{17} m)
Myr	Mega-year (one million years)
Gyr	Giga-year (one billion years)
<i>i</i>	The imaginary unit
Jy	Jansky (10^{-26} W m $^{-2}$ Hz $^{-1}$)
zodi	Density unit for dust discs, equivalent to the solar zodiacal disc

Notations

M_\odot	Mass of the Sun (1.98892×10^{30} kg)
R_\odot	Radius of the Sun (6.96×10^8 m)
L_\odot	Luminosity of the Sun (3.846×10^{26} W)
M_J	Mass of Jupiter (1.8987×10^{27} kg)
R_J	Radius of Jupiter (7.1492×10^7 m)
M_\oplus	Mass of the Earth (5.97370×10^{24} kg)
R_\oplus	Radius of the Earth (6.37814×10^6 m)
M_* , T_* , L_*	Mass, effective temperature and luminosity of a star
B_*	Photospheric brightness of a star
R_* , θ_*	Linear and angular radius of a star
rms	Root Mean Square (the quadratic mean)
η_\oplus	Percentage of solar-type stars that have Earth-like planets

Acronyms

ADU	Analog-to-Digital Unit
AGN	Active Galactic Nuclei
ALADDIN	Antarctic L-band Astrophysics Discovery Demonstrator for Interferometric Nulling
ALMA	Atacama Large Millimeter Array
AMOS	Advanced Mechanical and Optical Systems
AO	Adaptive Optics
APS	Achromatic Phase Shifter
AT	Auxiliary Telescope
BH	Black Hole
BLINC	Bracewell Infrared Nulling Cryostat
CHARA	Center for High Angular Resolution Astronomy (Georgia State University)
CNES	Centre National d'Etudes Spatiales
COAST	Cambridge Optical Aperture Synthesis Telescope
CoRoT	Convection Rotation and planetary Transits
DARWIN	Not an acronym - infrared space interferometer project (ESA)
EGP	Extrasolar Giant Planet
EPIC	Extrasolar Planetary Imaging Coronagraph
ESA	European Space Agency
ESO	European Southern Observatory
FWHM	Full Width at Half Maximum
FKSI	Fourier-Kelvin Stellar Interferometer
FLUOR	Fiber Linked Unit fOr Recombination
FSU	Fringe Sensing Unit
GAIA	Global Astrometric Interferometer for Astrophysics
GENIE	Ground-based European Nulling Interferometer Experiment
GI2T	Grand Interféromètre à 2 Télescopes
GPI	Gemini Planet Imager
GSFC	Goddard Space Flight Center (NASA)
HST	Hubble Space Telescope
HZ	Habitable Zone
IAS	Institut d'Astrophysique Spatiale
I2T	Interféromètre à 2 Télescopes
IOTA	Infrared-Optical Telescope Array
IRAS	Infra-Red Astronomical Satellite
ISI	Infrared Spatial Interferometer
ISO	Infrared Space Observatory
JPL	Jet Propulsion Laboratory
JWST	James Webb Space Telescope
KI	Keck Interferometer
KIN	Keck Interferometer Nuller
LBTI	Large Binocular Telescope Interferometer
MIPS	Multiband Imaging Photometer for Spitzer
MIRA	Mitaka optical and InfraRed Array
MMT	Multi-Mirror Telescope
MMZ	Modified Mach Zehnder
MIRI	Mid-InfraRed Instrument
MROI	Magdalena Ridge Observatory Interferometer
NACO	Nasmyth Adaptive Optics System Coronagraphic Near-Infrared Camera
NA	Not Applicable

NASA	National Aeronautics and Space Administration
NPOI	Navy Prototype Optical Interferometer
OB	Observation Block
ODL	Optical Delay Line
OPD	Optical Path Difference
PC	Phase Closure
PECO	Pupil-mapping Exoplanet Coronagraphic Observer
PEGASE	Not an acronym - infrared space interferometer project (CNES)
PRIMA	Phase-Referenced Imaging and Micro-arcsecond Astrometry
PSD	Power Spectral Density
PSF	Point Spread Function
PTI	Palomar Testbed Interferometer
RV	Radial Velocity
SCUBA	Submillimeter Common-User Bolometer Array
SEE-COAST	Super-Earth Explorer - Coronagraphic Off-Axis Space Telescope
SIM	Space Interferometry Mission
SNR	Signal-to-Noise Ratio
SPHERE	Spectro-Polarimetric High-contrast Exoplanet REsearch
SUSI	Sydney University Stellar Interferometer
TBD	To Be Determined
TPF-C	Terrestrial Planet Finder Coronograph
TPF-I	Terrestrial Planet Finder Interferometer
TTN	Three-Telescope Nuller
UT	Unit Telescope
VBA	Visual Basic for Applications
VLT	Very Large Telescope
VLTI	Very Large Telescope Interferometer
VSI	VLTI Spectro-Imager
YSO	Young Stellar Objects

Bibliography

Absil, O. 2003. GENIEsim: The GENIE Science Simulator. Master's thesis, Liège University, Liège, Belgium, <http://www.aeos.ulg.ac.be/>.

Absil, O. 2006. *Astophysical studies of extrasolar planetary systems using infrared interferometric techniques*. PhD thesis, Liège University, Liège, Belgium.

Absil, O. in prep. A near-infrared interferometric survey of debris disc stars. III. CHARA/FLUOR observations of debris disc stars.

Absil, O., Coudé Du Foresto, V., Barillot, M., and Swain, M. R. 2007. Nulling interferometry: performance comparison between Antarctica and other ground-based sites. *A&A*, 475:1185–1194.

Absil, O., Defrère, D., Coudé du Foresto, V., Di Folco, E., den Hartog, R., and Augereau, J.-C. 2008a. High dynamic range interferometric observations of exozodiacal discs: performance comparison between ground, space, and Antarctica. In *Proc. SPIE*, volume 7013.

Absil, O., den Hartog, R., Gondoin, P., Fabry, P., Wilhelm, R., Gitton, P., and Puech, F. 2006a. Performance study of ground-based infrared Bracewell interferometers. Application to the detection of exozodiacal dust disks with GENIE. *A&A*, 448:787–800.

Absil, O., di Folco, E., Mérand, A., Augereau, J.-C., Coudé Du Foresto, V., Aufdenberg, J. P., Kervella, P., Ridgway, S. T., Berger, D. H., Ten Brummelaar, T. A., Sturmann, J., Sturmann, L., Turner, N. H., and McAlister, H. A. 2006b. Circumstellar material in the Vega inner system revealed by CHARA/FLUOR. *A&A*, 452:237–244.

Absil, O., di Folco, E., Mérand, A., Augereau, J.-C., Coudé Du Foresto, V., Defrère, D., Kervella, P., Aufdenberg, J. P., Desort, M., Ehrenreich, D., Lagrange, A.-M., Montagnier, G., Olofsson, J., Ten Brummelaar, T. A., McAlister, H. A., Sturmann, J., Sturmann, L., and Turner, N. H. 2008b. A near-infrared interferometric survey of debris disc stars. II. CHARA/FLUOR observations of six early-type dwarfs. *A&A*, 487:1041–1054.

Absil, O., Mennesson, B., Le Bouquin, J.-B., Di Folco, E., Kervella, P., and Augereau, J.-C. 2009. An interferometric study of the Fomalhaut inner debris disk. I. Near-infrared detection of hot dust with VLTI/VINCI. *ArXiv e-prints*.

Akeson, R. L., Boden, A. F., Monnier, J. D., Millan-Gabet, R., Beichman, C., Beletic, J., Calvet, N., Hartmann, L., Hillenbrand, L., Koresko, C., Sargent, A., and Tannirkulam, A. 2005a. Keck Interferometer Observations of Classical and Weak-line T Tauri Stars. *ApJ*, 635:1173–1181.

Akeson, R. L., Ciardi, D. R., Millan-Gabet, R., Merand, A., Folco, E. D., Monnier, J. D., Beichman, C. A., Absil, O., Aufdenberg, J., McAlister, H., Brummelaar, T. t., Sturmann, J., Sturmann, L., and Turner, N. 2009. Dust in the inner regions of debris disks around a stars. *ApJ*, 691:1896–1908.

Akeson, R. L., Ciardi, D. R., van Belle, G. T., and Creech-Eakman, M. J. 2002. Constraints on Circumstellar Disk Parameters from Multiwavelength Observations: T Tauri and SU Aurigae. *ApJ*, 566:1124–1131.

Akeson, R. L., Ciardi, D. R., van Belle, G. T., Creech-Eakman, M. J., and Lada, E. A. 2000. Infrared Interferometric Observations of Young Stellar Objects. *ApJ*, 543:313–317.

Akeson, R. L., Walker, C. H., Wood, K., Eisner, J. A., Scire, E., Penprase, B., Ciardi, D. R., van Belle, G. T., Whitney, B., and Bjorkman, J. E. 2005b. Observations and Modeling of the Inner Disk Region of T Tauri Stars. *ApJ*, 622:440–450.

Alibert, Y., Baraffe, I., Benz, W., Chabrier, G., Mordasini, C., Lovis, C., Mayor, M., Pepe, F., Bouchy, F., Queloz, D., and Udry, S. 2006. Formation and structure of the three Neptune-mass planets system around HD 69830. *A&A*, 455:L25–L28.

Alibert, Y., Mordasini, C., Benz, W., and Winisdoerffer, C. 2005. Models of giant planet formation with migration and disc evolution. *A&A*, 434:343–353.

Alonso, R., Auvergne, M., Baglin, A., Ollivier, M., Moutou, C., Rouan, D., Deeg, H. J., Aigrain, S., Almenara, J. M., Barbieri, M., Barge, P., Benz, W., Bordé, P., et al. 2008. Transiting exoplanets from the CoRoT space mission II. CoRoT-Exo-2b: A transiting planet around an active G star. *A&A*, 482.

Angel, J. R. P. and Woolf, N. J. 1997. An Imaging Nulling Interferometer to Study Extrasolar Planets. *ApJ*, 475:373–+.

Armitage, P. J., Livio, M., Lubow, S. H., and Pringle, J. E. 2002. Predictions for the frequency and orbital radii of massive extrasolar planets. *MNRAS*, 334:248–256.

Arsenault, R., Donaldson, R., Dupuy, C., Fedrigo, E., Hubin, N. N., Ivanescu, L., Kasper, M. E., Oberti, S., Paufique, J., Rossi, S., Silber, A., Delabre, B., Lizon, J.-L., and Gigan, P. 2004. MACAO-VLTI adaptive optics systems performance. 5490:47–58.

Aufdenberg, J. P., Mérand, A., Coudé du Foresto, V., Absil, O., Di Folco, E., Kervella, P., Ridgway, S. T., Berger, D. H., ten Brummelaar, T. A., McAlister, H. A., Sturmann, J., Sturmann, L., and Turner, N. H. 2006. Erratum: “First Results from the CHARA Array. VII. Long-Baseline Interferometric Measurements of Vega Consistent with a Pole-On, Rapidly Rotating Star”. *ApJ*, 651:617–617.

Augereau, J. C., Lagrange, A. M., Mouillet, D., Papaloizou, J. C. B., and Grorod, P. A. 1999. On the HR 4796 A circumstellar disk. *A&A*, 348:557–569.

Aumann, H. H., Beichman, C. A., Gillett, F. C., de Jong, T., Houck, J. R., Low, F. J., Neugebauer, G., Walker, R. G., and Wesselius, P. R. 1984. Discovery of a shell around Alpha Lyrae. *ApJ*, 278:L23–L27.

Aumann, H. H. and Probst, R. G. 1991. Search for Vega-like nearby stars with 12 micron excess. *ApJ*, 368:264–271.

Backman, D. E. and Paresce, F. 1993. Main-sequence stars with circumstellar solid material - The VEGA phenomenon. In Levy, E. H. and Lunine, J. I., editors, *Protostars and Planets III*, pages 1253–1304.

Baglin, A., Auvergne, M., Barge, P., Michel, E., Catala, C., Deleuil, M., and Weiss, W. 2007. The CoRoT mission and its scientific objectives. In *American Institute of Physics Conference Series*, volume 895 of *American Institute of Physics Conference Series*, pages 201–209.

Baines, E. K., McAlister, H. A., ten Brummelaar, T. A., Turner, N. H., Sturmann, J., Sturmann, L., Goldfinger, P. J., and Ridgway, S. T. 2008. CHARA Array Measurements of the Angular Diameters of Exoplanet Host Stars. *ApJ*, 680:728–733.

Baines, E. K., van Belle, G. T., ten Brummelaar, T. A., McAlister, H. A., Swain, M., Turner, N. H., Sturmann, L., and Sturmann, J. 2007. Direct Measurement of the Radius and Density of the Transiting Exoplanet HD 189733b with the CHARA Array. *ApJ*, 661:L195–L198.

Baldwin, J. E., Beckett, M. G., Boysen, R. C., Burns, D., Buscher, D. F., Cox, G. C., Haniff, C. A., Mackay, C. D., Nightingale, N. S., Rogers, J., Scheuer, P. A. G., Scott, T. R., Tuthill, P. G., Warner, P. J., Wilson, D. M. A., and Wilson, R. W. 1996. The first images from an optical aperture synthesis array: mapping of Capella with COAST at two epochs. *A&A*, 306:L13+.

Bally, J., O'Dell, C. R., and McCaughrean, M. J. 2000. Disks, Microjets, Windblown Bubbles, and Outflows in the Orion Nebula. *AJ*, 119:2919–2959.

Bally, J., Sutherland, R. S., Devine, D., and Johnstone, D. 1998. Externally Illuminated Young Stellar Environments in the Orion Nebula: Hubble Space Telescope Planetary Camera and Ultraviolet Observations. *AJ*, 116:293–321.

Baraffe, I., Chabrier, G., Barman, T. S., Allard, F., and Hauschildt, P. H. 2003. Evolutionary models for cool brown dwarfs and extrasolar giant planets. The case of HD 209458. *A&A*, 402:701–712.

Barge, P., Baglin, A., Auvergne, M., Rauer, H., Leger, A., Schneider, J., Pont, F., Aigrain, S., Almenara, J., Alonso, R., Barbieri, M., Borde, P., Bouchy, F., et al. 2008. Transiting exoplanets from the CoRoT space mission I - CoRoT-Exo-1b: a low-density short-period planet around a G0V star. *A&A*, 482.

Barman, T. S., Hauschildt, P. H., and Allard, F. 2001. Irradiated Planets. *ApJ*, 556:885–895.

Barman, T. S., Hauschildt, P. H., and Allard, F. 2005. Phase-Dependent Properties of Extrasolar Planet Atmospheres. *ApJ*, 632:1132–1139.

Barry, R. K., Danchi, W. C., Deming, L. D., Richardson, L. J., Kuchner, M. J., Seager, S., Frey, B. J., Martino, A. J., Lee, K. A., Zuray, M., Rajagopal, J., Hyde, T. T., Millan-Gabete, R., Monnier, J. D., Allen, R. J., and Traub, W. A. 2006. The Fourier-Kelvin stellar interferometer: a low-complexity low-cost space mission for high-resolution astronomy and direct exoplanet detection. In *Proc. of the SPIE*, volume 6265.

Barry, R. K., Danchi, W. C., Traub, W. A., Sokoloski, J. L., Wisniewski, J. P., Serabyn, E., Kuchner, M. J., Akeson, R., Appleby, E., Bell, J., Booth, A., et al. 2008. Milliarcsecond N-Band Observations of the Nova RS Ophiuchi: First Science with the Keck Interferometer Nuller. *ApJ*, 677:1253–1267.

Baudoz, P., Boccaletti, A., Riaud, P., Cavarroc, C., Baudrand, J., Reess, J. M., and Rouan, D. 2006. Feasibility of the Four-Quadrant Phase Mask in the Mid-Infrared on the James Webb Space Telescope. *PASP*, 118:765–773.

Beaulieu, J.-P., Bennett, D. P., Fouqué, P., Williams, A., Dominik, M., Jørgensen, U. G., Kubas, D., Cassan, A., Coutures, C., Greenhill, J., Hill, K., Menzies, J., et al. 2006. Discovery of a cool planet of 5.5 Earth masses through gravitational microlensing. *Nature*, 439:437–440.

Beichman, C. A., Bryden, G., Gautier, T. N., Stapelfeldt, K. R., Werner, M. W., Misselt, K., Rieke, G., Stansberry, J., and Trilling, D. 2005a. An Excess Due to Small Grains around the Nearby K0 V Star HD 69830: Asteroid or Cometary Debris? *ApJ*, 626:1061–1069.

Beichman, C. A., Bryden, G., Rieke, G. H., Stansberry, J. A., Trilling, D. E., Stapelfeldt, K. R., Werner, M. W., Engelbracht, C. W., Blaylock, M., Gordon, K. D., Chen, C. H., Su, K. Y. L., and Hines, D. C. 2005b. Planets and Infrared Excesses: Preliminary Results from a Spitzer MIPS Survey of Solar-Type Stars. *ApJ*, 622:1160–1170.

Beichman, C. A., Bryden, G., Stapelfeldt, K. R., Gautier, T. N., Grogan, K., Shao, M., Velusamy, T., Lawler, S. M., Blaylock, M., Rieke, G. H., Lunine, J. I., Fischer, D. A., Marcy, G. W., Greaves, J. S., Wyatt, M. C., Holland, W. S., and Dent, W. R. F. 2006a. New Debris Disks around Nearby Main-Sequence Stars: Impact on the Direct Detection of Planets. *ApJ*, 652:1674–1693.

Beichman, C. A., Tanner, A., Bryden, G., Stapelfeldt, K. R., Werner, M. W., Rieke, G. H., Trilling, D. E., Lawler, S., and Gautier, T. N. 2006b. IRS Spectra of Solar-Type Stars: A Search for Asteroid Belt Analogs. *ApJ*, 639:1166–1176.

Bennett, D. P., Bond, I. A., Udalski, A., Sumi, T., Abe, F., Fukui, A., Furusawa, K., Hearnshaw, J. B., Holderness, S., Itow, Y., Kamiya, K., Korpela, A. V., Kilmartin, P. M., et al. 2008. A Low-Mass Planet with a Possible Sub-Stellar-Mass Host in Microlensing Event MOA-2007-BLG-192. *ApJ*, 684:663–683.

Berger, J., Haguenauer, P., Kern, P. Y., Roussellet-Perraut, K., Malbet, F., Gluck, S., Lagny, L., Schanen-Duport, I., Laurent, E., Delboulbe, A., Tatulli, E., Traub, W. A., Carleton, N., Millan-Gabet, R., Monnier, J. D., Pedretti, E., and Ragland, S. 2003. An integrated-optics 3-way beam combiner for IOTA. 4838:1099–1106.

Beust, H., Lagrange, A.-M., Plazy, F., and Mouillet, D. 1996. The β Pictoris circumstellar disk. XXII. Investigating the model of multiple cometary infalls. *A&A*, 310:181–198.

Beust, H. and Morbidelli, A. 2000. Falling Evaporating Bodies as a Clue to Outline the Structure of the β Pictoris Young Planetary System. *Icarus*, 143:170–188.

Beuzit, J.-L., Feldt, M., Dohlen, K., Mouillet, D., Puget, P., Wildi, F., Abe, L., Antichi, J., Baruffolo, A., Baudoz, P., et al. 2008. SPHERE: a planet finder instrument for the VLT. 7014.

Biller, B. A., Kasper, M., Close, L. M., Brandner, W., and Kellner, S. 2006. Discovery of a Brown Dwarf Very Close to the Sun: A Methane-rich Brown Dwarf Companion to the Low-Mass Star SCR 1845-6357. *ApJ*, 641:L141–L144.

Boden, A. F., Lane, B. F., Creech-Eakman, M. J., Queloz, D., and Koresko, C. D. 2000. Resolution and Orbit Reconstruction of Spectroscopic Binary Stars with the Palomar Testbed Interferometer. 32:867–+.

Boden, A. F., Torres, G., and Hummel, C. A. 2005. Testing Stellar Models with an Improved Physical Orbit for 12 Bootis. *ApJ*, 627:464–476.

Bodenheimer, P. 1997. The Role of Dust in Star and Planet Formation: Theory. In Pendleton, Y. J., editor, *From Stardust to Planetesimals*, volume 122 of *Astronomical Society of the Pacific Conference Series*, pages 37–+. 37–+.

Bordé, P., Coudé du Foresto, V., Chagnon, G., and Perrin, G. 2002. A catalogue of calibrator stars for long baseline stellar interferometry. *A&A*, 393:183–193.

Bordé, P., Rouan, D., and Léger, A. 2003. Exoplanet detection capability of the COROT space mission. *A&A*, 405:1137–1144.

Borucki, W. J., Koch, D. G., Lissauer, J., Basri, G., Brown, T., Caldwell, D. A., Jenkins, J. M., Caldwell, J. J., Christensen-Dalsgaard, J., Cochran, W. D., Dunham, E. W., Gautier, et al. 2007. KEPLER Mission Status. In Afonso, C., Weldrake, D., and Henning, T., editors, *Transiting Extrapolar Planets Workshop*, volume 366 of *Astronomical Society of the Pacific Conference Series*, pages 309–+.

Borucki, W. J., Koch, G., and Jenkins, J. 2009. Kepler's Optical Phase Curve of the Exoplanet HAT-P-7b. *Science*, 325:709.

Boss, A. P. 1998. The Jeans Mass Constraint and the Fragmentation of Molecular Cloud Cores. *ApJ*, 501:L77+.

Boss, A. P. 2003. Rapid Formation of Outer Giant Planets by Disk Instability. *ApJ*, 599:577–581.

Bouchy, F., Moutou, C., Queloz, D., and the CoRoT Exoplanet Science Team 2009. Radial velocity follow-up for confirmation and characterization of transiting exoplanets.

Bracewell, R. N. 1978. Detecting nonsolar planets by spinning infrared interferometer. *Nature*, 274:780–+.

Bryden, G., Beichman, C. A., Carpenter, J. M., Rieke, G. H., Stapelfeldt, K. R., Werner, M. W., Tanner, A. M., Lawler, S. M., Wyatt, M. C., Trilling, D. E., Su, K. Y. L., Blaylock, M., and Stansberry, J. A. 2009. Planets and Debris Disks: Results from a Spitzer/MIPS Search for Infrared Excess. *ApJ*, 705:1226–1236.

Bryden, G., Beichman, C. A., Trilling, D. E., Rieke, G. H., Holmes, E. K., Lawler, S. M., Stapelfeldt, K. R., Werner, M. W., Gautier, T. N., Blaylock, M., Gordon, K. D., Stansberry, J. A., and Su, K. Y. L. 2006. Frequency of Debris Disks around Solar-Type Stars: First Results from a Spitzer MIPS Survey. *ApJ*, 636:1098–1113.

Burrows, A., Sudarsky, D., and Hubeny, I. 2004. Spectra and Diagnostics for the Direct Detection of Wide-Separation Extrasolar Giant Planets. *ApJ*, 609:407–416.

Burrows, A., Sudarsky, D., and Hubeny, I. 2006. Theory for the Secondary Eclipse Fluxes, Spectra, Atmospheres, and Light Curves of Transiting Extrasolar Giant Planets. *ApJ*, 650:1140–1149.

Buscher, D. F., Baldwin, J. E., Warner, P. J., and Haniff, C. A. 1990. Detection of a bright feature on the surface of Betelgeuse. *MNRAS*, 245:7P–11P.

Butler, R. P., Vogt, S. S., Marcy, G. W., Fischer, D. A., Wright, J. T., Henry, G. W., Laughlin, G., and Lissauer, J. J. 2004. A Neptune-Mass Planet Orbiting the Nearby M Dwarf GJ 436. *ApJ*, 617:580–588.

Calvet, N., Patino, A., Magris, G. C., and D’Alessio, P. 1991. Irradiation of accretion disks around young objects. I - Near-infrared CO bands. *ApJ*, 380:617–630.

Cameron, A. G. W. 1978. Physics of the primitive solar accretion disk. *Moon and Planets*, 18:5–40.

Carle, E. 2005. EMMA configuration: evaluation of optical performances. Technical Report Issue 1, ESA (SCI-A/279).

Chabrier, G., Baraffe, I., Allard, F., and Hauschildt, P. 2000. Deuterium Burning in Substellar Objects. *ApJ*, 542:L119–L122.

Chabrier, G., Barman, T., Baraffe, I., Allard, F., and Hauschildt, P. H. 2004. The Evolution of Irradiated Planets: Application to Transits. *ApJ*, 603:L53–L56.

Charbonneau, D., Allen, L. E., Megeath, S. T., Torres, G., Alonso, R., Brown, T. M., Gilliland, R. L., Latham, D. W., Mandushev, G., O’Donovan, F. T., and Sozzetti, A. 2005. Detection of Thermal Emission from an Extrasolar Planet. *ApJ*, 626:523–529.

Charbonneau, D., Brown, T. M., Noyes, R. W., and Gilliland, R. L. 2002. Detection of an Extrasolar Planet Atmosphere. *ApJ*, 568:377–384.

Chauvin, G., Lagrange, A.-M., Dumas, C., Zuckerman, B., Mouillet, D., Song, I., Beuzit, J.-L., and Lowrance, P. 2005a. Giant planet companion to 2MASSW J1207334-393254. *A&A*, 438:L25–L28.

Chauvin, G., Lagrange, A.-M., Zuckerman, B., Dumas, C., Mouillet, D., Song, I., Beuzit, J.-L., Lowrance, P., and Bessell, M. S. 2005b. A companion to AB Pic at the planet/brown dwarf boundary. *A&A*, 438:L29–L32.

Chazelas, B., Brachet, F., Bordé, P., Mennesson, B., Ollivier, M., Absil, O., Labèque, A., Valette, C., and Léger, A. 2006. Instrumental stability requirements for exoplanet detection with a nulling interferometer: variability noise as a central issue. *Appl. Opt.*, 45:984–992.

Chen, C. H., Sargent, B. A., Bohac, C., Kim, K. H., Leibensperger, E., Jura, M., Najita, J., Forrest, W. J., Watson, D. M., Sloan, G. C., and Keller, L. D. 2006. Spitzer IRS Spectroscopy of IRAS-discovered Debris Disks. *ApJS*, 166:351–377.

Chiang, E. I. and Goldreich, P. 1997. Spectral Energy Distributions of T Tauri Stars with Passive Circumstellar Disks. *ApJ*, 490:368–+.

Ciardi, D. R., van Belle, G. T., Akeson, R. L., Thompson, R. R., Lada, E. A., and Howell, S. B. 2001. On the Near-Infrared Size of Vega. *ApJ*, 559:1147–1154.

Clampin, M. 2007. Optical Design of the James Webb Space Telescope (JWST). In Kalas, P., editor, *Proceedings of the conference In the Spirit of Bernard Lyot: The Direct Detection of Planets and Circumstellar Disks in the 21st Century. June 04 - 08, 2007. University of California, Berkeley, CA, USA. Edited by Paul Kalas.*, pages 49–+.

Clampin, M., Krist, J. E., Ardila, D. R., Golimowski, D. A., Hartig, G. F., Ford, H. C., Illingworth, G. D., Bartko, F., Benítez, et al. 2003. Hubble Space Telescope ACS Coronagraphic Imaging of the Circumstellar Disk around HD 141569A. *AJ*, 126:385–392.

Cohen, M., Walker, R. G., Carter, B., Hammersley, P., Kidger, M., and Noguchi, K. 1999. Spectral Irradiance Calibration in the Infrared. X. A Self-Consistent Radiometric All-Sky Network of Absolutely Calibrated Stellar Spectra. *AJ*, 117:1864–1889.

Colavita, M., Akeson, R., Wizinowich, P., Shao, M., Acton, S., Beletic, J., Bell, J., Berlin, J., Boden, A., Booth, A., Boutell, et al. 2003. Observations of DG Tauri with the Keck Interferometer. *ApJ*, 592:L83–L86.

Colavita, M. M., Serabyn, E., Booth, A. J., Crawford, S. L., Garcia-Gathright, J. I., Ligon, E. R., Mennesson, B. L., Paine, et al. 2008. Keck Interferometer nuller update. 7013.

Coudé du Foresto, V., Absil, O., Swain, M., Vakili, F., and Barillot, M. 2006. ALADDIN: an optimized nulling ground-based demonstrator for DARWIN. In *Proc. SPIE*, volume 6268.

Coudé du Foresto, V., Ridgway, S., and Mariotti, J. 1997. Deriving object visibilities from interferograms obtained with a fiber stellar interferometer. *A&AS*, 121:379–392.

Creech-Eakman, M. J., Romero, V., Westpfahl, D., Cormier, C., Haniff, C., Buscher, D., Bakker, E., Berger, L., Block, E., Coleman, T., et al. 2008. Magdalena Ridge Observatory Interferometer: progress toward first light. 7013.

Creevey, O. L., Monteiro, M. J. P. F. G., Metcalfe, T. S., Brown, T. M., Jiménez-Reyes, S. J., and Belmonte, J. A. 2007. The Complementary Roles of Interferometry and Asteroseismology in Determining the Mass of Solar-Type Stars. *ApJ*, 659:616–625.

Crifo, F. and The French Gaia Team 2006. GAIA: present status and preparation of data analysis. In Barret, D., Casoli, F., Lagache, G., Lecavelier, A., and Pagani, L., editors, *SF2A-2006: Semaine de l'Astrophysique Francaise*, pages 459–+.

Cutri, R. M., Skrutskie, M. F., van Dyk, S., Beichman, C. A., Carpenter, J. M., Chester, T., Cambresy, L., Evans, T., Fowler, J., et al. 2003. 2MASS All Sky Catalog of point sources.

Danchi, W. C., Barry, R. K., Deming, D., Kuchner, M., Monnier, J. D., Mundy, L. G., Rajagopal, J., Richardson, J., Seager, S., and Traub, W. 2006. Scientific rationale for exoplanet characterization from 3-8 microns: the FKSI mission. In *Proc. SPIE*, volume 6268.

Danchi, W. C., Bester, M., Degiacomi, C. G., Greenhill, L. J., and Townes, C. H. 1994. Characteristics of dust shells around 13 late-type stars. *AJ*, 107:1469–1513.

Danchi, W. C., Deming, D., Kuchner, M. J., and Seager, S. 2003. Detection of Close-In Extrasolar Giant Planets Using the Fourier-Kelvin Stellar Interferometer. *ApJ*, 597:L57–L60.

D'Angelo, G., Lubow, S. H., and Bate, M. R. 2006. Evolution of Giant Planets in Eccentric Disks. *ApJ*, 652:1698–1714.

D'Arcio, L. 2005. DARWIN. Variability noise sensitivity analysis. (Issue 1).

D'Arcio, L. L., Karlsson, A. L., and Gondoin, P. A. 2004. Use of OPD modulation techniques in nulling interferometry. In Traub, W. A., editor, *New Frontiers in Stellar Interferometry, Proceedings of SPIE Volume 5491*, pages 851–+.

Defrère, D., Absil, O., Coudé Du Foresto, V., Danchi, W. C., and den Hartog, R. 2008. Nulling interferometry: performance comparison between space and ground-based sites for exozodiacal disc detection. *A&A*, 490:435–445.

Defrère, D., Absil, O., den Hartog, R., Hanot, C., and Stark, C. in press. Nulling interferometry: impact of exozodiacal dust clouds on the performance of future life-finding space missions. *A&A*.

Defrère, D., Absil, O., Hanot, C., and Fridlund, M. 2007. Potential of space-based infrared Bracewell interferometers for planet detection. In *Proc. SPIE*, volume 6693, pages 53–+.

Deleuil, M., Deeg, H. J., Alonso, R., Bouchy, F., Rouan, D., Auvergne, M., Baglin, A., Aigrain, S., Almenara, J. M., Barbieri, et al. 2008. Transiting exoplanets from the CoRoT space mission . VI. CoRoT-Exo-3b: the first secure inhabitant of the brown-dwarf desert. *A&A*, 491:889–897.

Delplancke, F. 2008. The PRIMA facility phase-referenced imaging and micro-arcsecond astrometry. *New Astronomy Review*, 52:199–207.

Deming, D., Seager, S., Richardson, L. J., and Harrington, J. 2005. Infrared radiation from an extrasolar planet. *Nature*, 434:740–743.

den Hartog, R. 2005a. DARWIN science performance prediction. Technical Report Issue 1, ESA (SCI-A/300).

den Hartog, R. 2005b. The DARWINsim science simulator. Technical Report Issue 1, ESA (SCI-A/297).

den Hartog, R. H., Absil, O., Gondoin, P. A., D'Arcio, L. L., Fabry, P., Kaltenegger, L., Wilhelm, R. C., Gitton, P. B., Puech, F., and Fridlund, C. V. M. 2004. The simulated detection of low-mass companions with GENIE. In Traub, W. A., editor, *Proc. SPIE*, volume 5491, pages 160–+.

Di Folco, E., Absil, O., Augereau, J.-C., Mérand, A., Coudé Du Foresto, V., Thévenin, F., Defrère, D., Kervella, P., Ten Brummelaar, T. A., McAlister, H. A., Ridgway, S. T., Sturmann, J., Sturmann, L., and Turner, N. H. 2007. A near-infrared interferometric survey of debris disk stars. I. Probing the hot dust content around ϵ Eridani and τ Ceti with CHARA/FLUOR. *A&A*, 475:243–250.

Di Folco, E., Dutrey, A., Chesneau, O., Wolf, S., Schegerer, A., Leinert, C., and Lopez, B. 2009. The flared inner disk of the Herbig Ae star AB Aurigae revealed by VLTI/MIDI in the N-band. *A&A*, 500:1065–1076.

Di Folco, E., Thévenin, F., Kervella, P., Domiciano de Souza, A., Coudé du Foresto, V., Ségransan, D., and Morel, P. 2004. VLTI near-IR interferometric observations of Vega-like stars. Radius and age of α PsA, β Leo, β Pic, ϵ Eri and τ Cet. *A&A*, 426:601–617.

Domiciano de Souza, A., Kervella, P., Jankov, S., Abe, L., Vakili, F., di Folco, E., and Paresce, F. 2003. The spinning-top Be star Achernar from VLTI-VINCI. *A&A*, 407:L47–L50.

Domiciano de Souza, A., Kervella, P., Jankov, S., Vakili, F., Ohishi, N., Nordgren, T. E., and Abe, L. 2005. Gravitational-darkening of Altair from interferometry. *A&A*, 442:567–578.

Dullemond, C. P., Dominik, C., and Natta, A. 2001. Passive Irradiated Circumstellar Disks with an Inner Hole. *ApJ*, 560:957–969.

Dullemond, C. P., van Zadelhoff, G. J., and Natta, A. 2002. Vertical structure models of T Tauri and Herbig Ae/Be disks. *A&A*, 389:464–474.

Dutrey, A., Guilloteau, S., Duvert, G., Prato, L., Simon, M., Schuster, K., and Menard, F. 1996. Dust and gas distribution around T Tauri stars in Taurus-Auriga. I. Interferometric 2.7mm continuum and ^{13}CO $J=1-0$ observations. *A&A*, 309:493–504.

Ehrenreich, D., Hébrard, G., Lecavelier des Etangs, A., Sing, D. K., Désert, J.-M., Bouchy, F., Ferlet, R., and Vidal-Madjar, A. 2007. A Spitzer Search for Water in the Transiting Exoplanet HD 189733b. *ApJ*, 668:L179–L182.

Eisenhauer, F., Perrin, G., Straubmeier, C., Brandner, W., Boehm, A., Cassaing, F., Clenet, Y., Dodds-Eden, K., Eckart, A., Fedou, P., et al. 2008. GRAVITY: microarcsecond astrometry and deep interferometric imaging with the VLTI. *248:100–101*.

Eisner, J. A., Hillenbrand, L. A., White, R. J., Akeson, R. L., and Sargent, A. I. 2005. Observations of T Tauri Disks at Sub-AU Radii: Implications for Magnetospheric Accretion and Planet Formation. *ApJ*, 623:952–966.

Eisner, J. A., Lane, B. F., Hillenbrand, L. A., Akeson, R. L., and Sargent, A. I. 2004. Resolved Inner Disks around Herbig Ae/Be Stars. *ApJ*, 613:1049–1071.

Fajardo-Acosta, S. B., Beichman, C. A., and Cutri, R. M. 2000. Discovery of New Candidate Vega-type Systems from IRAS and the 2 Micron All-Sky Survey. *ApJ*, 538:L155–L158.

Fajardo-Acosta, S. B., Stencel, R. E., and Backman, D. E. 1998. Infrared Space Observatory Mapping of 60 Micron Dust Emission around Vega-Type Systems: Erratum. *ApJ*, 503:L193+.

Figueira, P., Pont, F., Mordasini, C., Alibert, Y., Georgy, C., and Benz, W. 2009. Bulk composition of the transiting hot Neptune around GJ 436. *A&A*, 493:671–676.

Fizeau, H. and Foucault, L. 1868. Ueber das Phänomen der Interferenz zweier Lichtstrahlen im Falle grosser Gangunterschiede. *Annalen der Physik*, 149:355–358.

Fortney, J. J., Marley, M. S., and Barnes, J. W. 2007. Planetary Radii across Five Orders of Magnitude in Mass and Stellar Insolation: Application to Transits. *ApJ*, 659:1661–1672.

Forveille, T., Bonfils, X., Delfosse, X., Gillon, M., Udry, S., Bouchy, F., Lovis, C., Mayor, M., Pepe, F., Perrier, C., Queloz, D., Santos, N., and Bertaux, J.-L. 2009. The HARPS search for southern extra-solar planets. XIV. Gl 176b, a super-Earth rather than a Neptune, and at a different period. *A&A*, 493:645–650.

Fridlund, C. V. M., d'Arcio, L., den Hartog, R., and Karlsson, A. 2006. Status and recent progress of the Darwin mission in the Cosmic Vision program. In *Proc. SPIE*, volume 6268.

Fridlund, M. 2005. Darwin Science Requirements Document. Technical Report Issue 5, ESA (SCI-A).

Gabor, P., Chazelas, B., Brachet, F., Ollivier, M., Decaudin, M., Jacquinod, S., Labèque, A., and Léger, A. 2008. Stabilising a nulling interferometer using optical path difference dithering. *A&A*, 483.

Gillon, M., Pont, F., Demory, B.-O., Mallmann, F., Mayor, M., Mazeh, T., Queloz, D., Shporer, A., Udry, S., and Vuissoz, C. 2007. Detection of transits of the nearby hot Neptune GJ 436 b. *A&A*, 472:L13–L16.

Goldreich, P. and Tremaine, S. 1979. The excitation of density waves at the Lindblad and corotation resonances by an external potential. *ApJ*, 233:857–871.

Goldreich, P. and Weber, S. V. 1980. Homologously collapsing stellar cores. *ApJ*, 238:991–997.

Gomes, R., Levison, H. F., Tsiganis, K., and Morbidelli, A. 2005. Origin of the cataclysmic Late Heavy Bombardment period of the terrestrial planets. *Nature*, 435:466–469.

Gondoin, P. A., Absil, O., den Hartog, R. H., Wilhelm, R. C., Gitton, et al. 2004. Darwin-GENIE: a nulling instrument at the VLTI. In Traub, W. A., editor, *Proc. SPIE*, volume 5491, pages 775–+.

Grady, C. A., Woodgate, B., Bruhweiler, F. C., Boggess, A., Plait, P., Lindler, D. J., Clampin, M., and Kalas, P. 1999. Hubble Space Telescope Space Telescope Imaging Spectrograph Coronagraphic Imaging of the Herbig AE Star AB Aurigae. *ApJ*, 523:L151–L154.

Greaves, J. S., Fischer, D. A., and Wyatt, M. C. 2006. Metallicity, debris discs and planets. *MNRAS*, 366:283–286.

Greaves, J. S., Wyatt, M. C., Holland, W. S., and Dent, W. R. F. 2004. The debris disc around τ Ceti: a massive analogue to the Kuiper Belt. *MNRAS*, 351:L54–L58.

Grillmair, C. J., Burrows, A., Charbonneau, D., Armus, L., Stauffer, J., Meadows, V., van Cleve, J., von Braun, K., and Levine, D. 2008. Strong water absorption in the dayside emission spectrum of the planet HD189733b. *Nature*, 456:767–769.

Grillmair, C. J., Charbonneau, D., Burrows, A., Armus, L., Stauffer, J., Meadows, V., Van Cleve, J., and Levine, D. 2007. A Spitzer Spectrum of the Exoplanet HD 189733b. *ApJ*, 658:L115–L118.

Haisch, Jr., K. E., Lada, E. A., and Lada, C. J. 2001. Disk Frequencies and Lifetimes in Young Clusters. *ApJ*, 553:L153–L156.

Hale, D. D. S., Bester, M., Danchi, W. C., Fitelson, W., Hoss, S., Lipman, E. A., Monnier, J. D., Tuthill, P. G., and Townes, C. H. 2000. The Berkeley Infrared Spatial Interferometer: A Heterodyne Stellar Interferometer for the Mid-Infrared. *ApJ*, 537:998–1012.

Hanbury Brown, R., Davis, J., and Allen, L. R. 1974. The angular diameters of 32 stars. *MNRAS*, 167:121–136.

Hanot, C. 2005. Investigation of a down scoped version of the darwin mission. Master's thesis, Liège University, Liège, Belgium.

Hanot, C., Absil, O., Defrère, D., Mawet, D., and Surdej, J. 2009. Coronagraphy of giant planets and debris discs in nearby moving groups .

Hanot, C. and Serabyn, G. in prep. Observations of debris disc stars with the fiber nuller.

Harrington, J., Hansen, B. M., Luszcz, S. H., Seager, S., Deming, D., Menou, K., Cho, J. Y.-K., and Richardson, L. J. 2006. The Phase-Dependent Infrared Brightness of the Extrasolar Planet ν Andromedae b. *Science*, 314:623–626.

Hartmann, L., Kenyon, S. J., and Calvet, N. 1993. The excess infrared emission of Herbig Ae/Be stars - Disks or envelopes? *ApJ*, 407:219–231.

Heap, S. R., Lindler, D. J., Lanz, T. M., Cornett, R. H., Hubeny, I., Maran, S. P., and Woodgate, B. 2000. Space Telescope Imaging Spectrograph Coronagraphic Observations of β Pictoris. *ApJ*, 539:435–444.

Hearnshaw, J. B. 1996. The Measurement of Starlight, Two Centuries of Astronomical Photometry.

Heinrichsen, I., Walker, H. J., and Klaas, U. 1998. Infrared mapping of the dust disc around VEGA. *MNRAS*, 293:L78–L82.

Hillenbrand, L. A., Carpenter, J. M., Kim, J. S., Meyer, M. R., Backman, D. E., Moro-Martín, A., Hollenbach, D. J., Hines, D. C., Pascucci, I., and Bouwman, J. 2008. The Complete Census of 70 μm -bright Debris Disks within “the Formation and Evolution of Planetary Systems” Spitzer Legacy Survey of Sun-like Stars. *ApJ*, 677:630–656.

Hillenbrand, L. A., Strom, S. E., Vrba, F. J., and Keene, J. 1992. Herbig Ae/Be stars - Intermediate-mass stars surrounded by massive circumstellar accretion disks. *ApJ*, 397:613–643.

Hinz, P. M., Angel, J. R. P., Hoffmann, W. F., McCarthy, D. W., McGuire, P. C., Cheselka, M., Hora, J. L., and Woolf, N. J. 1998a. First results of nulling interferometry with the Multiple-Mirror Telescope. In Reasenberg, R. D., editor, *Proc. SPIE*, volume 3350, pages 439–447.

Hinz, P. M., Angel, J. R. P., Hoffmann, W. F., McCarthy, D. W., Woolf, N. J., and McGuire, P. C. 1998b. Refining Nulling Interferometry with the Old and New Multiple Mirror Telescope. In *Bulletin of the American Astronomical Society*, volume 30 of *Bulletin of the American Astronomical Society*, pages 1393–+.

Hinz, P. M., Angel, J. R. P., Woolf, N. J., Hoffmann, W. F., and McCarthy, D. W. 2008a. Status of the LBT interferometer. In Lena, P. J. and Quirrenbach, A., editors, *Proc. SPIE*, volume 7013, page in press.

Hinz, P. M., Bippert-Plymate, T., Breuninger, A., Connors, T., Duffy, B., Esposito, S., Hoffmann, W., Kim, J., Kraus, J., McMahon, T., Montoya, M., Nash, R., Durney, O., Solheid, E., Tozzi, A., and Vaitheeswaran, V. 2008b. Status of the LBT interferometer. In *Proc. SPIE*, volume 7013.

Hinz, P. M., Hoffmann, W. F., and Hora, J. L. 2001. Constraints on Disk Sizes around Young Intermediate-Mass Stars: Nulling Interferometric Observations of Herbig Ae Objects. *ApJ*, 561:L131–L134.

Hogbom, J. A. and Brouw, W. N. 1974. The Synthesis Radio Telescope at Westerbork. Principles of Operation, Performance and Data Reduction. *A&A*, 33:289–+.

Holland, W. S., Greaves, J. S., Dent, W. R. F., Wyatt, M. C., Zuckerman, B., Webb, R. A., McCarthy, C., Coulson, I. M., Robson, E. I., and Gear, W. K. 2003. Submillimeter Observations of an Asymmetric Dust Disk around Fomalhaut. *ApJ*, 582:1141–1146.

Holland, W. S., Greaves, J. S., Zuckerman, B., Webb, R. A., McCarthy, C., Coulson, I. M., Walther, D. M., Dent, W. R. F., Gear, W. K., and Robson, I. 1998. Submillimetre images of dusty debris around nearby stars. *Nature*, 392:788–791.

Hummel, C. A., Armstrong, J. T., Quirrenbach, A., Buscher, D. F., Mozurkewich, D., Elias, II, N. M., and Wilson, R. E. 1994a. Very high precision orbit of Capella by long baseline interferometry. *AJ*, 107:1859–1867.

Hummel, C. A., Mozurkewich, D., Elias, II, N. M., Quirrenbach, A., Buscher, D. F., Armstrong, J. T., Johnston, K. J., Simon, R. S., and Hutter, D. J. 1994b. Four years of astrometric measurements with the Mark 3 optical interferometer. *AJ*, 108:326–336.

Hyde, T. T., Liu, K.-C., Blaurock, C., Bolognese, J., Howard, J. M., and Danchi, W. 2004. Requirements formulation and dynamic jitter analysis on Fourier-Kelvin stellar interferometer. In Craig, S. C. and Cullum, M. J., editors, *Proc. SPIE*, volume 5497, pages 553–564.

Ida, S. and Lin, D. N. C. 2004. Toward a Deterministic Model of Planetary Formation. I. A Desert in the Mass and Semimajor Axis Distributions of Extrasolar Planets. *Astrophysical Journal of Physics*, 604:388–413.

Jaffe, W., Meisenheimer, K., Röttgering, H. J. A., Leinert, C., Richichi, A., Chesneau, O., Fraix-Burnet, D., Glazeborg-Kluttig, A., et al. 2004. The central dusty torus in the active nucleus of NGC 1068. *Nature*, 429:47–49.

Jayawardhana, R., Wolk, S. J., Barrado y Navascués, D., Telesco, C. M., and Hearty, T. J. 2001. Proto-planetary Disks in the Nearest Star-Forming Cloud: Mid-Infrared Imaging and Optical Spectroscopy of MBM 12 Members. *ApJ*, 550:L197–L200.

Kalas, P., Graham, J. R., Chiang, E., Fitzgerald, M. P., Clampin, M., Kite, E. S., Stapelfeldt, K., Marois, C., and Krist, J. 2008. Optical Images of an Exosolar Planet 25 Light-Years from Earth. *Science*, 322:1345–.

Kalas, P., Graham, J. R., and Clampin, M. 2005. A planetary system as the origin of structure in Fomalhaut’s dust belt. volume 435, pages 1067–1070.

Kalas, P., Graham, J. R., Clampin, M. C., and Fitzgerald, M. P. 2006. First Scattered Light Images of Debris Disks around HD 53143 and HD 139664. *ApJ*, 637:L57–L60.

Kalas, P., Liu, M. C., and Matthews, B. C. 2004. Discovery of a Large Dust Disk Around the Nearby Star AU Microscopii. *Science*, 303:1990–1992.

Kaltenegger, L., Eiroa, C., and Fridlund, C. V. M. 2008. Target star catalog for Darwin: Nearby Stellar sample for a search for terrestrial planets. *ArXiv e-prints*.

Kaltenegger, L., Eiroa, C., and Fridlund, M. 2007a. Target star catalogue for Darwin: Nearby Stellar sample for a search for terrestrial planets. *A&A, submitted*.

Kaltenegger, L., Traub, W. A., and Jucks, K. W. 2007b. Spectral Evolution of an Earth-like Planet. *ApJ*, 658:598–616.

Karlsson, A. L., Wallner, O., Perdigues Armengol, J. M., and Absil, O. 2004. Three telescope nuller based on multibeam injection into single-mode waveguide. In Traub, W. A., editor, *Proc. SPIE*, volume 5491, pages 831–+.

Kasting, J. 1998. Habitable Zones Around Stars and the Search for Extraterrestrial Life. 30:1328–+.

Kasting, J. F., Whitmire, D. P., and Reynolds, R. T. 1993. Habitable Zones around Main Sequence Stars. *Icarus*, 101:108–128.

Kelsall, T., Weiland, J. L., Franz, B. A., Reach, W. T., Arendt, R. G., Dwek, E., Freudenreich, H. T., Hauser, M. G., Moseley, S. H., Odegard, N. P., Silverberg, R. F., and Wright, E. L. 1998. The COBE Diffuse Infrared Background Experiment Search for the Cosmic Infrared Background. II. Model of the Interplanetary Dust Cloud. *ApJ*, 508:44–73.

Kenyon, S. J. and Bromley, B. C. 2006. Terrestrial Planet Formation. I. The Transition from Oligarchic Growth to Chaotic Growth. *AJ*, 131:1837–1850.

Kenyon, S. J. and Hartmann, L. 1987. Spectral energy distributions of T Tauri stars - Disk flaring and limits on accretion. *ApJ*, 323:714–733.

Kervella, P., Bersier, D., Mourard, D., Nardetto, N., Fouqué, P., and Coudé du Foresto, V. 2004a. Cepheid distances from infrared long-baseline interferometry. III. Calibration of the surface brightness-color relations. *A&A*, 428:587–593.

Kervella, P., Nardetto, N., Bersier, D., Mourard, D., and Coudé du Foresto, V. 2004b. Cepheid distances from infrared long-baseline interferometry. I. VINCI/VLTI observations of seven Galactic Cepheids. *A&A*, 416:941–953.

Kervella, P., Ségransan, D., and Coudé du Foresto, V. 2004c. Data reduction methods for single-mode optical interferometry. Application to the VLTI two-telescopes beam combiner VINCI. *A&A*, 425:1161–1174.

Kervella, P., Thévenin, F., Ségransan, D., Berthomieu, G., Lopez, B., Morel, P., and Provost, J. 2003. The diameters of alpha Centauri A and B. A comparison of the asteroseismic and VINCI/VLTI views. *A&A*, 404:1087–1097.

Klahr, H. and Bodenheimer, P. 2006. Formation of Giant Planets by Concurrent Accretion of Solids and Gas inside an Anticyclonic Vortex. *ApJ*, 639:432–440.

Knutson, H. A., Charbonneau, D., Allen, L. E., Fortney, J. J., Agol, E., Cowan, N. B., Showman, A. P., Cooper, C. S., and Megeath, S. T. 2007. A map of the day-night contrast of the extrasolar planet HD 189733b. *Nature*, 447:183–186.

Knutson, H. A., Charbonneau, D., Cowan, N. B., Fortney, J. J., Showman, A. P., Agol, E., Henry, G. W., Everett, M. E., and Allen, L. E. 2009. Multiwavelength Constraints on the Day-Night Circulation Patterns of HD 189733b. *ApJ*, 690:822–836.

Koerner, D. W. and Sargent, A. I. 1995. Imaging the Small-Scale Circumstellar Gas Around T Tauri Stars. *AJ*, 109:2138–.

Koerner, D. W., Sargent, A. I., and Ostroff, N. A. 2001. Millimeter-Wave Aperture Synthesis Imaging of Vega: Evidence for a Ring Arc at 95 AU. *ApJ*, 560:L181–L184.

Kraus, S. 2007. Infrared Spectro-Interferometry of Massive Stars: Disks, Winds, Outflows, and Stellar Multiplicity.

Krist, J. E., Ardila, D. R., Golimowski, D. A., Clampin, M., Ford, H. C., Illingworth, G. D., Hartig, G. F., Bartko, F., Benítez, et al. 2005. Hubble Space Telescope Advanced Camera for Surveys Coronagraphic Imaging of the AU Microscopii Debris Disk. *AJ*, 129:1008–1017.

Kuchner, M. J. and Seager, S. 2005. Extrasolar Carbon Planets.

Labeyrie, A. 1975. Interference fringes obtained on VEGA with two optical telescopes. *ApJ*, 196:L71–L75.

Lada, C. J. 1987. Star formation - From OB associations to protostars. 115:1–17.

Lada, C. J. and Adams, F. C. 1992. Interpreting infrared color-color diagrams - Circumstellar disks around low- and intermediate-mass young stellar objects. *ApJ*, 393:278–288.

Lada, C. J., Margulis, M., and Dearborn, D. 1984. The formation and early dynamical evolution of bound stellar systems. *ApJ*, 285:141–152.

Lagarde, S., Lopez, B., Petrov, R. G., Hofmann, K. H., Kraus, S., Jaffe, W., Antonelli, P., Bresson, Y., Leinert, C., and Matter, A. 2008. MATISSE: concept analysis. 7013.

Lagrange, A.-M., Gratadour, D., Chauvin, G., Fusco, T., Ehrenreich, D., Mouillet, D., Rousset, G., Rouan, D., Allard, F., Gendron, É., Charton, J., Mugnier, L., Rabou, P., Montri, J., and Lacombe, F. 2009. A probable giant planet imaged in the β Pictoris disk. VLT/NaCo deep L'-band imaging. *A&A*, 493:L21–L25.

Lane, B. F. and Mutterspaugh, M. W. 2004. Differential Astrometry of Subarcsecond Scale Binaries at the Palomar Testbed Interferometer. *ApJ*, 601:1129–1135.

Lane, B. F., Mutterspaugh, M. W., and Shao, M. 2006. Calibrating an Interferometric Null. *ApJ*, 648:1276–1284.

Laureijs, R. J., Jourdain de Muizon, M., Leech, K., Siebenmorgen, R., Dominik, C., Habing, H. J., Trams, N., and Kessler, M. F. 2002. A 25 micron search for Vega-like disks around main-sequence stars with ISO. *A&A*, 387:285–293.

Lawson, P. 2006. Results of Laboratory Experiments Kin Nulling Interferometry (1998-2006). In *the proceedings of the TPF/Darwin 2006 conference*.

Lawson, P. and Traub, W. 2006. Earth-Like Exoplanets: The Science of NASA's Navigator Program. Technical report, NASA.

Lay, O. P. 2004. Systematic Errors in Nulling Interferometers. *Appl. Opt.*, 43:6100–6123.

Lay, O. P. 2005. Imaging properties of rotating nulling interferometers. *Appl. Opt.*, 44:5859–5871.

Lay, O. P. 2006. Removing instability noise in nulling interferometers. In *Proc. SPIE*, volume 6268.

Le Bouquin, J.-B., Absil, O., Benisty, M., Massi, F., Mérand, A., and Stefl, S. 2009. The spin-orbit alignment of the Fomalhaut planetary system probed by optical long baseline interferometry. *A&A*, 498:L41–L44.

Le Bouquin, J.-B., Bauvir, B., Haguenauer, P., Schöller, M., Rantakyrö, F., and Menardi, S. 2008. First result with AMBER+FINITO on the VLTI: the high-precision angular diameter of V3879 Sagittarii. *A&A*, 481:553–557.

Le Duigou, J. M., Ollivier, M., Léger, A., Cassaing, F., Sorrente, B., Fleury, B., Rousset, G., Absil, O., Mourard, D., et al. 2006. Pegase: a space-based nulling interferometer. In *Proc. SPIE*, volume 6265.

Léger, A. and Herbst, T. 2007. DARWIN mission proposal to ESA. *ArXiv e-prints*, 707.

Léger, A., Ollivier, M., Altweig, K., and Woolf, N. J. 1999. Is the presence of H_2O and O_3 in an exoplanet a reliable signature of a biological activity? *A&A*, 341:304–311.

Leger, A., Rouan, D., Schneider, J., Barge, P., Fridlund, M., Samuel, B., Ollivier, M., Guenther, E., Deleuil, M., Deeg, H. J., Auvergne, M., Alonso, R., Aigrain, S., Alapini, A., Almenara, et al. 2009. Transiting exoplanets from the CoRoT space mission VIII. CoRoT-7b: the first Super-Earth with measured radius. *ArXiv e-prints*.

Léger, A., Selsis, F., Sotin, C., Guillot, T., Despois, D., Mawet, D., Ollivier, M., Labèque, A., Valette, C., Brachet, F., Chazelas, B., and Lammer, H. 2004. A new family of planets? “Ocean-Planets”. *Icarus*, 169:499–504.

Leinert, C., van Boekel, R., Waters, L. B. F. M., Chesneau, O., Malbet, F., Köhler, R., Jaffe, W., Ratzka, T., Dutrey, A., et al. 2004. Mid-infrared sizes of circumstellar disks around Herbig Ae/Be stars measured with MIDI on the VLTI. *A&A*, 423:537–548.

Lin, D. N. C., Bodenheimer, P., and Richardson, D. C. 1996. Orbital migration of the planetary companion of 51 Pegasi to its present location. *Nature*, 380:606–607.

Lin, D. N. C. and Papaloizou, J. 1986. On the tidal interaction between protoplanets and the protoplanetary disk. III - Orbital migration of protoplanets. *ApJ*, 309:846–857.

Lineweaver, C. H. and Grether, D. 2003. What Fraction of Sun-like Stars Have Planets? *ApJ*, 598:1350–1360.

Liu, W. M., Hinz, P. M., Hoffmann, W. F., Brusa, G., Miller, D., and Kenworthy, M. A. 2005. Resolved Mid-Infrared Emission around AB Aurigae and V892 Tauri with Adaptive Optics Nulling Interferometric Observations. *ApJ*, 618:L133–L136.

Liu, W. M., Hinz, P. M., Hoffmann, W. F., Brusa, G., Miller, D., and Kenworthy, M. A. 2009. Observations of Main-Sequence Stars and Limits on Exozodical Dust with Nulling Interferometry. *ApJ*, 693:1500–1507.

Liu, W. M., Hinz, P. M., Hoffmann, W. F., Brusa, G., Wildi, F., Miller, D., Lloyd-Hart, M., Kenworthy, M. A., McGuire, P. C., and Angel, J. R. P. 2004. Adaptive Optics Nulling Interferometric Constraints on the Mid-Infrared Exozodiacal Dust Emission around Vega. *ApJ*, 610:L125–L128.

Liu, W. M., Hinz, P. M., Meyer, M. R., Mamajek, E. E., Hoffmann, W. F., Brusa, G., Miller, D., and Kenworthy, M. A. 2007. Observations of Herbig Ae Disks with Nulling Interferometry. *ApJ*, 658:1164–1172.

Liu, W. M., Hinz, P. M., Meyer, M. R., Mamajek, E. E., Hoffmann, W. F., and Hora, J. L. 2003. A Resolved Circumstellar Disk around the Herbig Ae Star HD 100546 in the Thermal Infrared. *ApJ*, 598:L111–L114.

Lovelock, J. E. 1975. Thermodynamics and the Recognition of Alien Biospheres. *Royal Society of London Proceedings Series B*, 189:167–180.

Lovis, C., Mayor, M., Pepe, F., Alibert, Y., Benz, W., Bouchy, F., Correia, A. C. M., Laskar, J., Mordasini, C., Queloz, D., Santos, N. C., Udry, S., Bertaux, J.-L., and Sivan, J.-P. 2006. An extrasolar planetary system with three Neptune-mass planets. *Nature*, 441:305–309.

Lucas, P. W. and Roche, P. F. 2000. A population of very young brown dwarfs and free-floating planets in Orion. *MNRAS*, 314:858–864.

Macintosh, B. A., Graham, J. R., Palmer, D. W., Doyon, R., Dunn, J., Gavel, D. T., Larkin, J., Oppenheimer, B., Saddlemyer, L., Sivaramakrishnan, A., Wallace, J. K., Bauman, B., Erickson, D. A., Marois, C., Poyneer, L. A., and Soummer, R. 2008. The Gemini Planet Imager: from science to design to construction. In *Proc. SPIE*, volume 7015.

Malbet, F., Berger, J.-P., Colavita, M. M., Koresko, C. D., Beichman, C., Boden, A. F., Kulkarni, S. R., Lane, B. F., Mobley, D. W., Pan, X. P., Shao, M., van Belle, G. T., and Wallace, J. K. 1998. FU Orionis Resolved by Infrared Long-Baseline Interferometry at a 2 AU Scale. *ApJ*, 507:L149–L152.

Malbet, F., Buscher, D., Weigelt, G., Garcia, P., Gai, M., Lorenzetti, D., Surdej, J., Hron, J., Neuhäuser, R., Kern, P., et al. 2008. VSI: the VLTI spectro-imager. 7013.

Malbet, F., Kern, P., Schanen-Duport, I., Berger, J.-P., Rousselet-Perraut, K., and Benech, P. 1999. Integrated optics for astronomical interferometry. I. Concept and astronomical applications. *A&AS*, 138:135–145.

Malbet, F., Lachaume, R., Berger, J.-P., Colavita, M. M., di Folco, E., Eisner, J. A., Lane, B. F., Millan-Gabet, R., Ségransan, D., and Traub, W. A. 2005. New insights on the AU-scale circumstellar structure of FU Orionis. *A&A*, 437:627–636.

Mannings, V. and Barlow, M. J. 1998. Candidate Main-Sequence Stars with Debris Disks: A New Sample of Vega-like Sources. *ApJ*, 497:330–+.

Mannings, V., Boss, A., and Russell, S. 2000. Protostars and Planets IV. *Icarus*, 143:1–+.

Marcy, G., Butler, R. P., Fischer, D., Vogt, S., Wright, J. T., Tinney, C. G., and Jones, H. R. A. 2005. Observed Properties of Exoplanets: Masses, Orbits, and Metallicities. *Progress of Theoretical Physics Supplement*, 158:24–42.

Marois, C., Macintosh, B., Barman, T., Zuckerman, B., Song, I., Patience, J., Lafrenière, D., and Doyon, R. 2008. Direct Imaging of Multiple Planets Orbiting the Star HR 8799. *Science*, 322:1348–.

Matsuo, T., Shibai, H., Ootsubo, T., and Tamura, M. 2007. Planetary Formation Scenarios Revisited: Core-Accretion Versus Disk Instability. *ArXiv Astrophysics e-prints*.

Mauron, N. and Dole, H. 1998. An attempt to detect the dust disk of VEGA by photopolarimetry, and constraints on the grain size. *A&A*, 337:808–814.

Mawet, D. 2006. *Subwavelength gratings for extrasolar planetary system imaging and characterization*. PhD thesis, Liège University, Liège, Belgium.

Mayor, M., Bonfils, X., Forveille, T., Delfosse, X., Udry, S., Bertaux, J.-L., Beust, H., Bouchy, F., Lovis, C., Pepe, F., Perrier, C., Queloz, D., and Santos, N. 2009a. The HARPS search for southern extra-solar planets. XVIII. An Earth-mass planet in the GJ 581 planetary system. *A&A*, in press.

Mayor, M. and Queloz, D. 1995. A Jupiter-Mass Companion to a Solar-Type Star. *Nature*, 378:355–+.

Mayor, M., Udry, S., Lovis, C., Pepe, F., Queloz, D., Benz, W., Bertaux, J.-L., Bouchy, F., Mordasini, C., and Segransan, D. 2009b. The HARPS search for southern extra-solar planets. XIII. A planetary system with 3 super-Earths (4.2, 6.9, and 9.2 M_⊕). *A&A*, 493:639–644.

McAlister, H. A., ten Brummelaar, T. A., Gies, D. R., Huang, W., Bagnuolo, Jr., W. G., Shure, M. A., Sturmann, J., Sturmann, L., Turner, N. H., Taylor, S. F., Berger, D. H., Baines, E. K., Grundstrom, E., Ogden, C., Ridgway, S. T., and van Belle, G. 2005. First Results from the CHARA Array. I. An Interferometric and Spectroscopic Study of the Fast Rotator α Leonis (Regulus). *ApJ*, 628:439–452.

McCaughrean, M. J. and O’dell, C. R. 1996. Direct Imaging of Circumstellar Disks in the Orion Nebula. *AJ*, 111:1977–+.

Mendoza V., E. E. 1966. Infrared Photometry of T Tauri Stars and Related Objects. *ApJ*, 143:1010–+.

Mennesson, B., Léger, A., and Ollivier, M. 2005. Direct detection and characterization of extrasolar planets: The Mariotti space interferometer. *Icarus*, 178:570–588.

Mennesson, B. and Mariotti, J. M. 1997. Array Configurations for a Space Infrared Nulling Interferometer Dedicated to the Search for Earthlike Extrasolar Planets. *Icarus*, 128:202–212.

Mérand, A. 2008. Determining Accurate Distances to Cepheids Using the Interferometric Baade-Wesselink Method: Possible Interferometric Biases. *28*:53–59.

Mérand, A., Bordé, P., and Coudé Du Foresto, V. 2005. A catalog of bright calibrator stars for 200-m baseline near-infrared stellar interferometry. *A&A*, 433:1155–1162.

Michelson, A. A. 1891. Measurement of Jupiter’s Satellites by Interference. *Nature*, 45:160–161.

Michelson, A. A. and Pease, F. G. 1921. Measurement of the diameter of alpha Orionis with the interferometer. *ApJ*, 53:249–259.

Millan-Gabet, R., Monnier, J. D., Akeson, R. L., Hartmann, L., Berger, J.-P., Tannirkulam, A., Melnikov, S., Billmeier, R., et al. 2006. Keck Interferometer Observations of FU Orionis Objects. *ApJ*, 641:547–555.

Millan-Gabet, R., Schloerb, F. P., and Traub, W. A. 2001. Spatially Resolved Circumstellar Structure of Herbig AE/BE Stars in the Near-Infrared. *ApJ*, 546:358–381.

Millan-Gabet, R. S., Schloerb, F. P., and Traub, W. A. 1998. High Angular Resolution Observations of Herbig AeBe Stars with the Infrared Optical Telescope Array. *30*:1361–+.

Miroshnichenko, A., Ivezić, Ž., Vinković, D., and Elitzur, M. 1999. Dust Emission from Herbig AE/BE Stars: Evidence for Disks and Envelopes. *ApJ*, 520:L115–L118.

Monnier, J. D. 2000. An Introduction to Closure Phases. pages 203–+.

Monnier, J. D., Berger, J., Millan-Gabet, R., Traub, W. A., Schloerb, F. P., Pedretti, E., Benisty, M., Carleton, N. P., Hagenauer, P., Kern, P., Labeye, P., Lacasse, M. G., Malbet, F., Perraut, K., Pearlman, M., and Zhao, M. 2006. Few Skewed Disks Found in First Closure-Phase Survey of Herbig Ae/Be Stars. *ApJ*, 647:444–463.

Monnier, J. D. and Millan-Gabet, R. 2002. On the Interferometric Sizes of Young Stellar Objects. *ApJ*, 579:694–698.

Monnier, J. D., Millan-Gabet, R., Billmeier, R., Akeson, R. L., Wallace, D., Berger, J.-P., Calvet, N., D’Alessio, P., Danchi, et al. 2005. The Near-Infrared Size-Luminosity Relations for Herbig Ae/Be Disks. *ApJ*, 624:832–840.

Monnier, J. D., Traub, W. A., Schloerb, F. P., Millan-Gabet, R., Berger, J., Pedretti, E., Carleton, N. P., Kraus, S., Lacasse, et al. 2004. First Results with the IOTA3 Imaging Interferometer: The Spectroscopic Binaries λ Virginis and WR 140. *ApJ*, 602:L57–L60.

Monnier, J. D., Zhao, M., Pedretti, E., Thureau, N., Ireland, M., Muirhead, P., Berger, J.-P., Millan-Gabet, R., Van Belle, G., ten Brummelaar, T., McAlister, H., Ridgway, S., Turner, N., Sturmann, L., Sturmann, J., and Berger, D. 2007. Imaging the Surface of Altair. *Science*, 317:342–.

Mordasini, C., Alibert, Y., Benz, W., and Naef, D. 2009. Extrasolar planet population synthesis II: Statistical comparison with observation. *ArXiv e-prints*.

Moutou, C., Bruntt, H., Guillot, T., Shporer, A., Guenther, E., Aigrain, S., Almenara, J. M., Alonso, R., Auvergne, M., Baglin, A., Barbieri, M., Barge, P., Benz, W., Bordé, P., Bouchy, F., et al. 2008. Transiting exoplanets from the CoRoT space mission. V. CoRoT-Exo-4b: stellar and planetary parameters. *A&A*, 488:L47–L50.

Mozurkewich, D., Armstrong, J. T., Hindsley, R. B., Quirrenbach, A., Hummel, C. A., Hutter, D. J., Johnston, K. J., Hajian, A. R., Elias, II, N. M., Buscher, D. F., and Simon, R. S. 2003. Angular Diameters of Stars from the Mark III Optical Interferometer. *AJ*, 126:2502–2520.

Mozurkewich, D., Johnston, K. J., Simon, R. S., Bowers, P. F., Gaume, R., Hutter, D. J., Colavita, M. M., Shao, M., and Pan, X. P. 1991. Angular diameter measurements of stars. *AJ*, 101:2207–2219.

Muterspaugh, M. W., Lane, B. F., Konacki, M., Burke, B. F., Colavita, M. M., Kulkarni, S. R., and Shao, M. 2005. PHASES High-Precision Differential Astrometry of δ Equulei. *AJ*, 130:2866–2875.

Muterspaugh, M. W., Lane, B. F., Kulkarni, S. R., Burke, B. F., Colavita, M. M., and Shao, M. 2006. Limits to Tertiary Astrometric Companions in Binary Systems. *ApJ*, 653:1469–1479.

Neuhäuser, R., Guenther, E. W., Wuchterl, G., Mugrauer, M., Bedalov, A., and Hauschildt, P. H. 2005. Evidence for a co-moving sub-stellar companion of GQ Lup. *A&A*, 435:L13–L16.

Nordgren, T. E., Germain, M. E., Benson, J. A., Mozurkewich, D., Sudol, J. J., Elias, II, N. M., Hajian, A. R., White, N. M., Hutter, D. J., Johnston, K. J., Gauss, F. S., Armstrong, J. T., Pauls, T. A., and Rickard, L. J. 1999. Stellar Angular Diameters of Late-Type Giants and Supergiants Measured with the Navy Prototype Optical Interferometer. *AJ*, 118:3032–3038.

O'Dell, C. R., Ferland, G. J., and Henney, W. J. 2001. Measurement and Interpretation of Deuterium-Line Emission in the Orion Nebula. *ApJ*, 556:203–214.

O'dell, C. R. and Wong, K. 1996. Hubble Space Telescope Mapping of the Orion Nebula. I. A Survey of Stars and Compact Objects. *AJ*, 111:846–+.

Owen, T. 1980. The Search for Early Forms of Life in Other Planetary Systems - Future Possibilities Afforded by Spectroscopic Techniques. In Papagiannis, M. D., editor, *Strategies for the Search for Life in the Universe*, volume 83 of *Astrophysics and Space Science Library*, pages 177–+.

Paczynski, B. 1980. A model of the subdwarf binary system LB 3459. *Acta Astronomica*, 30:113–125.

Pedretti, E., Millan-Gabet, R., Monnier, J. D., Traub, W. A., Carleton, N. P., Berger, J., Lacasse, M. G., Schloerb, F. P., and Brewer, M. K. 2004. The PICNIC Interferometry Camera at IOTA. *PASP*, 116:377–389.

Perrin, G. 2003. The calibration of interferometric visibilities obtained with single-mode optical interferometers. Computation of error bars and correlations. *A&A*, 400:1173–1181.

Perrin, G., Ridgway, S. T., Mennesson, B., Cotton, W. D., Woillez, J., Verhoelst, T., Schuller, P., Coudé du Foresto, V., Traub, W. A., Millan-Gabet, R., and Lacasse, M. G. 2004. Unveiling Mira stars behind the molecules. Confirmation of the molecular layer model with narrow band near-infrared interferometry. *A&A*, 426:279–296.

Perryman, M. A. C. 2000. Extra-solar planets. *Reports of Progress in Physics*, 63:1209–1272.

Peters., R., Gappinger, R., Lawson, P., and Lay, O. 2009. Exoplanet Interferometry Technology Milestone 3 Report: Broadband starlight suppression demonstration. *JPL*, Document D-60326.

Petrov, R. G. 1989. Differential Interferometry. pages 249–+.

Petrov, R. G., Malbet, F., Weigelt, G., Antonelli, P., Beckmann, U., Bresson, Y., Chelli, A., Dugué, M., Duvert, G., Gennari, S., Glück, L., Kern, P., Lagarde, S., Le Coarer, E., Lisi, F., et al. 2007. AMBER, the near-infrared spectro-interferometric three-telescope VLTI instrument. *A&A*, 464:1–12.

Pollack, J. B. 1984. Origin and History of the Outer Planets: Theoretical Models and Observations L Constraints. *ARA&A*, 22:389–424.

Pollack, J. B., Hubickyj, O., Bodenheimer, P., Lissauer, J. J., Podolak, M., and Greenzweig, Y. 1996. Formation of the Giant Planets by Concurrent Accretion of Solids and Gas. *Icarus*, 124:62–85.

Pont, F., Gilliland, R. L., Knutson, H., Holman, M., and Charbonneau, D. 2009. Transit infrared spectroscopy of the hot Neptune around GJ 436 with the Hubble Space Telescope. *MNRAS*, 393:L6–L10.

Pravdo, S. H. and Shaklan, S. B. 2009. An ultracool Star's Candidate Planet. *ApJ*, 700:623–632.

Quirrenbach, A. 2009. The development of astronomical interferometry. *Experimental Astronomy*, 26:49–63.

Quirrenbach, A., Bjorkman, K. S., Bjorkman, J. E., Hummel, C. A., Buscher, D. F., Armstrong, J. T., Mozurkewich, D., Elias, II, N. M., and Babler, B. L. 1997. Constraints on the Geometry of Circumstellar Envelopes: Optical Interferometric and Spectropolarimetric Observations of Seven Be Stars. *ApJ*, 479:477–+.

Quirrenbach, A., Mozurkewich, D., Buscher, D. F., Hummel, C. A., and Armstrong, J. T. 1996. Angular diameter and limb darkening of Arcturus. *A&A*, 312:160–166.

Raban, D., Jaffe, W., Röttgering, H., Meisenheimer, K., and Tristram, K. R. W. 2009. Resolving the obscuring torus in NGC 1068 with the power of infrared interferometry: revealing the inner funnel of dust. *MNRAS*, 394:1325–1337.

Raymond, S. N., Mandell, A. M., and Sigurdsson, S. 2006. Exotic Earths: Forming Habitable Worlds with Giant Planet Migration. *Science*, 313:1413–1416.

Reffert, S., Ségransan, D., Launhardt, R., Henning, T., Queloz, D., Quirrenbach, A., Pepe, F., Setiawan, J., and Weise, P. 2006. The PRIMA astrometric planet search: goals and prospects. In *Proc. SPIE*, volume 6268.

Ricci, L., Robberto, M., and Soderblom, D. R. 2008. The Hubble Space Telescope/Advanced Camera for Surveys Atlas of Protoplanetary Disks in the Great Orion Nebula. *AJ*, 136:2136–2151.

Richardson, L. J., Deming, D., Horning, K., Seager, S., and Harrington, J. 2007. A spectrum of an extrasolar planet. *Nature*, 445:892–895.

Rieke, G. H., Su, K. Y. L., Stansberry, J. A., Trilling, D., Bryden, G., Muzerolle, J., White, B., Gorlova, N., Young, E. T., Beichman, C. A., Stapelfeldt, K. R., and Hines, D. C. 2005. Decay of Planetary Debris Disks. *ApJ*, 620:1010–1026.

Rivera, E. J., Lissauer, J. J., Butler, R. P., Marcy, G. W., Vogt, S. S., Fischer, D. A., Brown, T. M., Laughlin, G., and Henry, G. W. 2005. A $7.5 M_{\oplus}$ Planet Orbiting the Nearby Star, GJ 876. *ApJ*, 634:625–640.

Roberge, A., Noecker, M. C., Glassman, T. M., Oakley, P., Turnbull, M. C., and NWO Study Team 2009. Detecting Exoplanets with the New Worlds Observer: The Problem of Exozodiacal Dust. In *Bulletin of the American Astronomical Society*, volume 41 of *Bulletin of the American Astronomical Society*, pages 196–+.

Rogers, A. E. E., Hinteregger, H. F., Whitney, A. R., Counselman, C. C., Shapiro, I. I., Wittels, J. J., Klemperer, W. K., Warnock, W. W., Clark, T. A., and Hutton, L. K. 1974. The structure of radio sources 3C 273B and 3C 84 deduced from the 'closure' phases and visibility amplitudes observed with three-element interferometers. *ApJ*, 193:293–301.

Rousselet-Perraut, K., Stehlé, C., Lanz, T., Le Bouquin, J. B., Boudouyen, T., Kilbinger, M., Kochukhov, O., and Jankov, S. 2004. Stellar activity and magnetism studied by optical interferometry. *A&A*, 422:193–203.

Rydgren, A. E., Strom, S. E., and Strom, K. M. 1976. The nature of the objects of Joy - A study of the T Tauri phenomenon. *ApJS*, 30:307–336.

Ryle, M. and Hewish, A. 1960. The synthesis of large radio telescopes. *MNRAS*, 120:220–+.

Santos, N. C., Israelian, G., Mayor, M., Bento, J. P., Almeida, P. C., Sousa, S. G., and Ecuvillon, A. 2005. Spectroscopic metallicities for planet-host stars: Extending the samples. *A&A*, 437:1127–1133.

Sasselov, D. D. and Lecar, M. 2000. On the Snow Line in Dusty Protoplanetary Disks. *ApJ*, 528:995–998.

Schneider, J. 2009. The extrasolar planet encyclopedia, <http://exoplanet.eu/catalog.php>.

Schöller, M., Wilhelm, R., and Koehler, B. 2000. Modeling the imaging process in optical stellar interferometers. *A&AS*, 144:541–552.

Ségransan, D., Kervella, P., Forveille, T., and Queloz, D. 2003. First radius measurements of very low mass stars with the VLTI. *A&A*, 397:L5–L8.

Segura, A., Krelove, K., Kasting, J. F., Sommerlatt, D., Meadows, V., Crisp, D., Cohen, M., and Mlawer, E. 2003. Ozone Concentrations and Ultraviolet Fluxes on Earth-Like Planets Around Other Stars. *Astrobiology*, 3:689–708.

Selsis, F., Chazelas, B., Borde, P., Ollivier, M., Brachet, F., Decaudin, M., Bouchy, F., Ehrenreich, D., Griessmeier, J. , Lammer, H., Sotin, C., Grasset, O., Moutou, C., Barge, P., Deleuil, M., Mawet, D., Despois, D., Kasting, J. F., and Leger, A. 2007. Could we identify hot Ocean-Planets with CoRoT, Kepler and Doppler velocimetry? *ArXiv Astrophysics e-prints*.

Selsis, F., Despois, D., and Parisot, J.-P. 2002. Signature of life on exoplanets: Can Darwin produce false positive detections? *A&A*, 388:985–1003.

Serabyn, E. 1999. Nanometer-Level Path-Length Control Scheme for Nulling Interferometry. *Appl. Opt.*, 38:4213–4216.

Serabyn, E., Booth, A., Colavita, M. M., Crawford, S., Garcia, J., Gathright, J., Hrynevych, M., Koresko, C., Ligon, R., Mennesson, et al. 2006. Science observations with the Keck Interferometer Nuller. In *Proc. SPIE*, volume 6268.

Shao, M. 2006. Search for terrestrial planets with SIM Planet Quest. In *Proc. SPIE*, volume 6268.

Shao, M. and Colavita, M. M. 1992. Potential of long-baseline infrared interferometry for narrow-angle astrometry. *A&A*, 262:353–358.

Shao, M., Colavita, M. M., Hines, B. E., Staelin, D. H., and Hutter, D. J. 1988. The Mark III stellar interferometer. *A&A*, 193:357–371.

Shao, M. and Staelin, D. H. 1980. First fringe measurements with a phase-tracking stellar interferometer. *Appl. Opt.*, 19:1519–1522.

Siegler, N., Muzerolle, J., Young, E. T., Rieke, G. H., Mamajek, E. E., Trilling, D. E., Gorlova, N., and Su, K. Y. L. 2007. Spitzer 24 μ m Observations of Open Cluster IC 2391 and Debris Disk Evolution of FGK Stars. *ApJ*, 654:580–594.

Skilling, J. 1984. The maximum entropy method for data analysis (reply). *Nature*, 312:382–+.

Smith, B. A. and Terrile, R. J. 1984. A circumstellar disk around Beta Pictoris. *Science*, 226:1421–1424.

Smith, N., Bally, J., Shuping, R. Y., Morris, M., and Kassis, M. 2005. Thermal Dust Emission from Proplyds, Unresolved Disks, and Shocks in the Orion Nebula. *AJ*, 130:1763–1777.

Sozzetti, A., Casertano, S., Lattanzi, M. G., and Spagna, A. 2003. The GAIA astrometric survey of the solar neighborhood and its contribution to the target database for DARWIN/TPF. In Fridlund, M., Henning, T., and Lacoste, H., editors, *Earths: DARWIN/TPF and the Search for Extrasolar Terrestrial Planets*, volume 539 of *ESA Special Publication*, pages 605–610.

Stankov, A. 2005. All sky target stars catalogue - no limit in ecliptic latitude.

Stapelfeldt, K. R., Holmes, E. K., Chen, C., Rieke, G. H., Su, K. Y. L., Hines, D. C., Werner, M. W., Beichman, C. A., Jura, M., Padgett, D. L., Stansberry, J. A., Bendo, G., Cadien, J., Marengo, et al. 2004. First Look at the Fomalhaut Debris Disk with the Spitzer Space Telescope. *ApJS*, 154:458–462.

Stark, C. C., Kuchner, M. J., Traub, W. A., Monnier, J. D., Serabyn, E., and Colavita, M. 2009. Keck Interferometer Nuller Observations of the 51 Ophiuchi Circumstellar Dust Disk. 41:501–+.

Stee, P. 2003. Estimation of the mass loss, opening angle and mass of Be circumstellar disks from Brmathsf γ continuum emission and interferometric measurements. *A&A*, 403:1023–1029.

Sterken, V. 2005. Impact of the space and satellite environment on the optical path differences of Darwin. Master's thesis, Delft University of Technology.

Sterken, V., Kamp, A., Kampen, S., and van den Dool, T. 2005. Impact of the space environment on Darwin and a low earth orbit (LEO) demonstration mission. In *Proceedings of the IAC (2005)*., IAC-05- C.2.5.

Su, K. Y. L., Rieke, G. H., Misselt, K. A., Stansberry, J. A., Moro-Martin, A., Stapelfeldt, K. R., Werner, M. W., Trilling, D. E., Bendo, G. J., Gordon, K. D., Hines, D. C., Wyatt, M. C., Holland, et al. 2005. The Vega Debris Disk: A Surprise from Spitzer. *ApJ*, 628:487–500.

Sudarsky, D., Burrows, A., and Hubeny, I. 2003. Theoretical Spectra and Atmospheres of Extrasolar Giant Planets. *ApJ*, 588:1121–1148.

Sudarsky, D., Burrows, A., and Pinto, P. 2000. Albedo and Reflection Spectra of Extrasolar Giant Planets. *ApJ*, 538:885–903.

Swain, M., Vasisht, G., Akeson, R., Monnier, J., Millan-Gabet, R., Serabyn, E., Creech-Eakman, M., van Belle, G., Beletic, J., Beichman, C., Boden, A., Booth, A., Colavita, M., Gathright, J., et al. 2003. Interferometer Observations of Subparsec-Scale Infrared Emission in the Nucleus of NGC 4151. *ApJ*, 596:L163–L166.

Swain, M. R., Bouwman, J., Akeson, R. L., Lawler, S., and Beichman, C. A. 2008a. The Mid-Infrared Spectrum of the Transiting Exoplanet HD 209458b. *ApJ*, 674:482–497.

Swain, M. R., Vasisht, G., and Tinetti, G. 2008b. The presence of methane in the atmosphere of an extrasolar planet. *Nature*, 452:329–331.

Swain, M. R., Vasisht, G., Tinetti, G., Bouwman, J., Chen, P., Yung, Y., Deming, D., and Deroo, P. 2009. Molecular Signatures in the Near-Infrared Dayside Spectrum of HD 189733b. *ApJ*, 690:L114–L117.

Takeuchi, T. and Artymowicz, P. 2001. Dust Migration and Morphology in Optically Thin Circumstellar Gas Disks. *ApJ*, 557:990–1006.

Tango, W. J., Davis, J., Jacob, A. P., Mendez, A., North, J. R., O'Byrne, J. W., Seneta, E. B., and Tuthill, P. G. 2009. A new determination of the orbit and masses of the Be binary system δ Scorpis. *MNRAS*, 396:842–848.

ten Brummelaar, T. A., McAlister, H. A., Ridgway, S., Gies, D. R., Sturmann, J., Sturmann, L., Turner, N. H., Mérand, A., Thompson, R., Farrington, C. D., and Goldfinger, P. J. 2008. An update on the CHARA array. In *Proc. SPIE*, volume 7013.

ten Brummelaar, T. A., McAlister, H. A., Ridgway, S. T., Bagnuolo, Jr., W. G., Turner, N. H., Sturmann, L., Sturmann, J., Berger, D. H., Ogden, C. E., Cadman, R., Hartkopf, W. I., Hopper, C. H., and Shure, M. A. 2005. First Results from the CHARA Array. II. A Description of the Instrument. *ApJ*, 628:453–465.

Tinetti, G., Vidal-Madjar, A., Liang, M.-C., Beaulieu, J.-P., Yung, Y., Carey, S., Barber, R. J., Tenenyson, J., Ribas, I., Allard, N., Ballester, G. E., Sing, D. K., and Selsis, F. 2007. Water vapour in the atmosphere of a transiting extrasolar planet. *Nature*, 448:169–171.

Traub, W. A., Ahearn, A., Carleton, N. P., Berger, J., Brewer, M. K., Hofmann, K., Kern, P. Y., Lacasse, M. G., Malbet, F., Millan-Gabet, R., Monnier, J. D., Ohnaka, K., Pedretti, E., Ragland, S., Schloerb, F. P., Souccar, K., and Weigelt, G. 2003. New Beam-Combination Techniques at IOTA. *ApJ*, 628:45–52.

Traub, W. A., Levine, M., Shaklan, S., Kasting, J., Angel, J. R., Brown, M. E., Brown, R. A., Burrows, C., Clampin, M., Dressler, A., et al. 2006. TPF-C: status and recent progress. In *Proc. SPIE*, volume 6268.

Trilling, D. E., Bryden, G., Beichman, C. A., Rieke, G. H., Su, K. Y. L., Stansberry, J. A., Blaylock, M., Stapelfeldt, K. R., Beeman, J. W., and Haller, E. E. 2008. Debris Disks around Sun-like Stars. *ApJ*, 674:1086–1105.

Trilling, D. E., Lunine, J. I., and Benz, W. 2002. Orbital migration and the frequency of giant planet formation. *A&A*, 394:241–251.

Tuthill, P. G., Monnier, J. D., and Danchi, W. C. 1999. A dusty pinwheel nebula around the massive star WR104. *Nature*, 398:487–489.

Tuthill, P. G., Monnier, J. D., Danchi, W. C., Hale, D. D. S., and Townes, C. H. 2002. Imaging the Disk around the Luminous Young Star LkH α 101 with Infrared Interferometry. *ApJ*, 577:826–838.

Udalski, A., Szymanski, M. K., Kubiak, M., Pietrzynski, G., Soszynski, I., Zebrun, K., Szewczyk, O., and Wyrzykowski, L. 2004. The Optical Gravitational Lensing Experiment. Planetary and Low-Luminosity Object Transits in the Fields of Galactic Disk. Results of the 2003 OGLE Observing Campaigns. *Acta Astronomica*, 54:313–345.

Udry, S., Bonfils, X., Delfosse, X., Forveille, T., Mayor, M., Perrier, C., Bouchy, F., Lovis, C., Pepe, F., Queloz, D., and Bertaux, J.-L. 2007. The HARPS search for southern extra-solar planets. XI. Super-Earths (5 and 8 M \oplus) in a 3-planet system. *A&A*, 469:L43–L47.

Valencia, D., Sasselov, D. D., and O'Connell, R. J. 2007. Detailed Models of Super-Earths: How Well Can We Infer Bulk Properties? *ApJ*, 665:1413–1420.

van Belle, G. T., Ciardi, D. R., ten Brummelaar, T., McAlister, H. A., Ridgway, S. T., Berger, D. H., Goldfinger, P. J., Sturmann, J., Sturmann, L., Turner, N., Boden, A. F., Thompson, R. R., and Coyne, J. 2006. First Results from the CHARA Array. III. Oblateness, Rotational Velocity, and Gravity Darkening of Alderamin. *ApJ*, 637:494–505.

van Belle, G. T., Ciardi, D. R., Thompson, R. R., Akeson, R. L., and Lada, E. A. 2001. Altair's Oblateness and Rotation Velocity from Long-Baseline Interferometry. *ApJ*, 559:1155–1164.

van Boekel, R., Kervella, P., Schöller, M., Herbst, T., Brandner, W., de Koter, A., Waters, L. B. F. M., Hillier, D. J., Paresce, F., Lenzen, R., and Lagrange, A.-M. 2003. Direct measurement of the size and shape of the present-day stellar wind of eta Carinae. *A&A*, 410:L37–L40.

van Boekel, R., Min, M., Waters, L. B. F. M., de Koter, A., Dominik, C., van den Ancker, M. E., and Bouwman, J. 2005. A 10 μm spectroscopic survey of Herbig Ae star disks: Grain growth and crystallization. *A&A*, 437:189–208.

van der Blieck, N. S., Prusti, T., and Waters, L. B. F. M. 1994. Vega: smaller dust grains in a larger shell. *A&A*, 285:229–232.

Villien, A., Morand, J., Delpech, M., and Guidotti, P. 2007. GNC for the Pegase Mission. 17th IFAC Symposium on Automatic Control in Aerospace.

Vinković, D., Ivezić, Ž., Jurkić, T., and Elitzur, M. 2006. Near-Infrared and the Inner Regions of Protoplanetary Disks. *ApJ*, 636:348–361.

Vinković, D., Ivezić, Ž., Miroshnichenko, A. S., and Elitzur, M. 2003. Discs and haloes in pre-main-sequence stars. *MNRAS*, 346:1151–1161.

Ward, W. R. 1997. Protoplanet Migration by Nebula Tides. *Icarus*, 126:261–281.

Ward, W. R. 2004. On Type III Protoplanet Migration. *AGU Fall Meeting Abstracts*, pages A6+.

Weiner, J. 2004. Mira's Apparent Size Variations due to a Surrounding Semiopaque H₂O Layer. *ApJ*, 611:L37–L40.

Weiner, J., Danchi, W. C., Hale, D. D. S., McMahon, J., Townes, C. H., Monnier, J. D., and Tuthill, P. G. 2000. Precision Measurements of the Diameters of α Orionis and α Ceti at 11 Microns. *ApJ*, 544:1097–1100.

Weiner, J., Hale, D. D. S., and Townes, C. H. 2003. Interferometry on Mira in the Mid-Infrared: Cyclic Variability of the Continuum Diameter and the Effect of Spectral Lines on Apparent Size. *ApJ*, 588:1064–1071.

Werner, M. W., Roellig, T. L., Low, F. J., Rieke, G. H., Rieke, M., Hoffmann, W. F., Young, E., Houck, J. R., Brandl, B., Fazio, G. G., Hora, J. L., Gehrz, R. D., Helou, G., Soifer, B. T., Stauffer, J., Keene, J., Eisenhardt, P., Gallagher, D., Gautier, T. N., Irace, W., Lawrence, C. R., Simmons, L., Van Cleve, J. E., Jura, M., Wright, E. L., and Cruikshank, D. P. 2004. The Spitzer Space Telescope Mission. *ApJS*, 154:1–9.

Wilking, B. A., Doering, C. R., Harvey, P. M., Lada, C. J., and Joy, M. 1984. The formation of massive stars along the W5 ionization front. *ApJ*, 279:291–303.

Wilner, D. J., Holman, M. J., Kuchner, M. J., and Ho, P. T. P. 2002. Structure in the Dusty Debris around Vega. *ApJ*, 569:L115–L119.

Wittkowski, M., Kervella, P., Arsenault, R., Paresce, F., Beckert, T., and Weigelt, G. 2004. VLTI/VINCI observations of the nucleus of NGC 1068 using the adaptive optics system MACAO. *A&A*, 418:L39–L42.

Wolszczan, A. and Frail, D. A. 1992. A planetary system around the millisecond pulsar PSR1257 + 12. *Nature*, 355:145–147.

Wyatt, M. C. and Dent, W. R. F. 2002. Collisional processes in extrasolar planetesimal discs - dust clumps in Fomalhaut's debris disc. *MNRAS*, 334:589–607.

Wyatt, M. C., Smith, R., Greaves, J. S., Beichman, C. A., Bryden, G., and Lisse, C. M. 2007. Transience of Hot Dust around Sun-like Stars. *ApJ*, 658:569–583.

Zhao, M., Gies, D., Monnier, J. D., Thureau, N., Pedretti, E., Baron, F., Merand, A., ten Brummelaar, T., McAlister, H., Ridgway, S. T., Turner, N., Sturmann, J., Sturmann, L., Farrington, C., and Goldfinger, P. J. 2008. First Resolved Images of the Eclipsing and Interacting Binary β Lyrae. *ApJ*, 684:L95–L98.